FIRST OBSERVATION OF ^{7}BE SOLAR NEUTRINOS WITH KAMLAND

by

GREGORY J. KEEFER

A DISSERTATION

Submitted in partial fullfillment of the requirements
for the degree of Doctor of Philosophy
in the Department of Physics
in the Graduate School of
The University of Alabama

TUSCALOOSA, ALABAMA

2009

Abstract

The international KamLAND collaboration operates a 1 kton liquid scintillation detector in the Kamioka mine in Gifu, Japan. KamLAND's main scientific results are the precision measurement of the solar $\Delta m^2{}_{12} = 7.58\ ^{+0.14}_{-0.13}$ (stat) $^{+0.15}_{-0.15}$ (syst) and $\tan^2\theta_{12} = 0.56\ ^{+0.10}_{-0.07}$ (stat) $^{+0.10}_{-0.06}$ (syst) utilizing reactor $\bar{\nu}_e$ and first evidence for the observation of geologically produced anti-neutrinos.

In an effort to extend KamLAND's scientific reach, extensive research has been performed on preparing a spectroscopic measurement of ^{7}Be solar ν_es. This work provides the first inclusive analysis of KamLAND's backgrounds below 1 MeV. ^{85}Kr and ^{210}Pb, dissolved in KamLAND liquid scintillator, were found to be the dominant source of low energy backgrounds. The concentration of these ultra-trace contaminants were determined to be 10^{-20} g/g. This is more then 6 orders of magnitude lower then commercially available ultra-pure liquids. To attain a signal-to-background ratio suitable for the detection of ^{7}Be solar ν_es, the concentration of these contaminants had to be reduced by 5 orders of magnitude.

A comprehensive study of ^{210}Pb removal was undertaken over the course of this thesis. This work further covers techniques for the removal of ^{220}Rn, ^{222}Rn and their daughter nuclei from liquid scintillator at concentrations of 10^{-18} g/g. Purification techniques studied in this work include water extraction, isotope exchange, adsorption, and distillation. These laboratory studies guided the design and implementation of a large scale purification system in the Kamioka mine. The purification system's design and operation is discussed in detail as well as specific experiments devised to control scintillator quality and radio-purity. The purification system's effectiveness in removing radioactive trace impurities is analyzed in detail. The total scintillator purified over two years of operation was more then 4.6 ktons.

It is shown here that the KamLAND collaboration has successfully reduced the ^{85}Kr activity of the scintillator by a factor of 2.6×10^4 while ^{210}Bi was reduced by a factor 2×10^3. Due to the success in reducing the intrinsic backgrounds through multiple purifications, this work provides the

first evidence for a ^{7}Be solar ν_{e} signal in KamLAND. The presented analysis covers 5.448 kton-days of exposure time. While the current work is not yet providing a robust measurement of the ^{7}Be solar ν_{e} flux, the presence of ^{7}Be solar ν_{e} is shown to be statistically preferred over a null hypothesis.

In loving memory of

Jason A. Keefer

(1980 - 2008)

List of Abbreviations

ADC	Analog-to-Digital Converter
AMS	Accelerator Mass Spectroscopy
ATWD	Analog Transient Waveform Digitizer
BO	Buffer Oil
CC	Charged Current
C.L.	Confidence Level
CERN	European Organization for Nuclear Research
DAQ	Data Acquisition
DI	De-Ionized
EC	Electron Capture
ES	Elastic Scattering
EVOH	Ethyl vinyl alcohol copolymer
FEE	Front-End Electronics
FPGA	Field Programmable Gate Array
FV	Fiducial Volume
FWHM	Full Width Half Max
GALLEX	Gallium Experiment
GC	Gas Chromotograph
GNO	Gallium Neutrino Observatory
GPS	Global Positions System
GUT	Grand Unified Theorie
ID	Inner Detector
IU	Instrumentation Unit
KamFEE	KamLAND Front End Electronics
KamLAND	Kamioka Liquid Anti-Neutrino Detector

LED	Light Emmitting Diode
LMA	Large Mixing Angle
LS	Liquid Scintillator
LT	Live Time
MC	Monte Carlo (Computer Simulated Data)
MESCO	Mitsui Engineering & Shipbuilding Company, LTD.
MINUIT	CERN Function Minimization and Error Analysis Package
MSDS	Material Safety Data Sheet
MSW	Mikheyev-Smirnov-Wolfenstein
NAA	Neutron Activation Analysis
NC	Neutral Current
Nsum	The number of PMT's with more then 1/3 p.e.
OD	Outer Detector
OP	Opacity Project
OPAL	Opacity Code run by Lawrence Livermore National Laboratory
PC	1,2,4-Trimethylbenzene (Pseudocumene)
PMT	Photomultiplier Tube
PPO	2,5-Diphenyloxazole
QCD	Quantum Chromodynamics
QED	Quantum Electrodynamics
RGA	Residual Gas Analyzer
RMS	Root Mean Square
ROOT	Object-Oriented Data Analysis Toolkit
SAGE	Soviet-American Gallium Experiment
SM	Standard Model
SN	Supernovae
SNO	Sudbury Neutrino Observatory
SNU	Solar Neutrino Unit (1 SNU = 10^{-36} captures per target atom per second)
SOHO	Solar Heliospheric Observatory
SPS	Spallation Proton Source
SS	Stainless Steel
SSM	Standard Solar Model
STP	Standard Temperature and Pressure

TDC	Time-to-Digital Converter
TOF	Time-Of-Flight
UTC	Coordinated Universal Time
h.c.	Hermition Conjugate
m.w.e	meter-water-equivalent
p.e.	Photo-electron
p.d.f.	Probability Density Function
q.e.	Quantum Efficiency

Acknowledgments

I would like to thank my advisor, Prof. Andreas Piepke, for providing me the opportunity to learn from him and for the countless advice bestowed upon me over the years. I want to thank Andreas, Dr. Brian Fujikawa and Dr. Evgeny Yakushev for teaching me what it means to do good physics and to voice one's opinion when you know you are right. This has allowed me the opportunity to make an impact in physics, and for this I am very grateful.

This work could not have been done without the help of all my KamLAND collaborators over the years. I would like to recognize Dr. Jason Detweiler, Dr. Kazumi Tolich, Prof. Nicolai Tolich, Dr. Sanshiro Enomoto, Dr. Dan Dwyer and Dr. Lindley Winslow. They taught me how to do respectable research and were excellent role models over the years, watching them develop and defend their dissertation topics. Special thanks goes to Dr. Patrick Decowski and Dr. Itaru Shimizu for assisting guiding me in my analysis. Thanks to Shin Takeuchi and Momoyo Ogawa for their hard work. Together we started the unforgiving, but necessary, laboratory research which has paved the way to KamLAND's current low background condition and ultimately to the first observation of ^{7}Be solar neutrinos with KamLAND.

I would like to thank Prof. Kunio Inoue for giving me the opportunity to participate in the development, shake-down and operation of the KamLAND purification system. Many thanks to all my Japanese collaborators, especially Dr. Yasuhiro Kishimoto, Dr. Kengo Nakamura, Dr. Sei Yoshida, Dr. Masayuki Koga and Dr. Tadao Mitsui. Without their perseverance during the building and shake-down of the purification system this project would never have been a success. They provided guidance and gave me the opportunity to develop and lead in many engineering and laboratory tasks associated with developing the large scale purification system. This has given me invaluable insight and experience. To everyone who endured the many long days and nights in the mine, and to Koga-san for taking me out and introducing me to the sake bar. If it were not for these much needed trips, the mine disease would have taken control.

I cannot forget to mention my office mates and fellow UA graduate students: Dr. Zelimir Djurcic, Dr. Timothy Classen, Christopher Grant (a.k.a. Penny), Denis Perevalov, and Igor Ostrovskiy. They have became good friends over the years and provided me with a working and social environment that was an essential component of my successful defense. Thanks to my best friends Ty Farr and Paul Luker, who never understood completely what it is I do, or why I do this to myself, but have always supported my insanity over the years.

Last, but certainly not least, I would like to thank my family. Their love and support over my life has given me the ability to push through the hard-times. To my niece and nephews, Jasmine, Elijah and Isaiah, who allowed me to forget my responsibilities and enjoy life every once and a while. To my brothers, Jason, Ryan and Gary Keefer, whose competitive nature always pushed me to strive to be the best. I would like to thank my step-father, Raymond Brown, for molding me into the respectable man that I am today. Finally, my success in life is due to the love and support of my mother, Vicky Brown. She always believed in me even when I didn't believe in myself, and to her I am eternally grateful.

Contents

List of Tables

List of Figures

Chapter 1

A Brief History of Solar Neutrino Physics

The existence of the neutrino was theorized for more then 20 years before Fred Reines and Clyde Cowan detected the first electron antineutrinos at the Savannah River nuclear reactor in 1956 [1]. It took another 20 years before electron neutrinos were detected by Ray Davis' solar neutrino experiment in the Homestake gold mine [2]. These experiments completed the theoretical picture for lepton number conservation in the electron sector and paved the way for the standard model (SM) of particle physics. In 1976, after 3 years of operating the Homestake experiment, John Bahcall and Ray Davis published a paper citing an unresolvable problem between the theoretically predicted and experimentally measured solar neutrino flux[3]. The Homestake experiment placed an upper limit on the flux which was 3 times smaller then the Standard Solar Model (SSM) theoretical expectation. This disagreement was the dawn of the "Solar Neutrino Problem" which fostered the growth and interest in neutrinos over the next 30 years.

Solar neutrino experiments have taken a long and arduous path, evolving from the radiochemical counting experiments of Homestake (1970-1994)[2], Gallex/GNO (1991-1997)[4] and SAGE (1990-2001)[5] into experiments which utilize charged current (CC) elastic scattering (ES) interactions to measure the solar neutrino energy spectrum. The Kamiokande experiment was the first to measure the composite ^{8}B and HEP solar neutrino spectrum above 5 MeV[6]. Furthermore, they were capable of determining the direction of the neutrinos; providing the first evidence that these events

were definitively coming from the Sun. The Sudbury Neutrino Observatory (SNO)[7] and Super-Kamiokande[8] experiments are second generation CC-ES experiments which have provided a precision measurement of the solar neutrino energy spectrum above 5 MeV.

The KamLAND experiment was designed to supplement the solar neutrino data and determine explicitly if the Large Mixing Angle (LMA) solution would provide evidence for electron antineutrino disappearance. The KamLAND experiment used reactor $\bar{\nu}_e$s to definitively prove that neutrinos oscillate[9]. The final piece of the puzzle came from the neutral current (NC) ^{8}B $\nu_{\rm e}$ flux measurement by SNO[10] which measured the total flavor independent flux from the Sun. This showed that the missing $\nu_{\rm e}$ are detected as ν_μ and ν_τ, verifying the occurrence of neutrino flavor oscillations. This proved that vacuum plus matter oscillations, Mikheyev-Smirnov-Wolfenstein (MSW) effect [11, 12], produce the deficit in the SSM flux above 5 MeV and yield the solution to the longstanding solar neutrino problem.

The growing amount of neutrino data, coupled with solar opacity calculations (OPAL[13]/OP[14]), and helioseismology measurements (SOHO Michelson Doppler Imager[15]) provide a way to test the SSM to unprecedented precision. As a result of these measurements a new conundrum has surfaced; refereed to as the "Solar Composition Problem." The current SSM, BPS08, is incapable of simultaneously reproducing the helioseismology data with the currently accepted solar abundances[16]. The solar composition, or heavy element abundance, directly effects the Sun's opacity and dominates the theoretical uncertainties in the predicted neutrino fluxes. Heavy element abundances dominate the theoretical uncertainty in the CNO (12-17%), ^{8}B (6.8%) and ^{7}Be (3.2%) fluxes. As a result, there is a need for high precision NC-ES ^{8}B measurement and for experiments which would measure the solar neutrino energy spectrum below 5 MeV.

Building an experiment capable of measuring solar neutrino energies below 5 MeV is dramatically hindered by naturally occurring radiation. Radio-purity requirements for target materials in multi-tonne experiments exceeds those of the cleanest materials in the World. Borexino was the first experiment to measure a portion of the ^{7}Be solar neutrino energy spectrum[17]. Currently the experimental uncertainty on the ^{7}Be flux is 10%, however it did provide bounds for the SSM and improved previous SSM uncertainties by a factor of 5.

Currently Borexino and KamLAND are the only experiments capable of performing a spectroscopic measurement of solar neutrino fluxes above 250 keV. If KamLAND reduces its low energy background by six orders of magnitude, it could verify the Borexino result and, with higher statistics, provide a more stringent measurement on the ^{7}Be flux. A statistical measurement of 5% or better

is needed to give additional constraints on the SSM and further verify the MSW effecy by showing the low energy solar neutrinos obey vacuum oscillations. Furthermore, KamLAND would verify the expected 6.3% deviation in solar flux due to the modulation in the Earth's orbit around the Sun. With the advent of new front-end electronics and a reduction in internal backgrounds, KamLAND would also be set limits on the flux of CNO neutrinos. A measurement of the CNO energy spectrum would contain the transition region from vacuum to matter oscillations and provide the irefutible evidence for the MSW effect. The final benifit of a purified liquid scintillator (LS) is the reduction in ^{210}Po alpha decays which is currently the largest background for geologically produced antineutrinos measured with KamLAND [18], making up approximately 1/3 of the signal. A modest factor of 10 reduction in ^{210}Po would make this a negligable background and allow for a more stringent measure of the geologically produced antineutrinos.

This thesis presents a detailed description of LS purification work and analysis studies performed to establish the sensitivity and capability for making a spectroscopic ^{7}Be solar neutrino measurement with the KamLAND detector. The basics of current SSM calculations, assumptions, predicted spectral distributions and fluxes and the relevant standard model particle physics which lead to neutrino oscillations is presented in Ch.2. KamLAND's detector design is outlined in Ch.3 while the data reconstruction and reduction methods are presented in Ch.4. From March 2002 to June 2008 KamLAND was operated as a reactor antineutrino detector and periodically took data to establish an understanding of the low energy backgrounds. A complete analysis of the low energy singles spectrum utilizing code developed by the author to generate probability density functions (p.d.f.s) of the underlying beta and solar neutrino spectra is presented in Ch.5. Special studies were performed utilizing fast coincidences of $\beta - \alpha$ tagging in the Uranium and Thorium chain and a $\beta - \gamma$ excited state mode in ^{85}Kr. The time evolution of all backgrounds is considered and their possible correlations with detector calibrations and monitoring is also presented to complete the understanding of internal backgrounds.

Analysis studies found backgrounds which inhibit a ^{7}Be measurement were introduced from exposure to air during initial filling in which ^{39}Ar, ^{85}Kr, and ^{222}Rn dissolved in the LS. ^{39}Ar and ^{85}Kr are noble gasses and can be removed through common sparging techniques with other inert or noble gasses. However, ^{222}Rn decays into a metallic state of ^{210}Pb which exists in an unknown form in the detector. Ch.6 presents detailed laboratory studies designed to specifically address this impurity. The results of these studies influenced and guided the design of a large scale, multi-million dollar, purification system which is capable of purifying ktons of highly combustible liquids underground

on the time-scale of a month. From May 12, 2007 to Aug. 1, 2007 KamLAND conducted the first phase of purification which consisted of recirculating 1500 m^3 of LS through this newly designed distillation and nitrogen purge purification system. A second phase was operated from June 16, 2008 to Feb. 6, 2009 in which the LS was subjected to three full volume exchanges. Ch.7 outlines the purification system and the detectors developed to make offline measurements which would monitor the radio-purity and optical properties of purified LS and on-line monitoring tools to compliment these systems and provide further constraints on the operation and control of the system. After two phases of purification KamLAND's low energy background has been reduced by nearly 5 orders of magnitude. Due to the success in background reduction, Ch.8 presents a detailed analysis of the data collected during the purification phases and provides an outline of the benefits for multiple volume transfers. Lastly, KamLAND's current ^{7}Be ν_e sensitivity is established after the final purification.

Chapter 2

Theoretical Considerations

Building an experiment to test Standard Solar Model (SSM) predictions requires one to assume the underlying Standard Model (SM) physics, then calculate the expected particle interactions based on this theory. Non-standard interaction terms can be included to explain experimental observations, however, a single experiment is typically not enough to rule out all the non-standard theories. The interdependence of the SSM on SM physics resulted in the original "solar neutrino problem" which took more then 20 years to disentangle.

Calculating the expected signal in KamLAND requires knowledge of the flavor content and energy dependence of the incident neutrino spectrum obtained by modeling neutrino transport through the Sun. Once this spectrum is known, the interaction in the detector must be calculated. In the case of KamLAND, the dominant interaction is neutrino-electron elastic scattering ($\nu + \mathrm{e} \rightarrow \nu' + \mathrm{e}'$).

A brief synopsis of the SM is given which helps describe the essential neutrino-electron scattering cross-section. Relevant second order radiative corrections to the cross-section are considered to include a non-standard magnetic moment term. The SM physics is expanded to included neutrino masses which produces results in neutrino oscillations. Neutrino oscillations in vacuum are explained briefly with a stronger focus on matter oscillations. Finally, the SSM is described in the context of the preceding physics and a model of neutrino propagation through the Sun based on these theories is described in detail. More details can be found in these essential references [19, 20, 21, 22, 23].

2.1 Standard Model of Particle Physics

The standard electroweak model of particle physics is based on the gauge group SU(2) $\otimes$ U(1) and is attributed to the work of Glashow[24], Weinberg[25], and Salam[26]. Quantum Electrodynamics (QED) is based on 24 fundamental spin 1/2 particles, referred to as fermions and broken into two groups consisting of six leptons (e, ν_e, μ, ν_μ, τ, ν_τ) and six quarks (u, d, c, s, t, b)[1] and their corresponding antiparticles. Quarks have fractional charge ($+\frac{2}{3}, -\frac{1}{3}$) and are always bound together by the strong force to form composite particles with integer charge such as the proton (uud) and neutron (udd). Leptons are not necessarily bound, except electromagnetically in the case of atoms, however even in this sense the electrons are seen as free fields relative to the quark nucleus.

This work focuses on outlining the theory of leptons, however the quarks follow a very similar framework [22]. To begin, leptons are grouped into SU(2) weak-isospin doublets, consisting of the charged lepton and its flavor coupled neutrino

$$\begin{pmatrix} \nu_l \\ l \end{pmatrix}_{\mathrm{L}} = \frac{1}{2}\left(1-\gamma_5\right)\begin{pmatrix} \nu_l \\ l \end{pmatrix} \tag{2.1}$$

where $l \in e, \mu, \tau$ is the lepton flavor, $\gamma_5 = i\gamma^0\gamma^1\gamma^2\gamma^3$ is a combination of Dirac gamma matrices, and the subscript L denotes a chirally[2] left-handed field. For massive particles only the fields on the right-hand side of the equation are solutions to the Dirac equation.

A theory of lepton interactions must include mass terms for the charged leptons. Mass terms are constructed by addition of SU(2) singlets for the charged leptons of the form:

$$l_R = \frac{1}{2}(1+\gamma_5)l \tag{2.2}$$

where the subscript R denotes a right-handed chiral field. In quantum field theory, lepton masses are achieved through a method referred to as spontaneous symmetry breaking. Three things occur during this process: 1) The charged lepton obtains a mass. 2) We obtain three massive gauge bosons (W^+, W^-, and Z^o) which mediate the weak force. 3) We obtain a massless gauge boson (photon) which is the mediator of the electromagnetic force.

Now that we have the building blocks of QED we can look at particle interactions. The most

[1] The quark abbreviations are up, down, charm, strange, top, and bottom. Quarks mix, as do neutrinos, and more recent theories group quarks into three doublets defined by color, retaining only up and down quark within each doublet.

[2] A chiral field is an eigenstate of the γ_5 operator.

general neutrino interaction terms in the Lagrangian take the form of

$$-\mathcal{L}_{\mathrm{CC}} = \frac{\mathrm{g}}{\sqrt{2}} \sum_{\mathrm{l}} \bar{\nu}_{\mathrm{lL}} \gamma^{\mu} \mathrm{l}_{\mathrm{l}}^{-} \mathrm{W}_{\mu}^{+} + \mathrm{h.c.} \tag{2.3}$$

$$-\mathcal{L}_{\mathrm{NC}} = \frac{\mathrm{g}}{2\cos\theta_{\mathrm{W}}} \sum_{\mathrm{l}} \bar{\nu}_{\mathrm{lL}} \gamma^{\mu} \nu_{\mathrm{lL}} \mathrm{Z}_{\mu}^{0}. \tag{2.4}$$

where γ^{μ} are Dirac gamma matrices s.t. $\mu \in 0, 1, 2, 3$, θ_W is the Weinberg angle, g is the coupling constant for the weak-isospin group $\mathrm{SU(2)_L}$ and h.c. denotes the Hermitian conjugate of the preceding terms. Eq. 2.3 denotes the charged current interaction and describes the interaction of $\mathrm{W}^{\pm}$ bosons with a charged lepton and a neutrino. These charged bosons are needed to conserve charge at the interaction vertex, graphically depicted by the Feynman diagrams in Fig. 2.1. Interactions which proceed without charge exchange are referred to as neutral current (NC) interactions and are mediated by the neutral $\mathrm{Z^o}$ boson, Eq. 2.4.

The standard model has been constructed under the assumption that neutrinos are massless particles. Furthermore, the theory is constructed in such a way as to inherently conserve lepton flavor at each interaction vertex. Experimental verification of neutrino oscillations over the past few years implies that we must modify the standard model from its current form. Neutrino oscillation experiments tell us two things: 1) At least two of the three neutrinos have a mass. 2) Lepton flavor is not conserved as a neutrino can oscillate between flavors. The standard model describes our world very well and it still conserves total lepton number and masses can be introduced into the model by constructing right-handed SU(2) singlets in the same manner as Eq. 2.2. However, this is not the only way to add neutrino masses to the theory (See-Saw Mechanism[27] and GUTs[28]) and development of such theories is outside the scope of this work.

2.2 Differential Scattering Cross-Sections

Charged current and neutral current lepton-lepton interactions where discussed in the previous section and in this section a description of the differential-scattering cross-section is given. The question we want to answer is: "Given a known interaction process, what is the probability of this process to occur in the detector?" First, we know the interaction process in KamLAND is predominantly neutrino-electron elastic scattering. The Feynman diagrams for the CC and NC processes are shown in Fig. 2.1. There is a strict procedure, defined by the "Feynman rules", which dictates how to obtain the cross-section from these diagrams[22].

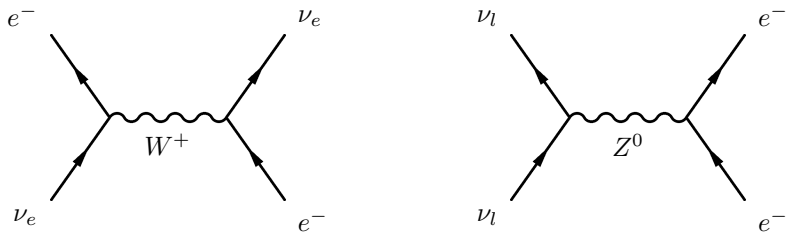

Figure 2.1: Charged current ($W^{\pm}$) and neutral current (Z^0) neutrino-electron elastic scattering tree-level Feynman diagrams.

The effective Lagrangian for neutrino-electron elastic scattering is:

$$\mathcal{L}_{\text{eff}} = -\frac{G_F}{\sqrt{2}}\Big\{ [\bar{\nu}_e\gamma^\mu(1-\gamma_5)e]\,[\bar{e}\gamma_\mu(1-\gamma_5)\nu_e] + [\bar{\nu}_e\gamma^\mu(1-\gamma_5)\nu_e]\,[\bar{e}\gamma^\mu(g_V - g_A\gamma_5)e]\Big\}. \tag{2.5}$$

The Lagrangian is written in terms of the Dirac fields and not the chiral fields. The first term in the sum is the CC interaction and the second term is the NC interaction. The g_V and g_A are the vector and axial vector coupling constants and G_F is the Fermi constant. A point of particular interest is the last product which depicts the electron-positron interaction. This term specifically shows the charged lepton fields are linear combinations of the left and right handed chiral fields. Furthermore, the chiral field e_R only participates in NC interactions.

The differential cross-section is calculated from the effective Lagrangian after a Fierz transformation, algebraic manipulations and integrations. The details can be found in any field theory text[22]. The differential cross-section was first calculated by t'Hooft[29] in 1971. With the specific form of the cross-section[30, 31] we can answer the second part of our question. Given an incident neutrino energy E_ν, the probability of producing a recoil electron with kinetic energy T is given by

$$\frac{d\sigma}{dT} = \frac{2G_F^2 m_e}{\pi\hbar^4}[g_L^2 + g_R^2(1-\frac{T}{E_\nu})^2 - g_L g_R\frac{m_e T}{E_\nu^2}] \;\; [\text{cm}^2/\text{MeV}] \tag{2.6}$$

where $g_{L,R} = \frac{1}{2}(g_V \pm g_A)$ and $g_L = \pm\frac{1}{2} + \sin^2\theta_W$, $g_R = \sin^2\theta_W$ ($+\,\nu_e e, -\,\nu_{\mu,\tau} e$), and μ_B is the Bohr magneton. The electron recoil energy is restricted kinematically by the equation

$$T_{max} = \frac{2E_\nu^2}{2E_\nu + m_e}. \tag{2.7}$$

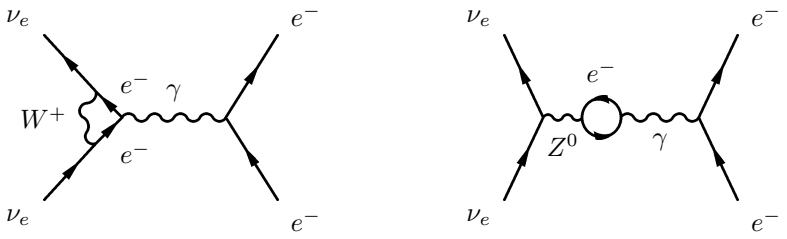

Figure 2.2: Feynman diagrams for electroweak radiative corrections to the neutrino-electron elastic scattering cross-section.

2.2.1 Radiative Corrections

Eq. 2.6 provides the zeroth order calculation, which will provide to within a few percent the number of events expected per energy bin in the detector. Bahcall [32] has shown that perturbative corrections to the differential scattering cross-section must be taken into account when considering a measurement of better then 5% on the solar neutrino flux. These corrections are found to be on the order of 4% for the higher energy (> 5 MeV) solar neutrinos while for ^{7}Be energies this is approximately a 2% correction.

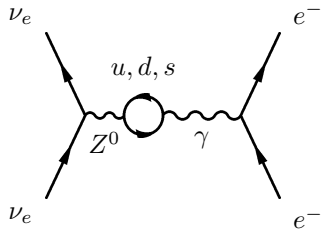

Figure 2.3: Feynman diagrams for QCD radiative corrections to the neutrino-electron elastic scattering cross-section.

The differential cross-section with radiative corrections has the following form:

$$\begin{aligned}\left(\frac{\mathrm{d}\sigma}{\mathrm{dT}}\right)_{\mathrm{Rad}} =& \frac{2G_F^2 m_e}{\pi\hbar^4}\Bigg\{ g_L^2(T)\left[1+\frac{\alpha}{\pi}f_-(z)\right] \\ &+ g_R^2(T)(1-\frac{T}{E_\nu})^2\left[1+\frac{\alpha}{\pi}f_+(z)\right] \\ &- g_L(T)g_R(T)\frac{m_e T}{E_\nu^2}\left[1+\frac{\alpha}{\pi}f_{+-}(z)\right]\Bigg\} \ [\mathrm{cm}^2/\mathrm{MeV}] \end{aligned} \tag{2.8}$$

where α is the fine structure constant, $\mathrm{z} = \frac{\mathrm{T}}{\mathrm{E}_\nu}$ and $\mathrm{f}_+(\mathrm{z})$, $\mathrm{f}_-(\mathrm{z})$ and $\mathrm{f}_{+-}(\mathrm{z})$ are energy dependent corrections to the cross-section. The formulae for these correction terms are extensive. The reader is referred to Appendix A and B of ref. [32] for the detailed formulae for the coupling constants and

f(z) which were used in the Monte Carlo (KNuSolar) described in Sec. 2.4.2. Eq. 2.8 above has been taken out of "natural" ($\hbar = c = 1$) units and is equivalent to Eq. A1 in appendix A [32].

Comparing Eq. 2.6 and Eq. 2.8, the form of the radiative corrections to the cross-section are immediately obvious. First, the coupling constants $g_{L,R}(T)$ have acquired an energy dependence. This is a result of virtual quark interactions (Fig. 2.3) resulting in quantum chromodynamic (QCD) corrections. The other obvious extension is seen in the expansion terms, of order α, which are due to the electroweak loop corrections in Fig. 2.2. It should be noted that these radiative corrections suffer from infrared divergences near the end-point. Therefore, numerical calculations are cut-off at $T = 0.99T_{max}$. This is not an issue for most experiments. This is because the rate drops off and becomes unobservable near the endpoint and for detectors like KamLAND, the energy resolution is on the order of $\frac{6\%}{\sqrt{E[MeV]}}$. Both of these effects makes truncating the correction factors unobservable experimentally.

2.2.2 Neutrino Magnetic Moment

The standard model allows neutrinos to acquire a magnetic and electric dipole moment through the CC interactions. It can be shown that the magnetic and electric dipole moments are indistinguishable for highly relativistic neutrinos with small masses [33]. Therefore, the "magnetic moment", μ_ν refers to both dipole moments. The differential scattering cross-section for the magnetic dipole moment [30] takes the form:

$$\left(\frac{d\sigma}{dT}\right)_\mu = \left(\frac{\pi\alpha^2\hbar^2}{m_e^2\ c^2}\right)\left(\frac{\mu_\nu}{\mu_B}\right)^2\left(\frac{1}{E_\nu} - \frac{1}{T}\right)\ [m^2/MeV] \tag{2.9}$$

where μ_B is the Bohr magneton. Only the magnetic moment depends on the flavor composition, and in general experiments measure the "effective" magnetic moment of the neutrino. The most appealing feature to the cross-section is the $\frac{1}{E_\nu}$ dependence which implies the effect is amplified for low energy neutrinos.

Flavor dependent magnetic moments come about due to the interaction taking place with the mass eigenstates while the experiment measures flavor eigenstates. The magnetic moment becomes a coherent superposition of magnetic moments μ_{ij} such that given an initial mass composition the

flavor basis according to Eq. 2.18 the flavor moment has the form [34]

$$\begin{aligned}\mu_{\mathrm{l}}^2 &= \sum_{\beta}\left|\sum_{\alpha} U_{l\alpha}\ \mu_{\beta\alpha}\ e^{-iE_{\alpha}L}\right|^2 \\ &= \sum_{\beta}\sum_{\alpha\alpha'} U_{l\alpha}\ U^{*}_{l\alpha'}\ \mu_{\beta\alpha}\ \mu^{*}_{\beta\alpha'} e^{-2i\pi L/L_{\alpha\alpha'}}\end{aligned} \tag{2.10}$$

where the sums are over the mass eigenstates and l denotes the flavor state and

$$\mathrm{L}_{\alpha\alpha'} = \frac{4\pi \mathrm{E}_{\nu}}{\Delta \mathrm{m}^2_{\alpha\alpha'}} \tag{2.11}$$

It can be seen that when the mass states are equal ($\alpha = \alpha'$) then the exponential is unity and the distance dependent phases drops out. Furthermore, the $\mu_{\beta\alpha}$ are the fundamental moments corresponding to the mass eigenstates. It is clear that a single experiment cannot distinguish all the possible moments and therefore experimentally it is relevant to consider only the effective moment.

Only elastic scattering experiments can directly measure a possible magnetic moment. Currently the best experimental limits come from reactor and solar neutrino experiments. Standard model calculations provide an expected theoretical value for the neutrino magnetic moment of $\mu_{\nu} \simeq 3.2 \times 10^{-19}\ \mu_{\mathrm{B}}[\mathrm{m}_{\nu}/(1\mathrm{eV})]$. The TEXONO and GEMMA experiments set limits for the $\bar{\nu}_e$ of $\mu_{\nu} < 7.4 \times 10^{-11}\ \mu_{\mathrm{B}}$ [35] and $\mu_{\nu} < 5.8 \times 10^{-11}\ \mu_{\mathrm{B}}$ [36] respectively. While the low energy ^{7}Be ν_{e} measurement of Borexino has set a new limit comparable to the long-standing reactor measurements of $\mu_{\nu} < 5.4 \times 10^{-11}\ \mu_{\mathrm{B}}$ [17]. This was a factor 10 improvement over the Super-Kamiokande measurement [37] using high energy ^{8}B neutrinos, reiterating the $1/\mathrm{E}_{\nu}$ effect in the cross-section. However, there are theories which give rise to large magnetic moments, and an experimental measurement would provide valuable insight into GUTs.

2.3 Neutrino Oscillations

Neutrino flavor oscillations were first proposed in 1962 by Maki, Nakagawa and Sakata [38] and the theory was later refined by Pontecorvo [39] who originally proposed neutrino-antineutrino oscillations several years earlier. Neutrinos were proposed to save conservation of energy in beta decay and thus it is only fitting to use this same process to develop an understanding of neutrino oscillations. Nuclear beta decay is a spontaneous process in which a nucleus of charge Z and mass A transitions to a more energetically favorable isobaric state. The most important beta decay reaction considered in this

work is the reaction:

$$^{85}_{36}\mathrm{Kr} \rightarrow ^{85}_{37}\mathrm{Rb} + \mathrm{e}^{-} + \bar{\nu}_{\mathrm{e}}. \tag{2.12}$$

On a sub-atomic level this process is purely leptonic; involving an up quark transition into a down quark leaving. Furthermore, beta decay conserves electric charge (electron + proton = 0), lepton number (e (+1) + $\bar{\nu}$ (-1) = 0) and lepton flavor (e (+1) + ν_e (-1) = 0). The electron and neutrino are ejected from the nucleus while the proton stays bound to the nucleus. This is rather evident as it is not really a "new" proton and we learned previously that the quarks are never free particles and are bound tightly by the strong force. However, in most beta decays the nuclear transition process excites nuclear levels and the de-excitation of these nuclear levels produces secondary gamma rays.

Neutrino flavor oscillations arise due to the inequality of basis states; the flavor eigenstates (ν_{e}, ν_μ, ν_τ) are not equal to the mass eigenstates (ν_1, ν_2, ν_3) . The mass eigenstate is the state which physically propagates while the flavor eigenstate participates in the electroweak interactions. The typical question neutrino oscillation experiments try to answer is this: "Given the process in Eq. 2.12 and a known activity (rate) of ^{85}Kr, if we setup a an experiment to detect all the $\bar{\nu}_e$ from this source will we observe the expected number of interactions given the calculated cross-section?" Immediately it can be seen that the idea of neutrino oscillations will not conserve flavor as it implies that at a later time we could detect instead of $\bar{\nu}_{\mathrm{e}}$, $\bar{\nu}_\mu$ or $\bar{\nu}_\tau$.

There is one subtle issue that will not be addressed in detail but should be noted before we proceed with the theory. As previously described in Sec 2.1, there are three flavor states which are referred to as "active" neutrinos. The number of active neutrinos is constrained by the invisible width of the Z boson to 2.92 ± 0.05 [40]. Therefore, if the mass eigenstates are not degenerate, and there are only three flavors, the total number of mass differences is two. There is however no constraint on "sterile" (do not participate in weak interactions) neutrinos. A possible sterile component can be added to by extending the basis set and all the formulae in the following section can readily be generalized to n-dimensions.

2.3.1 Vacuum Oscillations

Now that there is a conceptual picture let us parameterize the oscillation process. The time evolution of ultra-relativistic particles is governed by the Dirac equation. However, only the left-handed chiral state are relevant in neutrino interactions. If we further remove spin structure from the equations

we can describe neutrino propagation by the Klein-Gordon equation.

$$\left[\frac{\partial^2}{\partial x^2} + m^2\right] |\nu\rangle = \frac{\partial^2}{\partial t^2} |\nu\rangle \tag{2.13}$$

We now make the assumption that all the neutrino eigenstates have the same momentum or energy and this removes the spatial dependence. Defining the propagation direction of the neutrino removes the second "reflected" solution to the partial-differential equation. After these approximations are taken into account, Eq. 2.13 looks very similar to the Schrödinger equation. It is from this point that we derive the analytical form for neutrino propagation.

The flavor eigenstate l can be written as a coherent superposition of mass eigenstates α. The flavor eigenstate at time t, with definite energy E_ν, momentum p_α and position x, is expressed as a sum over the mass eigenstates:

$$|\nu_l(\mathrm{x},\mathrm{t})\rangle \;=\; \sum_{\alpha=1}^{\mathrm{N}} \mathrm{U}_{l\alpha}\, \mathrm{e}^{\mathrm{ip}_\alpha \mathrm{x}}\, \mathrm{e}^{-\mathrm{iE}_\nu \mathrm{t}}\; |\nu_\alpha\rangle \tag{2.14}$$

where U is a unitary leptonic mixing matrix. Similar to three-dimensional SO(3) rotations, the leptonic mixing matrix can be written as a rotation about the three "mass axis.". To account for quantum mechanical processes these rotations include a CP violating phase δ and two Majorana phases α_1, α_2.

$$\begin{aligned}\mathrm{U} = &\begin{pmatrix} 1 & 0 & 0 \\ 0 & \cos\theta_{23} & \sin\theta_{23} \\ 0 & -\sin\theta_{23} & \cos\theta_{23} \end{pmatrix} \begin{pmatrix} \cos\theta_{13} & 0 & e^{-i\delta}\sin\theta_{13} \\ 0 & 1 & 0 \\ -e^{-i\delta}\sin\theta_{13} & 0 & \cos\theta_{13} \end{pmatrix} \\ &\begin{pmatrix} \cos\theta_{12} & \sin\theta_{12} & 0 \\ -\sin\theta_{12} & \cos\theta_{12} & 0 \\ 0 & 0 & 1 \end{pmatrix} \begin{pmatrix} e^{-i\alpha_1/2} & 0 & 0 \\ 0 & e^{-i\alpha_1/2} & 0 \\ 0 & 0 & 1 \end{pmatrix}\end{aligned} \tag{2.15}$$

The 3×3 matrix containing the Majorana phases drops out when calculating the inner product. As a result these angles cannot be determined from neutrino oscillation experiments. The position of the CP violating phases are relatively arbitrary, however they are traditionally placed with the θ_{13} angles. This is due to the small value of the angle, and if it turns out to be zero, CP violation cannot be observed with neutrino oscillation experiments. Performing the product of matrices above provides a more useful form for evaluating oscillation probabilities. The following solution is devoid

of the Majorana phases.

$$\mathrm{U} = \begin{pmatrix} U_{e1} & U_{e2} & U_{e3} \\ U_{\mu 1} & U_{\mu 2} & U_{\mu 3} \\ U_{\tau 1} & U_{\tau 2} & U_{\tau 3} \end{pmatrix} = \begin{pmatrix} c_{12}c_{13} & s_{12}c_{13} & s_{13}e^{-i\delta} \\ -s_{12}c_{23} - c_{12}s_{23}s_{13}e^{i\delta} & c_{12}s_{23} - s_{12}s_{23}s_{13}e^{i\delta} & s_{23}c_{13} \\ s_{12}s_{23} - c_{12}c_{23}s_{13}e^{i\delta} & -c_{12}s_{23} - s_{12}c_{23}s_{13}e^{i\delta} & c_{23}c_{13} \end{pmatrix} \tag{2.16}$$

Here the notation $s_{ij} = \sin\theta_{ij}$ and $c_{ij} = \cos\theta_{ij}$ have the same meaning as the angles in Eq. 2.15.

There are a few approximations which will simplify the oscillation equations. First, the neutrino is ultra-relativistic, thus to a very good approximation $\mathrm{x} = \mathrm{t}$. The second approximation is that the individual masses are much smaller then the energy, $\mathrm{m}_\alpha \ll \mathrm{E}_\nu$. Solar neutrinos measured with KamLAND have $\mathrm{E}_\nu > 250$ keV and the current experimental upper limit on the average [3] electron neutrino masses is $\mathrm{m}^2(\nu_\mathrm{e}) < 2.3$ [41]. Now we can Taylor expand the energy-momentum relation to obtain the approximation

$$\mathrm{p}_\alpha = \sqrt{\mathrm{E}_\nu^2 - \mathrm{m}_\alpha^2} \simeq \mathrm{E}_\nu + \frac{\mathrm{m}_\alpha^2}{2\mathrm{E}_\nu} \tag{2.17}$$

Substituting this relationship into Eq. 2.14 we obtain:

$$|\nu_l(\mathrm{x},\mathrm{t})\rangle \;=\; \sum_{\alpha=1}^{\mathrm{N}} \mathrm{U}_{l\alpha}\; \mathrm{e}^{-\mathrm{i}(\frac{\mathrm{m}_\alpha^2}{\mathrm{E}_\nu})\mathrm{x}}\; |\nu_\alpha\rangle \tag{2.18}$$

which is the standard time-evolution equation for the flavor eigenstates.

As noted previously, the quantity of interest is the probability of a flavor eigenstate, defined by a specific reaction like Eq. 2.12, to transition into another flavor eigenstate. Quantum mechanically this is calculated by taking the inner product of the time-evolution eigenstates in Eq. 2.18. Outlined below is the most general three flavor oscillation probability assuming an initial flavor eigenstate l

[3] The experimentally measured quantity from tritium beta decay experiments is $\mathrm{m}^2(\nu_\mathrm{e}) = \sum_\alpha \left|\mathrm{U}_{\mathrm{e}\alpha}\right|^2 \mathrm{m}^2(\nu_\alpha$.

and a final flavor eigenstate $l^{'}$:

$$
\begin{aligned}
\mathrm{P}(\nu_l \rightarrow \nu_{l'}) &= \left|\langle \nu_l(0,0) | \nu_{l'}(x,t)\rangle\right|^2 \\
&= \left(\sum_\alpha U_{l\alpha}\, e^{-i(\frac{m_\alpha^2}{E_\nu})x}\, U^*_{l'\,\alpha}\right)^\dagger \left(\sum_\beta U_{l\beta}\, e^{-i(\frac{m_\beta^2}{E_\nu})x}\, U^*_{l'\,\beta}\right) \\
&= \sum_\alpha \sum_\beta U^*_{l\alpha} U_{l'\,\alpha} U_{l\beta} U^*_{l'\,\beta}\, e^{-i(\frac{m_\alpha^2 - m_\beta^2}{E_\nu})x} \\
&= \sum_\alpha \left|U_{l\alpha}\right|^2 \left|U_{l'\,\alpha}\right|^2 + \sum_{\alpha\neq\beta} U^*_{l\alpha} U_{l'\,\alpha} U_{l\beta} U^*_{l'\,\beta}\, e^{-i(\frac{m_\alpha^2 - m_\beta^2}{E_\nu})x} \\
&= \sum_\alpha \left|U_{l\alpha}\right|^2 \left|U_{l'\,\alpha}\right|^2 + \Re\left\{\sum_{\alpha\neq\beta} U^*_{l\alpha} U_{l'\,\alpha} U_{l\beta} U^*_{l'\,\beta}\, e^{-i(\frac{\Delta m^2_{\alpha\beta}}{E_\nu})L}\right\} \\
&+ \Im\left\{\sum_{\alpha\neq\beta} U^*_{l\alpha} U_{l'\,\alpha} U_{l\beta} U^*_{l'\,\beta}\, e^{-i(\frac{\Delta m^2_{\alpha\beta}}{E_\nu})L}\right\}
\end{aligned}
\tag{2.19}
$$

where in the last step the equation has been divided into real and imaginary parts and the conventional variables $\Delta \mathrm{m}^2_{\alpha\beta} = \mathrm{m}^2_\alpha - \mathrm{m}^2_\beta$ and x = L are used. Assumption of CP conservation makes U a real unitary matrix and therefore the $\Im$ term drops out.

Solar neutrino experiments are particularly interested in the electron neutrino survival probability as the neutrinos are produced from the nuclear fusion reactions depicted in Figs. A.1 and A.2. The conventional first order term, which expresses the sub-dominant θ_{13} dependence, is given by

$$
\mathrm{P}(\nu_\mathrm{e} \rightarrow \nu_\mathrm{x}) \simeq 1 - \sin^4\theta_{13} - \cos^4\theta_{13}\left[1 - \sin^2 2\theta_{12} \sin^2\left(\frac{1.27\ \Delta \mathrm{m}^2_{12}\ \mathrm{L[m]}}{\mathrm{E[MeV]}}\right)\right] \tag{2.20}
$$

where x represents all flavors except ν_e, and the value of 1.27 is obtained by inserting $\hbar$ and c to make the equation dimensionally correct. Complete three flavor survival probability equations can be found in the literature [42, 43].

Table 2.1 lists the current neutrino mixing parameter values. Most experiments designed as to amplify the effect of a specific mixing angle or mass-squared difference. As such they typically use a simplified version of the full three-flavor solution or consider only two-neutrino oscillations. The table gives the experimental values of the parameters and when we consider the multitude of data and the full three-neutrino case. It can be seen that the addition of the third neutrino typically shifts the central value for these parameters but in all cases the values are within the limits obtained by experiment.

Parameter	**Experiment** [40]	**3ν Analysis** [44]
Δm^2_{21} $[10^{-5}eV^2]$	$7.59^{+0.21}_{-0.21}$ [9]	$7.65^{+0.23}_{-0.20}$
$\lvert\Delta m^2_{32}\rvert$ $[10^{-3}eV^2]$	2.43 ± 0.13 [45]	$2.40^{+0.12}_{-0.11}$
$\sin^2 2\theta_{12}$	$0.86^{+0.03}_{-0.04}$ [9]	$0.846^{+0.086}_{-0.063}$
$\sin^2 2\theta_{23}$	> 0.90 [45]	$1.00^{+0.26}_{-0.23}$
$\sin^2 2\theta_{13}$	< 0.19 [40, 46]	$0.04^{+0.06}_{-0.04}$

Table 2.1: Current values for neutrino oscillation mixing parameters. The experimental values in the first column are taken from KamLAND + solar, Minos and Chooz results. Consideration of the full three neutrino probabilities is performed with the experimental solutions and is done primarily to try to extract a better limit on θ_{13}.

When simplifying the expansion of Eq. 2.19 we use the fact that $\Delta m^2_{12} << m^2_{23}$ and therefore the third $\Delta m^2_{13} = \Delta m^2_{12} + m^2_{23} \simeq m^2_{23}$. Furthermore, θ_{13} is small and therefore $\cos 2\theta_{13}$ is taken to be 1, further simplifying the three-neutrino survival probabilities. For the case at hand, the ν_e survival probability reduces to

$$P(\nu_e \to \nu_x) \simeq \sin^2 2\theta_{12} \sin^2\left(\frac{1.27\ \Delta m^2_{12}\ L[m]}{E[MeV]}\right) \tag{2.21}$$

$$P(\nu_e \to \nu_e) = 1 - P(\nu_e \to \nu_x) = 1 - \sin^2 2\theta_{12} \sin^2\left(\frac{1.27\ \Delta m^2_{12}\ L[m]}{E[MeV]}\right). \tag{2.22}$$

These equations are the exact solutions to two neutrino oscillation formulae. Neutrino oscillation experiments typically refer to an oscillation length; defined as the distance between extrema in the oscillatory portion of Eq. 2.22. The length is expressed mathematically as

$$L_{osc} = \frac{2\pi E}{1.27\Delta m^2} \tag{2.23}$$

where E is in MeV and the mass square difference is in eV^2. This equation is valid for all Δm^2 values.

2.3.2 Matter Oscillations

Why do we need matter oscillations? Given Eq. 2.23 and the measured Δm^2_{12} from Table 2.1, a 1 MeV solar neutrino has $L_{osc} = 65$ km. Therefore, a neutrino traversing the Earth-Sun distance of 1.5×10^8 km experiences many oscillation cycles, effectively averaging out the time dependent term.

This further simplifies the survival probability producing the time-averaged solution:

$$\langle \mathrm{P}(\nu_\mathrm{e} \to \nu_\mathrm{e}) \rangle_\mathrm{Avg} = 1 - \frac{1}{2}\sin^2 2\theta_{12} \tag{2.24}$$

One can conclude from this equation that the solar neutrino flux can be reduced by at most a factor $\frac{1}{2}$. However, the Homestake experiment measured a flux which was $\frac{1}{3}$ of the expected SSM flux. Matter oscillations are important as they provide an explanation for the measured fluxes of all solar neutrino experiments [47] which cannot be explained by vacuum oscillations alone. As such, the currently accepted solution to the "solar neutrino problem" is the LMA-MSW solution. Future experiments performing precision spectroscopy of the ^{7}Be and CNO fluxes will directly measure the MSW transition region explained in this section.

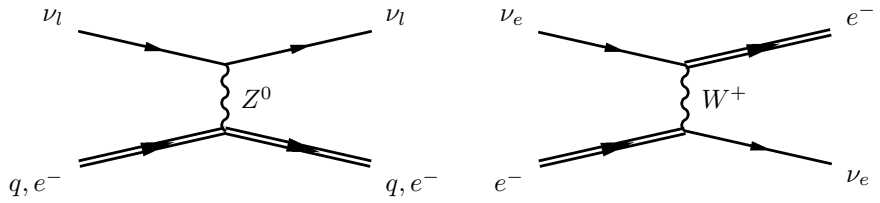

Figure 2.4: Coherent forward scattering Feynman diagrams which give rise to the MSW effect. All neutrino flavors interact via the NC channel while only ν_e interact with the W boson.

Matter oscillations were first proposed in 1978 by Wolfenstein [11]. He proposed that when a neutrino propagates through matter it will interact via the coherent forward scattering[4] diagrams shown in Fig. 2.4. Thus, when a ν_e propagates through matter it will feel a different potential then $\nu_{\mu,\tau}$ due to its CC interaction with electrons. The interaction potential is of the form

$$\mathrm{H_{eff}} = \frac{\mathrm{G_F}}{\sqrt{2}}\left[\bar{\mathrm{e}}\gamma^\mu(1-\gamma_5)\nu\right]\left[\bar{\nu}\gamma_\mu(1-\gamma_5)\mathrm{e}\right]. \tag{2.25}$$

As a result of this effective potential, the energy in the vacuum solution picks up a phase of the form

$$\mathrm{V} = \pm\sqrt{2}\mathrm{G_F}\mathrm{N_e} \tag{2.26}$$

where $\mathrm{N_e} = \mathrm{n_e}\mathrm{N_A} = \rho\frac{\mathrm{Z}}{\mathrm{A}}\mathrm{N_A}$ is the electron number density and ρ is in g/cm^3 and $\pm$ are for neutrinos and antineutrinos respectively. The sign of this phase is very important as it defines the level-crossing phenomena of the matter effect. Under the assumption that $\mathrm{m_2} > \mathrm{m_1}$ we will observe the MSW

[4]Coherent forward scattering implies that the electron momentum does not change.

effect for neutrinos. If this assumption is false and $m_2 < m_1$ then level-crossing will not occur for neutrinos and there will be no observation of an MSW effect. However, if $m_2 < m_1$ level-crossing will occur for anti-neutrinos as the sign on the potential term will change and effectively reverses the Δm^2 sign again.

Adding this potential term effects the propagation Eq. 2.18 by adding a phase

$$|\nu_l(x,t)\rangle \;=\; \sum_{\alpha=1}^{N} U_{l\alpha}\; e^{-i(\frac{m_\alpha^2}{E_\nu}+\sqrt{2}G_F N_e)x}\;\; |\nu_\alpha\rangle \tag{2.27}$$

For matter oscillations one typically considers only two neutrino oscillations ($\nu_e \rightarrow \nu_\mu$) which drastically simplifies the expressions. One can see from Eq. 2.27 that if the N_e is constant things are very similar to the vacuum case with different eigenvalues. However, if the density is not constant, as is the case for the Sun, then the exponential becomes position dependent and we must integrate the term in the exponential over all positions[5]. There are many representations and special cases in the literature [42, 48, 49, 50, 51], however adiabatic and non-adiabatic matter effects are best summarized by considering the form of the Hamiltonian.

In the flavor basis, the potential effects only the ν_e, producing an asymmetry in the Hamiltonian which takes the form:

$$i\frac{d}{dx}\begin{pmatrix}\nu_e\\ \nu_\mu\end{pmatrix} = \left\{ U \begin{pmatrix}\frac{m_1^2}{2E} & 0\\ 0 & \frac{m_2^2}{2E}\end{pmatrix} U^\dagger + \begin{pmatrix}V(x) & 0\\ 0 & 0\end{pmatrix}\right\}\begin{pmatrix}\nu_e\\ \nu_\mu\end{pmatrix} \tag{2.28}$$

where U is the unitary mixing matrix equivalent to the two-dimensional form of Eq. 2.15 and in general the density can vary allowing for a position dependent potential term V(x). Performing the algebra on Eq. 2.28 and pulling out a term proportional to the identity matrix we obtain

$$H_{MSW} = \frac{1}{4E}\begin{pmatrix}\xi(x) - \Delta m_{21}^2\cos 2\theta_{12} & \Delta m_{21}^2 \sin 2\theta_{12}\\ -\Delta m_{21}^2 \sin 2\theta_{12} & -\xi(x) + \Delta m_{21}^2 \cos 2\theta_{12}\end{pmatrix} \tag{2.29}$$

where

$$\xi(x) = \frac{2\sqrt{2}EG_F n_e(x)}{\Delta m_{12}^2} \tag{2.30}$$

[5]Some texts make the notation of time in the exponential which is equivalent to position under our ultra-relativistic assumption.

Adiabatic MSW Solution

For the special case of constant density profiles or slowly varying (adiabatic) densities, we can instantaneously diagonalize the matrix in Eq. 2.28. The matter potential has effectively changed the mass of the neutrino born in matter. The mass eigenstates in matter are not the same as those in vacuum and therefore we must associate a different rotation between the flavor and mass eigenstates. For matter the unitary matrix is

$$\mathrm{U_m} = \begin{pmatrix} \cos\theta_m & \sin\theta_m \\ -\sin\theta_m & \cos\theta_m \end{pmatrix}. \tag{2.31}$$

These rotations provide a relationship between the vacuum and matter angles:

$$\sin 2\theta_{\mathrm{m}} = \frac{\sin 2\theta_{12}}{\sqrt{\left(\xi(\mathrm{x}) - \cos 2\theta_{12}\right)^2 + \sin^2 2\theta_{12}}}. \tag{2.32}$$

and

$$\cos 2\theta_{\mathrm{m}} = \frac{\cos 2\theta_{12} - \xi(\mathrm{x})}{\sqrt{\left(\xi(\mathrm{x}) - \cos 2\theta_{12}\right)^2 + \sin^2 2\theta_{12}}}. \tag{2.33}$$

There are three logical situations to consider:

1. $\xi \to 0$: In this limit we get back the vacuum solution.

2. $\xi(x) = \cos 2\theta_{12}$: The resonance condition is the most interesting theoretically as the off-diagonal components of the Hamiltonian (Eq. 2.29) are maximal.

3. $\xi \to \infty$: This is not a physical condition in the Sun or Earth but could be the case when considering the early Universe or Supernovae. In this case the Hamiltonian is diagonal and the eigenstates are effectively $\pm\xi$.

Non-adiabatic MSW Solution

In an extended neutrino source such as the Sun with a varying density profile, it is possible for the neutrino to be born in a high density region and propagate through the resonance density on its way out of the Sun. At the resonance the mass splitting is minimal as can be seen by the relationship:

$$\Delta\mathrm{M}^2 = \Delta\mathrm{m}^2\sqrt{\sin^2 2\theta_{12} + (\cos 2\theta_{12} - \frac{2\sqrt{2}\mathrm{EG_F n_e}}{\Delta\mathrm{m}^2_{12}})^2}. \tag{2.34}$$

This allows a transition probability for the mass state to quantum mechanically "hop" to the other mass eigenstate, very similar to the tunneling effect in a typical square well boundary problem. When the Hamiltonian cannot be diagonalized instantaneously we must consider a set of coupled first-order differential equations given by Eq. 2.29. The most recognized way to solve this set of coupled differential equations is referred to as the Landau-Zenner approximation [52, 53]. This approximation as the following conditions:

1. Far from the resonance the eigenstates can be instantaneously diagonalized (adiabatic) for any density profile.

2. Around the resonance region the density profile is approximated as linear for the diagonal components and has constant off-diagonal components.

The form of this probability for a linear density profile is referred to as the Parke formula [48].

$$\mathrm{P_{jump}} = \exp\left(\frac{-\pi\Delta\mathrm{m}^2_{12}\sin^2 2\theta_{12}}{4\mathrm{E}_\nu\cos 2\theta_{12}\hbar c}\left(\frac{\mathrm{n_e}}{|\frac{\mathrm{dn_e}}{\mathrm{dr}}|}\right)\right) \tag{2.35}$$

Many different density profiles have been considered that approach the actual solar profile such as exponential[54] and tanh [55]. These solutions are superior to the linear approximation only for large $\Delta\mathrm{m}^2$ and small mixing angles where the linear approximations break down. However, we live in a world of large mixing and small $\Delta\mathrm{m}^2$ and therefore the linear density Parke formula is considered for non-adiabatic transitions in this work.

As mentioned previously, neutrino oscillation experiments are concerned with the ν_e survival probability. Parke calculated [48] the survival probability formula as an average over the production zone such that

$$|\langle\nu_\mathrm{e}|\nu_\mathrm{e}\rangle|^2 = \frac{1}{2} + \left(\frac{1}{2} - \mathrm{P_{jump}}\right)\cos 2\theta_\mathrm{m}\cos 2\theta_{12} \tag{2.36}$$

where $\mathrm{P_{jump}}$ is given in this work by Eq. 2.35. The adiabatic ν_e survival probability is obtained by taking $\mathrm{P_{jump}} = 0$.

The effect of this resonance transition is dependent on the vacuum oscillation parameter, $\sin^2 2\theta_{12}$ and $\Delta\mathrm{m}^2$. The non-adiabatic transition is defined by the critical density

$$\rho_\mathrm{c} = \frac{\Delta\mathrm{m}^2_{12}\cos 2\theta_{12}}{2\sqrt{2}\mathrm{EG_F}}. \tag{2.37}$$

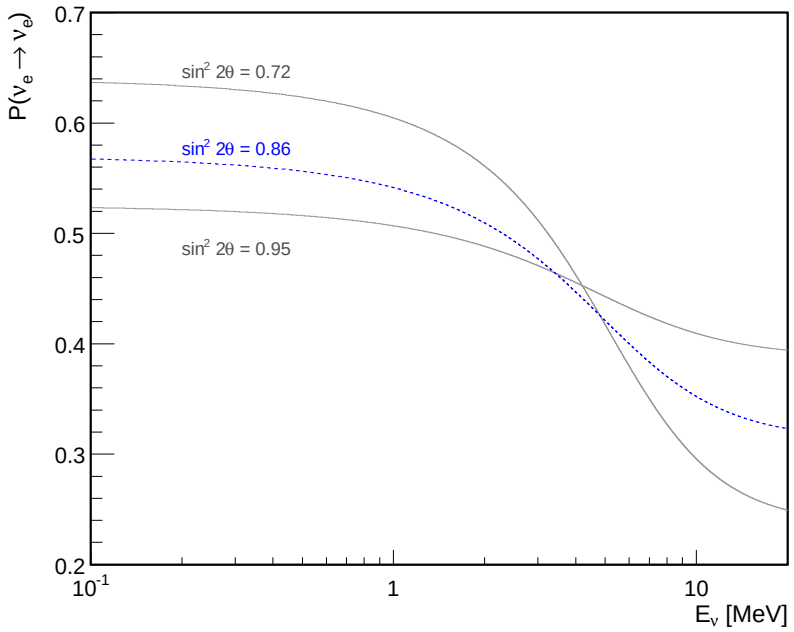

Figure 2.5: The MSW effect on the transition probability for ^{7}Be Solar ν_es within the uncertainty on the mixing angle from Table 2.1. The mass square difference is best determined by KamLAND [9], therefore this parameter was fixed to $\Delta m^2 = 7.59 \times 10^{-5}\text{eV}^2$. The survival probability was then calculated for ^{7}Be ν_e for different mixing angle solutions. The dashed blue line is the best fit value and the gray lines represent $\pm 3\sigma$.

This critical density is best cast into a minimum neutrino energy which experience the non-adiabatic level-crossing. Given the values in Table 2.1 one finds that for the density at the solar core, a neutrino must have a $\text{E}_{\text{min}} = 1.7\text{MeV}$ to be completely converted into the heavy mass state. Eq. 2.37 shows that as the neutrino travels to the edge of the Sun and the density gets smaller then the required energy for level-crossing increases.

The MSW effect on the transition probability for ^{7}Be Solar ν_es within the uncertainty on the mixing angle from Table 2.1 is shown in Fig. 2.5. It can be seen from this figure that for low energy we get the survival probability for vacuum oscillations as we expect. Furthermore, the transition region occurs over an energy range of approximately 10 MeV and the steepness of this transition is determined by the vacuum mixing angle. The smaller vacuum mixing angle allows for a larger survival probability at low energy and must transition faster around the resonance energy resulting in a larger slope. The transition width is determined by the density profile and production profile of

neutrinos in the Sun.

2.4 Standard Solar Models

The Sun is the closest stellar object to Earth and provides us with an extremely intense high energy laboratory to test our understanding of physics and astrophysical theories. The Sun is approximately 5 billion years old which puts it about half-way into the main sequence cycle where hydrogen burning is the primary means of generating energy. In approximately another 5 billion years the Sun will burn up most of its hydrogen rich environment and develop into a red giant as it is not massive enough to go supernovae which requires on order of 20 solar masses.

Theoretical modeling of stars has existed for some time but it was the perseverance of John Bahcall which has given standard solar models their high standard and accuracy. His early work with Ray Davis on the Homestake experiment [56, 57] can be considered as the culmination of the field to experimentally test solar models. Over the past 35 years Bahcall's SSM code has been the most detailed and readily cited. Always providing valuable insight into the differences in SSM calculations [58] and guided the direction of solar neutrino experiments. As such, the SSM used throughout this work is taken from Bahcall and Serenelli, BS05(OP) model[59], and details on the SSM not covered in this section can be found in his book[19] and the literature cited therein.

2.4.1 The Basics of Modeling Stellar Evolution

Standard solar model codes have two fundamental assumptions. 1) The Sun is in quasi-steady state equilibrium, requiring an energy balance between that produced in the core and the observed surface flux. 2) The primary means of energy production in the Sun is through nuclear fusion and not through other mechanical mechanisms such as expansion and contraction of the solar radius. The primary fusion cycle which generates energy in the Sun is initiated with the fusion of two protons by way of the reaction $\mathrm{p} + \mathrm{p} \rightarrow \mathrm{d} + \mathrm{e}^{+} + \nu_{\mathrm{e}}$. As such, this is referred to as the "PP Cycle" and the full reaction cycle is shown schematically in Fig. A.1.

A second, sub-dominant, solar fusion process is referred to as the "CNO Cycle" because Carbon, Nitrogen and Oxygen are the primary burning elements. There are four CNO cycles [60] which cycle back on themselves. Only the two most dominant CNO cycles are considered in this work and their fusion reactions are shown in Fig.A.2. These two cycles make up 99% of the energy production from the CNO chain which in itself only produces a few percent of the total solar energy.

SSM	**PP**	**PEP**	**HEP**	**^{7}Be**	**^{8}B**	**^{13}N**	**^{15}O**	**^{17}F**
BS05(OP)	5.99	1.42	7.93	4.84	5.69	3.07	2.33	5.84
BPS08(GS)	5.97	1.41	7.90	5.07	5.94	2.88	2.15	5.82
BPS08(AGS)	6.04	1.45	8.22	4.55	4.72	1.89	1.34	3.25

Table 2.2: Standard Solar Model predicted fluxes. BP05(OP) model fluxes are taken from ref.[61] while BPS08(GS) and BPS08(AGS) are taken from ref.[16]. The fluxes are expressed in units of 10^{10} (PP), 10^{9} (^{7}Be), 10^{8} (PEP,^{13}N,^{15}O), 10^{6} (^{8}B,^{17}F), 10^{3} (HEP) cm^{-2}s^{-1}

In this work and in most literature, solar neutrinos are referred to by their primary fusion element. Thus, ^{7}Be solar ν_{e}s are produced in the PP cycle via the fission reaction $^{7}\mathrm{Be}+\mathrm{e}^{-} \rightarrow ^{7}\mathrm{Li}+\nu_{e}$. Within each of these fusion cycles a neutrino is produced through electron capture or β^{-} decay processes. The astronomically compelling feature for using neutrinos to study the Sun is that they provide a snapshot of the energy production in the solar core just 8 min prior to their detection on Earth. Due to the mean-free path of photons in the Sun, the light we see today was produced by these same fusion processes more then 200,000 years ago [62]. Thus, comparison of the photon and neutrino luminosity will provide a unique constraint on the quasi-steady state equilibrium condition of SSM theories.

Stellar evolution codes define t_0 as the time the Sun entered the main sequence (Hydrogen burning phase) and rely on the following input parameters:

1. Primordial Heavy Elemental Abundances
2. Solar Luminosity
3. Solar Age
4. Radiative Opacity
5. Rate of Elemental Diffusion
6. Nuclear Fusion Cross Sections

SSM codes do not take into account mixing as a result of turbulent diffusion or solar rotation. There are two boundary conditions: the "luminosity constraint," which requires the code to reproduce the radiative luminosity at the solar surface and the code must reproduce the solar radius and heavy element abundances observed at the surface.

Stellar evolution codes provide a number of important output parameters for determining the expected flux for experiments on Earth. The most important number, if neutrinos did not oscillate,

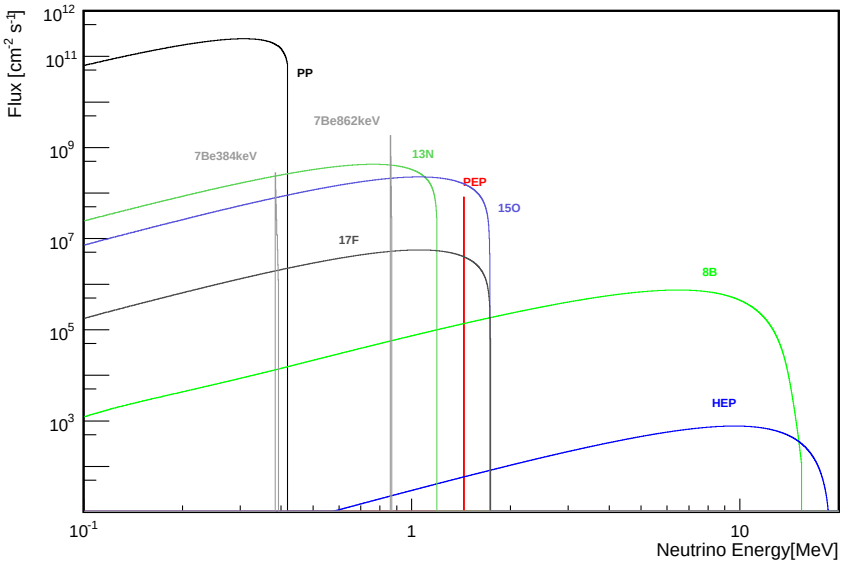

Figure 2.6: The PP and CNO neutrino energy spectra from the fusion cycles shown in Figs. A.1 and A.2. The solar fluxes are normalized to the BS05(OP) rates. The spectral shape of ^{8}B was taken from ref. [63] while all other spectral shapes were taken from Bahcall [64]. Thermal broadening was applied to the ^{7}Be lines in accordance with ref. [19].

would be the total fluxes of each of the different neutrino types. Table 2.2 gives the expected fluxes from three of the most prominent SSM calculations [61, 16]. The normalized energy distributions are obtained from laboratory measurements [64, 63] and then scaled to the SSM fluxes to produce the non-oscillated solar neutrino energy spectrum shown in Fig. 2.6. This work does not consider the CNO electron-capture modes which would contribute to this spectrum [65].

As previously discussed, neutrinos do oscillate, and in order to correctly model their propagation we must consider matter effects in the Sun. The ν_e survival probability is given by Eq. 2.36 which relies on several input parameters from SSM calculations. Adiabatic and non-adiabatic effects rely on knowledge of the electron density as a function of the solar radius and the neutrino production as a function of the solar radius as shown in Fig. 2.7. With these two parameters and the total expected flux we can correctly model solar neutrino propagation.

2.4.2 Modeling Solar Neutrino Propagation

The C++ code used to model solar neutrino propagation in this work is referred to as KNuSolar. This code was developed by the author and Lindley Winslow [66] to provide p.d.f.s for KamLAND

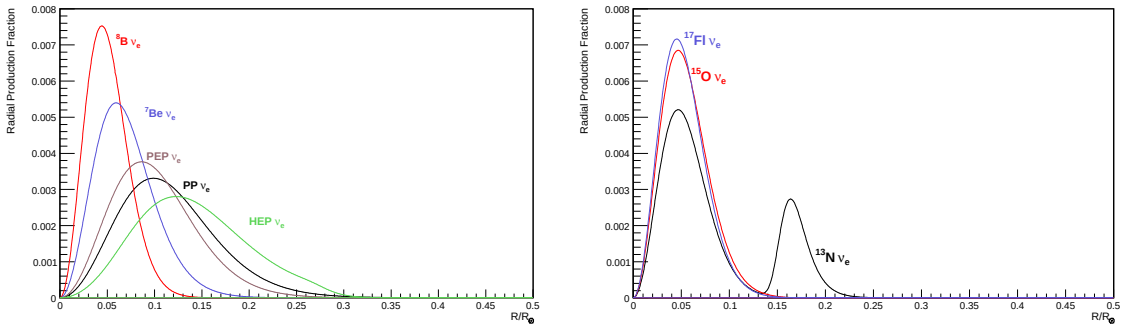

(a) (b)

Figure 2.7: Normalized neutrino production profile as a function of solar radius, $R_\odot$ for PP 2.7(a) and CNO 2.7(b) fusion.

data. However, KNuSolar is a stand-alone code which could be utilized for other solar neutrino experiments in the future.

Experimentally the quantity of interest is the spectrum-averaged differential cross-section:

$$\langle \frac{d\sigma}{dT} \rangle = \int_{E_{\nu,min}}^{E_{\nu,max}} dE_\nu \, S(E_\nu) \left(\frac{d\sigma}{dT} \right)_{Tot} \tag{2.38}$$

where $S(E_\nu)$ is the normalized neutrino energy spectrum from the SSM (Fig. 2.6), $E_{\nu,min}$ is the minimum neutrino energy that can produce an electron recoil with energy T, given by

$$E_{\nu,min} = \frac{1}{2}\sqrt{T + T\,(T+2)}. \tag{2.39}$$

and the total differential scattering cross-section is

$$\left(\frac{d\sigma}{dT} \right)_{Tot} = \left(\frac{d\sigma}{dT} \right)_{Rad} + \left(\frac{d\sigma}{dT} \right)_{\mu} \tag{2.40}$$

where the magnetic moment term $\left(\frac{d\sigma}{dT}\right)_\mu$ is only considered in special cases. The assumption of no neutrino oscillations implies that the expected neutrino type is of the electron flavor and only the CC portion of the cross-section needs to be considered in this integral.

When neutrino oscillations are taken into account we must calculate the ν_e survival probability by introducing Eq. 2.36 into the cross-section calculation. The quantities from the SSM needed for to correctly model the ν_e survival probability are

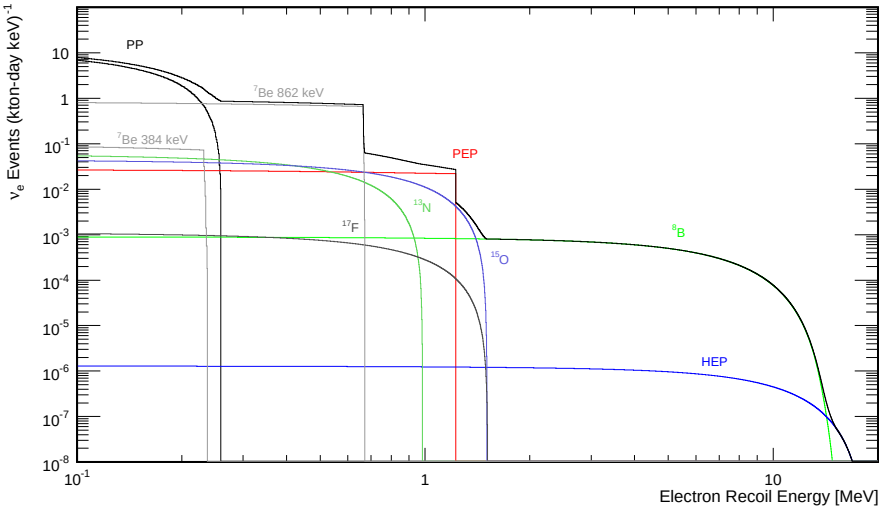

Figure 2.8: Expected neutrino-electron elastic scattering recoil energy spectrum in KamLAND with neutrino oscillations. This spectrum does not include detector response such as quenching and resolution.

1. Electron density as a function of solar radius [64].

2. Fraction of solar neutrinos produced in each radial zone, shown in Figs 2.7(a) and 2.7(b) .

3. Normalized neutrino energy spectrum, Fig. 2.6.

4. Total expected flux of each neutrino type given in Table 2.2.

Due to the energy and spatial dependence of these equations, the neutrino survival probability for the i$^{\text{th}}$ solar neutrino type takes the form:

$$P^{i}_{\nu_e \to \nu_e} = \int dR\ \Phi^{i}_{\nu}(R) \int dE^{i}\ \frac{1}{2}\{1 + (1 - 2P_{\text{jump}})\cos 2\theta_m \cos 2\theta_{12}\}\, S^{i}_{\nu}(E) \tag{2.41}$$

where $\Phi^{i}_{\nu}(R)$ specifies the fraction of neutrinos produced as a function of radius, $S^{i}_{\nu}(E)$ is the normalized neutrino energy spectrum, and the term in brackets is the neutrino survival probability from Eq. 2.36. The inner integral is over the neutrino energy and the outer integral is over the solar shells. The dR integration is divided into approximately 1200 radial regions for numerical integration.

Neutrino oscillation allows for conversion into different flavors and therefore the NC cross-section must also be considered. Thus, the average differential scattering cross-section is modified to include

oscillations such that

$$\langle \frac{d\sigma}{dT} \rangle^{i}_{osc} = \int_{E_{\nu,min}}^{E_{\nu,max}} dE_\nu \, P^{i}_{\nu_e \to \nu_e} \left(\frac{d\sigma}{dT} \right)^{CC}_{Tot} + \int_{E_{\nu,min}}^{E_{\nu,max}} dE_\nu \, \left(1 - P^{i}_{\nu_e \to \nu_e} \right) \left(\frac{d\sigma}{dT} \right)^{NC}_{Tot}. \tag{2.42}$$

The energy integral here must not be mistaken for the integral over the entire energy spectrum performed in Eq. 2.41. Effectively this is an integral over the electron recoil energy as is shown from the relation in Eq. 2.39.

The cross-section is then multiplied by the number of target electrons, N_e, to obtain the expected number of electron recoils per recoil energy bin dT in the detector

$$\frac{dN}{dT} = N_e \left(\sum_i \langle \frac{d\sigma}{dT} \rangle^{i}_{osc} \, N^{i}_{\nu} \right) \tag{2.43}$$

where N^{i}_{ν} is the expected total neutrino flux from Table 2.2. The expected oscillated electron recoil spectrum for KamLAND is shown in Fig.2.8. This spectrum does not consider the effects from detector response such as quenching and resolution which will be discussed in Ch. 4.

Chapter 3

The KamLAND Detector

The **Kam**iokande **L**iquid **A**nti-**N**eutrino **D**etector (KamLAND) was commissioned in the spring of 2002 to investigate the LMA solution to the solar neutrino problem described in Ch. 2.4. The KamLAND detector is situated 1 km (2700 m.w.e.) under Mt. Ikenoyama in Gifu prefecture, Japan. This cavern was home to the original Kamiokande [67] experiment.

3.1 Detector Description

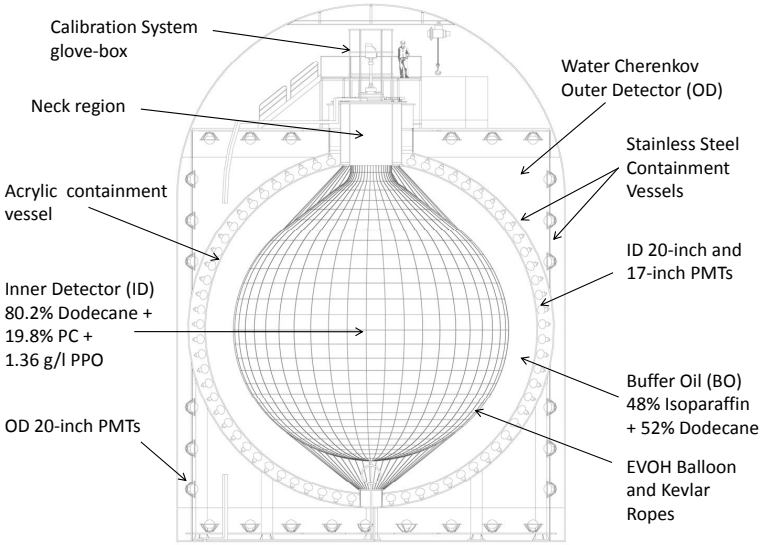

Figure 3.1: Labeled schematic of the KamLAND detector.

The KamLAND detector, as depicted in Fig. 3.1, has several layers of shielding which contribute to its low background capabilities. The 1 km of rock overburden reduces the muon flux at the surface by approximately a factor of 10^5 to 0.3 Hz at the detector. The cavern housing the detector is lined with a set of compensation coils to reduce the terrestrial magnetic field to < 50 mG allowing for proper operation of the photo-multiplier tubes (PMTs). PMTs work under the principle of the photo-electric effect and are sensitive to single photons, however, the influence of external electromagnetic fields can drastically impair this sensitivity.

The outer most layer of shielding is referred to as the outer detector (OD) and consists of 3.2 ktons of purified water, enclosed in a stainless steel (SS) cylinder, and operated as a Čerenkov detector. The OD is viewed by 225 20-inch PMTs (Hamamatsu R1449 [68]) providing a veto system for high energy events from the surrounding rock and cosmic rays. The OD is physically divided into four separate regions; top, upper, lower, and bottom which contain 50, 60, 60, and 55 20-inch PMTs respectively. Each region is lined with Tyvek sheets to enhance the reflectivity in each region.

The OD encloses an 18 m diameter, SS sphere, which houses the inner detector (ID). Mounted on the inside of the sphere, facing the center of the detector, are 1879 PMTs which measure 50 cm in diameter. There are 554 tubes reused from the KAMIOKANDE experiment which have a 20-inch photo-cathode. The other 1325 PMTs (Hamamatsu R7250 [69]) are a faster version [1] of the 20-inch tubes and are masked to a 17-inch photo-cathode. The 17-inch PMTs produce 22% photo-cathode coverage of the inner sphere's surface area. When all 1879 PMTs are considered, the photo-cathode coverage is increased to 34%. This SS sphere constitutes the beginning of the inner detector (ID).

The ID PMTs are encased in a 3.3 mm thick, 16.6 m diameter acrylic sphere. The volume between the acrylic and SS spheres is filled with a non-scintillating buffer oil, referred to as the outer buffer oil (BOO). The BOO helps to disseminate the heat produced by the PMTs and optically couples the PMTs to the acrylic. Acrylic was chosen because of its high impermeability to ^{222}Rn and the index of refraction is close to that of the oils used in the ID. The acrylic shields the active volume from ^{222}Rn out-gassing originating in the PMTs and the SS containment vessel. Between the acrylic and balloon lies 1.4 ktons of non-scintillating buffer oil, referred to as the inner buffer oil (BOI). The BOI is composed of 48% Isoparaffin and 52% Dodecane by volume. The volume ratio is such that the density is 0.04% less dense than the active scintillating volume. This produces bouyancy for the balloon, reducing the stress on the Kevlar ropes. Furthermore, the BOI provides shielding for the

[1] Faster refers to the difference in transit time spread. The 20-inch tubes use the standard Venetian-blind dynode while the 17-inch employ a Line-focus dynode. This improves the transit-time spread from 5.5 to 3 ns and the peak-to-valley ratio is improved by a factor 2 [69].

active volume from external radiation in the PMT glass and SS containment vessel.

The BOI region is separated from the active scintillating volume by a 135 μm thick balloon, held in place by Kevlar ropes. The balloon is composed of nylon and Ethyl vinyl alcohol copolymer (EVOH) materials. The balloon is 15 μm EVOH + three layers of nylon at 25 μm each and a final 15 μm layer of EVOH. The EVOH has a low permeability to ^{222}Rn and the nylon provides structural integrity to the balloon. The active scintillating target volume enclosed by the balloon is composed of 80.2% Dodecane, 19.8% 1,2,4-Trimethylbenzene (PC) and 1.36 ± 0.03 g/l of 2,5-Diphenlyoxazole (PPO) used as a fluor and is refered to as the liquid scintillator (LS). The LS has a density of 777.54 kg/m^3 at 15 °C and an average light attenuation length of 6.17 ± 0.19 m as will be discussed in more detail in Ch.7.2.4.

The neck of the detector consists of three SS concentric cylindrical volumes; 2, 3, and 4 m in diameter. The longest cylinder stretches 6.7 m from the base of the glove box to the balloon, while the other two cylinders stretch to the acrylic and SS outer sphere. Each of the three cylinders contain emergency overflow piping for the inner liquid volume and the height of the liquid is monitored to within 1 mm accuracy. The neck region contains the feedthroughs for cabling, thermometers, liquid level, pressure and rope tension monitors, CCD cameras, and other connections as well as all the piping for filling the different detector volumes (BOO, BOI, LS). This dead volume is constantly flushed with boil-off N_2 and acts as a fire retardant for the flammable LS as well as inhibits adsorption of oxygen and ^{222}Rn by the LS. To enhance detection of muons that pass through the neck of the detector, 6 5-inch PMTs are mounted at the top of the neck, which look down through the N_2 blanket into the LS. Furthermore, there are 16, 8-inch PMTs distributed throughout the BOO and BOI regions in the neck. Entrance into the active volume is gained through a 15.24 cm access flange and gate valve at the neck of the detector. Sitting on top of the neck is a hermetically sealed glove box which houses the calibration system. Access into the glove-box is gained through a transfer box which is continuously flushed with ultra-pure N_2.

3.2 Data Acquisition System

Gamma rays, with a few MeV of kinetic energy, predominantly transfer their energy through Compton scattering with electrons in the LS. The kinetic energy of the electrons are lost to radiative processes such as bremsstrahlung or Coulomb interactions which effectively transfers the kinetic energy into molecular excitations. Depending on the composition of the scintillator some of the

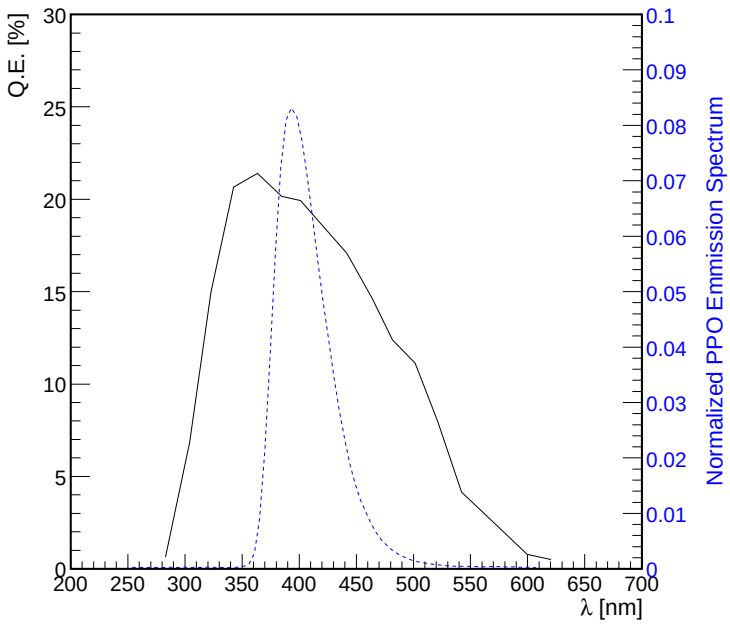

Figure 3.2: Quantum efficiency for KamLAND's 17-inch PMTs (solid-black) overlaid with the PPO emission spectrum (dotted-blue).

molecular excitation will de-excite producing scintillation light. However, for most organic liquids the energy is lost to non-radiative processes. Fluor is dissolved in the organic liquid to adsorb the molecular excitation energy and re-emits the light isotropically, shifting the wavelength into the visible region.

The key feature of any fluor is the re-emission spectrum is different then the adsorption spectrum, making it transparent to its own light. The scintillation light then propagates to the PMTs, which have approximately 20% quantum efficiency (q.e.) at the emission wavelength of the fluor ($\sim$ 400 nm) to produce a photoelectron (p.e.) at the photo-cathode of the PMT, see Fig. 3.2. Once ejected from the photo-cathode, the p.e. is focused by an electric field onto a set of dynodes which amplifies a single photon into a mV signal.

Each PMT voltage is sampled by a custom built [2] Analog Transient Waveform Digitizer (ATWD) which holds voltage information on an array of capacitors. An ATWD sample consists of 128, 10-bit samples with a configurable voltage sampling rate. This is set to 1.6 ns to yield a total sample time of 200 ns. There are 2 ATWDs (A and B) per PMT channel to minimize dead-time when the waveform is digitized ($\sim$ 30 μs). There are three gains acquired in parallel (high $\times$20, medium $\times$4, low $\times$0.5) to give enough sensitivity to detect single photo electrons while also collecting high

[2]Designed at Lawrence Berkeley National Laboratory

Data Period [m/d/y]	Prompt	Delayed	Prescale	Prescale [%]
Physics Trigger Conditions				
03/13/02 - 04/12/04	200	120	120	0.01024
04/13/04 - 05/30/07	180	120	120	0.01024
05/31/07 - 07/05/07	230	110	90	6.144
07/06/07 - 07/24/07	200	80	60	13.312
07/25/07 - 02/04/08	200	80	50	13.312
02/05/08 - 08/15/08	200	80	40	9.216
08/16/08 - 08/28/08	200	80	40	7.3728
08/28/08 - 10/10/08	180	80	40	5.12
10/11/08 - 11/19/08	180	80	40	7.168
11/19/08 - 04/03/09	90	90	40	1.024
04/03/09 - Current	70	70	40	1.024
Background Trigger Conditions				
08/12/03 - 05/31/07	disabled	disabled	35	9.216

Table 3.1: Trigger Nsum threshold conditions. The ID history trigger threshold is set to the lowest threshold trigger in each line of the table. After every prompt trigger the threshold is lowered to allow for a delay trigger within 100 μs. The prescale trigger collects data which exceed the threshold for a fraction of every second denoted by the prescale percentage.

energy muon events with > 1000 p.e. These and the accompanying electronics are mounted on the KamLAND Front-End Electronics (KamFEE) board. The KamFEE boards sum 12 PMT channels using a Field Programmable Gate Array (FPGA) to record the number of channels that exceeded the discriminator threshold (> 0.15 p.e.) in the previous 125 ns (hit-sum).

The KamFEE boards are read out by VME buses and are housed in 10 W-IE-N-ER Series 6000 VME crates [70]. Each VME crate contains 20 boards and the PMT channel mapping is done in such a way as to provide uniform coverage of the detector with each crate. This reduces the effects on event reconstruction during electronics problems. An independent VME crate houses the electronics for the OD and bestows a layer of independence between the two systems.

3.3 Trigger and Trigger Types

The trigger was developed at Stanford University [71, 72] and provides a dynamic link between the DAQ hardware and acquisition software Kinoko [73]. The trigger keeps track of the absolute event time through a 40 MHz clock on the trigger board and all event information is obtained in multiples of 25 ns. The number of clock ticks since the start of a run is referred to as the timestamp. This clock signals the FPGA to check the hit-sum for the previous 125 ns, every 25 ns, and then the trigger sums all the board hit-sums into a global Nsum value. Nsum is defined as the number

Trigger	Threshold [Nsum]	Triggers w/o Thresholds
OD top singles	6	1pps enabled
OD upper singles	5	ID to OD enabled
OD lower singles	6	OD to ID enabled
OD bottom singles	7	Forced acquisition on GPS
ID 5 inch PMTs	7	

Table 3.2: Water Čerenkov (OD) trigger thresholds, 5 inch PMTs thresholds which monitor the neck of the detector, and the triggers which allow read-out of all data upon a single ID or OD forced acquisition or during GPS and 1pps triggers.

of 17-inch PMTs over 1/3 p.e. at any given clock tick. Nsum does not include the 20-inch PMTs because they are not sensitive to single p.e. pulses. The trigger is composed of programmable logic which compares Nsum with preset threshold conditions. If one of these conditions is met, the trigger forces digitization of the ATWD.

The ATWD will hold its waveform for up to 175 ns after acquisition while it is waiting for a global acquire command from the trigger. When a global acquisition command is received from the trigger the launch offset is calculated. This is defined as the difference in timestamps from when the waveform was collected on the ATWD (went above discriminator threshold) and when the global acquisition command is issued (Nsum is greater then trigger threshold). During acquisition, each channel over threshold digitizes a 256 byte waveform. This block of information consists of the ATWD sample, which ATWD (A or B) was collected, the gain, timestamp, board channel (0-11), launch offset, and other information needed for data reconstruction.

The trigger synchronizes the 40 MHz clock signal with a Global Positioning System (GPS) every second providing an absolute time to each event to within $\pm$150 ns of Coordinated Universal Time (UTC). Absolute event times are needed to synchronize various detectors around the World in the rare instance that a supernovae is observed. Otherwise, the timestamp is a suitable clock for all other situations.

The physics trigger threshold values for the data analyzed in this work are given in Table 3.1. The trigger conditions referenced throughout the text are defined below:

1. The **1pps global acquisition trigger** forces read-out of the data once every second. This is a random trigger with respect to events and is used as a means of analyzing the dark rate in the detector.

2. The **ID prompt trigger** issues a global acquisition trigger if the ID Nsum $\geq$ a pre-designated threshold. It further opens a 1 ms time window in which an ID delayed trigger can occur.

3. The **ID delayed trigger** issues a global acquisition trigger if the ID Nsum $\geq$ a pre-designated threshold and it must occur within 1 ms of the ID prompt trigger.

4. The **ID prescale trigger** issues a global acquisition trigger for every event with an ID Nsum $\geq$ a pre-designated threshold for a specified fraction of each second (prescale fraction).

5. The **ID history trigger** records the ID Nsum when the Nsum goes above a pre-designated threshold. The history trigger then keeps track of the Nsum value for the subsequent 200 ns or until a global acquisition command is issued.

6. The **supernova trigger** is issued when at least 8 events with Nsum $\geq$ or 1100 (Nsum $>$ 772 before Feb. 2004) occur in 0.84 seconds. The trigger changes its state and goes into a singles only mode in which the ID prescale threshold is 170 Nsum and a ID history threshold of 100. This state is held for 1 min and locks out the user's ability to manually change run conditions. It further notifies the user of the supernova mode and an on-line data analyzer processes the data in real-time for supernova event candidates.

The 8 16-inch PMTs in the BOO are included in the Nsum for the OD top tubes. The 8 16-inch PMTs in the BOI are not considered in the trigger logic but the waveforms are collected when the OD data is acquired. To get a complete snapshot of the detector, whenever the ID or OD issues a global acquisition based on the Nsum thresholds, all PMTs over threshold in the ID and OD are read-out due to the OD-to-ID and ID-to-OD triggers listed in Table 3.2. This table lists the trigger thresholds relevant to the OD Čerenkov detection as well as the triggers which do not have thresholds but play an important role in data collection. These triggers did not change for the physics runs considered in this work. The ID triggers did change, as can be seen in Table 3.1, and the modifications to these conditions are described in detail in Ch. 4.6. The next step is to take the waveforms collected by Kinoko and create events. The event reconstruction is described in detail in Ch. 4.

Chapter 4

Data Reduction

Chapter 3 provided a description of the KamLAND detector and the hardware associated with data collection. In this chapter an overview of the off-line event reconstruction techniques, detector calibration and reconstruction stability is presented. A complete description of KamLAND's trigger hardware and DAQ software is given in other work [71, 72, 73]. An in-depth discussions of the primary algorithms for event reconstruction and the reactor antineutrino data quality can be found in reactor analysis studies [73, 74, 75, 76, 77]. This work focuses on extending the event reconstruction systematic errors for the reactor period down to 250 keV to accommodate the analysis of low energy backgrounds in Ch. 5. The event reconstruction systematics are further extended past the documented reactor period to include new data taken with purified LS as well as providing a description of new energy reconstruction techniques. A complete description of the work performed on optimization of trigger thresholds for a solar neutrino measurement is given as well as an in depth analysis of the trigger threshold efficiency.

A few historical events affect the reconstruction and analysis techniques and require special treatment. Table 3.1 establishes the trigger conditions as a function of time and details KamLAND's capabilities of collecting low energy events. Low energy event waveforms were not collected prior to Aug. 2003. Alternatively, history runs (only Nsum information, no waveforms) were taken instead to examine the low energy status. On Apr. 20, 2004 (run 3611) the thermometers which had been permanently deployed in the LS along the central z-axis were removed. The thermometers affect the background spectrum and hence the fiducial volume (FV [1]) which can be analyzed. The end of the "reactor" phase of KamLAND is defined by the start of purification on May 12, 2007 (run 6802).

[1] The fiducial volume is defined to be the volume of LS inside a specified set of vertex cuts used in a specific analysis.

Data from this time forward has not previously been published and thus this work will establish the data quality and reconstruction techniques since the start of purification.

4.1 Event Reconstruction

Data is continuously collected in KamLAND and is stopped at least once per day to start a new "run." Special circumstances such as detector calibrations, hardware failure, and maintenance produce downtime in the detector but this constitutes less then 1% of the total detector live-time (LT). The previous chapter discussed how the events are seen by KamLAND's hardware. We now proceed with the software oriented side of data aquisition and analysis.

When a global acquisition trigger is received the ATWDs are read-out asynchronously and stored to buffers on Front-End Electronics (FEE) cards. There are 200 FEE cards, each connected to a designated computer. Periodically the FEE buffer is pulled and stored on computer memory along with the trigger information which comes from a separate data stream. Event builder software sorts through the data blocks and matches time-stamps to create "events." These event data blocks are then compressed and written to disk. It is the cumulative event data blocks which are used to define the position and energy for a physics event.

Over extended periods of time, changes in temperature, humidity, aging hardware, electronic ground fluctuations and other external factors affect the relationship between an event today and the same event type at a later date. To calibrate out these affects 3 different test waveforms are collected for each ATWD at the start of each run. There are 50 pedestals waveforms to determine the baseline, 50 test pulser waveforms to calibrate the channel voltage and 50 clock waveforms to calibrate the channel timing for the ATWDs. These waveforms are averaged for each ATWD and then used in low-level event reconstruction for that run.

4.1.1 Waveform Analysis

During waveform analysis the pedestal is first subtracted from the event waveform. The waveform is then smoothed using an algorithm which calculates an average first derivative and special care is taken at the edges of the sample. After the pedestal subtraction the waveforms typically have a non-zero offset. This offset is calculated and the baseline is subtracted. Peaks in the waveform are located by determining the second and third derivatives of the waveform. The leading edge of the first peak in the waveform defines the first photon arrival time at the PMT. The arrival time is known

to within a fraction of the ATWD sample width of 1.5 ns. To illustrate the need for accurate event timing, 4.8 ns translates into a distance of 1.0 m in KamLAND. Each peak found in the waveform is then integrated to calculate the total charge which is normalized by the mean charge of the 1 p.e. peak for that channel.

After calculating the timing and charge of each waveform it is necessary to remove bad PMT channels before determining the position and energy. Noisy or dead channels will influence the PMT hit distribution and negatively impact event reconstruction quality. Bad channels are flagged under the following conditions:

1. If less then 80% of the time a waveform is not recorded in a channel for a muon event (high charge, high multiplicity).
2. A channel has a hit rate of less then 10% or a no-hit rate of more then 10%.
3. There is a difference of more then 22% in hit rates between ATWDs on the same channel.
4. If the 1 p.e. charge is not within 25% of the 17-inch 1 p.e. mean charge.

4.1.2 Position Reconstruction

Under the assumption of a point-like vertex and isotropically emitted light, the vertex can be reconstruction from the PMT hit-timing information. Localized events (β, γ and α decays) in the detector are very nearly point-like. Their energy deposit in the detector produces both Čerenkov light, which is directionally oriented, and scintillation light, which is isotropic. Čerenkov light is a sub-dominant effect due to the fluor which adsorbs and re-emits this light isotropically. Furthermore the fluor increases the light yield by transferring otherwise lost molecular thermal energy into scintillation light [78]. The loss of Čerenkov light means that KamLAND does not have the ability to reconstruct the directionality of events. However, the high light yield provided by the fluor (approx. 300 p.e./MeV) makes the KamLAND detector sensitive to very low energy events.

These characteristics enable the event vertex to be calculated using a time-of-flight (TOF) calculation. The speed of light in the LS is finite ($v = c/n_{eff} = 2.0819$ m/s), were n_{eff} is an average index of refraction for the BO and LS. Finite speeds imply geometrically that the PMT which receives the first photon will be closest to the event vertex. Plotting the charge of each PMT, q_i, as a function of the first photon arrival time[2] for each PMT, t_i^0, we obtain a distribution for each event referred

[2]If there is more then one p.e. peak in a waveform only the first photon arrival time is considered. However, the charge is taken to be the integral of all peak charges.

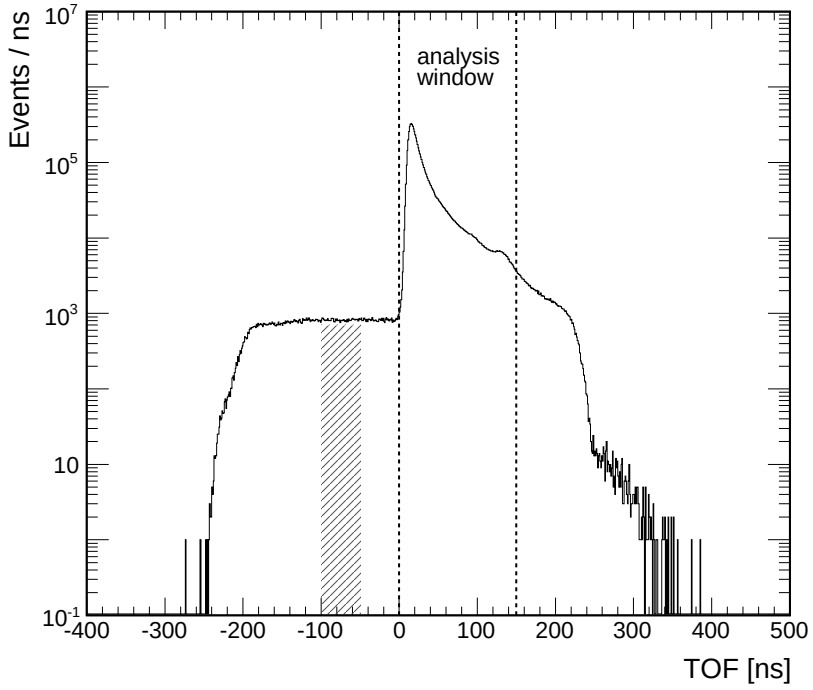

Figure 4.1: T_0 corrected arrival times, "pulse shape," for all ^{60}Co events from a source calibration at the center of the detector. The 150 ns region inside of the dashed lines is the analysis time-window for all waveforms. The hatched 50 ns time-window prior to the pulse is used to calculate the dark charge for the run.

to as the "pulse shape," $\phi(t_i^0)$. To calculate the correct timing distribution, ϕ is minimized using a log-likelihood method [79] such that the function

$$L = \prod_{i}^{Nhit} \phi(\tau_i(\bar{X}, t)) \tag{4.1}$$

$$\log L = \sum_{i}^{Nhit} \log \phi\left(\tau_i(\bar{X}, t)\right) \tag{4.2}$$

is minimized. The sum is over Nhit, which is defined as the total number of 17-inch PMTs with waveforms in an event. The optimal time is now written as

$$\tau_i = t_i^0 - T^{offset} - t_i(\bar{X}) \tag{4.3}$$

where T^{offset} is a global time offset for all PMT times and $t_i(\bar{X})$ is the TOF from an assumed vertex,

$\bar{X}$, to the i^{th} PMT. At the minimum of Eq. 4.2, the partial derivatives with respect to all four space-time parameters is zero. Fig 4.1 shows the average ^{60}Co pulse shapes, taken from a source calibration, after the minimization procedure. There is a clear rise-time at t = 0 associated with the start of the event after correcting for the time-of-flight. The average charge from noise, referred to as the dark charge, is calculated by taking an off-time window integral of the waveform prior to the distinct rise-time associated with the event. A special algorithm was developed for the vertex fitter, referred to as the V2 fitter, which minimizes the required processor time to determine the event vertex [77].

4.1.3 Energy Reconstruction

Once the event vertex is found and the t_0 corrected pulse shape is determined, we can proceed to calculate the "visible energy." Before a straight-forward calculation is performed the ATWD channel charges are calibrated using the test pulsers captured at the beginning of the run. For all good PMT channels, changes in gain for the 17-inch PMTs are calculated from the integral charge of the 1 p.e. peaks. The mean charge for the 1 p.e. peak is calculated for every run by analyzing the waveforms for low Nsum events. Due to the difference in dynode structure, the 20-inch tubes are incapable of resolving the 1 p.e. peak. Therefore, the 20-inch gain is calculated using high charge muon events. A gain scale factor is obtained by taking the ratio of total charge found in a 20-inch tube waveform and normalizing this with respect to the 8 surrounding 17-inch tubes.

Once the integrated charges in the waveforms are corrected for gain changes the visible energy can be computed. The reconstructed visible energy is defined as

$$E_{vis} = E_0 \left(\frac{\left(\sum_{i=1}^{Nhit} Q_i^{obs} \right) - Q^{dark}}{\sum_{i=1}^{Nhit} Q_i^{exp}} \right) \tag{4.4}$$

where E_0 is a constant such that $E_{vis} = 2.22$ MeV $= E_{real}$ for the gamma-ray emitted from the reaction $^1H(n,\gamma)^2H$. The numerator consists of a sum over all the PMT charges inside of a 150 ns time-window. The start of this time-window is defined by the TOF corrected pulse shape, as depicted in Fig. 4.1. The second term is the dark charge which is estimated by an off-time window integration of the TOF corrected pulse shape from [-100,-50] ns. The denominator is the expected

charge defined as

$$Q_i^{exp} = \frac{\eta_i e^{-L_i/\lambda}}{L_i^2} \xi_i \cos\theta_i \tag{4.5}$$

where the parameters are:

η_i : Is a correction factor for shadowing from the Kevlar support ropes and the balloon transparency.

L_i : Is the distance from the i^{th} PMT to the event vertex $\bar{X}$.

λ : Is the effective attenuation length of LS + BO

ξ_i : Is 1 p.e. threshold affect

θ_i : Is the angle subtended by the vector $\bar{L}_i$ and $\bar{X}_i$ which defines the distance from the i^{th} PMT to the center of the detector.

Calculation of the expected charge is based on Poisson statistics. Detailed descriptions of the energy reconstruction algorithms can be found in other thesis [75, 76].

4.2 Muon Track Reconstruction

At KamLAND's depth of 2700 m.w.e., the ID muon rate is 0.34 Hz (Fig. 4.2) with an average energy of 260 ± 8 GeV [80]. Given that muons produce internal radioisotopes through spallation in the detector, it is imperative that muon events are classified and tagged. Muon track reconstruction is a low-level procedure and is performed after the waveforms are calculated. The selection criteria for events to be fit with the muon fitter are:

- $Q_{ID17} \geq 10,000$ p.e.
- $Q_{ID17} \geq 500$ p.e. and $N_{200} \geq 5$

where Q_{ID17} is the total charge on the 17-inch PMTs and N_{200} is the total number of 20-inch OD tubes hit in a 200 ns time window. "Miss-reconstructed muons" are those muons which have stopped in the detector or have too little charge to reconstruct the track. "Showering muons" have too much charge deposit and typically results from multiple muon events or muons plus other high energy particles. The fraction of these events relative to the well reconstructed muons are 0.2% and 1.5% respectively.

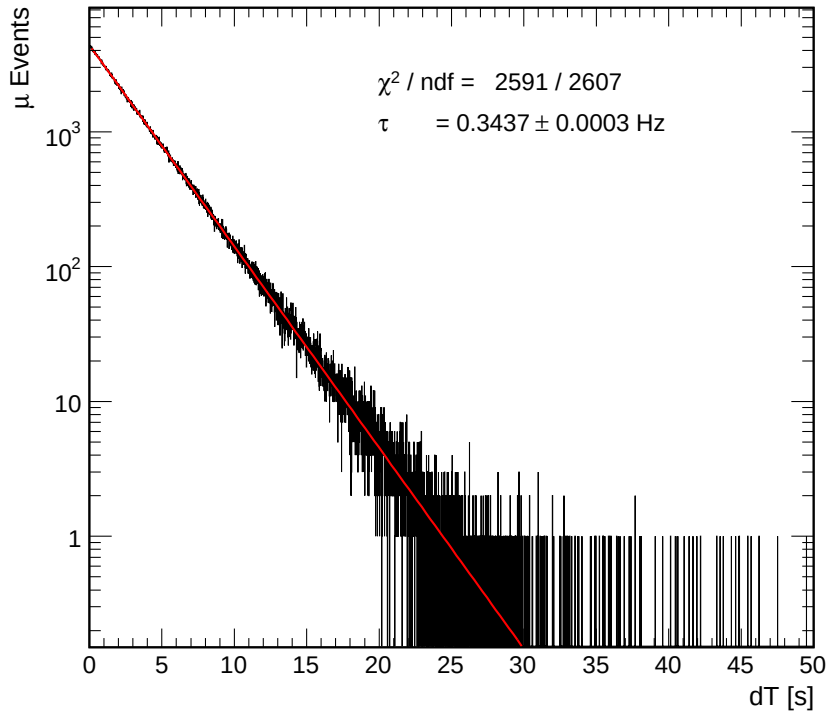

Figure 4.2: dT from last muon for well reconstructed muons.

Single muon events which pass through the detector are reconstructed based on the PMT hit-timing of Čerenkov photons. This is a different approach then for the point-like event vertex reconstruction discussed previously. Čerenkov photons are preferentially emitted into an opening angle relative to the particle's track which is dependent on the index of refraction of the liquid and the speed of the muon.

Muons are ultra-relativistic particles and for simplicity they are assumed to travel with the speed of light. Fig. 4.3 provides the parametrization for muon track reconstruction in KamLAND. Using this parametrization the arrival time, t, for a Čerenkov photon, γ, at a PMT can be calculated as

$$\begin{aligned} \mathrm{t} &= t_0 + \frac{l}{c} + \left(\frac{\mathrm{n}}{c}\right)\left(\frac{z-l}{\cos\phi}\right) \\ &= t_0 + \frac{l}{c} + \left(\frac{\mathrm{n}}{c}\right)\sqrt{(z-l)^2+\rho^2} \end{aligned} \tag{4.6}$$

where l is the distance from the entrance of the muon on the outer sphere, defined by the time t_0, to the vertex where the Čerenkov photon was emitted along the track. Minimizing this equation results

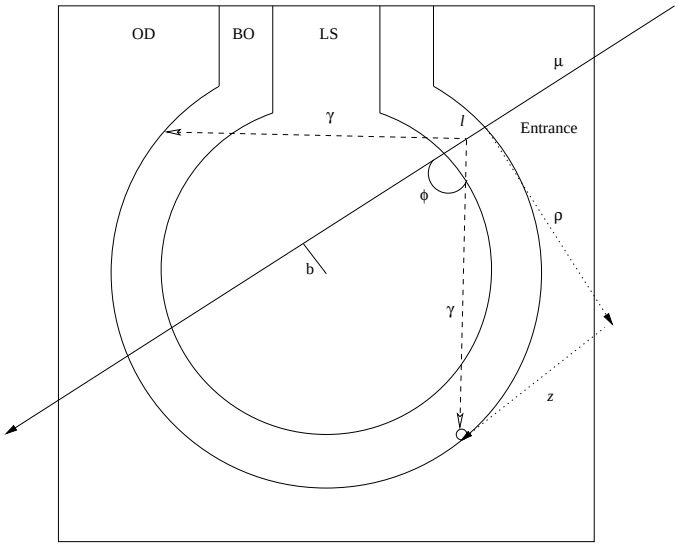

Figure 4.3: Parameterization of the muon track for Čerenkov photons, γ,d which are emitted at an angle ϕ defined by $\cos\phi = \frac{1}{\mathrm{n}}$, where n is the index of refraction for the liquid. The impact parameter, b, is the perpendicular distance from the muon track to the detector center.

in the following condition:

$$\frac{\mathrm{dt}}{\mathrm{dl}} = 0, \quad \cos\phi = \frac{1}{\mathrm{n}}. \tag{4.7}$$

Muon Characterization

An important characteristic of muons is the amount of charge deposited per unit track length in the LS and the BO. In Fig. 4.4 the total charge deposit, $\ln_{10}(\mathrm{Q}_{17})$, is expressed as a function of the impact parameter; defined to be the perpendicular distance between the muon track and the center of the detector as shown in Fig. 4.3. Q_{17} is defined as the total 17-inch PMT charge. The projection onto the y-axis reveals two distinct peaks in $\ln_{10}(\mathrm{Q}_{17})$ space. Fig. 4.4 depicts a charge correlation from which two distinct classes of muons are defined: through-going muons (LS) and clipping muons (BO). The larger charge deposit from through going muons is due to the increased number of scintillation photons in the LS while clipping muons primarily emit Čerenkov photons in the BO.

The total Q_{17} for well reconstructed muons (Badness < 100) is further correlated with the total track length in the LS and BO regions. The charge deposited per unit track length in the two detector

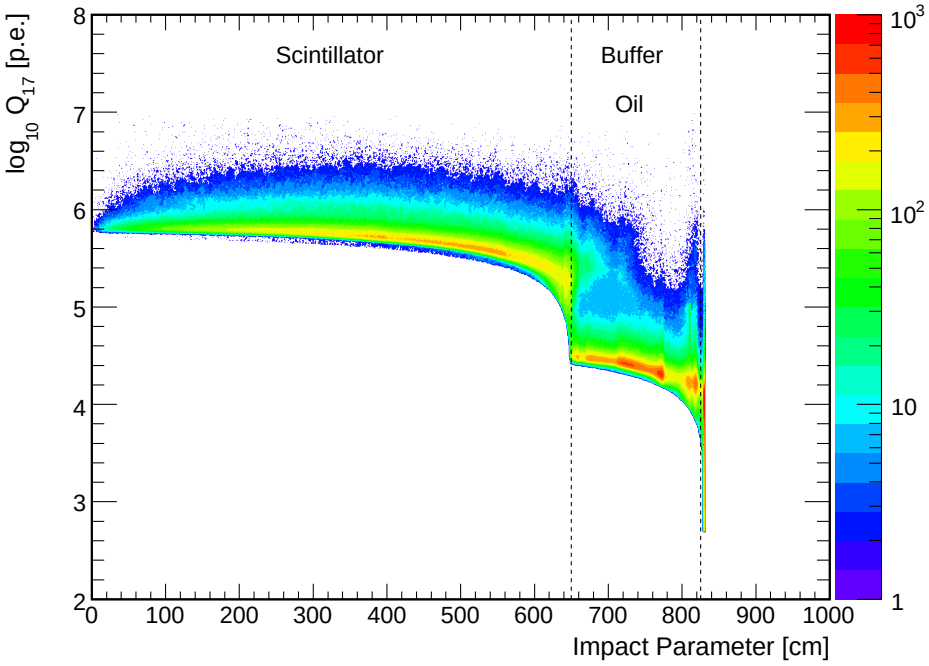

Figure 4.4: Muon $\ln_{10}(Q_{17})$ as a function impact parameter shows a clear correlation between through-going muons and clipping muons. The contour represents the number density of muons per bin.

regions is defined by:

$$\left(\frac{\mathrm{dQ}}{\mathrm{dx}}\right)_{\mathrm{Chern}} = \frac{Q_{17}}{L_{\mathrm{Chern}}} \tag{4.8}$$

$$\left(\frac{\mathrm{dQ}}{\mathrm{dx}}\right)_{\mathrm{Scint}} = \frac{Q_{17} - L_{\mathrm{Chern}} \left\langle \frac{dQ}{dx} \right\rangle_{\mathrm{Chern}}}{L_{\mathrm{Scint}}} \tag{4.9}$$

where $\mathrm{L_{Scint}}$ is the length of muon track passing through the LS, while $\mathrm{L_{Chern}}$ is the total length in the ID as Čerenkov photons are emitted along the entire path. Starting with muons which only pass through the BO ($6.6 \leq \mathrm{b} \leq 8.5$ m) allows a calculation of the mean charge deposit per unit track length associated with the BO as shown in Fig. 4.5(a). As the BO and LS are very similar chemically and have the same index of refraction to within 1%, the mean charge associated with scintillation photons can be calculated by subtracting off the expected Čerenkov charge contribution from a through-going muon. The dQ/dx distribution for through going muons ($\mathrm{b} \leq 6.4$ m) is shown

in Fig. 4.5(b). Fitting the peaks with a Gaussian function establishes the mean charge deposited per unit track for minimum ionizing muons:

$$\left\langle \frac{dQ}{dx} \right\rangle_{Chern} = 31.45 \quad [\text{p.e./cm}] \tag{4.10}$$

$$\left\langle \frac{dQ}{dx} \right\rangle_{Scint} = 629.4 \quad [\text{p.e./cm}]. \tag{4.11}$$

These nominal charge deposits are then used to define the residual muon charge, ΔQ, as the deviation from the expected charge deposit for a given track length:

$$\Delta Q = Q_{ID} - L_{ID} \left\langle \frac{dQ}{dx} \right\rangle_{Chern} - L_{Scint} \left\langle \frac{dQ}{dx} \right\rangle_{Scint}. \tag{4.12}$$

Showering muons are then defined relative to this residual charge: $\Delta Q \geq 10^6$ p.e.

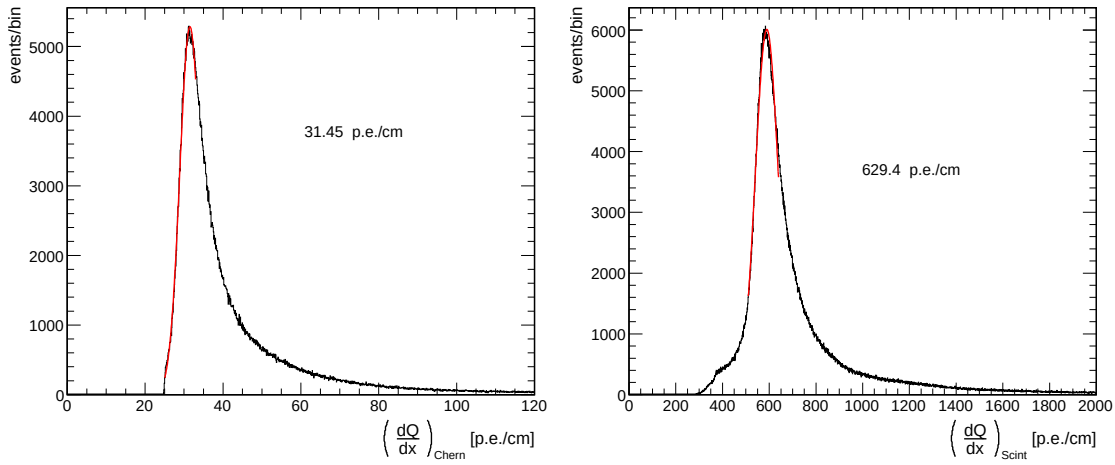

(a) (b)

Figure 4.5: dQ/dx distribution for clipping (4.5(a)) and through-going (4.5(b)) muons. The distributions are fit to a Gaussian to obtain a mean value used to define the residual charge.

4.3 Detector Calibrations

Detector calibrations with a known source are invaluable. They provide a means for defining the energy scale of the detector and to understand the reproducibility of both energy and vertex reconstruction. Table 4.1 provides a list of the manufactured calibration sources deployable in KamLAND.

Nomenclature	Particle Type	Energy [MeV]	Half-life
^{203}Hg	γ	0.2792	46.612 d
^{137}Cs	γ	0.6616	30.07 y
^{65}Zn	γ	1.1116	244.3 d
^{68}Ge	γ	2×0.511	270.8 d
^{60}Co	γ	1.1732, 1.3325	5.271 y
^{241}Am^{9}Be	γ, n	4.4, n$<$ 10	432 y
^{210}Po^{13}C	γ, n	6.13, n$<$ 7.5	22 y

Table 4.1: Calibration sources with their primary decay particle type and its corresponding real energy. The neutrons from the AmBe and PoC sources will thermalize and capture on Hydrogen and Carbon in the detector providing 2.225 MeV and 4.947 MeV gamma rays respectively.

Typically bi-weekly calibrations were performed along the central z-axis of the detector. The nominal calibration source was either the ^{60}Co or composite (^{68}Ge^{60}Co) source. Several times per year extensive calibration campaigns were performed, which sampled many z-axis positions and consisted of deploying several of the available calibration sources.

To reduce the systematic uncertainty on the FV for the reactor $\bar{\nu}_e$ measurement [81] a new "full volume" [3] calibration system was developed and deployed at the end of the reactor phase of KamLAND. The system was designed to reach off the central Z-axis into the radial direction as well as sweep through angles in ϕ and θ. Thus allowing a complete characterization of the position and energy reconstruction biases out to a radius of 5.5 m. A complete description of the calibration system, the material assay of its components and results were recently published [82]. Deployment of the off axis calibration system resulted in a reduction in the FV uncertainty for the reactor antineutrino measurement of a factor two [9].

Calibration of the PMT hit timing and charge (TQ) was performed with a dye laser which emits 500 nm light isotropically by way of a diffusion ball. The 500 nm wavelength is chosen as the PPO re-emission is minimal at this wavelength (see Fig.3.2) while still allowing for good PMT quantum efficiency. This minimizes absorption and re-emission light in the detector, thus providing high resolution charge distributions in the resultant waveforms. This allows laser calibrations to provide precision timing to all PMTs simultaneously. Differences in cable lengths, response times of PMTs, and other timing effects associated with the DAQ hardware are calibrated out with the

[3] This was also referred to as the 4π calibration system.

Parameter	Reactor Phase	Pur. Phase I	Pur. Phase II
17-inch Energy Resolution [%/$\sqrt{\text{E}}$]	7.6 (7.3)	8.6	8.6
$\text{E}_{\text{real}} \rightarrow \text{E}_{\text{vis}}$ [%]	6	6	6
17-inch Energy Position Dependence [%]	4 (1.5)	2.5	2.5
17-inch Energy Time Dependence [%]	1.3	2.5	2.5
Vertex Reconstruction [cm]	15	5	5
Vertex Resolution 17-inch [cm/$\sqrt{\text{E}}$]	12.1 ± 1.5	12.1 ± 1.5	12.1 ± 1.5

Table 4.2: Energy and vertex reconstruction systematic errors. Values listed in the reactor phase column in parenthesis are the errors associated with the reactor measurement. The energy reconstruction used during the purification phases is different then during the reactor phase and are presented for the corrected 17-inch energy explained in Sec.4.5

laser. A second order polynomial,

$$\text{T(Q)} = \text{P}_0 + \text{P}_1 \log_{10} \text{Q} + \text{P}_2 (\log_{10} \text{Q})^2, \tag{4.13}$$

is fit to the timing distributions as a function of charge (laser intensity) for each ATWD on every PMT channel. Application of this function to an event's timing distribution reduces the transit time spread and is applied prior to the waveform analysis.

Other calibration and measuring devices were deployed in KamLAND to include LED's, an instrumentation unit (IU) which was capable of measuring the temperature and pressure profile [82, 66] both on and off the central z-axis. A "LS sampler" was developed and deployed along the central z-axis to collect samples to measure optical properties and oxygen concentration for the actual KamLAND LS.

4.4 Reconstruction Biases for the Reactor Phase of KamLAND

This section presents the relevant energy and vertex reconstruction biases essential for a complete understanding of KamLAND's low-energy singles spectrum. This is the first work to present a detailed description of this energy region and its constituent radioactive background components which inhibited a ^{7}Be ν_{e} measurement during the reactor phase. As such, special consideration of

low energy biases, not considered during the reactor $\bar{\nu}_e$ measurement, are presented in this work. The analysis presented in this thesis uses only the 17-inch energy instead of the 17+20-inch energy used for the reactor analysis. The primary reason for using only the 17-inch energy is to allow for a direct comparison of energy reconstruction biases between all phases of KamLAND. The addition of the 20-inch tubes increases the resolution, however, the differences in resolution are negligible at this time. A summary of the results from this section is provided in Table 4.2.

4.4.1 Energy Reconstruction

Reconstruction uncertainties during the reactor $\bar{\nu}_e$ phase of KamLAND have been studied in extensive detail [9, 82, 76] for 17+20-inch energies above the inverse beta decay threshold of 1.8 MeV. The analysis presented in Ch. 5 is based on data taken during this period but only the 17-inch tubes are used. The energy is written as E_{17} to specify that only the 17-inch tubes were used. To compare with the well established reconstruction biases for the reactor measurement, E_{17+20} is overlaid for comparison when applicable.

To begin we must define two types of energy:

E_{real} : The true energy of a process calculated from first principles typically involving conservation of energy.

E_{vis} : The visible energy as measured in KamLAND which includes detector response, i.e. quenching and resolution.

Appendix C.1 provides the expected $E_{real} \rightarrow E_{vis}$ energy scale conversion factors obtained from MC. Estimating the reliability of the conversion functions for the different particle types is important as they play a key role in generating p.d.f.s for the low-energy spectral analysis. Deviations from the expected visible energy spectrum is determined from source calibration data. Fig. 4.6 shows the percent deviation of $\langle E_{17} \rangle$ from the expected E_{vis} for source calibration data as a function of Z-position.

The calibration source data is provided in Fig. 4.11(d) for Z-axis deployments within a 5.5 m FV. These data independently present a 2.5% systematic error as depicted with the horizontal dashed lines. However, the data begins to show a clear Z-bias for the low energy sources. The spread in the fitted mean energy is larger for ^{65}Zn than for the other low energy gammas (^{137}Ge, ^{68}Ge and ^{203}Hg). While the total energy deposit for ^{68}Ge is 1.022 MeV, the resultant energy deposit comes from electron-positron annhilation and calibrates the gamma energy of two instantanious 0.511

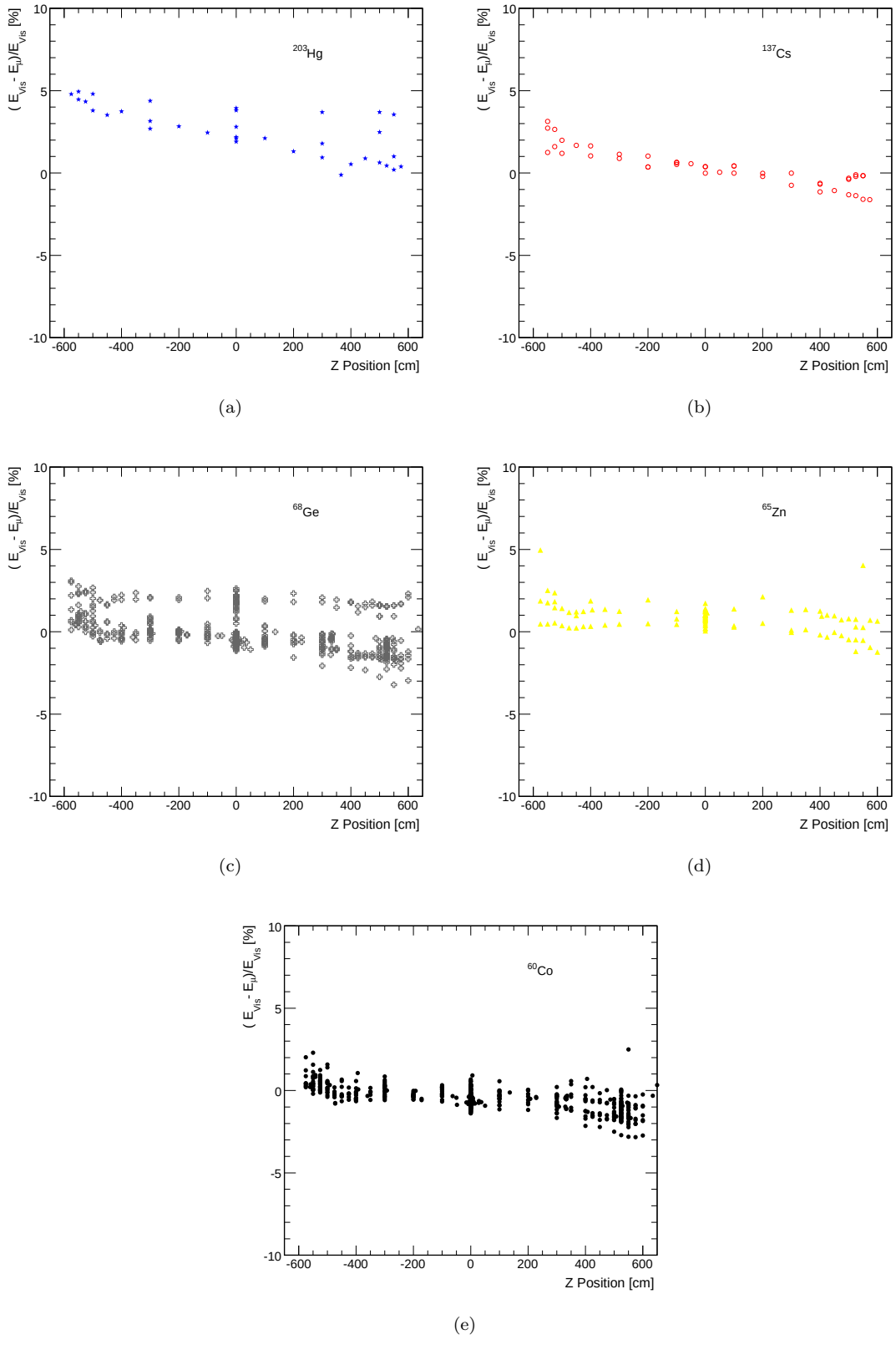

(a) (b) (c) (d) (e)

Figure 4.6: Z-dependent energy biases for the reactor period. The deviation from E_{vis} is larger for ^{203}Hg then for ^{60}Co. The individual sources are reproducible to within 2%.

MeV gamma-rays. ^{68}Ge further provides a measure of the zero kinetic energy positron scale which is essential to the reactor measurement. To cover the entire energy span from 0.25 - 5.0 MeV required for this thesis, the position dependent energy scale uncertainty is determined to be 4%.

The most important systematic error for this work is to establish the stability of the energy scale as a function of time. Large deviations would produce a biased spectral distortion in energy and inhibit integrating multiple runs. Fig. 4.7 indicates the percent deviation of $\langle E_{17} \rangle$ from the expected E_{vis} for all source calibration data as a function of time. While the time-variation of $\langle E_{17} \rangle$ is stable to within 1.2% the uncertainty in $E_{real} \rightarrow E_{vis}$ conversion is as great as 6% when taking into account the low energy ^{203}Hg data. These figures include the purification phases (hatched regions) which will be discussed in the next section.

4.4.2 Vertex Reconstruction

The reconstructed vertex for calibration sources deployed along the Z-axis are shown in Fig. 4.8. In these figures ^{60}Co and ^{68}Ge represent the largest deviation in fitted vertex positions as they provide the most statistics. The difference in the expected and fitted vertex is good to within 15 cm for all source energies.

Vertex resolution was previously calculated for the 17-inch PMTs to be (12.5±1.5) cm/$\sqrt{(}$E[MeV]) [76]. In actuality the position is not dependent on energy, rather it is dependent on the number of PMTs hit in the event through Eq. 4.2, which is linearly related to energy for low multiplicity events. More importantly the spread in vertex positions becomes larger as the PMT hit distribution relies on Poisson statistics to establish the difference between the expected noise and signal. The fitted vertex standard deviation is plotted against the real energy for all the calibration sources in Fig. 4.9. Fits to the functional form $\sigma/\sqrt{E}$ have very poor χ^2 values of more then 20 and can be improved slightly by adding a constant parameter. However, the best fit values were consistent with those established through MC methods [76].

4.5 Reconstruction Biases for the Purification Phase of KamLAND

During purification of KamLAND's LS, a physical distinction between purified volumes was maintained to amplify the effects of the procedure. The reasoning and results of this procedure are described in detail in Ch. 7. As a consequence of the deliberate stratification of LS, the purified

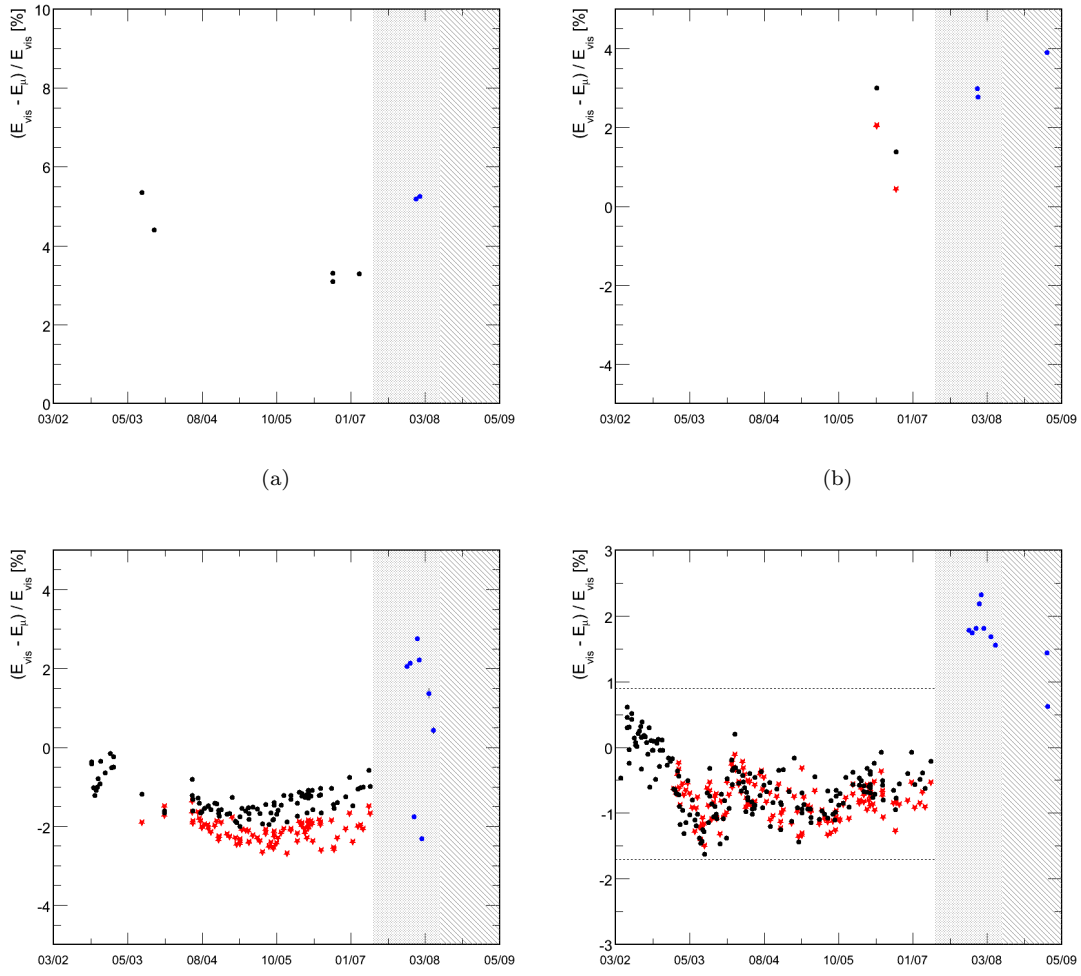

(a) (b)

(c) (d)

Figure 4.7: Time variation of source calibrations at Z = 0. The variation with respect to the expected energy (E_{vis} MeV) is shown for E_{17} (black circles), E_{17+20} (red star), E_{17Corr} (blue circles). The time-variation for the reactor period is 1.2% from the average fitted mean energy. For ^{60}Co, this produces an offset of -0.4% from E_{vis} and the 1.2% variation is shown with the dashed lines in Fig.4.7(d). Phase I and Phase II of purification are shown as the hatched time regions. Fits with pdfs require an uncertainty in the both the time-variation and the offset.

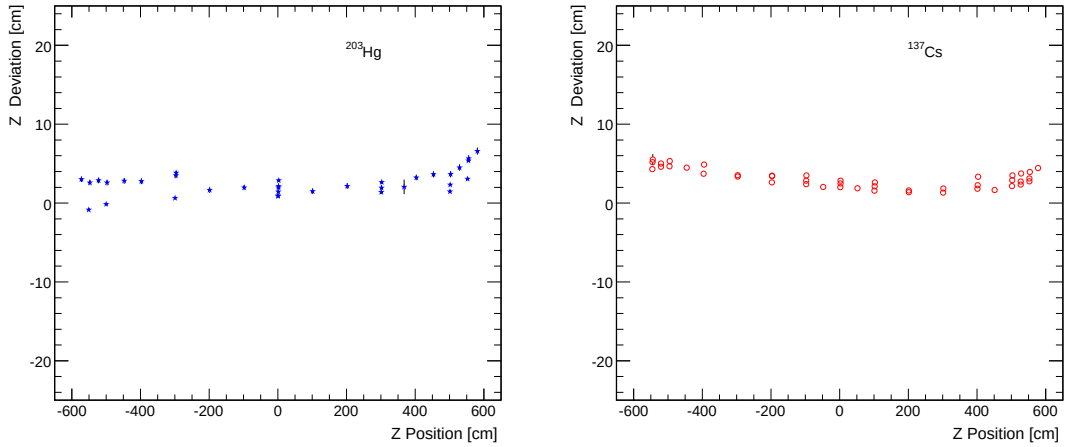

(a)

(b)

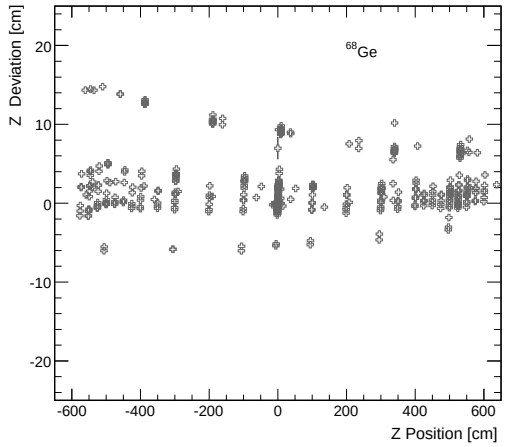

(c)

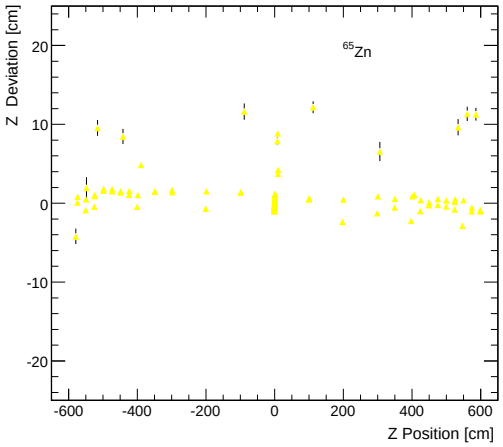

(d)

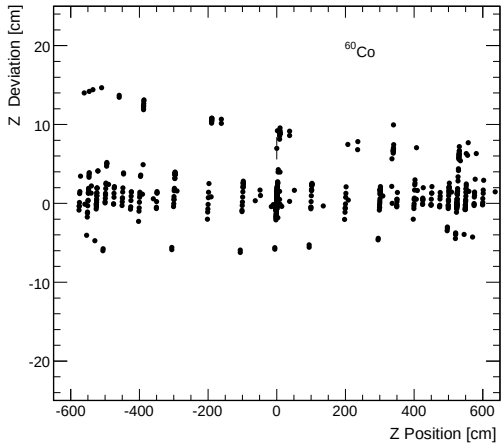

(e)

Figure 4.8: Z-dependent vertex bias for the reactor period. The vertex reconstruction is good to within 15 cm for all source energies.

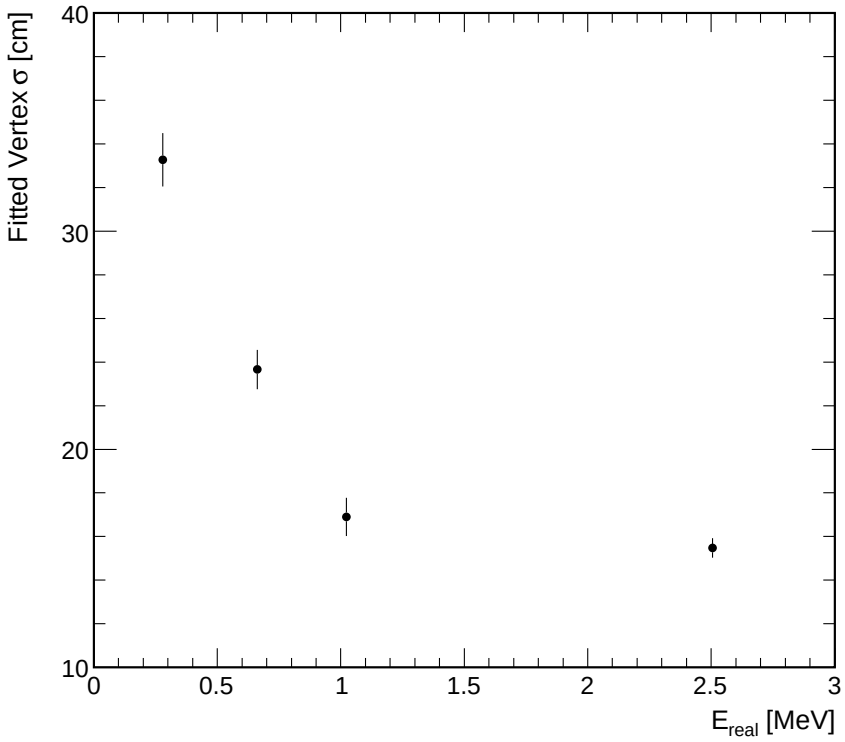

Figure 4.9: Distribution of the fitted vertex standard deviation as a function of energy. The distribution does not fit well to the functional form $\sigma/\sqrt{E}$ but instead seems to be follow a linear distribution for low energy and becomes constant for high energy.

volume was not completely homogeneous during or after the purification procedure. This method of purification produced a gradient in LS quality along the z-direction in the detector. Furthermore, mixing of the LS during purification induced effects which produced radial biases in the detector. This established a spatial dependence between the n and n-1 purified LS volumes.

As a result of purifying the LS, the major difference between the optical quality of the purified phases was found to be the amount of light output. While the density and composition were controlled to be homogeneous within less then 1%, a 10% loss in light yield was observed during the purification procedure, see Ch.7.3.1 for details. To calibrate out the effects from differences in optical properties between the LS volumes, a new spatially dependent energy correction was constructed for purification analysis. This new energy parameter is referred to as the corrected energy E_{17corr} and will only be used for 17-inch reconstructed energy. This energy correction is applied as a final step to E_{17}, which is calculated in the same manner as the reactor data period.

Isotope	Particle Type	Energy [MeV]	Source
^{40}K (EC)	γ	1.460	Balloon, Kevlar ropes
^{208}Tl	γ	2.614	Balloon, Kevlar ropes
^{1}H(n,γ)^{2}H	γ	2.225	muon spallation
^{12}C(n,γ)^{13}C	γ	4.947	muon spallation
$^{85}\mathrm{Kr} \rightarrow \beta + ^{85}\mathrm{Rb}^{*} + \nu_{\mathrm{e}}$	γ	0.514	^{85}Kr in LS
^{214}Po	α	7.687	^{238}U,^{222}Rn in LS
^{212}Po	α	8.784	^{232}Th,^{220}Rn in LS
^{210}Po	α	5.304	^{238}U,^{222}Rn in LS

Table 4.3: Radioactive backgrounds which occur in the detector components or are inherent in the LS. These naturally occurring radio-isotopes in KamLAND are used as calibration sources. They are also used to monitor time dependent and spatially dependent variations in energy. The primary particle used for calibration and the real energy of each decay is given as well as the location of the source in KamLAND.

4.5.1 Position Dependent Energy Correction after Purification

The position dependent energy correction is calculated by dividing the detector into two volumes R $>$ 5.5 and R $\leq$ 5.5 m. Spatial devisions are relevant because external gamma-rays were utilized as calibration sources. Due to attenuation, external gamma-ray sources lose their intensity as the analyzed radial distance becomes further from the source. This attenuation effect is measured in Fig. 5.21. Table 4.3 lists the nuclear reactions and radioisotopes which provide in-situ calibration points.

The following conditions define the spatial dependent energy correction:

R $>$ 5.5 m :

1. The outer spherical shell was divided into 91 Z-slices. The 1.46 MeV ^{40}K γ-ray from the balloon and Kevlar ropes was fit and a 3 day running average of $\langle \mathrm{E}_{17} \rangle$ was calculated. This allows for an ample number of events and provides a smooth time-dependent correction.
2. 10 equidistant ($\Delta R - 0.1$ m) radial shells were taken from 5.5 - 6.5 m in radius. The same ^{40}K γ-ray energy was fit in this region. Due to the low event rate in the inner shells, this required several months of data to produce the radial dependence. Thus the correction implicitly assumes a certain stability with time.

R $\leq$ 5.5 m :

1. Along the Z-axis, corrections are made using the ^{60}Co γ-ray calibration data. Calibrations are only performed to typically $\pm$5.5 m and the Z-slice dimensions are dependent on the calibration. This position dependent term is only calculated when source data is available.
2. Using the 2.2 MeV n-capture γ-ray, 55 ρ-slices ($\rho = \left|X^2 + Y^2\right|$) where used, extending in cylindrical shells from 0 - 5.5 m. The cylinders are centered on the Z-axis of the detector. To obtain the required statistics to fit each slice, this position dependent calibration also requires several months of data.

Z-axis calibration data are utilized in the same manner as Sec. 4.4 to measure the uncertainty in the energy scale. The effect of the stratification on E_{17} reconstruction and the application of correcting the energy to E_{17corr}, can be seen clearly in Fig. 4.10. The transition in the reconstructed ^{60}Co energy at Z 3.0 m is in good agreement with the expected position between the two purified volumes calculated from flow meters. After the energy correction is applied the position dependence of the energy is reproducible to within 1% along the Z-axis for all source energies. The energy reconstruction as a function of Z for all post-purification calibrations are shown in Fig.4.11. The Z-dependent diviation in the reconstructed energy is 2.5% for all data inside a 5.5 m radius.

To establish a systematic error with respect to the time dependence of the energy scale the data is plotted with the reactor data in Fig. 4.7. The time-frame for the two purified phases is rather short, however it can be seen that during the first phase of purification there is a 2.5% deviation in the energy scale with respect to time. While the second phase may be more stable the time-dependence cannot be established for a single calibration point. The procedure between the two phases was very similar and thus it is assumed that a 2.5% time-dependence is sufficient to account for the short period of data analyzed in this work around the single calibration point. The data in Fig. 4.7 further establishes the uncertainty in the energy scale. $E_{real} \rightarrow E_{vis}$ uncertainty is measured to be consistent with the reactor phase and a 6% systematic error is used.

Typically the energy resolution is determined from source calibrations at the detector center. Due to the relatively small number of calibrations, and to allow for a possible change in resolution as a function of positions, all the Z-axis calibration data inside of 5.5 m were used. The resultant standard deviation for each source position was divided by $\sqrt{E_{vis}[MeV]}$ for each source energy. Each value was filled into a histogram and this distribution was then fit to a Gaussian which provided an average resolution for each source energy over all Z-positions. Fig. 4.12 shows the energy resolution as a function of E_{real}.

The standard deviation of the fitted Gaussian provides an estimate of the uncertainty as a

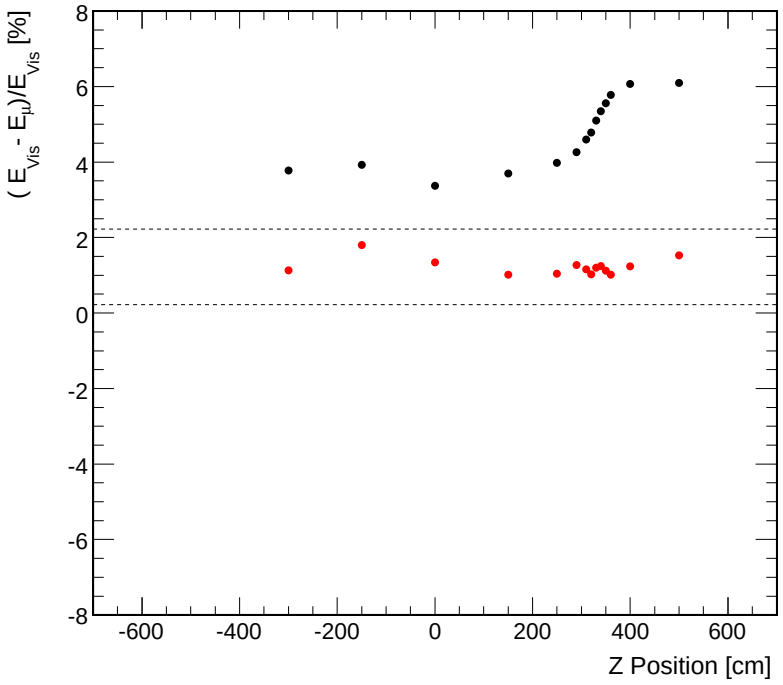

Figure 4.10: ^{60}Co source energy deviation as a function of z-position after Phase I of purification. The black stars show a clear change due to the expected phase change between the one and two times purified volumes. The red dots show the effect of the position dependent energy correction which makes the deviation along the z-axis less then 1%.

function of Z and was used as an estimate of the error on the mean. Fits to a first order polynomial established an energy resolution of 8.6% for both purification phases. It should be noted that this resolution is larger than during the reactor phase primarily because of the vertex dependent energy correction. Performing the same fits to E_{17} instead of E_{corr} yield an energy resolution of 8.0%. Thus, the additional vertex correction resulted in an artificial spread in energy, effectively decreasing the energy resolution. The 5.3% decrease in resolution for E_{17} between the reactor and purification phases can be attributed to the change in optical properties of the LS, specifically the light yield.

4.5.2 Vertex Reconstruction and Resolution

The deviation of reconstructed vertex positions for expected source calibration positions are shown in Fig.4.13. Vertex reconstruction is observed to be good to within 5 cm for all events inside a 5.5 m FV. In general the vertex reconstruction is consistent with that from the reactor phase, Fig. 4.8. Since the difference in LS composition from the reactor phase is less then 1%, and the position

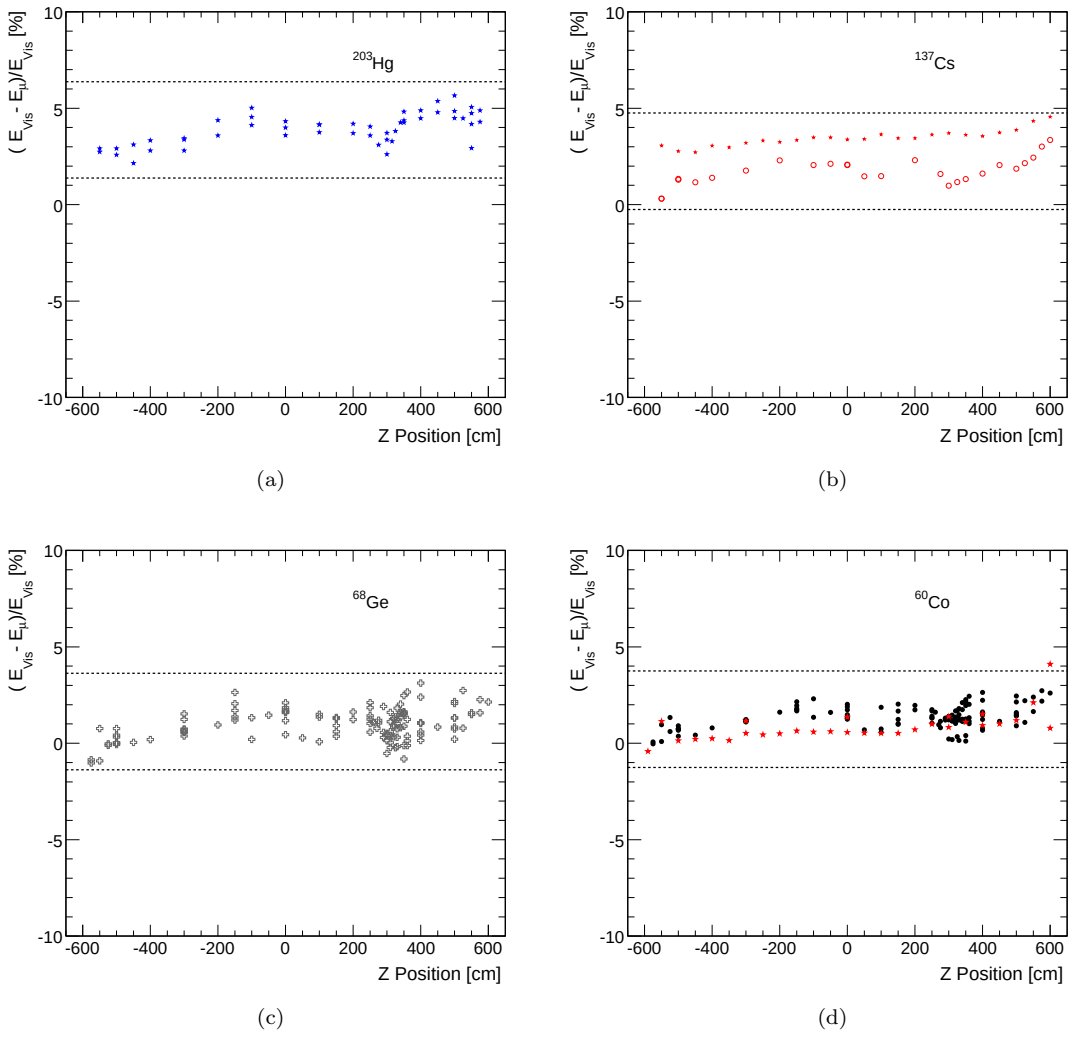

Figure 4.11: Z-dependent energy biases for purification phase I for four different source types. After the second phase of purification only the ^{60}Co and ^{137}Cs sources have been deployed. They are overlaid with the first purification data and are indicated by the red stars. The position dependent energy correction applied to the purification phase data improves the z-dependence relative to the reactor phase. The data shows a 2.5% energy deviation inside a 5.0 m FV.

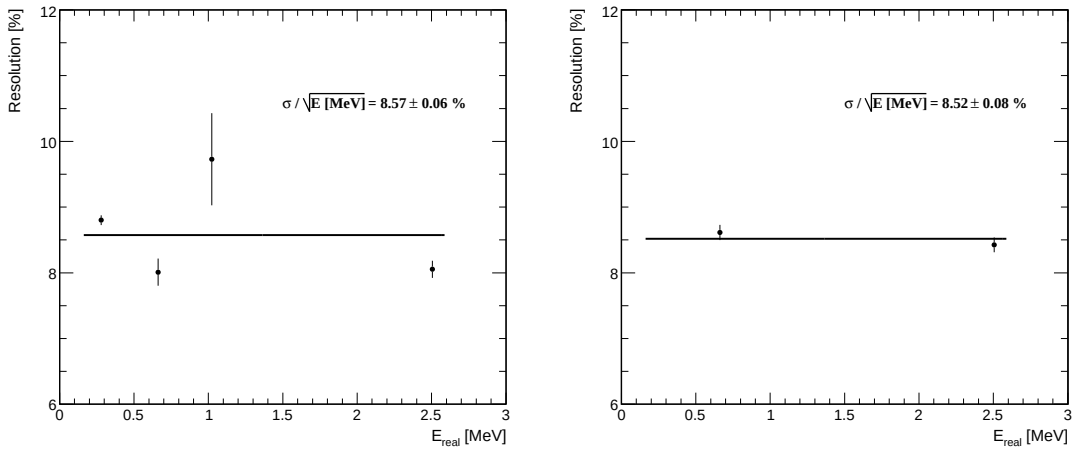

(a) (b)

Figure 4.12: Energy resolution obtained from fits to calibration source data for purification Phase I (4.12(a)) and Phase II (4.12(b)).

reconstruction is primarily dependent on the index of refraction of the liquid, one does not expect a significant deviation from previous data. As such, the systematic error due to the vertex resolution is taken to be the same as that established for the reactor period.

4.6 Optimizing the KamLAND Trigger for Solar Neutrinos

During the reactor phase the nominal trigger condition was optimized to collect reactor anti-neutrino data. A prompt-delayed trigger enabled the collection of all background data as well as the signal and provided a large reduction in the amount of collected data. The prompt threshold of Nsum 180 is equivalent to approximately 1 MeV of visible energy. After each prompt event the trigger threshold was lowered for 100 μs to the delayed Nsum threshold of 120. This is equivalent to approximately 0.6 MeV. Due to the high initial prompt trigger this condition is incapable of capturing ^{7}Be ν_{e} data. Several studies were performed to determine the optimal trigger conditions for solar ν_{e} collection.

Stress testing the DAQ provided an upper limit to the sustainable data rate. The current DAQ system is capable of sustaining raw data rates of up to 40 MB/s (1 kHz) before the DAQ has problems. Fig. 4.14 shows the raw integrated data-rate as a function of prompt Nsum threshold. It should be noted that the raw data rates correspond to the data stream before compression. Files are compressed before transfer and storage which provides a factor 3 reduction.

There are several requirements the trigger condition must meet for solar neutrino collection:

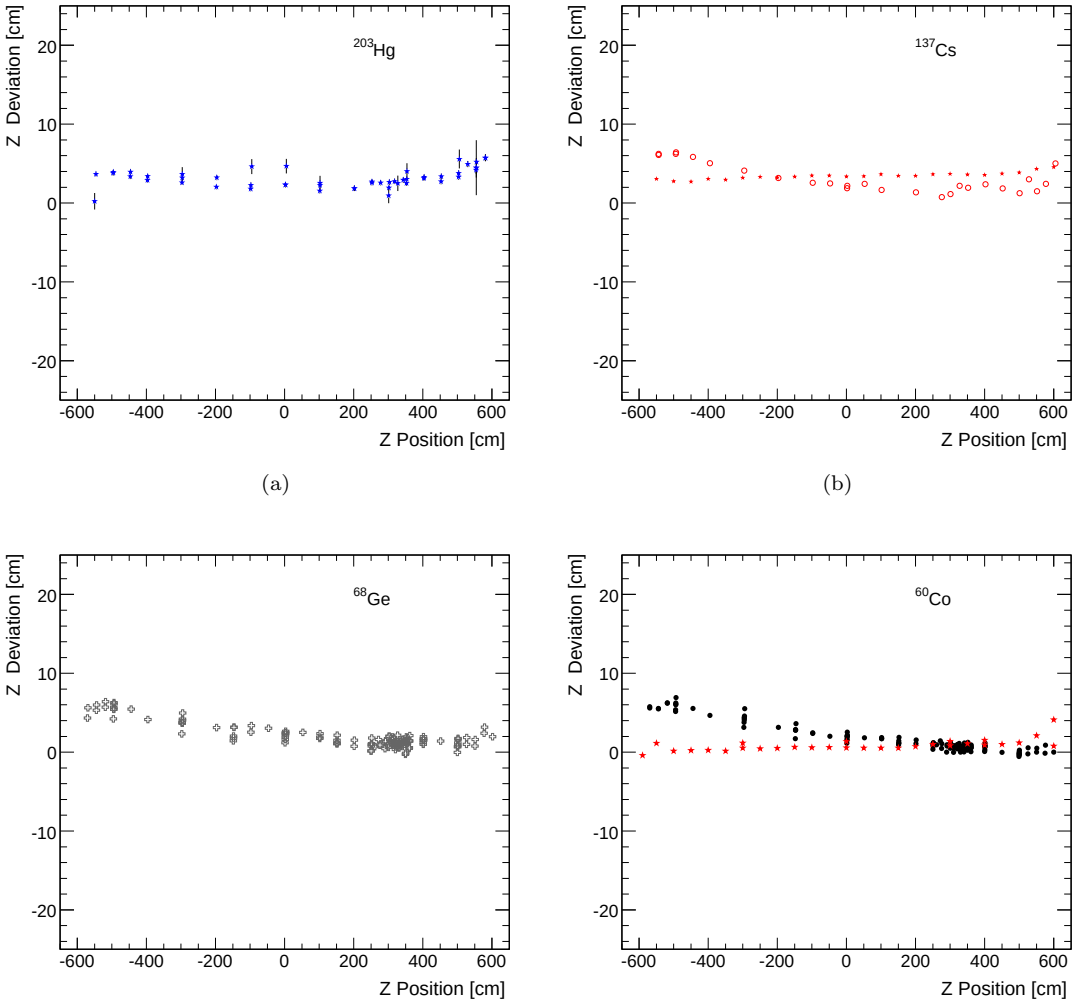

Figure 4.13: Z-dependent vertex bias for the purification period. After the second phase of purification only the ^{60}Co and ^{137}Cs sources have been deployed. They are overlaid with the first purification data and are indicated by the red stars. The vertex reconstruction is good to within 5 cm for all source energies.

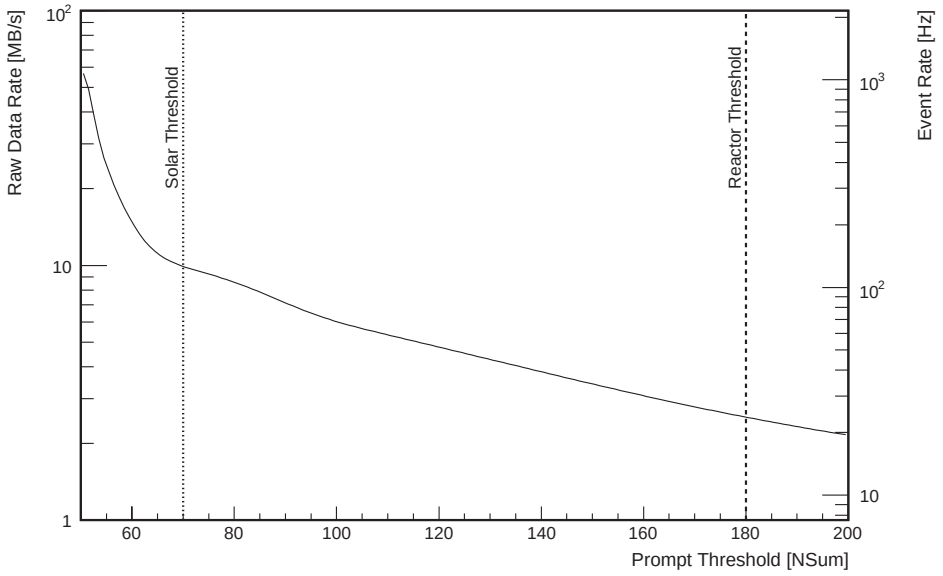

Figure 4.14: Integral data rate before compression for all events above the designated trigger thresholds. The primary prompt trigger dictates the data rate as all other triggers constitute less then 1% of the integral rate. The trigger thresholds of the reactor and solar phases are overlayed for comparison.

1. The data rate must be reasonable as to allow for storage of the collected data. At a Nsum threshold of 50 the data rate would require storing 1 TB/day after compression.

2. The collected data must be transferred to the US which can sustain compressed data rates on the order of 12 MBytes/sec.

3. Maintain sensitivity to a nominal 10 kpc supernovae event (SN). To mimic a SN event the DAQ was required to sustain an additional 100 Hz for 10 sec from pulsers [4]. This requirement mimics the expected number of interactions from our current understanding of neutrino production from SN and the neutrino interactions in a LS detector [83, 84].

4. Collect events with a threshold equivalent to real energy ≤ 350 keV to observe ^{7}Be ν_{e}.

5. Maintain sensitivity to reactor antineutrinos and geologically produced antineutrinos.

These requirements are approximations as the expected SN energy spectrum differs from KamLAND's singles spectrum and cannot be directly tested with pulsers. Furthermore, data rate is

[4]The expected time constant for SN neutrinos is on the order of 3 sec.

proportional to the energy deposit (dependent on the number of waveforms per event) and the pulser offers only an estimate of a mean energy deposit. However, it is expected that a 10 kpc SN would double the current data rate for a period of 10 s.

Table 3.1 lists the trigger thresholds for solar neutrino collection. The current trigger condition is equivalent to two singles triggers in which all events above an Nsum of 70 (250 keV) are collected with no loss in LT. To sample the very low energy spectrum, a second singles trigger takes data for a fraction of every second (defined by the prescale fraction) and records all events above a Nsum threshold of 40 (160 keV). With these trigger conditions KamLAND acquires approximately 8 MB/s, making the total data rate approximately 250 Gbytes/day. Amazingly, even with these low thresholds, this is only twice as much data as was collected during the reactor phase. Currently the low energy threshold is driven by external radiation inhibiting a lower threshold without allowing for higher rates.

4.7 Trigger Threshold Efficiency

The most prominent effect seen in the singles energy spectrum arises from the trigger threshold. Threshold conditions dictate that the DAQ will only collect events with an Nsum value above some designated threshold which is dependent on the number of PMT hit not on the event's energy. The mapping from Nsum to visible energy is Gaussian for events with Nsum greater then the dark rate (10 Nsum). All events with equal Nsum correspond to an energy distribution with a mean and sigma. Therefore, the total singles energy spectrum is the sum of Gaussian mappings from Nsum to energy. For events near the trigger threshold the mapping produces an inefficiency in energy and this efficiency function must be calculated to fully understand the singles spectrum.

As the mapping from Nsum to visible energy is Gaussian, statistically only the amplitude of the Gaussian changes as the event Nsum values gets closer to the trigger threshold. The threshold efficiency is therefore represented by an error function with a mean μ and sigma σ. The trigger efficiency ϵ can be written analytically as

$$\epsilon\left(\mathrm{E},\mu,\sigma\right)=\frac{1}{2}\left\{1+\mathrm{Erf}\left(\frac{\mathrm{E}-\mu}{\sqrt{2}\sigma}\right)\right\}. \tag{4.14}$$

To calculate the efficiency function for current physics trigger conditions, special low threshold (Nsum 30) runs were taken. After applying appropriate analysis cuts the nominal trigger efficiency

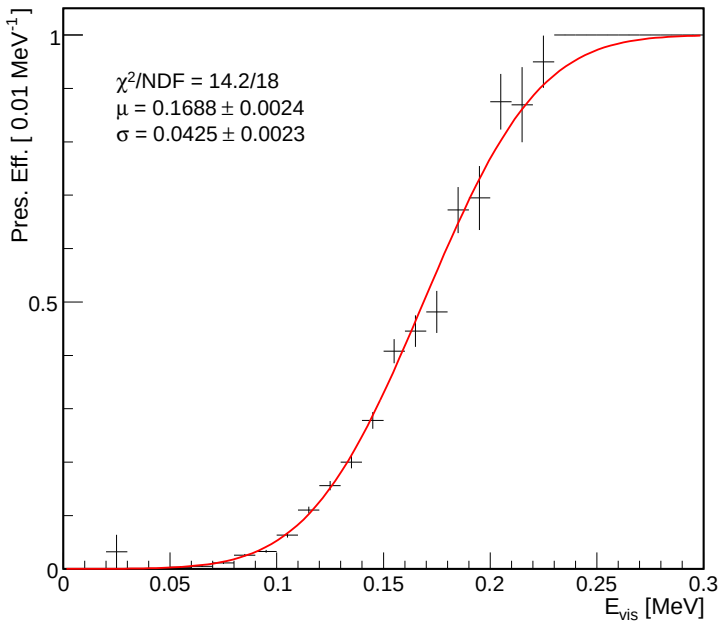

Figure 4.15: Trigger efficiency ϵ, for Nsum 40 threshold (prescale trigger). The functional form fit to the data is given by Eq.4.14. The data is fit for the 17-inch corrected energy after Phase II of purification.

is calculated as

$$\epsilon\,(\mathrm{E}) = \frac{\mathrm{f(Nsum > Threshold)}}{\mathrm{f(AllData)}} \tag{4.15}$$

and then fit to Eq.4.14. By using the same data in both histograms no scale factor is needed to account for detector live-time (LT) or cut efficiencies. The prescale trigger (Nsum > 40) efficiency curve is shown in Fig. 4.15. This is the lowest energy data currently being collected by KamLAND.

4.7.1 Trigger Efficiency Correction

As noted in the previous section, energy and Nsum are not one-to-one mappings. Furthermore, there is a difference in Nsum for a 1 MeV event at the center and near the balloon edge due to the detector's geometry. This difference is removed in energy space through calibrations but when considering threshold efficiencies it becomes important to study the spatial dependence of the mapping. As previously noted, after purification the LS was stratified in the detector and each

volume had different optical properties. Thus, in order to best understand the threshold efficiency after purification a position dependent efficiency mapping was designed.

The detector was divided into 5 radial shells $\{[0.0, 3.0], (3.0, 3.5], ..., (4.5, 5.0]\}$ m. These shells were then split into an upper ($Z \geq 3.0$ m) and lower ($Z < 3.0$ m) region. The Z-position defined the one and two-times purified LS phases as seen in Fig. 4.10. By fitting different radial shells to Eq.4.14, a position dependent map of the efficiency function was generated. Eq.4.14 now becomes:

$$\epsilon\left(\mathrm{E}, \mu(\mathrm{Z},\mathrm{R}), \sigma(\mathrm{Z},\mathrm{R})\right) = \frac{1}{2}\left\{1 + \mathrm{Erf}\left(\frac{\mathrm{E} - \mu(\mathrm{Z},\mathrm{R})}{\sqrt{2}\sigma(\mathrm{Z},\mathrm{R})}\right)\right\}. \tag{4.16}$$

Using this mapping the singles energy spectrum could be corrected using the fitted efficiency's mean and sigma and their associated errors. The uncertainty in the efficiency function has to take into account the correlation between the fitted mean and sigma. The error on the threshold efficiency correction is therefore given by:

$$\Delta\epsilon\left(\mathrm{E}, \mu(\mathrm{Z},\mathrm{R}), \sigma(\mathrm{Z},\mathrm{R})\right) = \left\{\left(\frac{\partial\epsilon}{\partial\mu}(\Delta\mu)\right)^2 + \left(\frac{\partial\epsilon}{\partial\sigma}(\Delta\sigma)\right)^2 + 2\frac{\partial\epsilon}{\partial\mu}\frac{\partial\epsilon}{\partial\sigma}\mathrm{cov}(\mu,\sigma)\right\}^{1/2}. \tag{4.17}$$

The partial derivative can be calculated analytically by making use of the Maclaurin series expansion

$$\mathrm{Erf}(\alpha) = \frac{2}{\sqrt{\pi}}\sum_{\mathrm{n}=0}^{\infty}\frac{(-1)^{\mathrm{n}}\,\alpha^{2\mathrm{n}+1}}{\mathrm{n!}\,(2\mathrm{n}+1)} \tag{4.18}$$

for the error function. One also needs to make use of the series expansion for the exponential to obtain the following functional form

$$\Delta\epsilon\left(\mathrm{E}, \mu, \sigma\right) = \frac{2}{\sqrt{\pi}}\mathrm{e}^{-\left(\frac{\mathrm{E}-\mu}{\sqrt{2}\sigma}\right)^2}\left\{\left(\frac{\mu\,\Delta\mu}{\sqrt{2}\,\sigma}\right)^2 + \left(\frac{(E-\mu)\,\Delta\sigma}{\sqrt{2}\,\sigma^2}\right)^2 + 2\left(\frac{\mu}{\sqrt{2}\,\sigma}\right)\left(\frac{(E-\mu)}{\sqrt{2}\,\sigma^2}\right)\mathrm{cov}(\mu,\sigma)\right\}^{\frac{1}{2}}. \tag{4.19}$$

With Eq. 4.16 and 4.19 a C++ class was designed which returns the correction and the corresponding error, given the position and energy of the event.

This efficiency correction class (KVFPreTriggEffCorr) allows the energy spectrum to be corrected independent of any histogram bin size as the events are "scaled" by the efficiency such that the new

event will have a weight of $1/\epsilon$. Thus when an energy spectrum is filled into a histogram, bin j has

$$\mathrm{N_j^{'}} = \sum_{\mathrm{i=1}}^{\mathrm{N}} \frac{\mathrm{N_i}}{\epsilon_\mathrm{i}} \tag{4.20}$$

and the statistical error on the bin is calculated as

$$\Delta\mathrm{N_j^{'}} = \sqrt{\sum_{\mathrm{i=1}}^{\mathrm{N}} (\frac{\Delta\epsilon}{\epsilon_\mathrm{i}^2})^2 + \sum_{\mathrm{i=1}}^{\mathrm{N}} (\frac{\Delta\mathrm{N_i}}{\epsilon_\mathrm{i}})^2} \tag{4.21}$$

where in the limit $\epsilon \to 1$ then $\Delta N_j^{'} \to \sqrt{N}$ as expected.

Chapter 5

^{7}Be Solar Neutrino Backgrounds

The primary focus of this chapter is to understand where KamLAND stands as a high-purity LS detector and what needs to be done to improve on the current radio-purity levels to enable a solar neutrino measurement. Fig. 5.1 provides a guide as to the low energy background rates prior to purification. The hatched region is the ^{7}Be solar ν_{e} region of interest. The studies presented in this chapter were initially performed prior to the full-scale KamLAND purification. This section provides the first published analysis of low energy backgrounds from the entire reactor period starting March 2002 and ending May 2007.

The most essential element in determining the steps toward making KamLAND a solar neutrino detector is to classify as completely as possible the backgrounds. Sec. 5.1 will describe in situ measurements of the intrinsic internal backgrounds in the KamLAND LS. Continuing with data analysis, Sec. 5.2 describes the external gamma-ray background and extracts a radial volume suitable for reducing the influence of the external background in the context of a solar neutrino measurement. Cosmogenic backgrounds have been studied in great detail [80] for the reactor phase of KamLAND. Sec. 5.3 summarizes the relevant cosmogenic backgrounds for a low energy solar neutrino measurement. Sec. 5.4 presents a detailed analysis of radioactive backgrounds introduced during detector calibrations. Finally, in Sec. 5.5 the measured rates are used to simulate KamLAND's energy spectrum to determine the required background levels to provide a measurement of ^{7}Be solar ν_{e} based on the SSM fluxes from Ch. 2.4.

The results from this chapter were used to guide the laboratory experiments presented in Ch. 6. Furthermore, the results from the laboratory purification experiments paved the way for the design and operation of the full-scale purification system described in Ch. 7. Detailed analysis of radiation

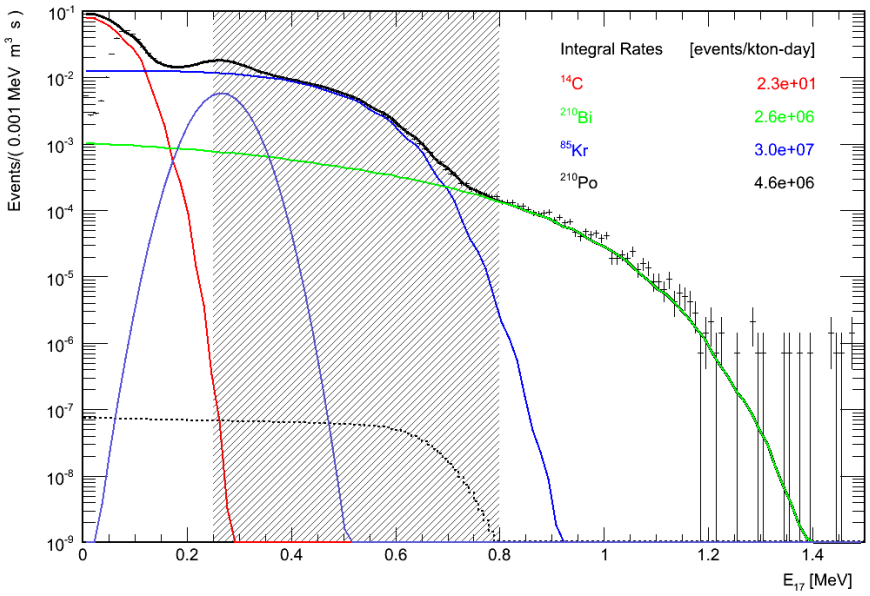

Figure 5.1: Low energy singles spectrum with major background contributions labeled along with their integral rates inside the energy interval $[0.25, 0.8]$ MeV (hatched region) of importance for a ^{7}Be solar ν_e measurement. The expected ^{7}Be solar signal is overlaid to provide the appropriate scale.

introduced during calibrations was recently published [82]. The results from this study presented the need for a new calibration system and drove the design and implementation of a new Z-axis calibration system. Finally, the techniques outlined in this section to extract specific radioisotope background levels are employed in Ch. 8 to quantify the effectiveness of the KamLAND LS purification.

Prior to the construction of KamLAND, detailed spectroscopic measurements of potential construction materials were performed [86, 87] using a Ge detector and Neutron Activation Analysis (NAA) for the most sensitive measurements. A method was developed to measure the radioactive constituents of the KamLAND LS using NAA [88] and establishes limits on the ^{40}K, ^{232}Th, and ^{238}U concentrations on the order of $< 10^{-15}$ g/g. Table 5.1 lists the published values for LS contaminates from in situ measurements prior to this work, summarizes the values obtained in this section and presents the required reduction needed to facilitate a future solar neutrino measurement.

Isotope	Published Values [g/g]	This Work [g/g]	^{7}Be Goal [g/g]
^{14}C	no estimate	$(3.98 \pm 0.94) \times 10^{-18}$	OK
^{40}K	$< 2.7 \times 10^{-16}$ [85]	$(1.30 \pm 0.11) \times 10^{-16}$	$< 10^{-18}$
^{39}Ar	no estimate	$< 4.3 \times 10^{-21}$	$< 10^{-24}$
^{85}Kr	no estimate	$(6.10 \pm 0.14) \times 10^{-20}$	$< 10^{-26}$
^{210}Pb	$(2.17 \pm 0.09) \times 10^{-20}$ [9]	$(2.06 \pm 0.04) \times 10^{-20}$	$< 10^{-25}$
^{232}Th	$(5.2 \pm 0.8) \times 10^{-17}$ [85]	$(8.24 \pm 0.49) \times 10^{-17}$	$< 10^{-16}$
^{238}U	$(3.5 \pm 0.5) \times 10^{-18}$ [85]	$(1.87 \pm 0.10) \times 10^{-18}$	$< 10^{-17}$

Table 5.1: Measured internal radioactivity concentrations in KamLAND LS. The first column of values are previously published values relevant for the reactor and geo-neutrino measurements. The second column are the measured values from this work and shows the improvement from previous measurements primarily from an increase in statistics. The limit for ^{39}Ar was derived from solubility arguments discussed in Sec.5.1.6. The last column establishes the requirements for a ^{7}Be solar neutrino measurement. The value quoted for ^{85}Kr is the concentration in KamLAND on March 1, 2002.

5.1 Internal Backgrounds

Considering KamLAND's LS composition, the solubility of gasses in these components, and a compilation of naturally occurring radioactive nuclei, thus defined an initial list of elements which should be examined in the context of this work. Carbon based systems are known to contain some fraction of the radioactive isotope ^{14}C. The extraction of oil from underground opens the possibility of finding metallic radio-nuclei known to exist in all earthen materials: ^{40}K, ^{232}Th, and ^{238}U. Possible contact of the LS with air during processing, transportation and detector filling presents the possibility of contamination with known air-borne radioactivity: ^{39}Ar, ^{85}Kr, ^{222}Rn. ^{39}Ar is a radio-nuclide produced in the upper atmosphere through spallation reactions of cosmic radiation with air. ^{85}Kr is predominantly produced in nuclear fission processes and exist in different quantities around the world. ^{222}Rn exists in variable levels in the air. On average ^{222}Rn is found in air with a specific activity of approximately 10 mBq/m^3. However, confined underground environments, such as the Kamioka mine, can see amplifications of this concentration by more then a factor 100.

5.1.1 ^{238}U Concentration

The complete decay chain for ^{238}U is provided in Fig. A.4 of the appendix. In this decay scheme there exists a fast coincidence from the ^{214}Bi $\rightarrow^{214}$ Po decay sequence. This produces a prompt beta

^{214}**BiPo Event Cuts**	**Efficiency** [ϵ]	^{212}**BiPo Event Cuts**	**Efficiency** [ϵ]
$1.3 \leq E_p \leq 3.5$ MeV	0.894	$1.0 \leq E_p \leq 2.5$ MeV	0.276
$0.4 \leq E_d \leq 0.8$ MeV	1.000	$0.55 \leq E_d \leq 0.95$ MeV	0.999
$10 \leq \Delta T \leq 500$ μs	0.837	$0.35 \leq \Delta T \leq 3.35$ μs	0.444
$\Delta R \leq 60$ cm	0.981	$\Delta R \leq 60$ cm	0.987
Total Cut Efficiency	0.734	Total Cut Efficiency	0.121
Beta Branching Ratio	0.9979	Beta Branching Ratio	0.6406

Table 5.2: ^{214}BiPo and ^{212}BiPo coincidence event cut conditions and their respective efficiencies. To extrapolate the Uranium and Thorium concentrations the branching ratio of the various decay modes must also be taken into account.

event above 1 MeV which is recognized by KamLAND's prompt trigger, as discussed in Sec. 3.3. The delayed event is a low energy alpha particle, emitted by ^{214}Po, which decays with a half-life ($T_{1/2}$) of 164.3 μs. This sequence of events is captured by KamLAND's prompt-delayed trigger, providing a mechanism to constantly monitor the ^{238}U concentration.

Even though the fast coincidence greatly reduces random backgrounds, the observed ^{214}BiPo coincidence can be fed by either ^{222}Rn, ^{226}Ra or ^{238}U. While KamLAND is hermetically sealed, the LS is periodically exposed to calibration sources which can introduce ^{222}Rn into the detector. ^{222}Rn provides a unique time signature when analyzing ^{214}BiPo events. If ^{222}Rn is the parent, the ^{214}BiPo events will exhibit a characteristic half-life of 3.82 days. In the ^{238}U decay chain, from ^{238}U down to ^{226}Ra, all nuclei have very long lifetimes and no distinguishing decay feature which would allow characterization of a disequilibrium. Therefore, in the following analysis the assumption is made that these long lived nuclei are in radioactive equilibrium with one another.

Analysis Cut Conditions

The analysis cuts used to identify the ^{214}BiPo coincidence events are listed in Table 5.2. Fig. 5.2(a) shows the vertex distribution of prompt events plotted as a function of R^3. By extending the prompt radius out to the balloon edge ($R_{balloon} = 6.5$ m) the event rate increases from several factors. First, there are more random coincidences due to the dramatic increase in the event rate from intrinsic balloon radiation and the ^{40}K and ^{208}Tl external gamma rays. Second, the balloon out-gasses ^{222}Rn into the LS from the intrinsic ^{238}U. Thus, to eliminate these backgrounds a 4.4 m prompt vertex cut is made, as indicated by the vertical line in Fig. 5.2(a).

Timing is a key consideration in picking out the coincidence events. The timing between two coincidence events exhibits an exponential probability distribution, with the time constant being equal to the delayed event's half-life. The upper limit cut on the difference in time (dT) between prompt and delayed is set to 500 μs. The primary consideration in defining the lower cut limit is the contribution from correlated ^{212}BiPo coincidence events from the ^{232}Th chain as discussed later.

The prompt energy cuts are defined by the increase in random coincidences from ^{40}K. Fig. 5.3 shows a fit to the prompt beta energy spectrum for events inside a fiducial radius of 5.5 m. At the lower edge of the spectrum the increase above the expected MC spectrum can be seen. The vertical lines designate the prompt energy cut conditions.

Alpha particle energies are highly quenched in LS, see Fig. C.3. The ^{214}Po alpha has an initial kinetic energy of 7.687 MeV. However, due to quenching, the visible energy in KamLAND is 0.560 MeV. A fit to the resultant alpha spectrum is shown in Fig. 5.2(d). Appropriate intervals around the mean of the Gaussian alpha spectrum are taken to include approximately $\pm 3\sigma$ from the mean fitted value

Systematic Error Estimation

To estimate the uncertainty in the energy scale a fit to the ^{214}Bi beta spectrum was performed using probability density functions (p.d.f.). Appendix B describes the method for generating electron and positron p.d.f.s used in this thesis. A slightly larger volume was used for this fit (5.5 m) in order to increase the statistics. All other event selection cuts are the same as those listed in Table 5.2. The ^{214}Bi energy spectrum is fit with a p.d.f. folded with $7.6/\sqrt{\mathrm{E}}$ energy resolution and a free floating normalization factor. The resolution was calculated for E_{17} in Sec 4.1.3.

To allow for a variation in the visible energy scale an energy dependent scale factor is defined. A possible energy deviation can be defined for calibration sources such that

$$f = \frac{\mathrm{E_{vis}} - \langle \mathrm{E_{17}} \rangle}{\mathrm{E_{vis}}} \tag{5.1}$$

where $\mathrm{E_{vis}}$ is the visible energy and $\langle \mathrm{E_{17}} \rangle$ is the fitted mean energy as shown in Fig. 4.6. The mean histogram bin energy $\langle \mathrm{E} \rangle$ can be related to the expected visible energy, $\mathrm{E_{vis}}$, by rearranging the terms in Eq. 5.1. The beta function energy scale factor is defined as

$$\langle \mathrm{E} \rangle = (1 - f)\, \mathrm{E_{vis}}. \tag{5.2}$$

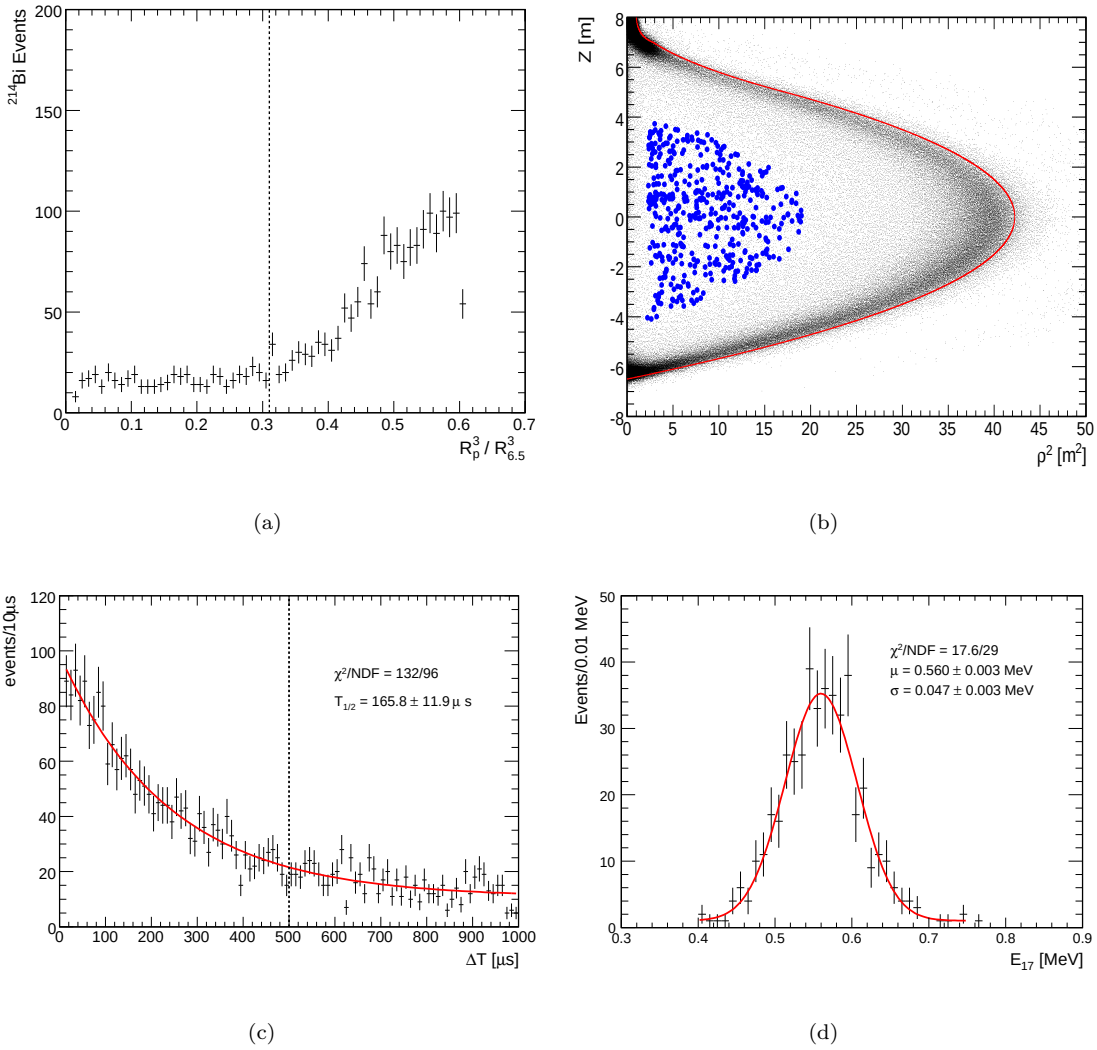

(a) (b)

(c) (d)

Figure 5.2: ^{214}BiPo event selection criteria to determine Uranium concentration in KamLAND LS. The fitted half-life in Fig. 5.2(c) is in good agreement with the expected $T_{1/2} = 164.3$ μs [89]. The ρ^2 distribution shows in Fig. 5.2(b) provides the expected geometric position of the balloon outlined in red. The increase in events when considering larger radii is clearly seen by the density of points. The final events are overlaid in blue to show their random distribution inside the FV considered. Further evidence for externals is seen in Fig 5.2(a) which has the final radial cut of 4.4 m designated by the vertical dashed line. The fitted alpha spectrum is shown in Fig. 5.2(d).

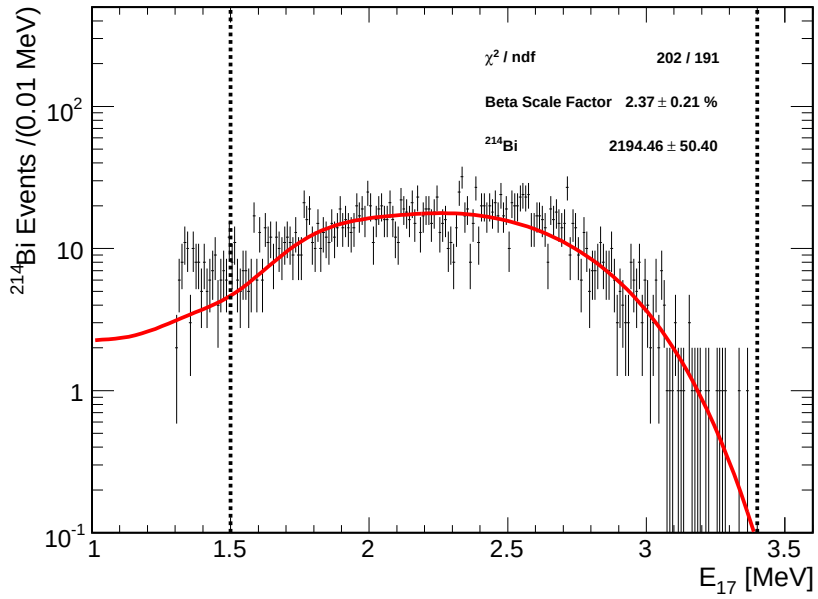

Figure 5.3: ^{214}Bi beta spectrum fit to MC spectrum folded with $7.6/\sqrt{\mathrm{E}}$ energy resolution. Allowing for an uncertainty in the energy scale while also fitting the amplitude of the spectrum provides a best fit scale factor of $2.37 \pm 0.21\%$. The live-time is 1174.59 days and the fiducial volume is $626.22\mathrm{m}^3$.

The fit parameter in Fig. 5.3 is the value for f, represented as a percentage change in the visible energy. Requiring both the amplitude and the scale factor to be simultaneously minimized results in a $2.37 \pm 0.21\%$ deviation in the expected visible energy. Since this beta spectrum is a composite of many beta and gamma particles the measured uncertainty provides a constraint on both the β and γ energy scale simulataniously. From this analysis a 2.3% systematic error on the number of prompt beta events is determined from the unceratinty in the energy scale.

Cut Efficiency Estimation

To obtain the ^{238}U concentration, the event selection criteria listed in Table 5.2 were used. The associated cut efficiencies are defined by

$$\epsilon_\eta = \frac{\int_{\eta_\mathrm{i}}^{\eta_\mathrm{f}} \mathrm{d}\eta\ \mathrm{f}(\eta)}{\int_0^\infty \mathrm{d}\eta\ \mathrm{f}(\eta)} \tag{5.3}$$

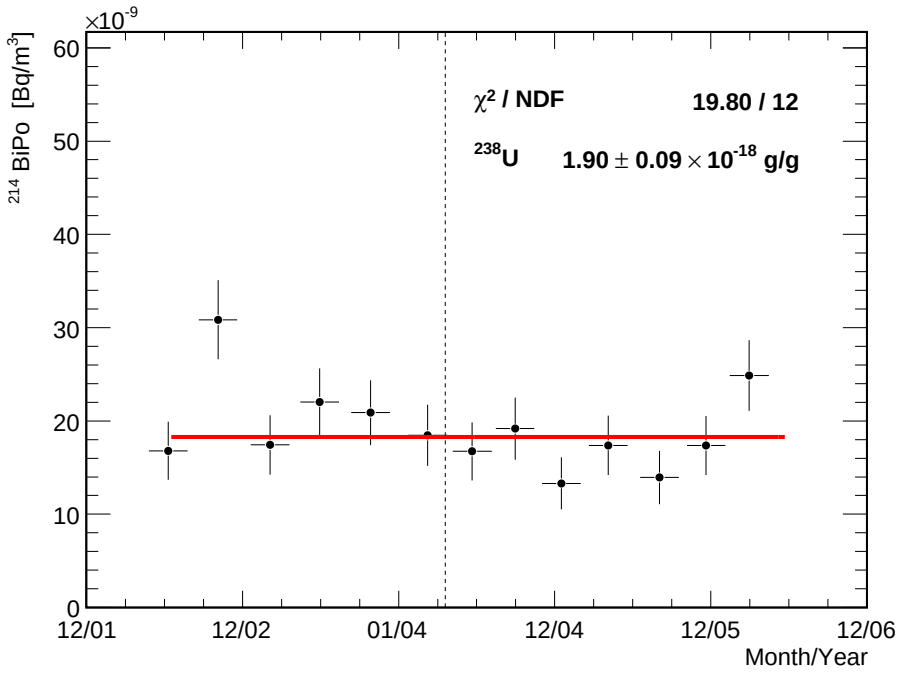

Figure 5.4: Fit to ^{214}BiPo coincidence events to extract ^{238}U concentration. The data is grouped into equal time bins of 90 days, with a total LT = 1174.59 days and a FV = 301.68m^3. The vertical dashed line indicates the time when the internal thermometers were removed. The clean transition between these two periods and the stable time variation indicates that the 1.5 m cylinder cut is sufficient to remove all z-axis related events.

where ϵ is the efficiency of each cut condition η. $f(\eta)$ is the expected probability distribution for each η. For instance, for $\eta = t$,

$$f(\eta) = e^{-\ln(2)t/\tau}. \tag{5.4}$$

The dR distribution is assumed to be Gaussian, which is true to first order for events far from the balloon edge where the exponential increase due to externals can be neglected.

The final cut is on the prompt and delayed event vertices. All events are required to lie within a fiducial radius of 4.4 m and outside a cylinder defined by $\rho > 1.5$ m, centered along the Z-axis of the detector. The cylinder cut removes residual activities left from Z-axis deployments and the thermometers which were deployed there for approximately half the reactor period.

To determine the uncertainty due to time variations, the ^{214}BiPo events are summed over a period of 90 days. All events which pass the selection cuts are summed and scaled such that the i$^{\text{th}}$

time bin has a normalized activity of

$$A(\langle t\rangle_i) = \frac{\int N(t_i)dt_i}{\epsilon_c \epsilon_\beta V T_i} \tag{5.5}$$

where the numerator is the total number of events for the i^{th} time bin. The limits on the bin times are based on the Unix start time of the event. Therefore, the total time integrated live-time T_i will be different for each bin due to vetoes [1]. The cut efficiency ϵ_c, branching ratio ϵ_β, and the fiducial volume, V, do not vary with time. The bins are therefore normalized to activity per unit volume as shown in Fig. 5.4. Fitting the time distribution provides a measure of the time-variation.

The mean activity per unit volume, $\langle A\rangle$, from the fit in Fig. 5.4 is converted into a concentration by multiplying by the LS density, $\rho = 777.54$ kg/m^3 and a conversion factor based on the molar mass and ^{238}U life-time:

$$8.1 \times 10^{-8} \frac{g^{238}U/gLS}{Bq/kg}. \tag{5.6}$$

In order to correctly estimate the ^{238}U concentration, the 2.3% systematic error due to the uncertainty in the energy scale and the 4.8% systematic due to time variations are added in quadrature as they are assumed to be uncorrelated errors.

Thus, the ^{238}U concentration in KamLAND LS during the reactor phase is $(1.87 \pm 0.10) \times 10^{-18}$ g/g. This results in a factor 5 improvement in the error from the previously published value of $(3.5 \pm 0.5) \times 10^{-18}$ g/g [85]. This improvement is almost strictly attributed to the the difference in LT which improved the statistics and allowed for tighter event selection cuts to establish a constant ^{214}BiPo rate over the 5 year analysis period. This measurement yields the smallest known concentration ever positively detected for ^{238}U, making KamLAND LS the most radio-pure substance known to mankind in terms of ^{238}U content!

5.1.2 ^{232}Th Concentration

The ^{232}Th concentration is determined most effectively by using a prompt-delayed selection from the fast coincidence of ^{212}Bi $\rightarrow^{212}$ Po decays. Fig. A.3 illustrates the ^{232}Th decay scheme which includes the ^{212}BiPo branch. The event selection criteria are very similar to what was explained in detail for ^{238}U. Table 5.2 provides the cut conditions and efficiency calculation for ^{212}BiPo.

The life-time of ^{212}Po is extremely short and serves as an excellent tool for removing backgrounds.

[1] There are bad run vetoes to remove periods with electronics problems. There is also a 2 ms veto after all muon events applied to the dataset to remove spallation products with time-correlations.

This quick time coincidence between events allows a larger fiducial volume region to be considered for analysis. The radial distribution of prompt events is shown in Fig. 5.5(a) and in the ρ^2 distribution is given in Fig. 5.5(b). The ρ^2 distribution provides an overlay of the balloon boundary, indicating the increase in event rate associated with the balloon. The events which satisfy all selection criteria from Table 5.2 are shown in blue.

A fiducial radius of 5.75 m was used to calculate the systematic error on the number of events associated with the energy scale. Unlike the ^{214}Bi spectrum, the ^{212}Bi spectrum is composed primarily of ground state electrons. The gamma ray transitions are shown in the decay diagram for ^{214}Bi in the appendix, Fig. C.4. Thus, the fit to the ^{212}Bi spectrum shown in Fig 5.6 predominantly samples the uncertainty in the beta energy scale. The low energy cut at 1 MeV is due strictly to the prompt energy threshold which was explained in Sec. 4.6. The upper cut at 2.5 MeV is taken to allow for events which go beyond the expected endpoint energy due to detector resolution. However, the beta spectrum has an endpoint of 2.3 MeV, in good agreement with the expected 2.254 MeV endpoint energy. Fitting the beta spectrum results in a 4.92% uncertainty on the number of prompt events due to the energy scale. The best fit value for the scale factor gives a $2.49 \pm 0.36\%$ uncertainty in the energy scale.

Fits to the Δt between prompt and delayed events, shown in Fig. 5.5(c), results in a half-life of 324 ± 13 ns which is in very good agreement with the expected half-life of 299 ns [89]. The cut at 350 ns is due to the restriction imposed by the KamLAND's DAQ system. The current software is unable to distinguish between two events in a single waveform, thus requiring the prompt and delayed event to be classified as separate events by the hardware. This imposes a lower Δt limit due to the width of the ATWD time-window and the fact that a second trigger cannot be issued within 8 clock-ticks (200 ns) from a previous global acquisition trigger. This is unfortunate as this time cut removes approximately 2/3 of the event signal. Fig. 5.5(d) shows the fit to the alpha spectrum for ^{212}Po. The selection criteria provide a clean Gaussian event distribution.

Calculation of the ^{232}Th concentration is performed in the same way as ^{238}U. The events are binned in 90 day intervals and the event rate for each bin is calculated using Eq. 5.5. The conversion factor for ^{232}Th is

$$2.46 \times 10^{-7} \frac{\mathrm{g}\ ^{232}\mathrm{Th/g\ LS}}{\mathrm{Bq\ /\ kg}}. \tag{5.7}$$

From the time evolution of the normalized event rate, shown in Fig 5.7, the time variation is found to be 3.28%. Adding the time and energy scale uncertainties in quadrature yield a total uncertainty

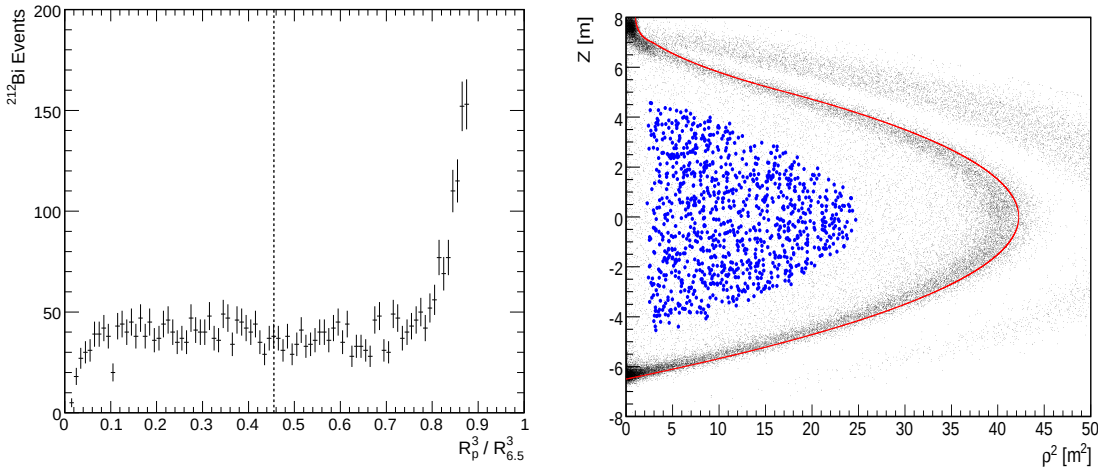

(a) (b)

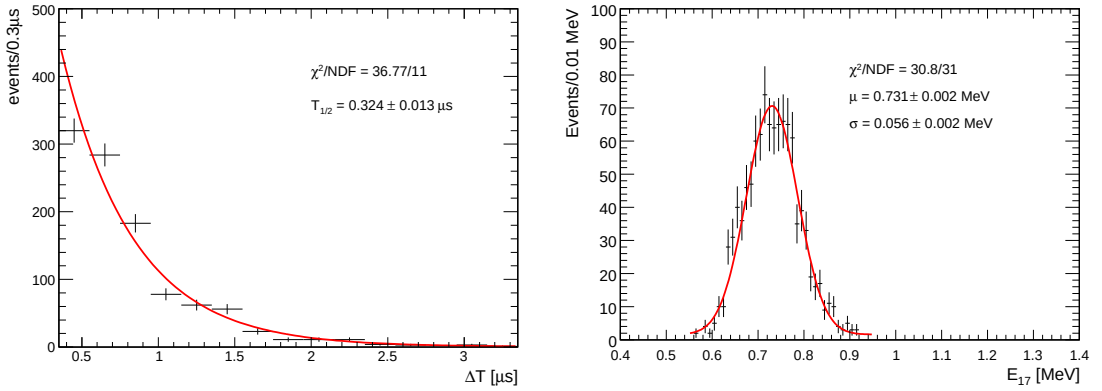

(c) (d)

Figure 5.5: Thorium concentration ^{212}BiPo event selection criteria. The fitted half-life in Fig. 5.5(c) is in good agreement with the expected $T_{1/2} = 0.299$ μs [89]. The ρ^2 distribution shows in Fig. 5.5(b) provides the expected geometric position of the balloon outlined in red. The increase in events when considering larger radii is clearly seen by the density of dots. The final events are overlaid in blue to show their random distribution in the FV considered. Fig 5.5(a) shows the final radial cut of 5.0 m designated by the vertical dashed line and the expected constant distribution of events. The fitted alpha spectrum is shown in Fig. 5.5(d).

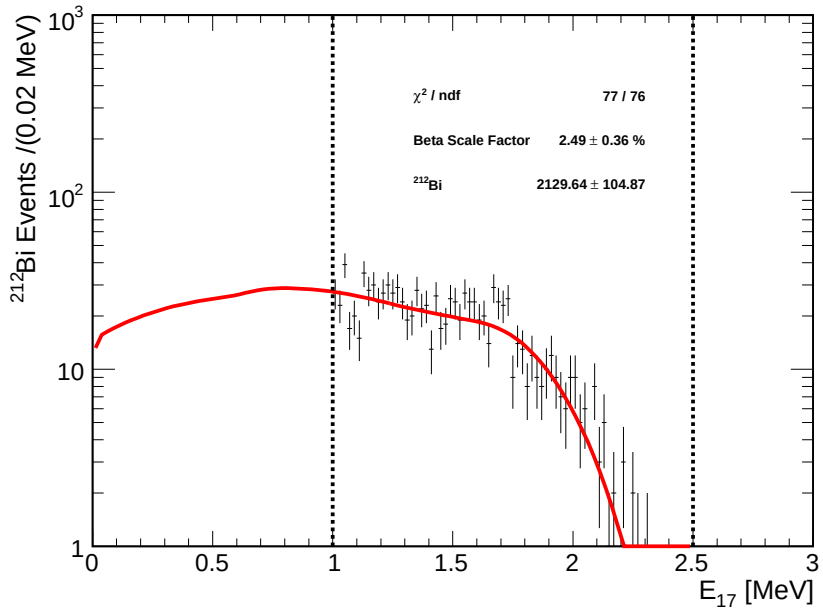

Figure 5.6: ^{212}Bi beta spectrum fit to generated p.d.f. folded with $7.6\%/\sqrt{\mathrm{E[MeV]}}$ energy resolution. The spectrum was obtained using a 5.75 m radial cut and the lower threshold was set to 1 MeV. Allowing for an uncertainty in the energy scale while simultaneously fitting the amplitude of the spectrum provides a best fit scale factor of $2.49 \pm 0.36\%$.

of 5.91% results in a ^{232}Th concentration of $(8.24 \pm 0.49) \times 10^{-17}$ g/g.

The time-evolution of Thorium events in Fig 5.7 shows a down-ward trend which cannot be removed by re-binning or considering different fiducial volumes. The prompt and delayed energy spectra provide evidence for a very clean measurement of ^{212}BiPo events as is further indicated by the fit to the Δt distribution. All the diagnostic figures substantiate the claim that this is inherently an effect seen only with ^{232}Th. A very similar procedure for ^{238}U does not provide evidence for a decay curve, indicating that this is most likely not due to an unaccounted systematic.

If the two isotopes of ^{232}Th and ^{228}Th are out of equilibrium in the LS then the observed time structure can be accounted for by the shorter half-life of ^{228}Th. A break in equilibrium concentrations, by means of ^{228}Ra or ^{228}Ac, could have occurred during the water purification of the KamLAND LS during initial filling. If the ^{232}Th concentration is lower then the ^{228}Th concentration the time-evolution should exhibit a 1.91 year half-life. Performing a free fit to a single exponential yields a half-life of 3.1 ± 0.4 years which is within 3σ of the expected half-life. To establish a better estimate of the underlying ^{232}Th concentration the half-life was fixed to 1.91 years and a constant term (i.e. the ^{232}Th concentration) was added to the fit. The result is shown in Fig. 5.8. The χ^2 is improved

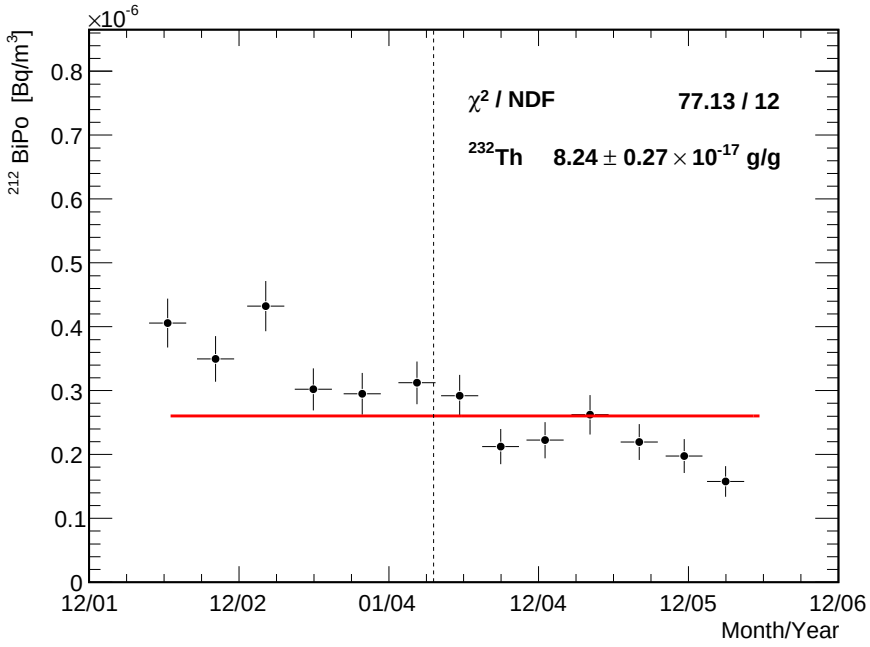

Figure 5.7: Fit to ^{212}BiPo coincidence events to extract ^{232}Th concentration. The data is grouped into equal time bins of 90 days, with a total LT = 1174.59 days and a FV = 459.98m^3. The vertical dashed line indicates the time when the internal thermometers were removed. This line is also associated with the change in the prompt trigger threshold.

dramatically with the inclusion of the exponential. Unfortunately the life-time is very long and this dramatically increases the uncertainty on the underlying ^{232}Th concentration.

The best fit value for the ^{232}Th concentration with the assumption of a ^{228}Th background is $(3.26 \pm 0.72) \times 10^{-17}$ g/g. The ratio between fitted initial ^{228}Th and ^{232}Th concentrations is a factor 3.8. This is consistent with what was observed for ^{212}Pb in laboratory experiments, performed in the context of this thesis, which used water extraction techniques similar to the initial KamLAND LS filling, as explained in Ch. 6.3.1.

5.1.3 ^{40}K Concentration

An absolute measurement of the ^{40}K concentration in KamLAND LS has not been previously reported. The value quoted in the literature [85] is a limit of $< 2.7 \times 10^{-16}$g/g. This section will provide a detailed energy spectrum analysis resulting in an absolute measurement for the ^{40}K concentration.

^{40}K has two decay modes which must be considered during spectroscopic analysis. The beta decay mode has a branching ratio of 89.28% and is a third unique-forbidden decay mode, see Table B.1.1,

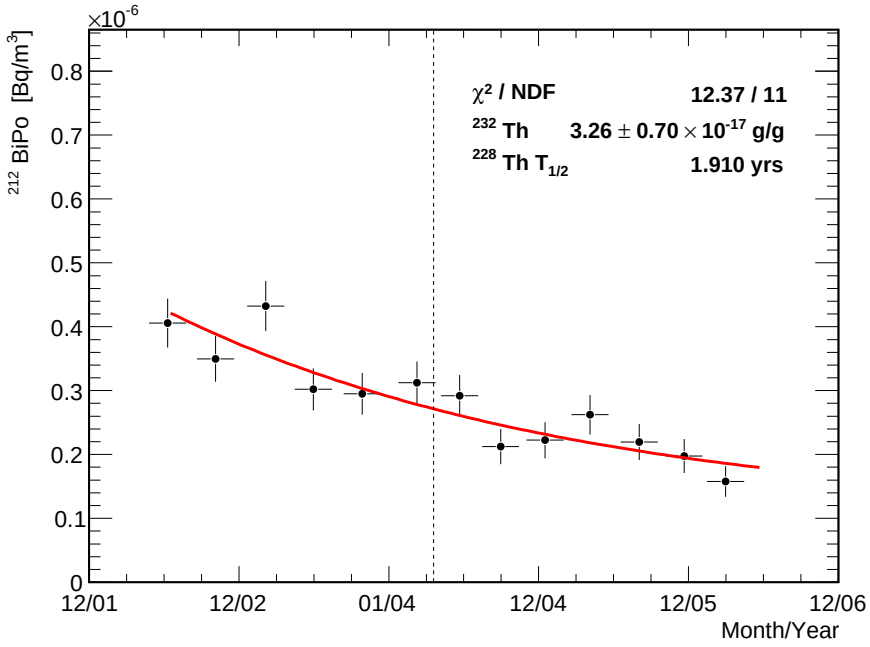

Figure 5.8: Fit to ^{212}BiPo coincidence events to extract ^{232}Th concentration using an exponential decay curve. The underlying distribution is fixed to the ^{228}Th half-life of 1.91 days. A constant term is added to the fit function and the ^{232}Th concentration is calculated from the best fit values for the constant background. All other conditions are equivalent to those in Fig. 5.7.

which immediately transitions to the ground state. This results in a continuous energy spectrum with an endpoint energy of 1.3 MeV. As a result, if the internal ^{40}K rate is too high, the low energy tail of the beta spectrum would be a background for a solar neutrino measurement. The second decay mode is electron capture (EC) which primarily proceeds to an excited state with a branching ratio of 10.72%. This results in the emission of a 1.461 MeV mono-energetic gamma ray.

The low energy spectrum, as depicted in Fig 5.1, is dominated by other radioactive decay products which swamp the spectral signal, making a measurement of ^{40}K impossible. As such, deriving a ^{40}K concentration relies on the EC process which produces a Gaussian gamma-ray spectrum at the tail of the ^{210}Bi beta spectrum.

Unfortunately ^{40}K exists in all materials to varying degrees and as such is present in the materials which makes up the balloon and Kevlar ropes. The beta particles which originate from these materials will not penetrate the balloon and the fraction emitted from the surface will only penetrate a few cm into the LS. However, the gamma ray will penetrate into the LS to a distance dependent on its mass attenuation length in the liquid. The mass attenuation for ^{40}K is measured and discussed in Sec 5.2.

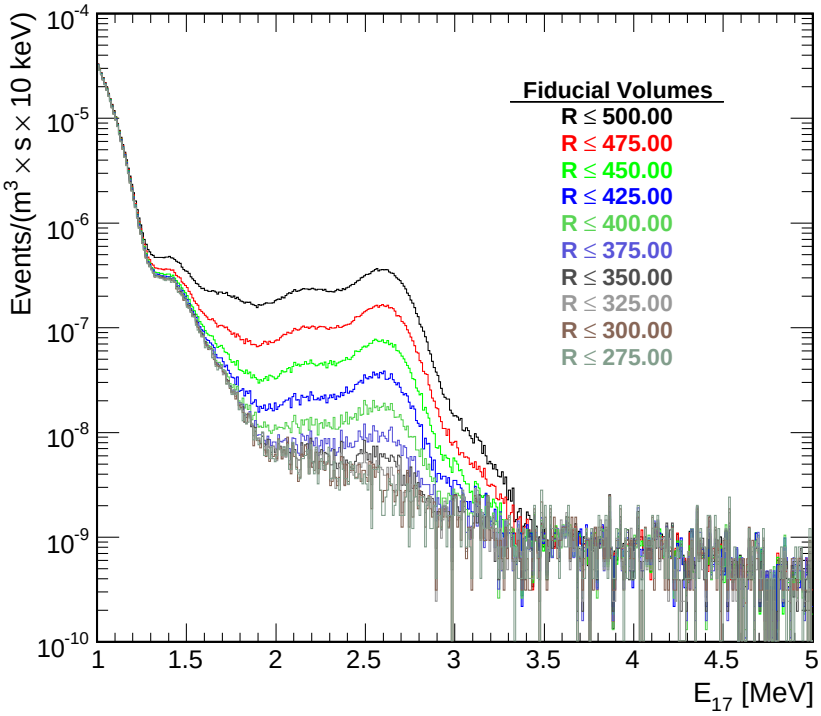

Figure 5.9: Singles spectrum for different fiducial radii and for E_{17} = 1.0 - 5.0 MeV. The decrease in the ^{208}Tl gamma ray peak intensity at 2.6 MeV is clearly visible. The Compton tail influences the spectrum outside of a radius of 3.5 m. The ^{40}K external gamma ray can be seen to effect the spectrum at 1.4 MeV. The effect of this external background diminishes at a radius of approximately 4.0 m.

Therefore, in order to avoid obtaining an inflated concentration due to external contributions of EC gammas this study was restricted to a small fiducial radius.

The data selection criteria used for calculating the ^{40}K concentration consists of all data above 0.8 MeV taken from April 19, 2004 to July 9, 2006. This time-frame was chosen as the start time is commensurate with the removal of the LS thermometers and the decrease in the prompt trigger Nsum threshold (Nsum 200 to 180). The upper time limit is the start of the off-axis calibrations. This is chosen as calibrations introduced more ^{222}Rn into the LS (see Fig 5.22), and therefore potentially more background to the fit performed here. All good runs were selected during this period and a 2 ms veto after all minimum ionizing muons was applied. A 2 s veto was applied after showering muon events.

To calculate the ^{40}K concentration the event energies were histogrammed depending on their vertex position from R $\in [2.5, 6.25]$ m in 0.25 m increments as shown in Fig 5.9. This provides a

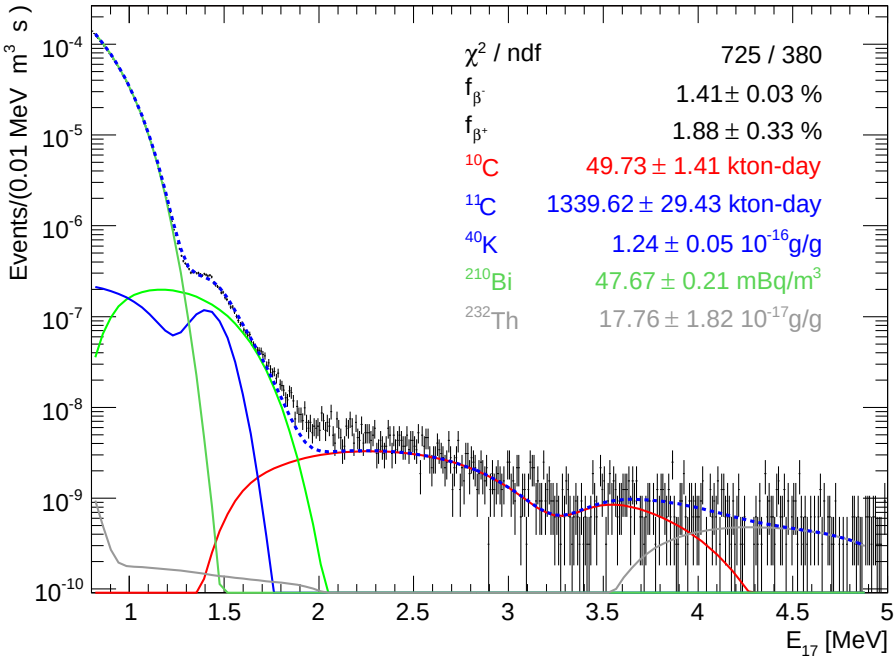

Figure 5.10: Spectral fit from 1.0 - 5.0 MeV to extract ^{40}K concentration. The fiducial radius is 3.0 m and the total integrated LT = 329.597 days. In this fit there are two energy scale factors to try and detect a difference between the electron and positron energy scales. Unfortunately there are not enough statistics to constrain the ^{10}C spectrum well enough and as a result the error on the positron energy scale is 17%.

means of determining the external stopped gamma ray contribution to the singles spectrum. A p.d.f. was constructed consisting of the sum of normalized electron and positron spectra such that

$$\mathrm{f}(\mathrm{E}, \alpha, \mathrm{f}_\beta) = \sum_{\mathrm{i}}^{\text{isotopes}} \alpha_\mathrm{i}\, \mathrm{f}_\mathrm{i}(\mathrm{E}(\mathrm{f}_\beta)) \tag{5.8}$$

where the free parameters are the amplitudes α_i and the shift in energy scale, f_β, parameterized in Eq. 5.2. The sum is over the isotope p.d.f.s for: ^{210}Bi, ^{40}K, ^{10}C, ^{11}C, ^{232}Th. The analytical form and construction of these p.d.f.s are described in Appendix B.

The p.d.f. was then minimized using the ROOT [90] analysis package which uses an object-oriented version of the CERN minimization algorithm MINUIT [91]. The Pearson's chi-square term [79, 92] is calculated for each bin, j, and summed

$$\chi^2(\alpha, \mathrm{f}_\beta) = \sum_{\mathrm{j}}^{\text{bins}} \frac{\left(\mathrm{f}(\mathrm{E}, \alpha_\mathrm{j}, \mathrm{f}_\beta) - \mathrm{y}_\mathrm{j}\right)^2}{\left(\Delta \mathrm{y}_\mathrm{j}\right)^2} \tag{5.9}$$

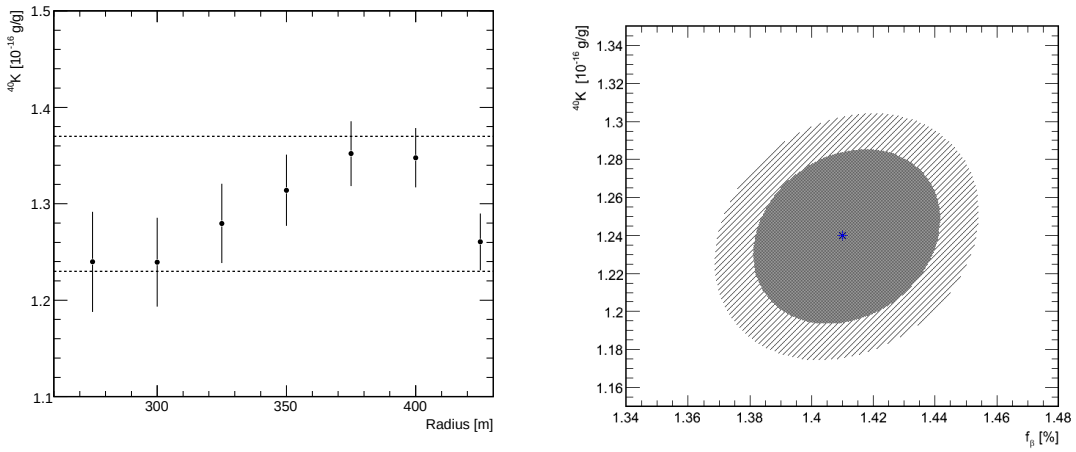

(a) (b)

Figure 5.11: The FV uncertainty is taken by plotting the fitted values out to 4.25 m and fitting with a first order polynomial to obtain a central value of 1.30×10^{-16}g/g. The systematic uncertainty is taken to be 5.4% as indicated with all points lying within the dashed lines in Fig. 5.11(a). ^{40}K contour plot with the beta scale factor. Fig 5.11(b) shows a weak correlation between the energy scale and the ^{40}K concentration. Overall the effect of the change in energy scale on the ^{40}K concentration is 4.5% at one sigma.

where y and Δy are the data and the associated error.

Constraint terms are added for the independently measured cosmogenic spallation isotopes rates of ^{10}C and ^{11}C described in Sec. 5.3. The constraint term for the i$^{\text{th}}$ parameter value is defined as

$$\chi^2_{\text{i}} = \frac{(\alpha_{\text{i}} - \mu_{\text{i}})^2}{\sigma^2_{\text{i}}}, \tag{5.10}$$

where μ is the measured value and σ is the error on the measured value. The minimized χ^2 term is the composite

$$\chi^2 = \chi^2(\alpha, \beta) + \sum_{\text{i}} \chi^2_{\text{i}}. \tag{5.11}$$

Fig. 5.10 shows the fit to the prompt energy spectrum from 1.0 - 5.0 MeV. The fiducial radius is restricted to 3.0 m to reduce external background contributions. The total integrated live-time (LT) is 329.597 days. To consider the effect of the choice in radial cut the fitted values are plotted as a function of fiducial radius as shown in Fig. 5.11(a). All the data lie within 5.4% of the central value. To estimate the systematic error with respect to the energy scale the 1 and 2σ countours are plotted in Fig. 5.11(b). There is a very small correlation between these two paramters and the systematic error is taken to be 4.5%. Summing the statistical error in quadrature with the FV and energy scale

systematic errors the measured ^{40}K concentration in KamLAND is $(1.30 \pm 0.11) \times 10^{-16}$g/g.

5.1.4 ^{14}C, ^{85}Kr, ^{210}Bi, ^{210}Pb, and ^{210}Po Concentrations

To obtain an energy spectrum for events below 1.0 MeV a special background trigger had to be used which collects data for a fraction of a second. This is necessary because of the high event rate in this energy region. The minimum energy associated with the Nsum 30 threshold is approximately 0.125 MeV. Background runs were taken once a week for approximately 10 - 15 min with a prescale fraction of 9.216%. This means in order to get 1 day of total LT we need to collect 260 days of data. Due to the small amount of LT there are essentially no events above 1.0 MeV in the background spectrum. We can estimate the contribution from Fig.5.10 to be approxiamtely 10 events/(0.01 MeV day) at 1.0 MeV. To maximize the number of events in the tail of the low energy spectrum the data was summed into 8 six month intergrals. The total LT was 0.6156 days for the background data collected over nearly 5 years from 08/12/2003 - 04/01.2007.

It is sufficient to use the ^{40}K analysis as the basis for choosing the maximum radial cut. The low energy gamma rays will have shorter mass attenuation lengths and will not penetrate beyond the ^{208}Tl which has the maximum reach. The only effect which will show up at low energy will be the Compton background from the higher energy gammas.

Mis-reconstructed Event Veto

As the event energy becomes lower it is more likely that the noise in the PMTs contribute significantly to the events energy. Events below 0.250 MeV correspond to an Nsum of approximately 30-40. The dark rate is determined from the 1pps trigger which collects waveforms once every second. This trigger is completely random with respect to the events in the detector and is therefore a measure of the dark rate. This trigger results in a mean Nsum of 10 PMTs. Thus, for low energy events the dark rate can contribute up to 30% of the signal. The dark rate has been steadily increasing over the life-time of KamLAND and therefore this could introduce a time-dependent effect into the spectrum.

To minimize the effect from mis-reconstructed events a parameterization of the event's reconstruction quality is utilized. During the minimization procedure for finding the t_0 and energy a determination of the minimization's goodness of fit is calculated [75]. These goodness of fit parameters are χ^2_T and χ^2_Q, for the time and charge respectively. The sum of these two parameters is taken

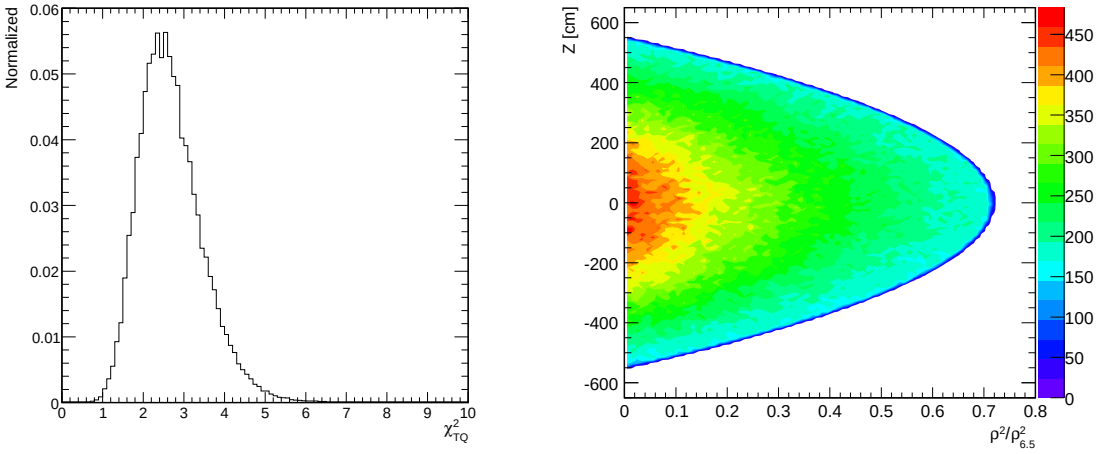

(a) (b)

Figure 5.12: Normalized χ^2_{TQ} distribution for Hg source events. The mean and standard deviation of χ^2_{TQ} is 2.5 and 0.8 respectively. The spatial distribution of all events with $\chi^2_{TQ} \geq 8.0$ taken from the first 2 years of low background data is shown in Fig. 5.12(b). The mis-reconstructed vertices for these events are reconstructed preferentially toward the center of the detector, indicating a biased PMT hit distribution.

as a measure of the event's reconstruction quality and for identifying poorly reconstructed events.

$$\chi^2_{\mathrm{TQ}} = \chi^2_{\mathrm{T}} + \chi^2_{\mathrm{Q}} \tag{5.12}$$

To determine the optimal χ^2_{TQ} cut condition and quantify the fraction of mis-reconstructed events, ^{203}Hg and ^{137}Cs source calibration data were used. All the calibration data within a radius of 2.5 m of the source positions Z = 6.0, 0.0, −6.0 were used to estimate the optimal χ^2_{TQ}. Considering different Z-positions takes into account geometrical effects (balloon shadowing, loss of PMT coverage, etc) which can artificially decrease the reconstruction quality. The mean of the χ^2_{TQ} distribution for ^{203}Hg events within 50 cm of the expected source position is found to be $\chi^2_{\mathrm{TQ}} = 2.5$ with $\sigma = 0.8$, as shown in Fig. 5.12(a). Analysis of the ^{203}Hg and ^{137}Cs data showed no source events survived the cut $\chi^2_{\mathrm{TQ}} \geq 8.0$. The 50 cm cut was then removed and all source events with $\chi^2_{\mathrm{TQ}} \geq 8.0$ were analyzed as a function of the distance from the expected source position, their energy and Nsum values. Analysis of the Nsum spectrum showed an exponential Nsum distribution starting at the trigger threshold and ending at approximately Nsum 50. The spatial distribution is shown in Fig. 5.12(b). Bad events are preferentially reconstructed toward the center of the detector. Fig. 5.13 shows the reconstructed energy distribution. The vetoed events make up roughly 10% of the events below 0.3 MeV in a

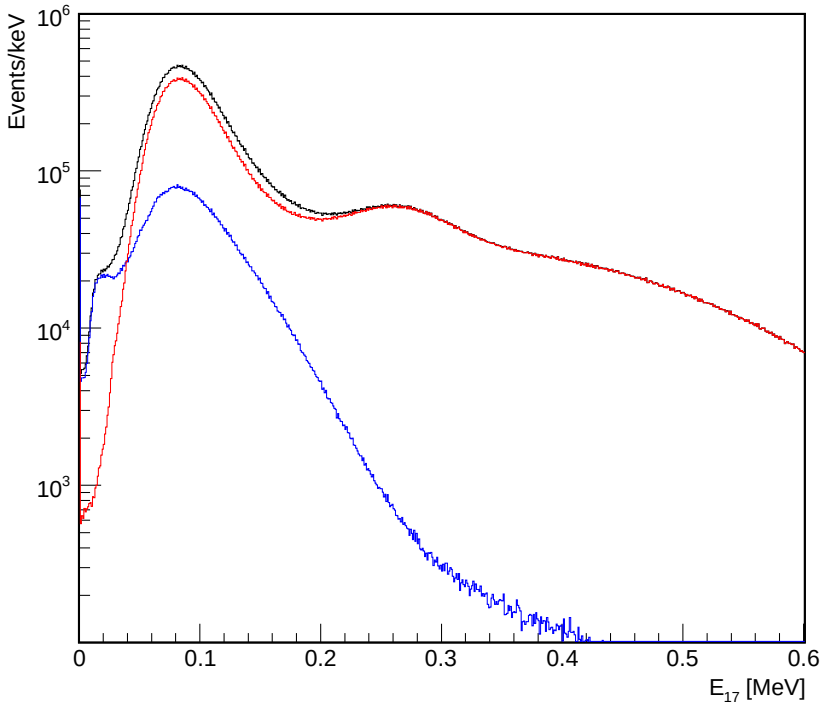

Figure 5.13: Effect of removing low energy miss-reconstructed events with the cut $\chi^2_{TQ} \geq 8.0$ from physics data. The full spectrum with no cuts is shown for data inside a 5.0 m fiducial volume. Overlaid in blue is the energy spectrum of events with $\chi^2_{TQ} \geq 8.0$ which shows a distribution which ends around 0.5 MeV and has no real spectral shape. The red spectrum are the events which survive the veto. The vetoed events account for roughly 9% of the events below 300 keV.

normal physics run.

Fitting the Low Energy Spectral Distribution

To accumulate enough statistics the background data were integrated over six month time-frames. The FV cuts applied to the low energy data-set are R $\leq$ R_{cut} m and $\rho > 1.0$ m. Different values of R_{cut} were taken from 3.5 out to 5.5 m to look for spatial correlations. All data have the mis-reconstructed event veto $\chi^2_{TQ} \geq 8.0$ applied. Furthermore, all events are vetoed within 2.0 ms a muon. The histogrammed data is normalized to the total LT and FV. The data is then fit to a p.d.f. constructed according to the described in Appendix B. The beta functions of ^{14}C, ^{85}Kr and ^{210}Bi are smeared with $7.6\%/\sqrt{(\text{E[MeV]})}$ energy resolution. Fig. 5.14 shows a typical fit to the low energy distribution.

An energy dependent correction is applied to the ^{14}C and ^{85}Kr beta spectra according to Eq. 5.1.

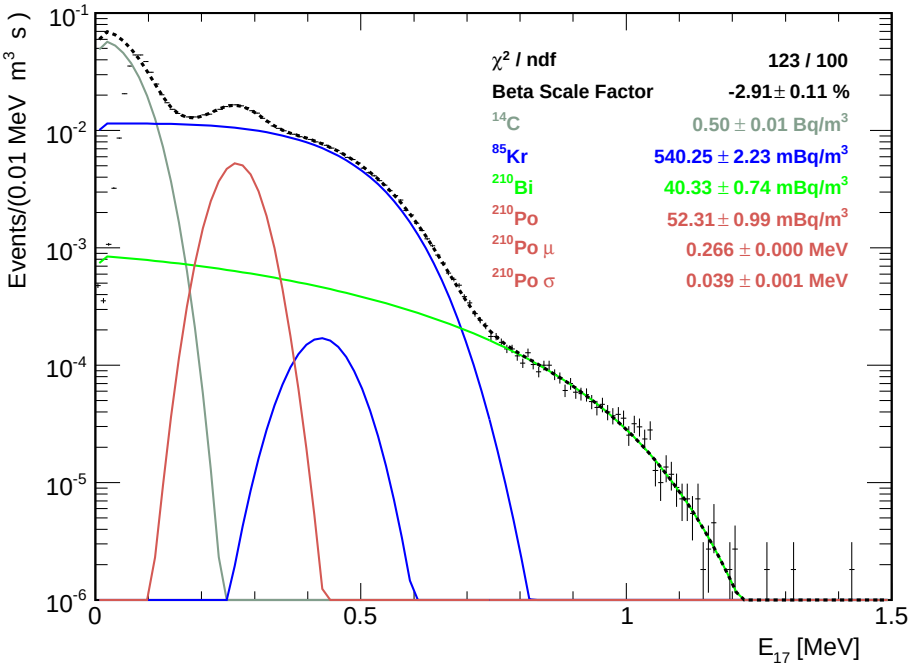

Figure 5.14: Low energy fit to six month of data with FV cut of R $\leq$ 4.0 m and $\rho > 1.0$ m. The functional form of the fit is extended beyond the fit region of $E_{17} \in [0.2, 1.2]$ MeV to show the expected distribution over the entire energy region.

The ^{210}Bi energy scale was fixed according to the measured value in Sec 5.1.3. The reason is two-fold:

1. ^{210}Bi beta spectrum is statistically a sub-dominant spectrum with respect to ^{85}Kr which pulls the energy correction to its best-fit value.

2. Appendix C.1 shows the energy scale for beta functions. The β energy scale only corrects down to 0.5 MeV. All data below 0.5 MeV are given a single correction equal to the value at 0.5 MeV. Thus, the energy correction for ^{85}Kr and that for ^{210}Bi are sampling two different aspects of the $E_{vis} \rightarrow E_{real}$ conversion.

The ^{210}Bi energy scale was also left to float freely, however there is not enough statistics to pin-down the energy scale. If the energy scale is left to be equal to that associated with ^{85}Kr the spectral fit was poor above 0.8 MeV and the resultant ^{210}Bi activity resulted in a time-correlation associated with the decay of ^{85}Kr.

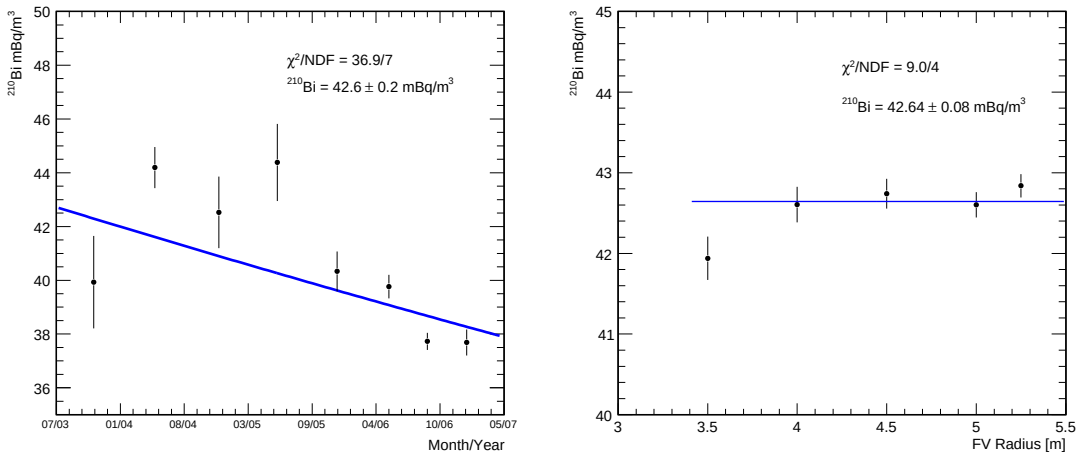

(a) (b)

Figure 5.15: Low energy fit values for ^{210}Bi specific activity in KamLAND LS as a function of time for all data within R $<$ 4.0 m is shown in Fig. 5.15(a). The different FV were then fit and plotted as a function of FV radius. From Fig. 5.15(b) the ^{210}Bi is determined to be 45.2 ± 0.8 mBq/m^3.

^{210}Bi and ^{210}Pb Concentration

To obtain the most robust measurement, two independent methods and data-sets are used to calculate the ^{210}Bi concentration. The first calculation was performed in Sec 5.1.3 where the ^{210}Bi calculation is a pre-requisite for a determination of the underlying ^{40}K concentration. In the spectrum shown in Fig. 5.10, ^{210}Bi is the dominating spectral feature. Performing an analysis in the same way as that described for ^{40}K, the measured ^{210}Bi activity is 47.4 ± 0.6 mBq/m^3. The error quoted here accounts for a 1% systematic from the FV error and a 0.5% systematic error from the uncertanty in the energy scale.

An alternate calculation is performed using independent events taken from special low threshold runs. The resultant fits rely on different systematic errors then those associated with the prompt trigger spectral fits. To fit the low energy background runs the ^{210}Bi energy scale is fixed to f_β = 1.41%. Six month intervals were fit independently and the resultant fit values were plotted as a function of time. This time-evolution data was then fit to an exponential distribution with a fixed half-life of 22.3 years, corresponding to ^{210}Pb. Due to the long half-life the resultant fit function is actually a line corresponding to the first order Taylor series expansion of the exponential.

The time-evolution of all data within a 4.0 m fiducial radius is shown in Fig. 5.15(a). This fit was performed for different fiducial volumes and then the time evolution fit parameters were plotted as

a function of the fiducial radius as shown in Fig. 5.15(b). The activity taken from the exponential decay curve is the activity on Aug. 11, 2003, corresponding to the date of the first background run. This figure takes into account the time evolution and the fiducial volume uncertainty. A fit to this data yields and activity of $42.64 \pm 0.6\,\mathrm{mBq/m^3}$. The error is taken to include all the data point in Fig. 5.15(b) which represents the total uncertainty in the fit.

An absolute measure of the ^{210}Bi specific activity in KamLAND LS is calculated from the mean of these two independent calculations. The errors are uncorrelated and thus summed in quadrature. The measured ^{210}Bi activity is $45.2 \pm 0.8\,\mathrm{mBq/m^3}$.

As assumed through the time-evolution fit, ^{210}Bi is a measure of the underlying ^{210}Pb concentration. To calculate the resultant ^{210}Pb concentration the activity is multiplied by the conversion factor:

$$4.548 \times 10^{-19} \frac{\mathrm{g}\ ^{210}\mathrm{Pb/g\ LS}}{\mathrm{Bq}\ ^{210}\mathrm{Pb/m^3\ LS}}. \tag{5.13}$$

Thus, the ^{210}Pb concentration measured to be $2.06 \pm 0.04 \times 10^{-20}$ g/g. This is beyond the range of any laboratory analytics even before LS purification.

^{85}Kr Concentration

As Fig. 5.14 indicates, the largest background contribution in the sub MeV region comes from ^{85}Kr. The dominant beta particle emitted in this decay is from the ground state decay. Special consideration is given to an excited state nuclear transition which has a branching ratio of 0.43%. Due to the long half-life (1.015 μs) of this excited state, the β and γ particles are observed as indpendent events, 0.0171% of the time [2]. Thus, the two events are completely independent of one another and the spectral shape contribution from the composite transition mode is neglected. This also implies that f_β predominantly measures the ^{85}Kr uncertainty in the energy scale for the β-energy scale between 0.4 and 0.7 MeV.

Another key feature of ^{85}Kr is the 10.756 year half-life which is evident in the fitted activity's time-evolution seen in Fig. 5.16(a). A free fit to an exponential reproduces the expected half-life to within one sigma. Due to the obvious time-dependence, the activity is quoted with respect to March 1, 2002. This date is chosen as it is to within a few months of the filling of KamLAND and will be compared to an analytical calculation based on solubility arguments in Sec. 5.1.6.

The fitted activities from the time evolution curves are plotted as a function of fiducial radius in Fig. 5.16(b). Fitting this distribution yields a mean activity of $687.9 \pm 1.3\,\mathrm{mBq/m^3}$. The systematic

[2] This is caused by finite ATWD time-window of 250 ns.

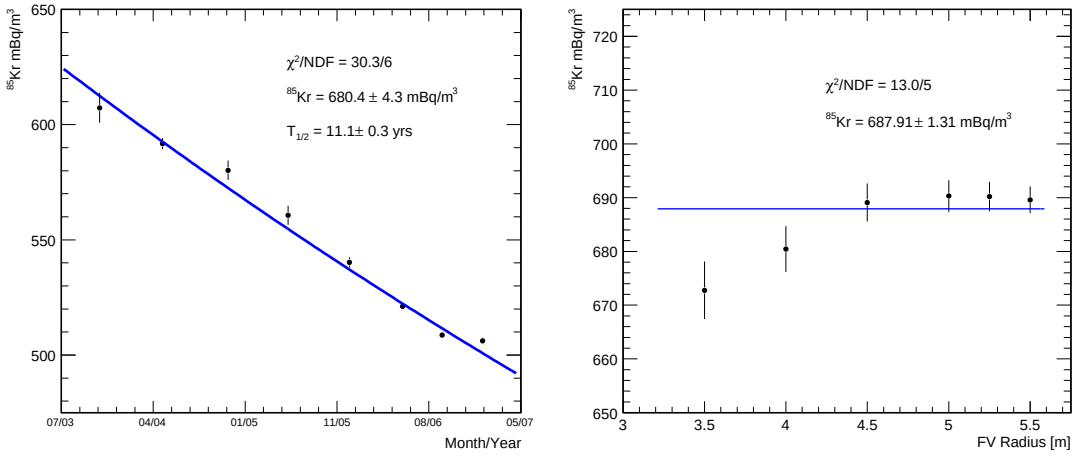

(a) (b)

Figure 5.16: Fit to the time evolution of ^{85}Kr activity for a fiducial radius of 4.0 m is shown in Fig. 5.16(a). The fit agrees with the expected half-life of 10.756 ± 0.018 y within one sigma. The specific activity quoted on this figure is with respect to a start time of March 1, 2002. Fig. 5.16(b) shows the specific activity as a function of fiducial radius.

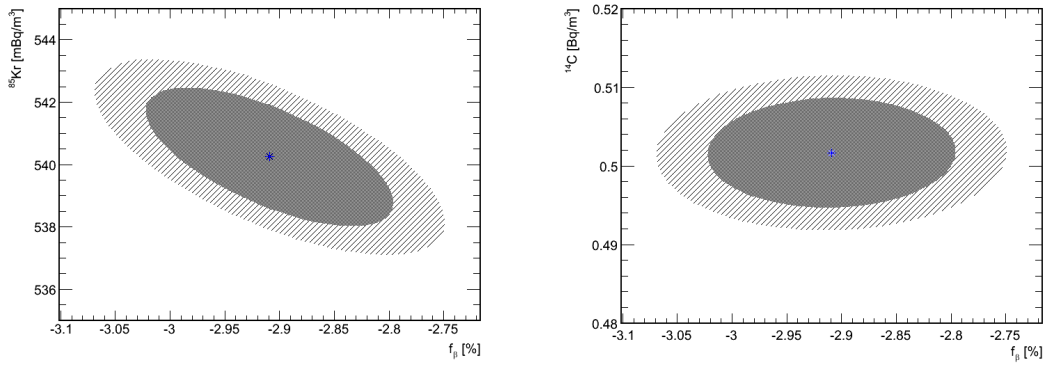

(a) (b)

Figure 5.17: One and two sigma contours showing the correlation of f_β with the fitted activities for ^{85}Kr (Fig. 5.17(a)) and ^{14}C (Fig. 5.17(b)). The contours clearly show that the ^{85}Kr spectrum determines the energy scale factor.

error over the fiducial radius is 2.24% and the uncertanty due to the energy scale factor is 0.4%. Adding all the errors in quadrature yields an activity in KamLAND as of March 1, 2002 of $687.9 \pm 15.7\,\mathrm{mBq/m^3}$.

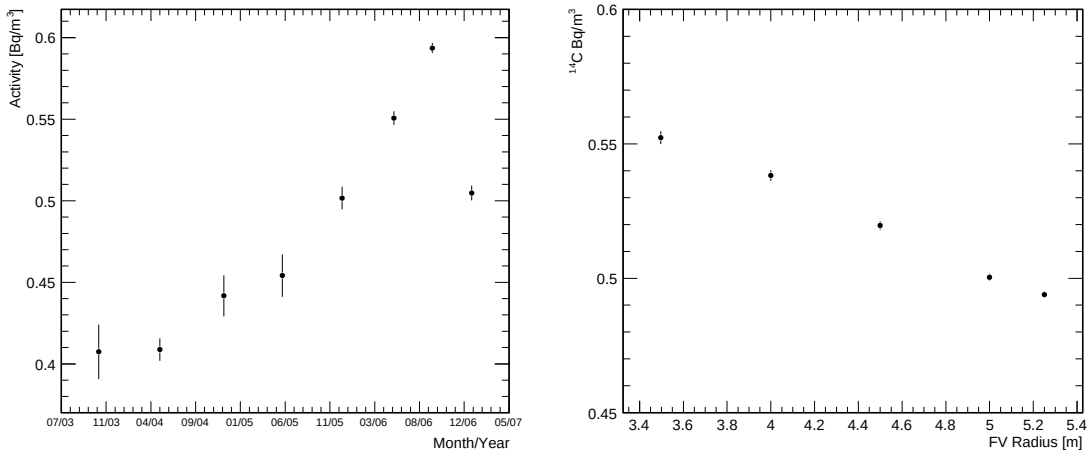

(a) (b)

Figure 5.18: Time-evolution (Fig. 5.18(a)) and fiducial radius (Fig. 5.18(b)) dependence of the measured specific activity of ^{14}C. There is a clear time and fiducial radius dependence observed in these figures.

Converting the activity into a concentration requires the scale factor

$$8.887 \times 10^{-20} \frac{\text{g } ^{85}\text{Kr/g LS}}{\text{Bq } ^{85}\text{Kr/m}^3 \text{ LS}}. \tag{5.14}$$

Thus, the ^{85}Kr concentration is $6.10 \pm 0.14 \times 10^{-20}$ g/g.

^{14}C Concentration

The ^{14}C beta spectrum has an endpoint energy of $E_{real} = 0.156$ MeV and restricts a lower trigger threshold. The current trigger threshold captures only the tail of the ^{14}C beta spectrum. With the LS being composed primarily of carbon atoms this background is difficult to reduce as all organic compounds contain some amount of ^{14}C. However, the spectrum turns out to be independent of the energy scale as shown in Fig. 5.17(b). This is a result of the exponential structure of the energy spectrum which makes shifts in the energy scale easily accounted for in the spectral shape.

While the ^{14}C is not a background for the energy region of interest to measure the ^{7}Be ν_e it does need to be accounted for in the low energy fits. The half-life of ^{14}C is 5730 y thus, we do not expect to see any decay with respect to time. Fig. 5.18(a) shows the time-evolution of ^{14}C for a 4.0 m fiducial radius. There is a clear upward trend in the spectrum. This same trend is evident in all radial volumes considered. Furthermore, Fig. 5.18(b) shows the fitted activity with respect to the volume

which has a downward trend. This is reminiscent of the radial dependence seen in Fig. 5.12(b) for the mis-reconstructed events. Due to the structure of these two figures the expectation is that the temperature increase in the LS caused higher backgrounds. These backgrounds tend to push more of the ^{14}C spectrum above threshold which can increase the observable number of events. The radial dependence implies that the mis-reconstructed events are not completely removed by the χ^2_{TQ} cut.

While there are plausible explanations for the trends this does make estimating the concentration of ^{14}C difficult. A 20% systematic error is taken with respect to time to cover the spread in values seen in Fig. 5.18(a). The systematic error due to the fiducial radius is 7.8%. This is very close to the 9% reduction observed below 0.3 MeV from the misreconstructed event cut. As it is difficult to distinguish if any of the removed events are truly ^{14}C, a 9% systematic error is given to the activity due to the mis-reconstruction veto uncertainty. Taking the mean value from the the radial dependence, fit the ^{14}C activity is measured to be 0.51 ± 0.12 Bq/m^3.

Converting this activity into a concentration requires the scale factor

$$7.795 \times 10^{-18} \frac{\text{g } ^{14}\text{C/g LS}}{\text{Bq } ^{14}\text{C/m}^3 \text{ LS}}. \tag{5.15}$$

Thus, the ^{14}C concentration in KamLAND is $3.98 \pm 0.94 \times 10^{-18}$ g/g.

5.1.5 Measurement of ^{14}C/^{12}C Ratio in KamLAND

The CTF experiment in Italy, published a spectroscopically measured value for the ^{14}C/^{12}C ratio of $1.94 \pm 0.09 \times 10^{-18}$ [93]. While chemically very similar to KamLAND, CTF was only 4.8 m^3 and is composed of PC and PPO. The number of ^{12}C target atoms in KamLAND is a well established quantity due to its importance for the reactor antineutrino measurement and is 4.30×10^{31} ^{12}C atoms per k-ton of KamLAND LS [80]. Using the measured value above for the ^{14}C concentration this results in a measurement of the ^{14}C/^{12}C ratio in KamLAND LS of $3.98 \pm 0.94 \times 10^{-18}$.

If the PPO alone was responsible for the measured ^{14}C background, due to the small amount dissolved in the LS, the ^{14}C/^{12}C ratio would be on the order of 10^{-15} which is reachable with conventional measuring devices. As PPO is a replaceable detector component, analytical studies were performed to understand if the ^{14}C rate from the fluor was the common factor between KamLAND and CTF.

Four samples were measured using accelerator mass spectroscopy (AMS) [3] which has a sensitivity on the ratio of $^{14}C/^{12}C$ of approximately 10^{-16}g/g. There were two separate measurements performed. The first measurement was a sample of Dojindo PPO and a standard to measure the background of the AMS. The second round of measurements were made with a different Dojindo PPO sample, a sample of the previous used Dojindo PPO, a sample of Packard PPO (making up the bulk of the dissolved fluor in KamLAND) and a standard.

After background subtraction the $^{14}C/^{12}C$ ratio for Packard PPO was found to be $3.4 \pm 1.0 \times 10^{-16}$. The sample of Dojindo PPO measured during both runs resulted in the ratios $2.5 \pm 1.0 \times 10^{-16}$ and $3.0 \pm 0.8 \times 10^{-16}$. The other Dojindo sample resulted in a ratio of $1.1 \pm 1.0 \times 10^{-16}$. As a result it was concluded that the fluor was not responsible for the ^{14}C activity measured in the KamLAND and CTF experiments [94].

^{210}Po Concentration

The final radioactive isotope analyzed through low energy spectral fits is ^{210}Po. This should be relatively simple to deduce since it is the parent isotope of ^{210}Bi and as such it is also fed by the ^{210}Pb decays. Therefore the measurement of ^{210}Bi should also be a measure of ^{210}Po. It can be seen from Fig. 5.14 that the fitted values are very close to one another. ^{210}Po is important in a different aspect as it is the lowest energy alpha decay observable to constrain the energy scale model for alpha particles.

There is a problem with making a precision measurement of the ^{210}Po activity depicted in Fig. 5.19. This figure shows that the underlying ^{85}Kr distribution effects the fitted value for ^{210}Po. The ^{210}Po is highly correlated with the specific activity of the ^{85}Kr. Several fits were performed to determine a way to measure the underlying contribution from ^{210}Po. The final measurement taking into account the systematic errors gives a mean value of 50.2 ± 9.9 mBq/m^3.

^{210}Po provides a measure of the alpha energy scale. Figs. 5.20(a) and 5.20(c) show the stability of the fitted mean and sigma of the Gaussian ^{210}Po peak. These parameters are very stable over the 5 year period. The change in the fitted mean and sigma as a function of radius is depicted in Figs. 5.20(b) and 5.20(d). There is a clear trend which is also seen in source data. The results from these fits are used in the energy scale shown in Fig. C.3.

[3] The accelerator mass spectroscopy was performed at the Micro Analysis Laboratory Tandem Accelerator at the University of Tokyo.

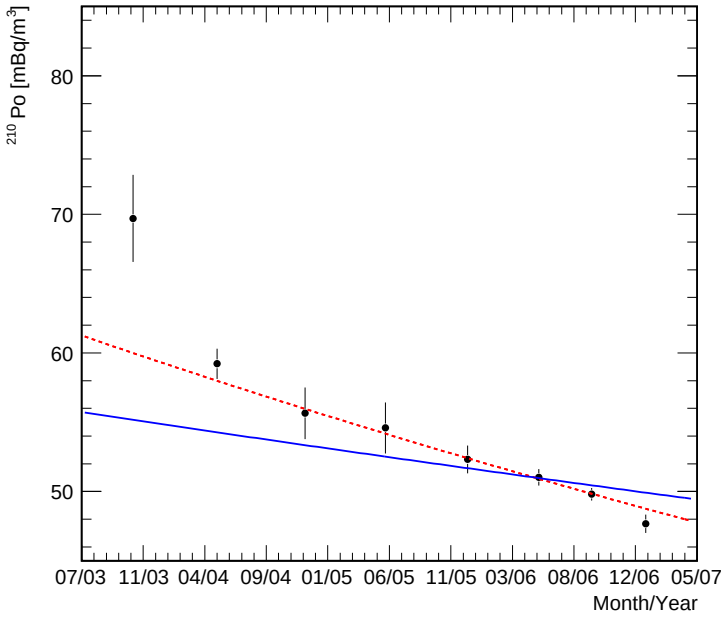

Figure 5.19: Time-evolution of the fitted ^{210}Po activity. The blue curve is the fit to the expected ^{210}Pb life-time while the red dashed line is a fit to the ^{85}Kr life-time.

5.1.6 Solubility Estimate of ^{39}Ar and ^{85}Kr Concentration

A direct measure of ^{85}Kr was obtained by spectroscopic analysis in the previous section. It is our working hypothesis that radioactive noble gases were introduced to the LS by contact with air during filling. Thus it is beneficial to calculate the maximum concentration expected in KamLAND assuming saturation of the noble gases in the LS. This calculation will further allow a limit to be placed on the ^{39}Ar activity which cannot be spectroscopically measured but should contribute to the solar neutrino energy region.

It is instructive to calculate the maximum concentrations of ^{39}Ar and ^{85}Kr expected in KamLAND assuming saturation of the noble gases in the LS. This can be done by first expressing the number of atoms (N) in terms of an activity (A)

$$\mathrm{A} = \frac{\mathrm{N}\ \mathrm{C_G}\ \mathrm{R_G}\ \ln(2)}{\mathrm{T_{1/2}}} \tag{5.16}$$

and then substituting this into the ideal gas law at STP to obtain the relationship between the

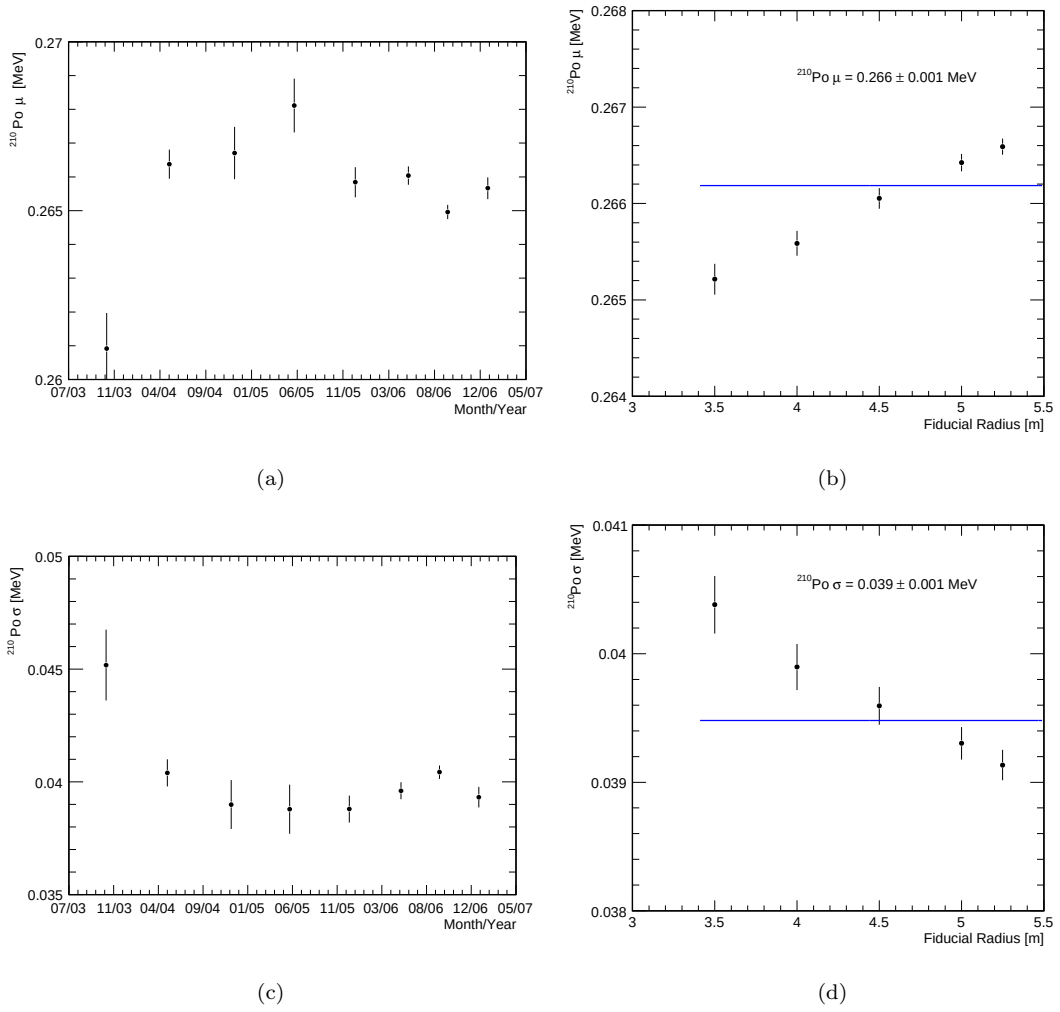

Figure 5.20: Time evolution and fiducial radius dependence of the fitted ^{210}Po Gaussian mean (Fig. 5.20(a) and 5.20(b)) and sigma (Fig. 5.20(c) and 5.20(d)).

concentration of the noble gas in air and the saturation activity in the LS:

$$A = \frac{\ln(2)\ P\ V_G\ C_G\ R_G\ N_A}{R\ T\ T_{1/2}} \tag{5.17}$$

Here N_A denotes Avogadro's number, $V_G = V_{Liq}\ S_G$ is the volume equivalent of the isotopic noble gas of interest and V_{Liq} is the volume of liquid, S_G is the solubility of the gas in liquid, C_G is the concentration of the gas found in air and R_G is the natural abundance of the isotope of interest with the half-life $T_{1/2}$.

Using the data in Table 5.3 to substitute into Eq. 5.17 the maximum specific activity in Dodecane

Gas	R_G	C_G	$S_{Dodecane}$	$\mathbf{T}_{1/2}$
^{39}Ar	$9.332 \pm 0.006 \times 10^{-3}$ [95]	$8.1 \pm 0.3 \times 10^{-16}$ [96]	0.2794 [97]	269 yrs
^{85}Kr	$1.099 \pm 0.009 \times 10^{-6}$ [98]	2.8×10^{-11} [96]	0.8137 [97]	10.76 yrs

Table 5.3: Characteristics of Krypton and Argon used to determine the maximum concentration of the radioactive isotope in LS. S_G is the solubility of the gas in liquid, C_G is the concentration of the gas found in air and R_G is the natural abundance of the isotope of interest with the half-life $T_{1/2}$. The ^{85}Kr/Kr ratio was scaled to measurements in Japan [98].

is calculated to be 1.3 Bq/m^3 for ^{85}Kr and 4.2 mBq/m^3 of ^{39}Ar. Fits to KamLAND data show the initial concentration of ^{85}Kr were 688 ± 16 Bq/m^3. The measured activity implies either that the LS was not fully saturated with ^{85}Kr during filling or a lower saturation value for the ^{85}Kr in LS. A lower saturation value could be accounted for by possible differences in solubility between Dodecane and PC.

5.2 External Gamma Ray Backgrounds

One method for understanding the influence of external backgrounds is to analyze successively smaller fiducial volumes. If the background is coming from an external source, such as the balloon or PMTs, then the number of events per unit volume will decrease, due to absorption, as smaller radii are considered. The effect of different fiducial volume cuts is shown in Fig. 5.9 where all events within $R \leq R_{cut}$ are shown in different colors. The decrease in the ^{208}Tl gamma ray peak at 2.6 MeV is clearly visible at large volume and begins to disappear as smaller radii are considered.

In order to establish that the effect seen in these figures is due to external gamma rays and not a vertex reconstruction efficiency the data can be used to calculate the mass attenuation coefficient. Measurement of an attenuation length requires normalizing the data with respect to the spherical surface area. Fig. 5.21(a) shows the fitted ^{40}K activity normalized to the surface area of the spherical volume plotted as a function of the total distance from the balloon ($R_{6.5} - R_{FV}$). The ^{208}Tl gamma ray data is given in Fig. 5.21(a). The data is fit to the following function form:

$$f(R, \lambda, A_0, A_1) = A_0 e^{\frac{-R}{\lambda}} + \frac{A_1}{R} \tag{5.18}$$

where the first term represents the reduction in flux due to attenuation and the second term is the reduced flux through the spherical surface due to the volume which goes like 1/R. The fitted values

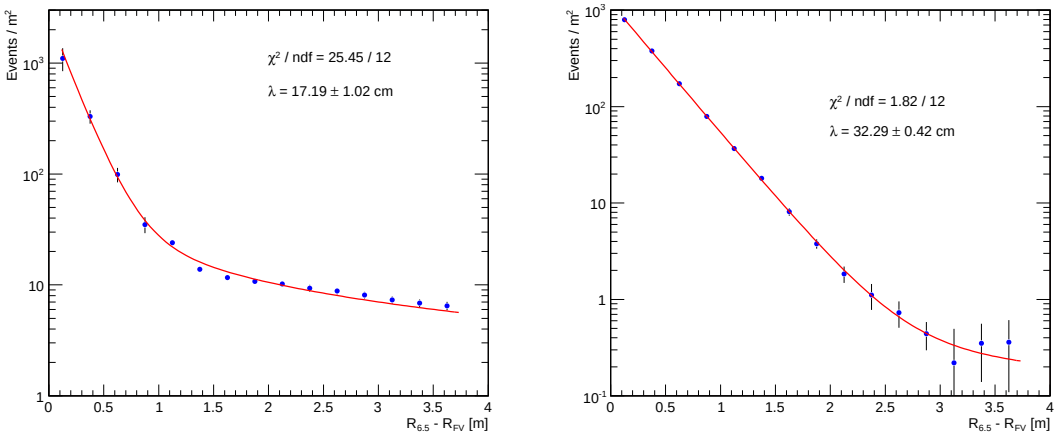

(a) (b)

Figure 5.21: Mass attenuation length measurement of ^{208}Tl and ^{40}K external gamma rays in KamLAND.

for the attenuation length of ^{40}K is 17.19 ± 1.02 cm and for ^{208}Tl 32.29 ± 0.42. The figures already depict that the higher energy gamma penetrates to smaller radii then does the lower energy gamma ray.

Mass attenuation coefficients μ were calculated using the NIST Photon Cross Section Database [99] for a 2.614 MeV and 1.461 MeV γ-ray in KamLAND LS. The resultant mass attenuation lengths are 21.47 ± 0.64 and $\lambda = 29.43 \pm 0.88$ cm for ^{40}K and ^{208}Tl respectively. The uncertainties on the total attenuation with Coherent Scattering from the NIST database is estimated to be between 2-3% for gamma rays above 200 keV in liquid. The fit value λ from Eq. 5.18 is related to the mass attenuation coefficient μ from the NIST table through the equation $\lambda = \frac{1}{\mu\rho}$ where ρ is the density of the liquid scintillator. The measured values agree to within their quoted errors with the theoretical calculations from the NIST database.

5.3 Cosmogenic Backgrounds

Cosmic ray muon induced production of ^{12}C was first investigated using the Super Proton Synchrotron (SPS) muon beam at CERN [100]. Scintillator based experiments use the production rates measured from this experiment and scale them to the mean muon energy at the experimental site to estimate the spallation induced backgrounds. Since this publication, KamLAND has accumulated

more then 5 years of data and recently published a detailed analysis of the muon produced radioactivity in the detector [80]. The spallation isotopes which are relevant to a low energy solar neutrino measurement are ^{7}Be, ^{10}C, ^{11}C,

Of the three spallation products, only ^{7}Be cannot be tagged using a delayed coincidence. The life-time is 53.12 days and is too long to look for coincidences with muons in KamLAND at a muon rate of 0.3 Hz. ^{7}Be is an electron capture process and therefore only the excited state mode is a background. The branching ratio is 10.52% and results in a mono-energetic 0.478 MeV gamma-ray. The expected production rate from this reaction in KamLAND is 132.8 ± 8.7 events/kton-day [4] based on Hagner [100].

The ^{10}C and ^{11}C can be directly measured in KamLAND by associating the delayed beta particle energy with respect to the prompt n-capture that has occurred in spatial and temporal correlations with a muon event. The respective half-live are 19.26 sec and 20.39 min which make time-correlations with the n-capture feasible. The measured rates [80] are 21.1 ± 1.8 events/kton-day and 1106 ± 178 event/kton-day respectively. Both nuclei are positron decays and therefore the beta spectrum is shifted by the sum of the two 0.511 MeV gamma rays emitted from electron-positron annihilation. This pushes their energy well above the ^{7}Be solar neutrino region which ends at approximately 0.8 MeV. However, they would be important backgrounds for a CNO solar neutrino measurement, especially the ^{11}C positron spectrum. The rates and spectral shapes will be discussed in more detail below.

5.4 Radioisotope Contamination from Detector Calibrations

Calibrations are an indispensable tool for defining the energy scale of the detector. Since the start of KamLAND more then 100 calibration source deployments have been made which allowed for a complete characterization of the calibration system. Before any material is exposed to the LS for a calibration deployment, the pieces go through a rigorous cleaning and certification procedure. This minimized the risk of contaminating the LS with the calibration source isotope and other radioactive contaminants. The certification procedure and the results discussed in this section were recently published [82].

The ^{214}BiPo analysis technique discussed in Sec. 5.1.1 was used to measure the contamination from ^{222}Rn and its daughter nuclei. The cylinder cut $\rho \leq 1.0$ m used before to remove the central

[4] This is specific to KamLAND LS and to convert this value to events/(m^3 s) we need to multiply by the value 8.9993×10^{-9} which takes into account the specific density of the LS.

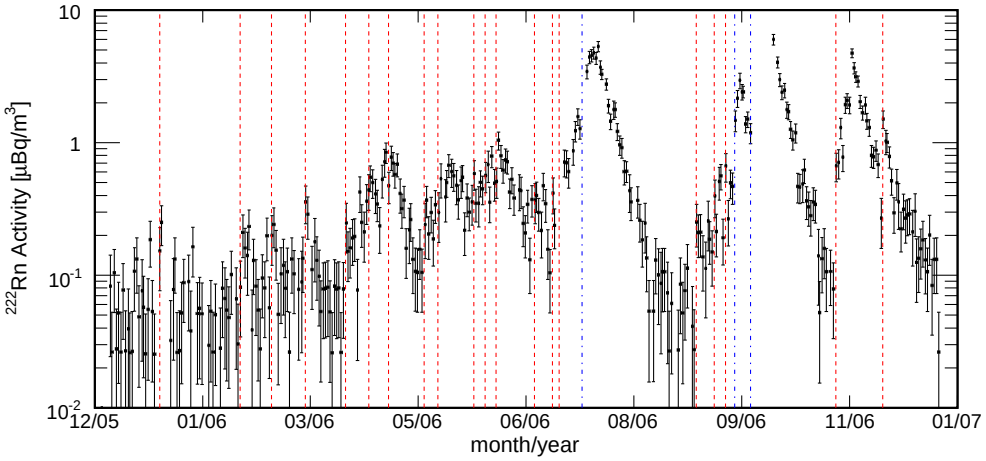

Figure 5.22: One year of KamLAND data in which ^{214}Bi-Po coincidences inside a 5.5 m fiducial volume are used to extract a ^{222}Rn activity: The red (dash-dash) lines indicate the start of calibration periods in which we took data along the central z-axis of the detector. The blue (dash-dot) lines indicate the beginning of off-axis calibrations. Offsets in the decay curves from the calibration start time are due to long calibrations lasting up to a week.

Z-axis events is now used to identify ^{214}BiPo events correlated with source calibrations. There were two calibration systems deployed into KamLAND during the reactor phase. Both deployed sources along the Z-axis, while the most recent system also deployed in the off-axis direction.

To analyze the ^{222}Rn contribution from both systems the time-evolution of ^{214}BiPo events are plotted as a function of time in Figure 5.22. The vertical lines overlaid on this figure represent the times when the calibration system was deployed in the detector. The blue dash-dot lines represent the off-axis deployments and the red dashed lines are Z-axis deployments. The exponential decay curves observed in this figure can be fit to the 3.8 day half-life of ^{222}Rn. This indicates that it was radon that was introduced into the LS by the calibration system and not ^{238}U. There is a slight offset before the decay curve in relation to some of the vertical lines. This is due to the calibration system being deployed over multiple days, sometimes up to several weeks. The ^{222}Rn decay is only evident after the calibration system has been completely removed.

While ^{222}Rn itself is not a concern for a low background solar neutrino measurement, its long-lived daughter ^{210}Pb is problematic. The largest ^{222}Rn activity was introduced from the off-axis calibrations which lead to an increased ^{210}Pb activity of approximately 10 μBq per typical deployment series of 150 hours inside a 5.5 m fiducial radius.

Analysis of special cable-only deployments revealed that small quantities of ^{222}Rn daughters

collected on the deployment cables while being stored inside the glove-box [5]. Once deployed into the detector, the secular equilibrium with ^{222}Rn is broken, and the daughters decay with the half-life of ^{214}Pb. Owing to the short half-life of ^{214}Pb , it was not detected in the data following off-axis deployments, and thus represented an additional contribution of 0.23 μBq of ^{210}Pb per deployment-hr per cable.

In order to characterize the intrinsic radioactivity of the off-axis calibration system, the data taken during the special cable only deployments were used to search for heightened levels of ^{40}K and ^{208}Tl. All searches for these isotopes gave negative results. Furthermore, there was no evidence for an increase in the bulk rate of low threshold events when comparing to background runs taken before and after regular calibration deployments. Thus, it was concluded that the only effects from calibration are attributed to ^{222}Rn contamination.

Though the measured ^{210}Pb contamination is very small, multiple deployments of the system could eventually lead to a non-negligible increase in the long-lived isotope ^{210}Pb. Additional studies of ^{222}Rn contamination following on-axis deployments revealed that the level of post-deployment ^{222}Rn varied greatly depending on factors surrounding the handling of the deployment hardware and pre-deployment glove-box manipulations. The result of this study, presented here, led the KamLAND collaboration to postpone any further deployments of the 4π-system until the end of the solar neutrino phase.

5.5 Simulation of Solar ν_e and Backgrounds

After determination of all the backgrounds associated with a low energy solar neutrino measurement a MC can be used to understand the effective rates of the different backgrounds and the solar neutrinos. The spectral form was calculated from theory for electrons and positrons. The model has been used throughout this chapter to fit the different isotopes and calculated their concentrations in the LS. Alpha particles and mono-energetic gammas from EC processes are modeled as delta functions and then smeared with the appropriate energy resolution to produce Gaussian p.d.f.s. Solar neutrinos are modeled according to the theory presented in Sec. 2.4. The kinetic energy of the electrons are quenched according to the same energy scale model as was the beta particles. The 7.6%/sqrt(E[MeV]) energy resolution was then applied to the spectra and then the spectrum is normalized to unity. These p.d.f. functions can then be used to model the spectral distribution from

[5] The daughters are thought to be introduced (via ^{222}Rn) when the glove-box is opened to transfer materials and from ^{222}Rn out-gassing of materials in contact with the interior of the box.

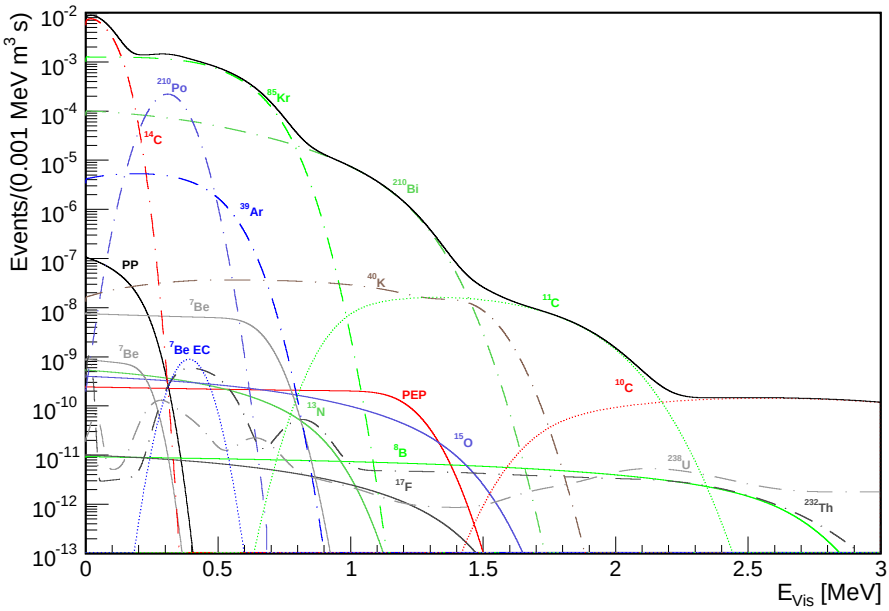

Figure 5.23: BS05(OP) expected solar neutrino elastic scattering spectra (solid lines) with measured internal background rates (long dash-dot lines) and muon spallation product rates (dot-dot lines). All spectra have been folded with $7.8\%/\sqrt{\mathrm{E[MeV]}}$ and quenched to yield the expected visible energy spectrum.

the background and solar neutrino rates.

The spectrum in Fig. 5.23 depicts the expected solar neutrino elastic scattering spectrum assuming the BS05(OP) Standard Solar Model rates[59]. The solar spectra have been generated with vacuum oscillation parameters of $\Delta m^2 = 7.59 \times^{-5}$ eV^2 and $\sin^2(2\theta) = 0.87$ [9]. Overlaid on this spectrum are the measured internal backgrounds. Fig. 5.23 clearly shows the 5-6 orders of magnitude difference in rates between the neutrino signal and background. Cosmogenic backgrounds are also plotted with the measured rates given in Sec. 5.3.

Fig. 5.24 shows the same backgrounds and solar neutrino rates with a set of hypothetical reduction factors listed in Table 5.1. These factors defined the goals for the studies presented in the rest of this work. Assuming the key backgrounds of ^{210}Pb and ^{85}Kr have been removed, the ^{7}Be solar ν_e clearly becomes visible. The characteristic "smoking gun" signature is the bend, or knee, in the spectrum around 0.7 MeV. Table 5.5 lists the integral rates for the [0.25-0.8] MeV ^{7}Be solar ν_e region. This shows that the projected background reduction would give a signal-to-background ratio of 2.6 in the ^{7}Be solar ν_e energy region.

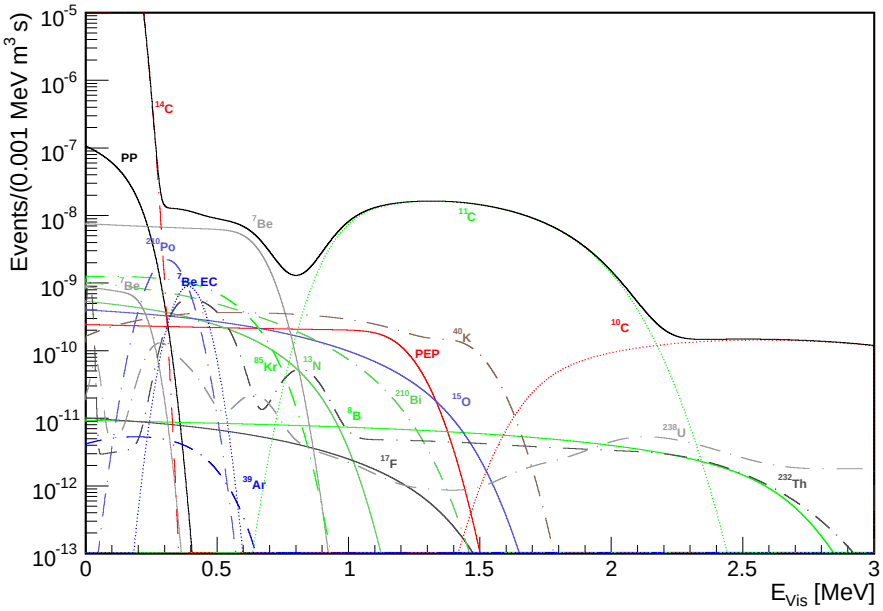

Figure 5.24: Monte Carlo of expected solar neutrino elastic scattering spectra (solid lines) with after expected reduction (Table 5.1) in internal backgrounds (long dash-dot lines) and muon spallation products (dot-dot lines). All spectra have been folded with $7.8\%/\sqrt{\mathrm{E[MeV]}}$ and quenched with the appropriate quenching factors to yield the expected visible energy for each spectrum.

Solar ν_e	**Events/kton-day**	**Background**	**Events/kton-day**
^{13}N	13.7	^{11}C	0.5
^{15}O	15.8	^{40}K	21.6
^{17}F	0.4	^{39}Ar	0.1
^{7}Be (0.862 MeV)	290.8	^{85}Kr	37.6
^{7}Be (0.384 MeV)	0.5	^{210}Po	29.1
^{8}B	0.5	^{210}Bi	30.7
PEP	13.4	^{238}U	2.0
PP	12.2	^{232}Th	13.1
Total	347	Total	135

Table 5.4: Integrated rates from Fig. 5.24 for the $[0.25 - 0.8]$ MeV ^{7}Be solar ν_e region of interest. The resultant signal-to-background ratio in the ^{7}Be solar ν_e region is 2.6.

Chapter 6

Laboratory Studies of Liquid Scintillator Purification

The previous chapter detailed the backgrounds which inhibited a ^{7}Be solar ν_{e} measurement with KamLAND during the reactor phase. Fig. 5.23 sums up the sheer magnitude of these backgrounds, indicating a difference of up to 6 orders of magnitude between the ^{7}Be electron recoil and internal background spectrum. The internal backgrounds measured in the previous chapter can be classified into two categories: 1) metallic radio-nuclei and 2) inert or noble gasses.

Sparging is the purification technique used to remove dissolved gasses from LS. In this process an extremely pure inert gas is bubbled through the liquid. The dissolved gas is removed from the LS due to the differences in chemical potentials (solubility) between the two phases. Care must be taken to correctly distribute the gas through the liquid, providing the smallest bubbles to maximize the surface to volume ratio. If the LS is exposed to enough purge gas the effective purification limit is equal to the ratio of solubilities times the concentration of the impurity in the purge gas. It is relatively easy to remove dissolved impurities from noble gasses. The procedure is based on the differences in the differences in boiling points for the gasses of interest and therefore the process of removing dissolved gasses from KamLAND was not as intensely researched as that of metal contaminants.

While most procedures that address the removal of metals from liquids rely on the same thermodynamic principles as sparging, the procedure is not as simple. This is primarily due to the

dissolved gasses not being molecularly bound to the liquid molecules. However, this is not a necessary condition for metals introduced to the liquid through energetic decay processes. The metallic radio-nuclei of interest in KamLAND are ^{210}Pb, ^{210}Po, and ^{210}Bi. As ^{210}Pb is the progenitor, the work described in this section focuses on ^{210}Pb removal techniques. The goal of this research was to develop a method or sequence of methods which yield at least a factor 10,000 reduction in ^{210}Pb. Many techniques were studied and those found to be effective were performed in series to determine if their purification factors scaled. Extensive analysis of each purification method was undertaken as well as a complete determination of all associated systematic errors.

The transition from one experimental procedure to the next was not always a simple logical reasoning. The work described in this section spanned more then 5 years and over this time consultation with colleagues, industry experts [101, 102, 103] and the literature affected the day-to-day operations. Most of the work presented here was performed in parallel with independent work from the Borexino collaboration. Very little information was shared and only after the fact could publications from Borexino's work [104, 105] be compared to work done by the author. To further the knowledge of a subject which has vast implications in the growing field of ultra-low background detectors, the work presented in detail below is being prepared for publication.

This chapter will discuss the specific methods and techniques designed specifically to remove and measure ultra-low concentrations of radioactivity in LS. The measurement of contaminant concentrations on the level of 10^{-20} g/g in the laboratory are an achievement of this study. The most sensitive commercially available analytical instruments typically measure concentration levels down to 10^{-12} g/g. The ultimate goal of this work was to develop a method which would reduce the ^{210}Pb concentration in LS down to approximately 400 atoms per m^3! [1] The preparatory studies examined in this chapter guided the design and implementation of a multi-million dollar purification system which will be discussed in Ch. 7.

6.1 Methodology

The ^{210}Pb in KamLAND LS was introduced during initial filling through exposure of the LS to air leaks in the piping. However, this concentration level one has to work with is extremely small with respect to the capabilities of available measuring devices. Therefore, the experiments carried out in this work rely on a fundamental assumption to allow experiments to be performed in the laboratory

[1] 2×10^{-25} g/g is equal to 0.57 atoms per kg of LS.

at the same concentration levels found in KamLAND:

> All isotopes of Pb born through Rn decay will have similar chemical characteristics in the LS and hence similar purification factors.

Under this assumption the short-lived isotopes of ^{212}Pb and ^{214}Pb can be used to test purification techniques in the laboratory. To see the scaling affect obtained from the short lived isotopes of Pb, the concentration listed in Table 5.1 can be converted into an activity

$$\mathrm{C} = \frac{m_{Pb}}{m_{LS}} = \frac{M_{Pb}\, N_{Pb}}{N_A\, \rho_{LS}\, V_{LS}} = \frac{A_{Pb}\, N_{Pb}}{\lambda_{Pb}\, N_A\, \rho_{LS}\, V_{LS}} \tag{6.1}$$

$$\mathrm{A_{Pb}} = \frac{C\, \lambda_{Pb}\, N_A\, \rho_{LS}\, V_{LS}}{M_{Pb}} \tag{6.2}$$

where $\mathrm{N_A} = 6.022 \times 10^{23}$ mol^{-1}, $\mathrm{A_{Pb}}$ is the lead activity in Bq, $\lambda_{\mathrm{Pb}} = \frac{\ln 2}{\mathrm{T}_{1/2}}$ is the decay constant, ρ_{LS} is the LS density which can be found in Table 6.7, $\mathrm{V_{LS}}$ is the volume of LS and $\mathrm{M_{Pb}}$ is the molar mass of the isotope. This shows that the activities of the different isotopes allow a scaling proportional to the ratio of half-lives. Thus, in using the shorter lived isotopes of lead the measured activities are increased from 10^{-6} Bq/l to $0.1 - 1$ Bq/l.

6.1.1 Radioactive Decay Equations

All the fits to data in this chapter rely on a set of equations describing the growth and decay of radioactive species. These equations will be derived here as typically only the second order equation is readily available in the literature. Radioactive decay is governed by the differential equation

$$\frac{\mathrm{dN_1}}{\mathrm{dt}} = -\lambda_1 \mathrm{N_1(t)} \tag{6.3}$$

were $\mathrm{N_1(t)}$ refers to the number of atoms of the parent nuclei at some time t. The solution to the first order equation is obtained by integration:

$$\begin{aligned} \int_{\mathrm{t_0}}^{\mathrm{t}} \frac{\mathrm{dN_1}}{\mathrm{N_1(t)}} &= \int_{t_0}^{t} -\lambda_1 dt \\ \ln(\mathrm{N_1(t)}) - \ln(\mathrm{N_1(0)}) &= -\lambda_1 t \\ \mathrm{A_1(t)} &= A_1(0) e^{-\lambda_1 t} \end{aligned} \tag{6.4}$$

where we take $t_0 = 0$ and in the last line, the number of atoms has been converted into the measured quantity $A_1 = N_1\lambda_1$, referred to as the activity. This first order equation describes simple decay models such as the time dependence between the prompt and delayed events in the ^{214}BiPo study in Sec. 5.1.1. However, this section will be concerned with decays in which more then one decay constant must be considered. Specifically in Sec. 6.2.2, the growth and decay of several radio-nuclei in the ^{222}Rn chain must be considered simultaneously.

To obtain the analytical form for the i^{th} nuclei in the decay chain, $N_i(t)$, the resultant integrals must be solved iteratively. Thus, one must first solve the equation for $N_{i-1}(t)$ and substitute this solution into the equation for $N_i(t)$. Using ^{222}Rn as an example; to get the equation which determines the number of ^{218}Po atoms given that it is fed by the parent isotope ^{222}Rn one must solve the following equation:

$$\begin{aligned} \frac{dN_2(t)}{dt} &= \lambda_1 N_1(t) - \lambda_2 N_2(t) \\ \frac{d}{dt}\left(N_2(t)e^{\lambda_2 t}\right) &= \lambda_1 N_1(0) e^{-\lambda_1 t} e^{\lambda_2 t}. \end{aligned} \tag{6.5}$$

Here the solution to the first order decay, Eq. 6.4, is substituted in for $N_1(t)$. Both sides of the equation are multiplied through by $e^{\lambda_2 t}$ so that the left hand side becomes a complete differential. Integrating both sides and defining the resultant integration constant to be the activity of the second decay product at time zero, $N_2(0)$ we obtain

$$A_2(t) = A_2(0)e^{-\lambda_2 t} + A_1(0))\left(\frac{\lambda_2}{\lambda_1 - \lambda_2}\right)\left(e^{-\lambda_2 t} - e^{-\lambda_1 t}\right). \tag{6.6}$$

This relates the activity of ^{218}Po to the parent isotope's initial activity.

Using this same procedure, the third order decay term is:

$$\begin{aligned} A_3(t) = A_3(0)e^{-\lambda_0 t} + A_2(0)\left(\frac{\lambda_3}{\lambda_2 - \lambda_3}\right)\left(e^{-\lambda_3 t} - e^{-\lambda_2 t}\right) + \\ A_1(0)\left(\frac{\lambda_2\lambda_3}{(\lambda_1 - \lambda_2)}\right)\left\{\frac{(e^{-\lambda_2 t} - e^{-\lambda_3 t})}{(\lambda_3 - \lambda_2)} + \frac{(e^{-\lambda_3 t} - e^{-\lambda_1 t})}{(\lambda_3 - \lambda_1)}\right\} \end{aligned} \tag{6.7}$$

and the fourth order term is:

$$\begin{aligned}
\mathrm{A_4(t)} = A_4(0)e^{-\lambda_3 t} - A_3(0)\left(\frac{\lambda_4}{\lambda_4-\lambda_3}\right)\left(e^{-\lambda_4 t}-e^{-\lambda_3 t}\right) + \\
A_2(0)\left(\frac{\lambda_3\lambda_4}{(\lambda_3-\lambda_2)}\right)\left\{\frac{(e^{-\lambda_4 t}-e^{-\lambda_3 t})}{(\lambda_4-\lambda_3)} + \frac{(e^{-\lambda_4 t}-e^{-\lambda_2 t})}{(\lambda_4-\lambda_2)}\right\} + \\
A_1(0)\left(\frac{\lambda_2}{(\lambda_2-\lambda_1)}\right)\left\{\left(\frac{\lambda_4\lambda_3}{(\lambda_3-\lambda_2)}\right)\left[\frac{(e^{-\lambda_4 t}-e^{-\lambda_2 t})}{(\lambda_4-\lambda_2)} - \frac{(e^{-\lambda_4 t}-e^{-\lambda_3 t})}{(\lambda_4-\lambda_3)}\right] - \right. \\
\left.\left(\frac{\lambda_4\lambda_3}{(\lambda_3-\lambda_1)}\right)\left[\frac{(e^{-\lambda_4 t}-e^{-\lambda_1 t})}{(\lambda_4-\lambda_1)} - \frac{(e^{-\lambda_4 t}-e^{-\lambda_3 t})}{(\lambda_4-\lambda_3)}\right]\right\}. \qquad (6.8)
\end{aligned}$$

These equations are used to determine the initial activities for all experiments described in this section. For the majority of experiments, in which ^{212}Pb is the primary isotope of interest, only Eq. 6.4 is used. However, in Sec. 6.3.6 all of these equations become important in extrapolating multiple isotope purification factors. It should be noted that when considering a daughter nuclei whose decay is governed by a branching ratio, the decay constant for that decay must be substituted for $\lambda \rightarrow \lambda_\mathrm{i} \mathrm{f_i}$ where $\mathrm{f_i}$ is the branching ratio of the decay mode.

6.1.2 Solid-Liquid Chromatography Theory

The purification technique discussed in extensive detail in this chapter is chromatography. It is a common tool used in chemistry and biology to remove atomic and molecular solutes from organic solvents. The solute is removed via polar hydroxyl bonds on the surface of the silica. A typical silica gel particle has a diameter of a few hundred μm while the pore site diameter on the particle is $10-100$Å. This results in a large surface to volume ratio. A 1 cm^3 volume has more then 1000 m^2 of surface area. Plate theory [106] is commonly used to describe liquid-solid chromatography which requires mass and thermodynamic equilibrium between the mobile and stationary phases.

In plate theory one defines a distribution coefficient, k, which represents the solute concentration between the two phases.

$$dX_s = k\, dX_m \qquad (6.9)$$

where X is the concentration in of the solute in the stationary (s) and mobile (m) phases respectively. To allow direct comparison of data collection collected during the course of this work with that found in the literature [104, 105] the distribution coefficient is written as:

$$k = \frac{\mathrm{n(Y\ in\ SG)} \cdot \mathrm{n(LS)}}{\mathrm{n(Y\ in\ LS)} \cdot \mathrm{n(LS\ in\ SG)}} \qquad (6.10)$$

where n(Y in SG) is the number of moles of solute (^{212}Pb) in the adsorbed phase (Silica Gel), n(LS) is the number of moles of solvent (LS) in the non-adsorbed phase (LS), n(Y in LS) is the number of moles of solute in the non-adsorbed phase, and n(LS in SG) is the number of moles of solute in the adsorbed phase. The distribution coefficient represents thermodynamic equilibrium and can therefore be expressed in terms of the Gibbs free energy:

$$\Delta \mathrm{G} = -\mathrm{R}\ \mathrm{T}\ \ln(k) \tag{6.11}$$

where R is the gas constant and T is the temperature in Kelvin. If $\Delta G < 0$ then the reaction is spontaneous.

To relate the distribution coefficient to an experimentally determined quantity we defined the purification factor as the activity in the LS before purification divided by the activity in the LS after purification:

$$f = \frac{\mathrm{n(Y\ in\ LS)_I}}{\mathrm{n(Y\ in\ LS)_F}}. \tag{6.12}$$

The distribution coefficient can then be written in terms of known quantities [105]:

$$k = (f-1)\frac{\mathrm{n(LS)}}{\mathrm{a}\cdot\mathrm{s}\cdot\rho_{\mathrm{p}}} \tag{6.13}$$

where n(LS) is the number of moles of LS, $\mathrm{a} = 4.6\ \mathrm{nm}^{-2}$ is a physicochemical constant [107] describing the concentration of hydroxyl groups ($-$OH) on the surface of the adsorbent [2], s is the total surface area per gram of adsorbent and ρ_p is the pore bulk density, equal to the inverse of the pore volume.

6.2 Experimental Procedures and Detection Methods

This section presents the general procedure for loading, measuring and removing ^{220}Rn, ^{222}Rn and their subsequent daughter nuclei. All samples were prepared following the loading procedure outlined in this section. There were four different instruments utilized to determine a sample's activity: two Ge detectors and two scintillation coincidence systems. The coincidence systems are described in detail as they were designed specifically for these measurements. The Ge detector systems are explained in detail elsewhere [108] and are a common gamma ray counting device explained in detail in textbooks [78]. Finally, the general handling procedures of the samples are defined in this section. If there was a notable deviation from the norm the specific procedure will be described in

[2] This constant is the same for all adsorbents considered in this work.

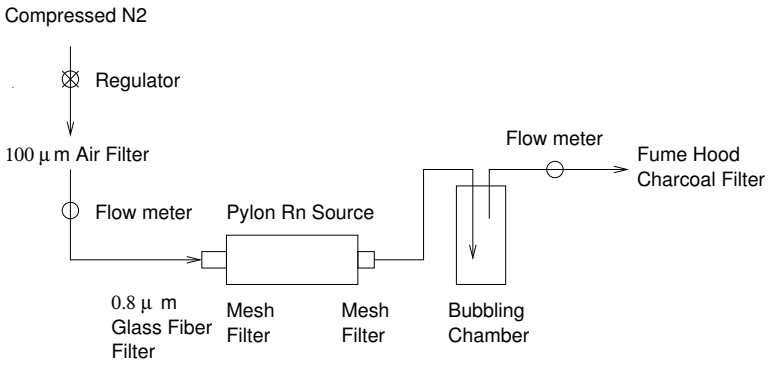

Figure 6.1: Diagram of the bubbling procedure use to load LS, Dodecane and PC with Rn for purification experiments.

the appropriate section.

6.2.1 ^{220}Rn and ^{222}Rn Loading of Liquid Scintillator

It was necessary to find an effective and reproducible method for dissolving Rn gas in LS and its individual liquid components. The experiments in this work used two commercial available sources from Pylon Electronics [109] driven by ^{228}Th and ^{226}Ra for loading LS with ^{220}Rn and ^{222}Rn, respectively. A schematic of the loading procedure is given in Fig. 6.1. Commercially available compressed N_2 was used as the carrier gas. The N_2 is first filtered to remove any particulates and then dried with a glass fiber filter before entering the source chamber. The exit stream was again filtered and then directed to a 500 ml glass bubbler fitted with a bubbling stone to maximize Rn exposure to the liquid. Flow meters allowed good control of flow rates and provided a means of monitoring the exhaust. The exhaust is loaded with Rn and organic vapors and was therefore sent to a fume hood equipped with an activated charcoal filter.

6.2.2 Spectroscopic Techniques and Measurement Devices

Determining the effectiveness of different purification techniques requires an accurate and reproducible method for measuring the activity of samples. Several aspects of the Rn decay schemes can be used to determine the activity of the sample. The first and most direct means is to measure the gamma rays listed in Table 6.1 which can be directly measured with a Germanium (Ge) detector. While Ge detectors offer excellent energy resolution when compared to scintillation detectors, their

Isotope	**E_γ [keV]**	I_γ
^{212}Pb	238.632	0.4330
^{212}Pb	300.087	0.0328
^{208}Tl	583.191	0.8450
^{212}Bi	727.330	0.0658
^{208}Tl	860.564	0.1242
^{208}Tl	2614.551	0.9900

Isotope	**E_γ [keV]**	I_γ
^{214}Pb	241.997	0.0743
^{214}Pb	295.224	0.1930
^{214}Pb	351.932	0.3760
^{214}Bi	609.312	0.4610
^{214}Bi	768.356	0.0494
^{214}Bi	1120.287	0.1510
^{214}Bi	1238.110	0.0579
^{214}Bi	1764.494	0.1540
^{214}Bi	2204.210	0.0508

Table 6.1: Gamma rays considered when performing spectroscopic analysis using the HPGe detectors. The energy and branching ratios for the gamma rays used to measure the ^{220}Rn (left) and ^{222}Rn (right) daughters are listed. These are only the gamma intensity and must be multiplied by the appropriate branching ratios when applicable.

sensitivity is restricted by environmental backgrounds dominated by Uranium and Thorium in the construction materials, cosmogenics and ambient ^{222}Rn.

The nuclear physics group at The University of Alabama is equipped with a high purity Ge detector fitted with a muon veto and N_2 purge line to keep a positive pressure in the chamber to stave off the ambient ^{222}Rn. A second Ge detector is utilized for higher activity sources as it has higher backgrounds, a lower detection efficiency, a very basic muon veto and no N_2 purge. Independent measurements of two isotopes of Pb and two isotopes of Bi through their gamma lines provide an opportunity to test the underlying assumption of this work (presented in Sec. 6.1).

To mitigate the problem associated with backgrounds influencing detector sensitivity, a second counting technique was developed which takes advantage of the fast coincidence decays of ^{214}BiPo and ^{212}BiPo. These coincidence schemes were previously used in Sec. 5.1.1 and 5.1.2 to measure the ^{238}U and ^{232}Th concentrations in KamLAND. However, in the laboratory ^{212}BiPo is a direct measure of the ^{212}Pb activity due to the extremely fast decay times of the higher order nuclei in the chain. ^{214}BiPo is more complicated as the coincidence directly measures the ^{214}Bi activity and the nuclei which feed this decay have long half-lives. However, the parent isotopes can be deduced using the equations from Sec. 6.1.1 and the time evolution of the ^{214}BiPo rate.

The Rn sources provide initial activities of approximately 10 kBq/l in the loaded LS. Experimentally the requirement was to be sensitive to purification factors of 10^5. After background subtraction

(a) (b)

Figure 6.2: Pictures of the laboratory $\beta - \alpha$ system. The figure on the left shows the PMT placed inside a specially designed SS dark box. A copper housing was designed to fit around the base of the PMT to reduce ambient electronic noise. The SS dark box is then placed inside Pb bricks to shield from external backgrounds and enclosed in a steel and iron box seen in the figure on the left. This figure also shows the CAMAC/NIM rack and DAQ system set up for the coincidence systems.

the Ge detectors have a sensitivity of 1 Bq/l while the $\beta - \alpha$ coincidence detectors extend the sensitivity by two orders of magnitude.

Each detector counts the number of events after making some event selection cuts. As previously mentioned, the activity is related to the number of atoms by $A = N\lambda$. However, one must take into account the finite detection efficiency. For a typical measurement the activity is calculated as

$$A = \frac{N\lambda}{\epsilon_G \, \epsilon_C \, I_b} \tag{6.14}$$

where ϵ_G is a geometric efficiency, ϵ_C is the cut efficiency and I_b is the branching ratio for the decay mode. To minimize the systematics associated with the calculation of an absolute activity, all samples are counted using the same detector, in the same geometry, utilizing the same analysis cuts such that the determination of the purification factor, defined by Eq. 6.12, allows a cancellation of the efficiency terms in Eq 6.14 reducing Eq. 6.12 to $f = \frac{N_i}{N_f}$. As this assumes ideal conditions, systematic studies were performed to estimate the uncertainty in performing a measurement in this manner. Typically the systematic error associated with reproducing the same measurement is on the order of 5%.

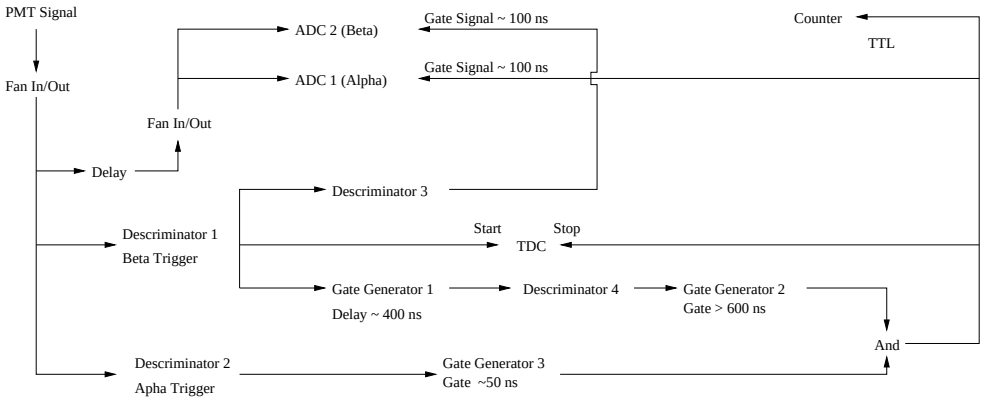

Figure 6.3: Electronics diagram of CAMAC/NIM detector setup for isolating the ^{212}BiPo $\beta - \alpha$ events with a fast coincidence time of $T_{1/2} = 0.299$ μs. The PMT signal is split by a Fan In/Out and sent to logic modules. The delays and timing are such to allow the signals to lie inside the gates.

Description of $\beta - \alpha$ Coincidence Detectors

Two scintillation detectors were designed using a 76 mm Head-on Hamamatsu PMT (R1307) to detect the scintillation light produced in the ^{212}BiPo and ^{214}BiPo decays. CAMAC and NIM modules were used to measure the timing and charge associated with these events and a DAQ was setup to read the data with a computer. The DAQ was programmed in C++ which ran on a Linux operating system. Cylindrical acrylic cells were manufactured to fit over the face of the PMT and were optically coupled together with optical grease. The cells measured 10.80×4.44 cm and could hold approximately 200 cm^3 of LS. Fig. 6.2(a) shows the coupling between the acrylic cells and the PMT. Reliably securing the cells was essential to reproduce the coupling between the PMT and acrylic and ensured the system did not move during measurements which could last up to 7 days.

As PMTs are sensitive to single photons it is essential that the system is operated in a dark environment. Fig. 6.2(a) shows the PMT in a SS box which had electronic feedthroughs for the signal and power cables. The box was secured with bolts and a Viton o-ring to ensure a light-tight environment. To reduce the affects of ambient radiation the dark box was surrounded by approximately $15 - 20$ cm of Pb. The entire system was then sealed in a large steel box, shown in Fig. 6.2(b).

The electronics setup itself is relatively simple for the extremely fast ^{212}BiPo coincidence which occurs on the 300 ns time-scale. A suitable time-to-digital converter (TDC) module with a dynamic range of $1 - 10$ μs and ns sampling time was purchased. The flow diagram in Fig. 6.3 indicates the logic and electronics modules used to extract the ^{212}BiPo coincidence events.

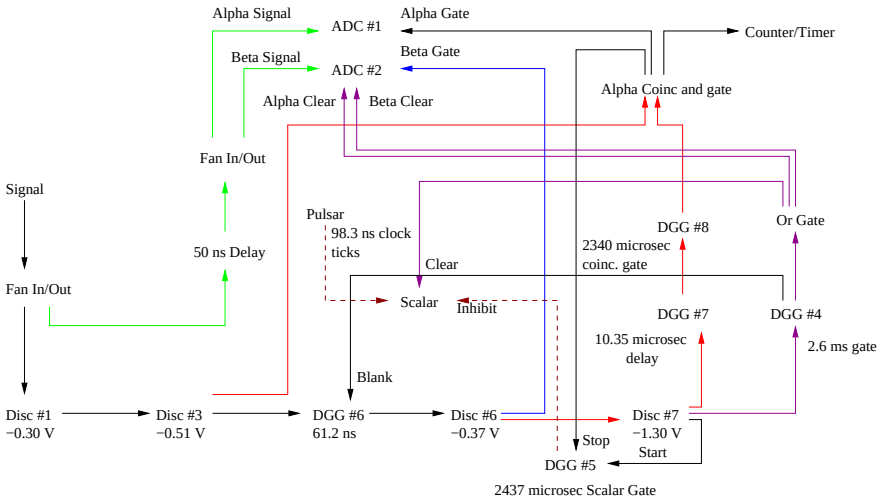

Figure 6.4: Electronics diagram of CAMAC/NIM detector setup for isolating the ^{214}BiPo $\beta - \alpha$ coincidence events with a characteristic time of $T_{1/2} = 164.3\ \mu$s.

The signal from the PMT is split using a Fan In/Out. One signal goes directly to LeCroy Analog-to-Digital converters (ADC) which measures the PMT's signal (charge) and effectively the event's energy after calibration. The other signal initializes the logic, providing the gates and signal windows. A measure of the dead-time is obtained by sending the delayed gate to a counter which measures the absolute number of gates sent to the ADC.

For ^{214}BiPo coincidences the time-scale between prompt and delayed events is much longer requiring hundreds of microseconds. The logic and timing is a bit more complicated as it requires an external pulse generator to replace the TDC. The pulse generator provides 98.3 ns clock ticks to a scalar which is activated by the prompt signal gate and stopped by the delayed signals gate which mimics a TDC. Due to the large time differences between events, more gate-and-delay generators where needed to match up the pulses and signal gates. However, in the end the logic of the system was very similar to the ^{212}BiPo coincidence setup. The schematic for the ^{214}BiPo coincidence system is provided in Fig. 6.4.

The ADC channel to energy mapping is calculated with commercially available disk sources: ^{22}Na, ^{54}Mn, ^{60}Co and ^{137}Cs. Calibrations yield an ADC bin equivalent energy of 22 keV. The TDC is calibrated using a pulse generator with known dT between pulses measured on an oscilloscope.

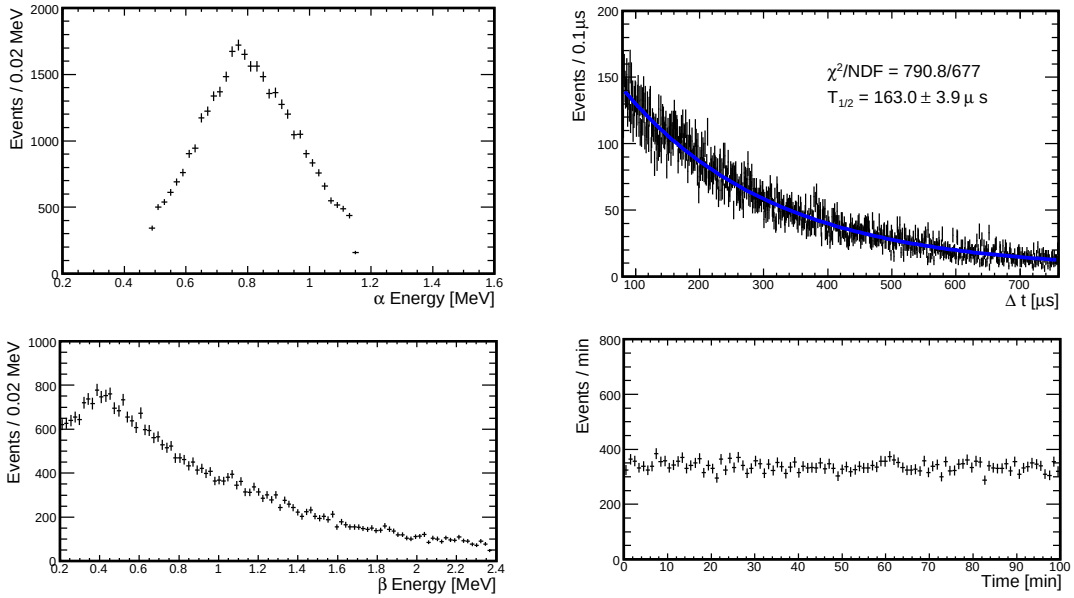

Figure 6.5: Typical diagnostics figures obtained from an acrylic cell bubbled with ^{214}BiPo source. There is a clear alpha and beta particle signal present and the time correlation between events gives a half-life in very good agreement with the expected $T_{1/2} = 164.3$ μs. The bottom right figure shows the timing of all events with respect to the start of the run.

The diagnostics plots from a freshly bubbled LS sample is shown in Fig. 6.5. The two figures on the left are the energy spectra. Unlike KamLAND, this detector does not see all of the delayed energy (beta + gamma) as most of the gamma rays escape the cell. Therefore, the delayed energy spectrum is very close to an idealized beta spectrum. The top right corner shows the Δt between the prompt and delayed ^{214}BiPo events which agrees very nicely with the expected $T_{1/2}$ of 164.3 μs. The bottom right plot indicates the time evolution of coincidence events as a function of time. If the ^{214}Bi is in disequilibrium with ^{214}Pb or ^{222}Rn then a growth or decay curve would be observed in this plot. The background rate is on the order of 10 events per day.

6.2.3 General Experimental Procedure

Experiments described in this chapter were performed with pure Dodecane, PC or the mixture which constitutes the KamLAND LS. In general this section will refer to LS as the liquid being used. However, it should be noted that all liquids underwent the following procedures:

1. Bubble LS up to 24 hours with Rn loaded nitrogen. [3]

2. Transfer loaded LS into two 125 ml Nalgene bottles when being counted on Ge detectors. If the LS is counted on the $\beta - \alpha$ coincidence detector then it is transferred into an acrylic cell.

3. When using Nalgene bottles the liquid is removed from the bottles and placed into the purification system. When using the acrylic cells, enough liquid was bubbled to allow counting of the cell only. Purification was performed on the remaining liquid from the bubbling flask. This method assumes a homogeneous distribution of atoms in the LS after bubbling.

4. After the purification procedure was performed on the liquid then the purified liquid was counted on the appropriate detector. The same detector was used for an entire process to allow for cancellation of geometric efficiency and better estimation of systematic errors.

In some instances it was necessary to use only a single component of LS during the purification process. This liquid was then counted on the coincidence system and required the addition of PPO. For these special cases, the pure Dodecane or PC was mixed with the appropriate quantity to make LS. This dilution was taken into account in all calculations.

6.2.4 Systematic Errors

Detailed studies of systematic errors were performed on every aspect of the purification processes and counting procedure. The largest systematic error was found to be associated with activity sticking to the surfaces of all the equipment. Experiments showed that the polyurethane tubing, Nalgene bottles and glassware used in the experiments were in some instances more efficient in removing Pb then the actual purification procedure. To examine the effect, experiments were performed using Nalgene bottles. The bottle was filled with loaded LS, counted, the LS was transferred to a new bottle and both bottles were counted to determine the amount which had stuck to the initial bottle's wall. Mass measurements were made to determine contributions from left-over LS in the bottle which could account for lost activity. Fig. 6.6 shows the percentage of activity stuck to the bottle as a function of the LS activity.

If not properly accounted for this contribution will change the associated initial activity by a factor of 2 to 3 and subsequently inflate the predicted reduction factor. Therefore, each measurement

[3] Care must be taken when using LS or pure PC. PC has a high vapor pressure causing it to boil off during bubbling, resulting in a lower concentration of PC and corrosion of filters and membranes.

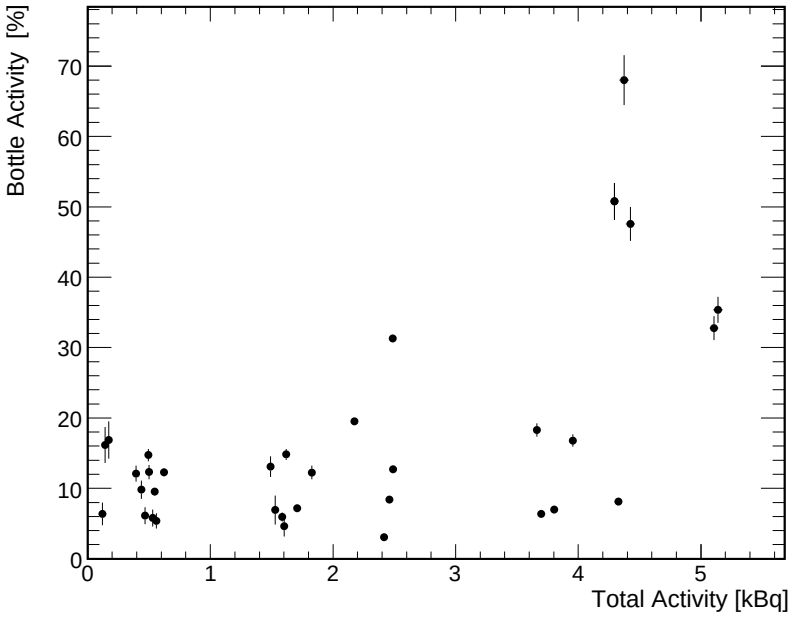

Figure 6.6: The bottle activity after transferring the LS to the purification system. There is no clear functional form to predict the value. This is an important systematic as it causes the initial activity to vary by up to 70% and is therefore determined for every experiment.

corrects for the bottle activity and the initial activity in the LS is defined as

$$A_i(t_0) = A_{LS} - A_{Bottle} \tag{6.15}$$

where A_{LS} is the activity obtained from the initial counting of the bottles filled with the LS to be purified from step 2 above. A_{Bottle} is the activity obtained from step 3 after the transfer of LS has occurred. All activities are calculated with respect to a designated start time. t_0 is defined by the removal of the LS from the bubbling flask. The initial activity of the LS placed into the purification system is therefore a well defined quantity free of systematic error.

The final activity, which is needed to calculate the purification factor defined in Eq. 6.12, is obtained from the purified liquid. This value can depend on the purification system and the procedure. Typically the same experiment was repeated multiple times to establish the reproducibility and an average systematic error for the purification factor. When possible tests were performed in which loaded LS was run through the purification system without the purification material, such as water,

(a) (b) (c)

Figure 6.7: The figure on the left shows the glass apparatus used for water purification. The middle figure shows the stainless steel holding container used before the liquid is sent through the adsorption column depicted on the right. The containment unit was also used to pre-heat the liquid before passing it through the silica gel column. This could also be pressurized to speed up the liquid flow through the adsorption column.

silica gel, etc. In this way the reduction due to the system itself could be quantified and deducted.

Once large purification factors were obtained the surface cleaning procedures became a source for systematic errors for the purification factors. It is therefore imperative to properly clean all equipment which comes into contact with the purified LS when dealing with extremely low levels of radioactivity. A cleaning procedure was developed according to a previously tested method [82, 108]. All purification system components and counting bottles were cleaned by rinsing with alcohol, acetone and a 1 molar solution of nitric acid [4].

6.3 Purification Techniques

A multitude of purification techniques were studied to determine their effectiveness in removing ^{212}Pb from LS to include: water extraction, introduction of ions with water extraction, isotope exchange, filtering, adsorption and distillation. A few of the major experimental systems are shown in Fig. 6.7. This section will describe the relevant procedures, observations, and purification factors

[4]This was the general cleaning procedure. However, this requires that all materials are chemically compatible with these cleaning liquids. For instance, the acrylic cells where only cleaned with nitric acid and alcohol.

obtained for all experiments performed by the author in preparation for a solar neutrino phase of KamLAND. LS is defined in this section to be the composite mixture of 20% PC, 80% Dodecane and 1.5 g/l PPO. The LS was mixed from its components in the lab. The PC was purchased from Bicron and the Dodecane is from the same batch used to fill KamLAND. The PPO used was from Packard [110] and was left over from KamLAND construction. All tests described in this section were performed on these specific scintillator components or some combination thereof.

6.3.1 Water Extraction and pH Dependence

Water extraction was employed during the initial KamLAND filling [111]. Since a purification facility already existed, this was the first procedure tested in the laboratory. Water extraction works under the principle of mass transfer due to solubility differences between liquid phases. This technique best addresses ionic or polar impurities which have a high solubility in water such as Na or K. The transfer of impurities occurs at the surface between phases the two liquid phases. In a static system a concentration gradient will develop from the interaction surface.

The experimental setup consisted of a fixed speed peristaltic pump (Cole Parmer Inst. Co. Model 7543-60) used to provide multiple volume transfers and provide sufficient exposure of the H_2O to the LS. Fig. 6.7(a) shows the setup used to perform the water purification experiments. The LS, which is less dense than water, was removed from the top of the water column and returned to the bottom. The system uses 0.9525 cm diameter polyurethane Tygon tubing[5]. To increase the surface area of the LS, which effectively increases the probability to transfer impurities, the LS was broken into small bubbles via a glass frit at the bottom of the water column. Purification was performed in a cyclic process and the speed was defined by the rotation speed of the pump. As this was a constant value, stop cocks were placed into the flow line to provide resistance and allow the flow rate to be regulated and measured by flow meters.

Experiments showed that water purification was not an efficient method for removing ^{212}Pb from LS. Water extraction experiments resulted in a modest dependence of the purification factor with respect to time. There is some evidence for a saturation affect after approximately 10 hours, seen in Fig. 6.8(a). For the nominal volumes of 500 cm^3 of water and 250 cm^3 of LS, a circulation time of 5 hours and a flow rate of 200 cm^3/min was found to be the most efficient.

De-ionized (DI) water was initially used and therefore a study of the purification efficiency as

[5]One must ensure the tubing is compatible with the LS which typically requires fuel grade polyurethane tubing. Incompatible tubing can become too soft or brittle and develop leaks.

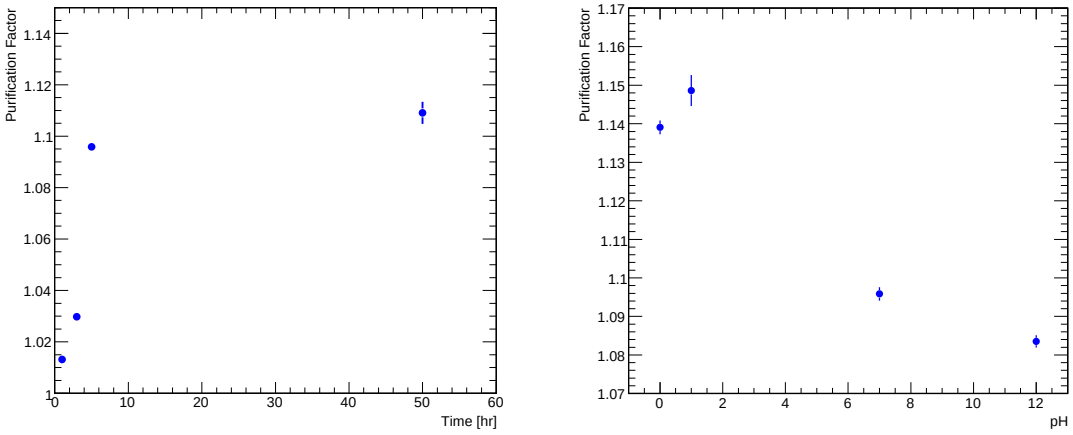

(a) (b)

Figure 6.8: Water purification factor as a function of time and pH. Each run used 250 cm^3 of LS pumped through 500 cm^3 of DI water. The flow rate was 170-210 cm^3/min. The pH of the water was changed by using different concentrations of HNO_3 and NaOH.

a function of the number of free H^+ ions was performed to expand the scope of the existing large scale water purification system. The conclusion is that the purification factor decreases linearly as a function of pH as seen in Fig. 6.8(b). However, the overall reduction factor is too small and water was deemed to be an ineffective method for purifying KamLAND.

6.3.2 Isotope Exchange

Another suggested method of purification analyzed was isotope exchange. In this procedure the LS was passed over a bed of granular lead. For another experiment lead shot was used. The principle idea was that by providing the LS with an infinite number of stable Pb isotopes one could exchange the ^{212}Pb for a stable Pb isotope. The system was setup in a similar manner as the water purification system in which the LS was continuously pumped over a bed of stable lead isotopes. While there was a reduction observed this was consistent with the amount of activity lost to the pumping system. Therefore, the isotope exchange experiments were found to have no affect on the ^{212}Pb reduction.

6.3.3 Filtering and HTiO Loaded Filters

Filtering was initially treated as a source of systematic error. Tests showed filtering had a measurable affect on the lead removal efficiency. As a result it was considered as a purification method. Typically

Flow rate [ml/min]	Efficiency	LS Mass [g]
16.5 ±1.0	1.06 ± 0.01	202.5 ± 0.2
3.27±0.06	1.07 ± 0.01	172.7 ± 0.2

Table 6.2: ^{212}Pb purification factors using HTiO on KamLAND LS. The flow rate and LS mass are given and the HTiO concentration on the PTFE filters is provided in Sec. 6.3.3.

this process addresses charged molecular or atomic species and is best suited for "filtering" large particulates from the liquid. The data reported here are derived from independent tests performed with two different systems [112].

The filter types used in these studies were ADVANTEC 5A (7μm), ADVANTEC 5B (7μm), ADVANTEC 5C (1μm), and a 0.2 μm sol-vent DCF pharmaceutical grade filter. The mean reduction factor for all four filter types was found to be 1.09 ± 0.09 per filtration. Experiments showed no dependence of the purification factor on the size or type of filter. Up to three passes through the filter were performed in series, each producing at most a 10% reduction in ^{212}Pb. Furthermore, experiments showed that if the carrier gas which loads the ^{212}Pb is not pre-filtered, small particulates are transferred to the LS and increased the first filtration efficiency by 30-40%. This was the only observed systematic error.

In a similar aspect, HTiO has been used by the SNO collaboration [113] operating a multi-tonne neutrino experiment. It was utilized to remove actinides from water and heavy water. HTiO was therefore analyzed as a possible purification medium for organic liquids. The HTiO was pre-loaded onto a HEPA PTFE filter (S.A. = 3.9 cm^2 with 2.5 g of Ti/g HTiO) by a SNO colleague familiar with the loading process. The ^{212}Pb loaded LS was placed into a 60 ml syringe and the pre-loaded filter was attached to the end of the syringe. The LS was slowly pushed through the syringe. To minimize any saturation affect, the HTiO loaded filter was replaced after every 125 cm^3 of LS transferred. Results from these test are listed in Table 6.2. HTiO was found to provide only a modest purification factor for ^{212}Pb in LS.

6.3.4 Chromatography with SiO_2, Alusil and Aerosil Gels

Adsorbent purification was the procedure studied most extensively by the author. Chromatography provided relatively large purification factors, was reproducible, and contributed to the understanding of how the ^{212}Pb was chemically distributed throughout the LS.

The chromatographic process relies on several factors. First is the difference in solubility between

Adsorbent	mass [g]	Batch	Loop
32-63 μm Selecto	10.0	22.73 $\pm$ 0.52	4.98 $\pm$ 0.12
100-200 μm Selecto	10.0	15.38 $\pm$ 0.24	7.04 $\pm$ 0.10
Aerosil 200	0.5	3.45 $\pm$ 0.02	1.49 $\pm$ 0.02

Table 6.3: Comparison of batch and loop mode ^{212}Pb reduction factors using adsrobtion. The adsorbent type and total mass of adsorbent are listed. The amount of LS purified in each experiment was 250 ml.

the liquid and solid phases. Different types of adsorbents are readily available which are designed to boost the solubility through pH changes on the pore sites or a change in the pore volume. As the transfer occurs at the surface, adsorbents are ideal in that they provide an enormous amount of surface. 100 cm^3 of silica, (approximate volume of a softball) provides more surface area then the Sears Tower! [114]

Operating a chromatographic column was itself an experimental test. A "loop" mode operation was studied first as this was similar to the operational conditions of previous experiments. It further seemed plausible that the highest purification factor would be achieved by allowing the LS to pass through the adsorbent as many times as possible. Experiments found that this was the worst operational mode. This was later confirmed in the literature [105, 106]. Ideally the purification was performed in a "batch" process. In batch mode the LS makes a single pass through the adsorption column which sets up a ^{212}Pb concentration gradient in the direction of liquid flow. Along this concentration gradient a saturation front is formed. In order to achieve the highest purification factor, this saturation front should never reach the end of the column, referred to as breakthrough. Table 6.3 shows the experimental results for three different adsorption materials, clearly indicating the batch mode is superior to loop mode operation.

Selecto Scientific [101] provided many different types of silica for experimental test and their $32-63$ μm silica gel was used as the standard. This gel was used to define the operation procedures and systematic errors. The final system design is depicted in Fig. 6.9. A picture of the system is shown in Fig. 6.7. A key factor to the reproducibility of the experiments was the adsorbent conditioning procedure. The final procedure consisted of the following steps:

1. Clean all parts with acetone, ethanol, $0.1-1.0$ molar HNO_3 and DI water.

2. Partially assemble the purification system, attach the Cu nipple and SS mesh filter to the bottom of the chromatographic column and then add $1-2$ g of silica gel to the column.

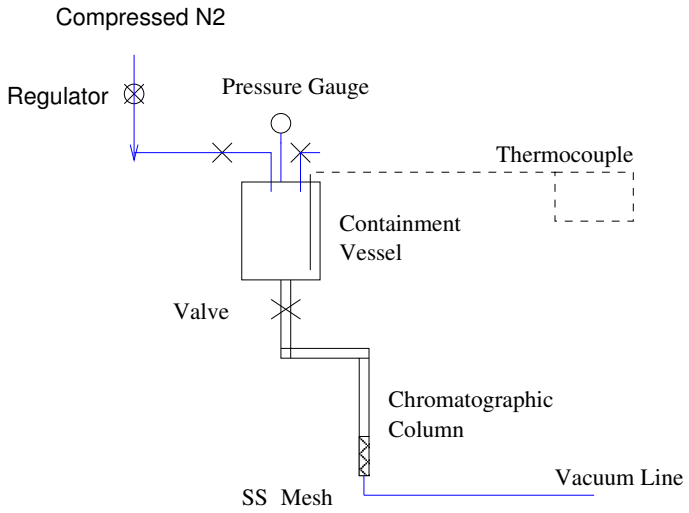

Figure 6.9: Diagram of the chromatography purification system. Blue lines represent N_2 or air lines, black lines represent the 304 SS structure and the dashed line represents the thermocouple which is placed into a thin capillary reaching into the liquid. The containment vessel holds 10 l of LS. The pressure was controlled in the containment vessel by a gas pressure regulator and valves. A thermocouple and temperature controller was implemented to heat the LS in the vessel. All seals were made with Viton o-rings. The inner diameter of the chromatographic column is 10 mm. The hatched region in the lower portion of the chromatographic column represents the position of the adsorbent material. Between this material and the vacuum line lies a system of seals and o-rings to support a SS mesh filter and the copper nipple. At this point the vacuum line could be attached as well as a beaker and Tygon tubing system for capturing the liquid and pulling vacuum.

3. Attach the column to the containment vessel and seal the system. Seals were made with Viton o-rings.

4. Affix the vacuum pump to the Cu nipple and pump down the pressure to 100 hPa. Periodically knocking the side of the column removes the dead space between silica granules and helps prevent eddies from forming during liquid flow.

5. Once 100 hPa pressure was reached, apply 103 kPa [6] to the top of the column and continue to knock the column to set the silica in place. When the pressure reaches approximately 300 hPa the conditioning process is complete.

6. Allow the system to come back to atmospheric pressure and remove the vacuum line. Do not release the pressure first as removal of the vacuum line can produce a backwards force

[6] The pressure gauge was held to 15 PSI.

Adsorbent	**[pH]**	**[%]**	**[μm]**	**[m^2/g]**	**[cm^3/g]**	**[Å]**
Silica $32-63$ μm	7.0	3	55	520	0.72	60
Silica $100-200$ μm	7.0	4	140	505	0.70	60
Alusil Coarse	9.8	10	500	85	0.14	95
Alusil 70	9.9	4	34	183	0.53	116
Alusil NanoSmart	9.5	1	45	145	0.56	104
Alusil Plus	9.9	1	45	145	0.58	105
Alusil NanoSmart ACT	9.0	12	30	385	0.25	26

Table 6.4: Characteristics of Silica Gels used in adsorbtion experiments provided by Selecto Scientific. The characteristics are pH, percent moisture, mean particle size, BET surface, pore volume and pore diameter.

which destroys the conditioning procedure. The constant downward force from the N_2 pressure mitigates this problem.

7. Slowly release the pressure from the containment vessel. At this point the system has been conditioned and is ready for purification.

8. The top of the containment vessel can now be removed to add the ^{212}Pb loaded LS. Before adding liquid ensure the valves to the chromatographic column are closed.

9. Reseal the top of the containment vessel, close all valves and pressurized the system to 103 kPa.

10. At this point, the valve between the containment vessel and the silica column was opened slowly to keep the LS from rapidly flowing into the silica. This can create a divot in the top of the silica column effectively reducing the purification efficiency. The nominal LS flow rate under 103 kPa of N_2 pressure was 50 cm^3/min for 1.5 g of silica.

11. After purification with the chromatographic column the LS was passed through a 0.2 μm PTFE HEPA filter to remove any particulates.

Further conditioning tests were performed using heating tapes, hot plates (100 - 120 °C) and a vacuum pump to try and boil off any water vapor from the surface of the gel. This was suggested [106] as potentially the water vapor would take up pore space. This conditioning step did not provide any benefit to the experiments carried out in this work, however it may need to be considered under different conditions[7].

[7]One possibility would be if the silica gel was exposed to a humid environment or if it was washed before using to remove any surface contaminants.

Adsorbent Type	Purification Factor	ΔG [kJ/mol]
Selecto, Lot #301286301, Si-gel 32-63 μm	19.4 ± 0.47	-6.33 ± 0.07
Selecto, Lot #306279301, Si-gel 100-200 μm	15.38 ± 0.24	-5.97 ± 0.04
Selecto, Lot #102085402, Alusil 70	27.03 ± 0.73	-9.13 ± 0.08
Selecto, Lot #109110402, Alusil Plus	8.33 ± 0.07	-6.80 ± 0.03
Selecto, Lot #108110403, Alusil NanoSmart	8.20 ± 0.07	-6.54 ± 0.03
Selecto, Lot #900110401, Si-gel NanoSmart ACT	3.58 ± 0.01	-3.96 ± 0.02
Selecto, Lot #900110401, Alusil Coarse	28.57 ± 0.82	-7.73 ± 0.08
Adsorbent Type	**Purification Factor**	**Adsorbent Mass [g]**
Selecto, Lot #107223405, Alusil 40 without K	10.31 ± 0.21	2.0 ± 0.05
Aldrich, 3-(Diethylenetriamino) Propyl-Functionalized gel	8.33 ± 0.69	10.0 ± 0.05
Aldrich, Triamine Tetraacetate-Functionalized gel	11.11 ± 0.12	10.2 ± 0.05
Aerosil 200	8.26 ± 0.07	15.0 ± 0.05
SÜD-CHEMIE, Cu/Mn Catalyst T-2550	3.45 ± 0.02	0.5 ± 0.05
SÜD-CHEMIE, Cu/Mn Catalyst T-2550, Crushed	26.32 ± 0.69	7.166 ± 0.001
$Ca_3(PO_4)_2$ 'Fish Bone'	6.54 ± 6.54	2.0 ± 0.05

Table 6.5: Measured adsorption purification factors for ^{212}Pb in LS using the system described in Fig. 6.9. When possible the Gibbs free energy was calculated for comparison with the literature [105, 104]. Experiments performed with the 32-64 μm gel provide a procedural systematic error of 7.2%. When multiple experiments were performed the mean is reported. Only statistical errors are quoted.

Experiments performed on many different silica gels and adsorbent materials are listed in Table 6.5. Table 6.4 provides the details for the silica gels obtained from Selecto Scientific. Using these characteristics the distribution coefficient is calculated using Eq. 6.13 which then provides the Gibbs free energy based on Eq. 6.11. Extensive studies found that at most 95% of the ^{212}Pb could be removed using silica gel chromotography in batch mode. The other 5% could not be removed by changing any operational procedure, running multiple columns in series, performing multiple adsorption procedures or increasing the amount of adsorbent (the resonance time in the adsorbent). A hypothesis was developed from these experimental facts and is explained in detail in Sec. 6.3.7.

6.3.5 Experimental Determination of Elution Curves

Understanding the break-through properties of adsorbents is important to estimate how much would be required to purify a specific amount of LS. Going back to Eq. 6.9, the equation for elution can be derived from plate theory. In each theoretical plate, p, there exists a specific volume of the mobile

phase V_m which is the LS in this instance, a specific volume of the stationary phase V_s or adsorbent material, a measurable concentration of solute, or ^{212}Pb, in the mobile phase $X_{m(p)}$, and likewise a measurable amount of solute in the stationary phase, $X_{s(p)}$. Applying mass balance between plates one obtains the differential equation

$$\begin{aligned} dm &= X_{m(p-1)} - X_{m(p)}dV \\ \frac{dX_{m(p)}}{dv} &= X_{m(p-1)} - X_{m(p)} \end{aligned} \tag{6.16}$$

where v is the plate volume: volume of mobile phase that can contain all of the solute in the plate at the equilibrium concentration of the solute in the mobile phase [106]. Through recursive integration this yields the elution equation

$$X_{m(p)} = \frac{X_0 v^p}{p!} e^{-v} \tag{6.17}$$

which is just the Poisson equation and is a purely theoretical quantity. Experimentally this corresponds to a very small cylindrical slice along the adsorption column and Eq. 6.17 describes the distribution of the mobile phase throughout these slices as it travels down the column. In this work the number of plates is large enough that the Poisson equation is best expressed as a Gaussian moving along the liquid path. The integral of this Gaussian, is an experimentally measurable quantity.

For the specific case at hand, a constant concentration mobile phase is added to the top of the column. Far from the front end of the "saturation front" the exiting liquid will have the highest purity. Once the edge of the front reaches the end of the column the purified liquid will begin to contain more of the solute. One expects that the measured amount of solute in the purified liquid would be equal to the integral of Eq. 6.17 and is therefore well described by an Error function.

Initial experiments with silica gel found that the PPO was being removed (reduced the light yield) from the LS. As the PPO concentration is very large compared to the ^{212}Pb concentration, this presented an opportunity to experimentally measure the saturation front of a high concentration solute. A batch of LS was made without loading and a control sample was taken to establish the absolute concentration of PPO. The LS was then purified using the chromatographic column. Approximately 20 cm^3 samples were collected and labeled as the LS was purified. The PPO concentration in these samples were measured using a flame ionization gas chromatograph (GC) [102]. The GC measures the mass number and the integral of the peak given by the GC is normalized to the control sample and then each subsequent sample was divided by this absolute value. Fig. 6.10 shows the results of two different measurements which indicate a clear elution curve for PPO where

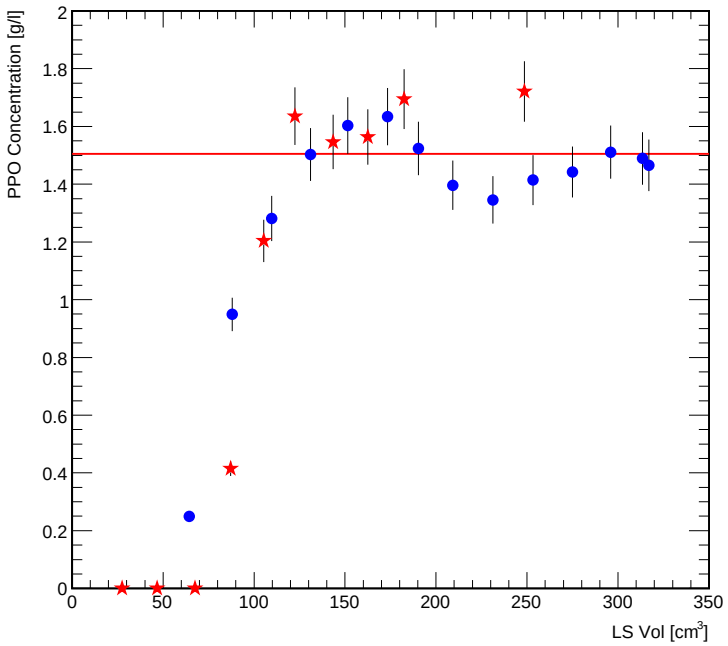

Figure 6.10: Elution curve for PPO adsorption onto 2.00 ± 0.05g of 32-63 μm Silica Gel. The red line indicates the initial PPO concentration of the purified LS. The blue dots indicate the LS purified at 17°C and the red stars are data for 90°C. The data include the statistical and systematic error added in quadrature. The systematic error was measurements to be 6.1%.

break-through occurs at 125 cm^3.

As the equations for thermodynamic equilibrium between the two phases are temperature dependent a test was performed to determine if increasing the temperature affected the elution curve's break-through point. Performing the same test and heating the column to 90°C did not influence the break-though position as indicated in Fig. 6.10. The resultant saturation concentration of PPO on the 32-63 μm Selecto Scientific Silica Gel is calculated to be 0.23 g PPO/g SiO_2. The systematic error on the GC measurements was found to be 6.1%.

While ^{212}Pb cannot be measured on a GC at the concentrations analyzed in this work, a similar experimental test was performed to determine if a break-through could be observed in the concentration curve of ^{212}Pb. As the ^{212}Pb activity is assumed to be homogeneously distributed in the liquid prior to purification the concentration is defined to be the integral rate of 239 keV ^{212}Pb gamma line divided by the volume of the sample. Only the rates are measured as the absolute geometric efficiency was not known for the small sample bottles used in this experiment.

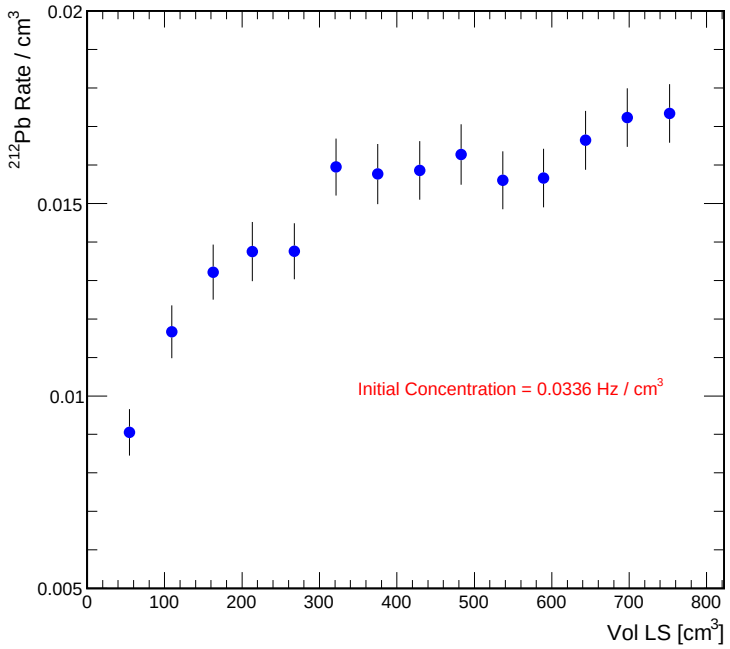

Figure 6.11: Elution curve for ^{212}Pb using PC/Dodecane mixture and 1.5 g 32-63 μm Silica Gel. There is possible evidence for a plateau, however, this cannot be related to break-through as this is still a factor two lower then expected initial concentration. The resultant saturation concentration of PPO on the 32-63 μm Selecto Scientific Silica Gel is calculated to be 0.23 g PPO/g SiO_2.

Approximately 800 cm^3 of Dodecane was loaded with ^{212}Pb which is the maximum amount the system could load. A control sample was counted to determine the initial rate of ^{212}Pb in the Dodecane and then the liquid was purified with the chromatographic column. Samples where collected in approximately 50 cm^3 integrals and counted on the Ge detector for 10 min to determine the rates. The rates where corrected back to a common t_0 and the concentration was plotted as a function of the volume which passed through the silica gel, shown in Fig. 6.11. While there is some evidence in this figure of a saturation affect, this could not be directly contributed to a break-though point as the final concentration was not equal to the expected value of 0.0336 Hz/cm^3.

6.3.6 Purification Factors for ^{212}Pb, ^{214}Pb, ^{212}Bi, ^{214}Bi, ^{218}Po and ^{208}Tl

Due to the differences in solubilities of metals between the two phases, it is not a necessary condition for the different nuclei in the Rn decay chains to be in equilibrium after the purification procedure. In KamLAND, even if the ^{210}Pb is removed, it is useful to understand the efficiency with which the

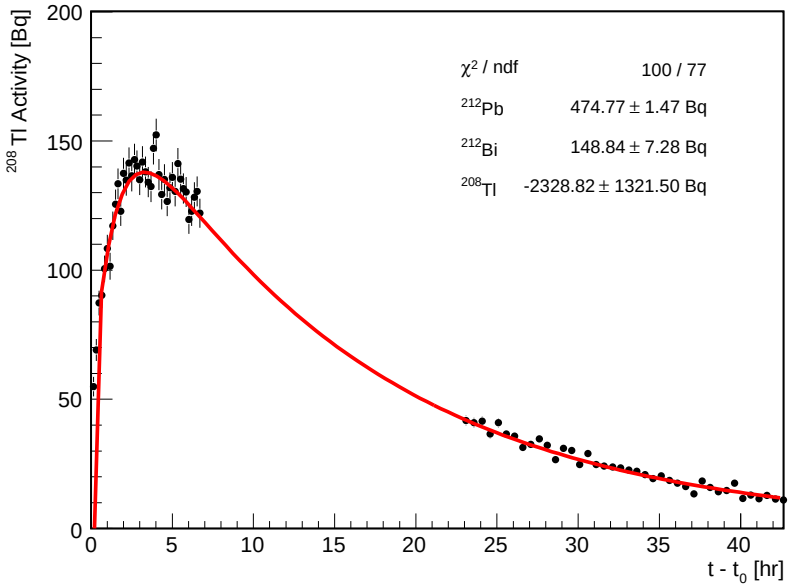

Figure 6.12: Fit to data taken with ^{220}Rn loaded LS. This is used to extract the daughter concentrations immediately after silica gel purification using Eq. 6.8. The data shown is for pure Dodecane purified with 1.5 g of 32-64 μm Selecto Scientific silica gel. While the ^{212}Bi growth is obvious the ability to determine ^{208}Tl relies on the first few points as the half-life is only 3.05 min.

^{210}Bi and ^{210}Po will also be extracted. The ^{210}Bi has a short half-life and will come into equilibrium with the ^{210}Pb rather quickly. However, ^{210}Po has a half-life of 138 days and a large disequilibrium would not be advantageous.

Using the Ge detector it is possible to distinguish the gamma lines of several different nuclei listed in Table 6.1. However, the half-lives for the majority of these nuclei are between 3 and 30 min. The only purification process which provides a fast enough response time to measure these short-lived nuclei is silica gel purification. After optimizing the system, the total time required to purify 250 cm^3 of LS is approximately 5 minutes with the procedure outlined in Sec. 6.3.4.

An initial sample was loaded and counted. For this specific measurement timing is essential and becomes an important systematic error. The "clock" does not start until the purification process begins as this is what will define the point at which homogeneity is broken. For all samples t_0 is defined as the mean time during LS purification. All times were considered including the time it took to pass the liquid through the silica gel column, the time required for filtration, bottling, labeling, and counting of the samples on the Ge detector. All clocks used in this measurement were synchronized to minimize differences associated with using different clocks.

After purification the sample was counted on the Ge detector. To extract the short lived isotopes ^{218}Po and ^{208}Tl which dominate the spectral shape in the first 10-20 min, counting times were 5 min per point for the first 30 min. At this point the spectrum is dominated by the moderately longer half-lives of approximately 25 min. The samples were counted for $10-15$ min which provided much better statistics. The final decay curves would follow the ^{212}Pb and ^{222}Rn life-times and for these the samples were counted again over a two day period. A fit to the time-evolution for ^{212}Pb and its daughters is shown in Fig. 6.12 which indicates a clear growth and decay expected from disequilibrium between the parent and daughter nuclei.

Due to the total number of possible free parameters, fitting the decay curves is complicated. To minimize the number of free parameters, the half-lives are fixed to their tabulated values. Germanium counting of ^{220}Rn loaded LS provides gamma lines for 3 separate nuclei in the decay chain: ^{212}Pb, ^{212}Bi and ^{208}Tl [8]. As seen in Fig. 6.12,^{212}Pb has a 10.64 hr half-life that fits well to the data. The following procedure was used to obtain activities for ^{212}Bi and ^{208}Tl:

1. The time distribution of gamma lines associate with ^{212}Pb was fit to determine the ^{212}Pb activity.

2. The tail of time distributions for ^{212}Bi and ^{208}Tl were fit to the determine the ^{212}Pb activity after the short-lived daughters had established equilibrium with their parent.

3. The next nuclei in the sequence is ^{212}Bi whose gammas are measured directly. To help guide MINUIT to fit the ^{212}Bi gamma rates to Eq. 6.5 the fit information from the previous stage was used as a χ^2 constraint term in the fit.

4. Likewise, the ^{208}Tl gamma lines were fit to using the previous fit values for ^{212}Pb and ^{212}Bi as χ^2 constraint terms.

The result of this method is shown in Fig. 6.12. This figure shows several key features which should be discussed. First, the growth of ^{212}Bi and the decay of ^{212}Pb are obvious and they can be fit without using a penalty term in the χ^2 statistic. However, ^{208}Tl lives 3.053 min and has a 35% branching ratio for this decay mode. Not only are there fewer events but when the purification procedure takes $1-2$ lifetimes the first few data points drives the result. This is why the constraints on the ^{208}Tl activity are so poor. To get the best possible constraint on the ^{208}Tl concentration requires a χ^2 constraint term for the previously fit Bi and Pb activities.

[8] The branching ratio of ^{208}Tl ($I_b = 0.3594$) must be taken into account when performing the fits to the individual gamma intensities.

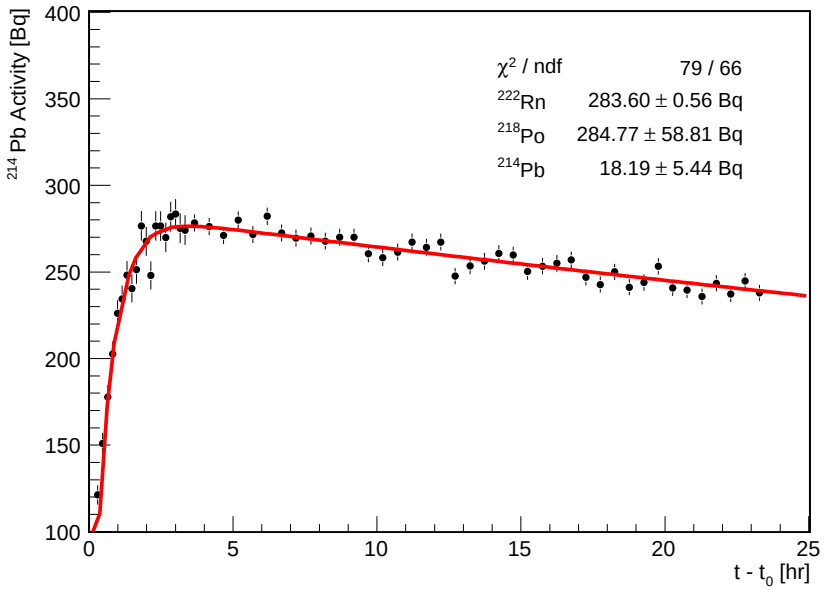

Figure 6.13: Fit to data taken with ^{222}Rn loaded LS. This spectrum is used to extract the daughter concentration immediately after silica gel purification using Eq. 6.8. The data is pre-fit without ^{218}Po and then the term is added with constraints on the fitted values for the other three nuclei. ^{218}Po is difficult to fit because the half-life is 3.1 min. The data shown is for a solution of 80% Dodeacane and 20% PC purified with 1.5 g of 32-64 μm Selecto Scientific silica gel.

In a very similar manner the measurable quantities in the ^{222}Rn decay chain are determined. For this case the measured nuclei are ^{214}Pb and ^{214}Bi. Between the ^{222}Rn and ^{214}Pb is the decay of ^{218}Po which has a half-life of only 3.10 min. With only two gamma lines there are four possible nuclei which can be measured. To obtain the best possible constraint on ^{218}Po the following procedure was used:

1. The tail of the ^{214}Pb time distribution (5-20 hrs) was fit to determine the resultant constant activity corresponding to the ^{222}Rn concentration.

2. The full time distribution for ^{214}Pb was then fit to Eq. 6.5 to extract the ^{214}Pb activity.

3. The full time distribution for ^{214}Pb was fit again, but this time to Eq. 6.7 which allows the possibility of ^{218}Po. The fit was performed with χ^2 constraints using the previously fit values and the associated errors.

4. Eq. 6.7 was then used to fit to the ^{214}Bi data, assuming that only the ^{222}Rn and ^{214}Pb contributed and using the appropriate penalty terms. This is important as ^{214}Pb and ^{214}Bi

Component	^{222}Rn	^{218}Po	^{214}Pb	^{214}Bi
Pseudocumene	2.67 ± 0.04	> 14	28.0 ± 11.4	> 396
Dodecane	3.60 ± 0.16	3.92 ± 0.97	20.4 ± 2.0	48.6 ± 13.9
80% Dodecane 20% Pseudocumene	2.58 ± 0.01	2.57 ± 0.53	39.3 ± 8.4	78.7 ± 32.2

	^{212}Pb	^{212}Bi	^{208}Tl
Pseudocumene	94.2 ± 1.9	NA	NA
Dodecane	4.09 ± 0.02	11.12 ± 1.22	> 2.03
80% Dodecane 20% Pseudocumene	89.3 ± 2.4	> 633	NA

Table 6.6: Purification factor for each of the measured nuclei in the ^{222}Rn decay series. Fig. 6.13 shows the fits to the data which are used to obtain the values in this table. All experiments used 2.0 g of Selecto 32-63 μm silica gel and were performed using the procedures described in Sec. 6.2.3. All limits are 99% CL. For some of the runs the rates were too low because of the gamma branches and NA implies a limit could not be reasonably extracted.

have very similar half-lives.

In this manner all the information is used in a way to best constrain the fits and obtain the best possible estimates on all the nuclei in the decay sequence. The ^{214}Bi data was fit to Eq. 6.8 using constraints on ^{222}Rn, ^{214}Pb, and ^{214}Bi to extract a ^{218}Po activity. However, at this point there are too many exponentials and the best possible value for ^{218}Po is obtained from the ^{214}Pb data. The resultant fit, which provided some evidence for ^{218}Po growth, is shown in Fig. 6.13.

Experience with different LS components used throughout these studies provided some initial evidence that there could be a different purification factor associated with each component. Therefore, to study this affect, this procedure was performed on PC, Dodecane and the composite of 80% Dodecane plus 20% PC. There was no PPO used in these measurements to minimize the affect of possibly saturating adsorption sites with PPO. Tables 6.6 lists the resulting purification factors for each nuclei and liquid component. These experiments show that purification factors are higher for PC than for Dodecane.

The experimental data shows that PC has the highest purification factor compared to Dodecane. The reduction factors differ by a factor of 20 for ^{212}Pb. The columns with NA indicated that the activity was too low to be measured.

Searching the literature revealed an interesting study which provides some insight into these observations. In this study [115] a ^{60}Co source was used to irradiate different organic solutions, specifically Dodecane was used as one solvent. The sample was first distilled before irradiation to

remove the free radicals (broken carbon chains) to achieve a pure sample indicated by a single mass peak in the GC. After irradiation with the ^{60}Co source the samples where analyzed again on the GC. The authors of this study mixed small amounts of aromatic compounds into the solution an performed the analysis again to compare the fraction of broken carbon chains as a function of the abundance of aromatic compounds [9]. The results of this study showed that by introducing aromatic compounds into Dodecane, the number of free radicals was reduced.

6.3.7 Organo-Metallic Separation

The extensive studies performed with adsorbents provided invaluable insight into the manner in which the radioactive nuclei are distributed in the LS. Chromatographic experiments specifically address polar molecules or ionic atomic states which are drawn to the hydroxyl group (-OH) on the adsorption site. The reproducibility of these experiments and the fact that we could never achieve greater than a 95% reduction in ^{212}Pb gave credence to the possibility that on the balance of ^{212}Pb was in a neutral form. Furthermore, the previous section indicates that the purification factor depends on the solvent used and an independent study [115] provided evidence that this was due to the aromatic compounds of PC.

In consultation with colleagues [103, 116] it was hypothesized that the ^{212}Pb atom was forming an organo-metallic compound by binding to the free radicals in the vicinity of the recoil nucleus. Typically the recoil nucleus left over from alpha decay will have a positive charge in the form of Pb^{+} or Pb^{++} states caused by the removal of outer shells electrons from a perturbative affect [117, 118, 118, 119] of ejecting a particle from the nucleus. The free Pb^{+} then combines with the broken carbon chains to form an organo-metallic compound of Pb. This organo-metallic compound of ^{212}Pb would be chemically stable and have no excess charge. These facts indicate that the silica gel would not remove all the Pb created in alpha decays.

Dodecane is a linear chain of carbon and hydrogen bonds. The recoiling Pb nucleus has enough kinetic energy ($\geq$ 117 keV) to break the carbon-carbon bonds which are on the order of tens of eV. A compilation of all stable organo-metallic Pb compounds is provided in Table 6.7. Their chemical characteristics are taken from the literature [121]. Due to these characteristics, experiments where performed to exploit the temperature dependences and instabilities of the organic compounds. All of the resultant compounds have low boiling points relative to PC and Dodecane and C_8H_2Pb is unstable and should decompose in a thermal bath. A further verification of the organo-metallic

[9] PC and PPO are aromatic compounds.

Name	Formula	ρ [g/cm^3]	Boiling Point [°C]
n-Dodecane	$C_{12}H_{26}$	0.7526 [111]	215
Isoparaffin	$C_nH_{2n+2}, n \sim 15$	0.7958 [111]	$180 - 210$
1,2,4-Trimethybenzene (PC)	C_9H_{12}	0.8796 [111]	169
2,5 Diphenyloxazole (PPO)	$C_{15}H_{11}NO$	1.0940	360 [a]
KamLAND LS [c]		0.77754 [120]	
KamLAND Buffer Oil [d]		0.77732 [74]	
Tetraethyllead	$C_8H_{20}Pb$	1.653	200 [b]
Methyltriethyllead	$C_7H_{18}Pb$	1.71	70
Diethyldimethyllead	$C_6H_{16}Pb$	1.79	51
Ehtyltrimethyllead	$C_5H_{14}Pb$	1.88	27
Tetramethyllead	$C_4H_{12}Pb$	1.995	110

[a] PPO has a melting point of 74 °C
[b] Tetraethyllead will decompose at the stated temperature before it boils.
[c] KamLAND LS is composed of 80.2% dodecane and 19.8% 1,2,4-trimethylbenzene by volume with 1.36 g/l of 2,5-Diphenyloxazole [9]
[d] The KamLAND buffer oil is composed of 48% isoparaffin and 52% dodecane by volume.

Table 6.7: Chemical characteristics of the KamLAND LS, its components and the suspected organo-metallic compounds which would allow for separation through distillation. The values in this table are compiled from the literature [111, 120, 74, 121]. All densities are quoted at 20°C except Isoparaffin, Dodecane and PC which were measured at 15°C.

hypothesis was studied using reagents with known chemical affinity to organic lead component. This directly tested our hypothesis.

To verify our hypothesis on the formation of organo-metallic lead compounds, experiments were performed using reagents known to react with such compounds: $FeCl_3$ [122], $SnCl_4$ [123], MoS_2 [124] and a thiol resin [125]. The following procedure was developed in collaboration with Prof. Schweitzer [10]:

1. Purify the LS using silica gel to remove the ionic component.
2. Stir the LS (150 cm^3) with the reagent for 45 min in a glass beaker with a stirring rod.
3. 15 cm^3 of 0.5 M EDTA ($[CH_2N(CH_2CO_2H)_2]_2$) solution (pH of 8) was added to the LS and stirred for an additional 15 min.
4. The mixture was filtered using filter paper and and partial vacuum.
5. The filtered solution was run over a bed of 4A molecular sieves(4-8 mesh) to remove any access water.

[10] George Schweitzer is a professor of inorganic chemistry at The University of Tennessee and a research scientist at Oak Ridge National Laboratory.

Method	Purification Factor
$SiO_2 \rightarrow FeCl_3$	> 1060
$SiO_2 \rightarrow FeCl_3 \rightarrow SiO_2$	> 1263
$SiO_2 \rightarrow SnCl_4$	47.0 ± 1.1
$SiO_2 \rightarrow MoS_2$	24.9 ± 0.6
$SiO_2 \rightarrow$ ThiolResin	22.7 ± 0.5
HeatedLS $\rightarrow SiO_2$	278 ± 23
$SiO_2 \rightarrow$ Distillation	> 4389 [1]

[1] This experiment was performed only with Dodecane.

Table 6.8: Purification factors from experiments designed to specifically address an organic Pb component in LS. All experiments were analyzed using a Ge detector and 68.27 % CL. limits are derived utilizing the method by Feldmon Cousins [126].

6. The LS was filtered a second time to remove any access particulates left from the molecular sieve [11].

7. The LS was counted to determine the purification factors.

The results from these experiments are tabulated in Table 6.8. The increased purification factor provides evidence that an organo-metallic form of lead exists in the LS. The unfortunate side effect from these experiments was that the LS no longer scintillated. Experiments (longer exposure to EDTA, filtering and silica gel extraction) were performed to try and improve the optical properties, however none of the methods improved the transparency.

While the organo-metallic lead targeting reagents gave good results in terms of Pb removal, the LS was opaque and thus useless as a scintillation material. As an alternative, heating was studied to possibly improve purification factors while not hopefully not destroying the optical properties. Fig. 6.7(b) shows one of the systems used to heat the LS. The procedure was similar in that the LS was first purified to remove the ionic component via silica gel extraction. The LS was then heated and purified again with silica gel. The reason for this method is that the process of heating potentially breaks the organic Pb bond, ionizing the Pb atom which could then be removed via chromatographic techniques. The SS container was externally heated with heating tapes (Omega FGH051-020) and the LS temperature was regulated through a temperature controller (Omega CN

[11] Molecular sieves are known to contain large amounts of ^{238}U and ^{232}Th.

Time [hrs]	**Avg Temp** [°C]	**Purification Factor**
2	142	277.8 ± 23.2 [1]
2	187	5.3 ± 0.06
2	187	200 ± 16 [1]
2	157	5.08 ± 0.05
8	152	9.35 ± 0.09
2	152	10.99 ± 0.12 [2]
1.5	160	172.4 ± 2.97 [3]
3	17	1.11 ± 0.01 [4]

[1] The liquid was first heated for two hours and then passed through 5 g of SiO_2.
[2] 10 g of glass beads with a diameter of 0.021 cm (surface area = 1076 cm^2) was added to the SS container.
[3] The silica gel and liquid were heated at the same time in the column holding the 5 g of SiO_2.
[4] This was the control sample. No heat was applied to the stainless vessel holding the LS.

Table 6.9: Purification factors from heating experiments designed to break organometallic bonds. All experiments were performed inside a stainless steel container unless otherwise noted.

21110) and thermocouple.

Table 6.9 lists the results from heating tests. These experiments show that heating is complementary to silica gel extraction and increases the purification a factor by an order of magnitude. This provides further evidence of the existence of an organo-metallic component. In order to achieve the desired purification goals, it is necessary to specifically address this organic component.

There is one experimental fact which should be mentioned at this point. While the heating did improve the purification efficiency, it would also impair the optical properties if the temperature was above 120 °C. Heating was not as destructive as the reagent tests, but these affects must be taken into consideration. Furthermore, one must consider the O_2 concentration of the LS before heating. Heating LS under high concentrations of O_2 oxidizes the LS and contributes to diminishing its transparency. Bubbling with N_2 prior to heating and using N_2 as a cover gas in the heating apparatus dramatically reduced the destructive affects of heating.

The last purification method which addresses all of the organic lead removal scenarios is distillation. Distillation heats the liquid, which in turn will break the organic bonds causing more ionic or polar forms of lead. These are effectively removed by the distillation column. Furthermore, distillation allows for the separation of impurities due to their difference in boiling points. This purification procedure and its results are discussed in detail in the next section.

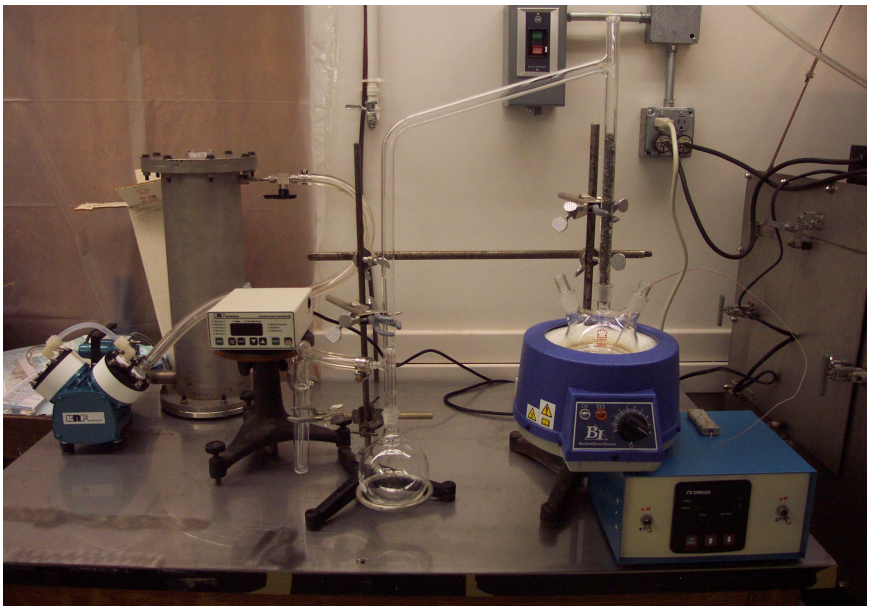

Figure 6.14: Picture of the laboratory distillation system. The temperature controller regulated the mantle heater through a thermocouple which was placed directly into the three-neck flask through a glass nipple which protruded into the liquid. The packing material is visible in the main distillation column. At the top of the column a Hg thermometer was used to measure the temperature at the point in which the vapor is carried into the distillate flask. A condenser was placed after the distillate column and the vacuum pump to keep oil vapors out of the vacuum system.

6.3.8 Distillation

Distillation experiments were performed with the individual components in laboratory tests. Dodecane was used to determine the effectiveness of lead removal and to optimize the operational procedures. Dodecane makes up 80% of the KamLAND LS and is the easist to distill.

The distillation apparatus is shown in Fig. 6.14. The setup consists of a mantle heater which is regulated by temperature controller. The temperature controller regulates the current supplied to the mantle heater by taking reading from a thermocouple which is placed into the liquid via a glass dipstick. To couple the thermocouple to the glass a small amount of Dodecane is placed into the dipstick which protrudes into the oil at the bottom of the three neck flask. The middle neck leads into the main distillation column. This column is packed with SS wool which provides several benefits: 1) The wool helps to prevent rapid boil-over. 2) The SS will act as an adsorbent similar to the surface adsorption experiment performed in Sec. 6.2.4. 3) The wool provides multiple theoretical plates; which means it causes the vapor to re-condense many times before it is carried over into the distillate flask.

A key operating condition which were observed early on was that the purification factor is highly dependent on how fast the liquid is distilled. The slower the distillation process the better. The objective was to keep only small amounts of liquid distilling over into the product flask by monitoring the temperature and flow by eye at the top of the distillation column. Further improvements were made by removing the first 50 cm^3 of distilled liquid. The motivation for this is the observation of the lower boiling points of the organo-metallic compounds compared to Dodecane. Finally, not all of the liquid was boiled. A small amount was left in the bottom of the flask which contained the high boiling point metals and other possible contaminants. Typical operating conditions for distillation of Dodecane were 170 hPa and 160°C. The result for a single distillation is given in Table 6.7.

Successive distillations of Dodecane were performed in series to determine the maximum effectiveness of this procedure. After the third distillation, the measured reduction factors were consistent to within systematic errors. The purification factors achieved from 3, 5, and 7 times distillation were $(2.4 \pm 1.0) \times 10^4$, $(2.5 \pm 2.8) \times 10^4$ and $(2.9 \pm 0.5) \times 10^4$ respectively [127, 128]. The measured plateau in purification factors seen after three distillations is not due to low event rates. However, there could be some procedural contamination which did not allow higher purification factors to be achieved through multiple distillations. While distillation was the best purification method found for removing ^{212}Pb in this work, experimental reproducibility was very difficult. Repeated measurements varied by a factor of 2.

The author contributed to the initial distillation studies which were performed together with colleagues from Japan [129, 130] at The University of Alabama during the summer of 2004. These preliminary measurements resulted in the construction of a larger scale test-bench in Japan, capable of distilling 10 L of liquid at a time [12]. The culmination of all of these measurements and studies resulted in the design and operation of the full scale distillation system in the Kamioka Mine to purify KamLAND. This system will be discussed in detail in the next chapter.

6.4 Adsorption and Desorption of ^{212}Pb from the KamLAND Balloon

The active volume of the KamLAND detector is separated from the buffer oil by a composite balloon made of nylon and EVOH as described in Ch. 3.1. As the balloon is a source of ^{222}Rn and it is further a reservoir for radioactivity which has adhered to its inner surface, tests were performed

[12] This system was designed and purchased by Tohoku University, Research Center for Neutrino Science, Japan.

Cleaning Procedure	Adsorption [%]	Desorption [%]
Acetone, Ethanol, HNO_3	6.8 ± 0.1	2.7 ± 0.2
Acetone, Ethanol,N_2	1.68 ± 0.03	15.3 ± 2.2
Acetone, Ethanol,N_2	1.55 ± 0.03	27.6 ± 1.5 [1]
Acetone, Isopropyl Alcohol,N_2	1.24 ± 0.03	11.4 ± 2.6

[1] Used stirring rod to simulate turbulent flow along the balloon.

Table 6.10: Systematic study of the cleaning procedure for KamLAND balloon samples and its effect on the adsorption and desorption of ^{212}Pb. The addition of a turbulent flow increased the amount of activity lost to the clean LS by the addition of convection as expected.

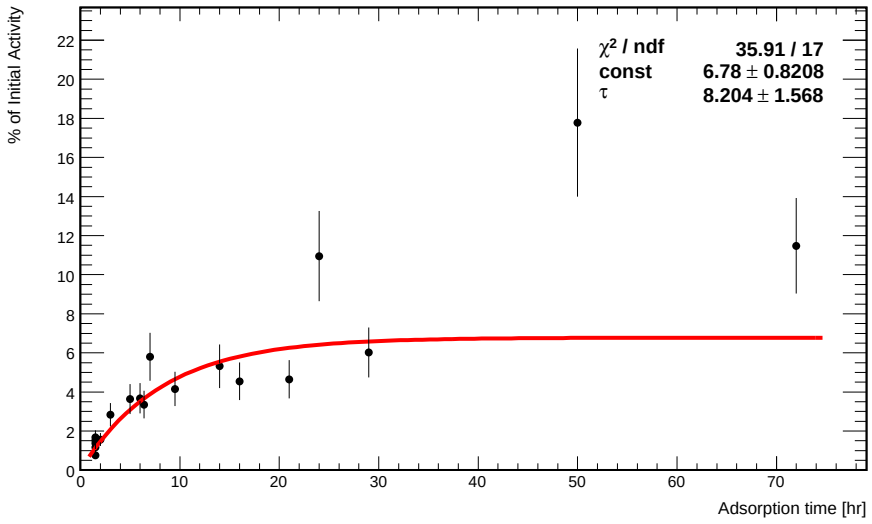

Figure 6.15: Adsorption of ^{212}Pb onto the surface of the KamLAND balloon film. The plotted values include statistical and systematic errors summed in quadrature.

to understand possible leaching affects. The operational conditions of the full scale purification of KamLAND would not permit replacement or cleaning of the balloon. Therefore, these studies were pertinent in determining the possible affects of recontamination after the LS was purified and refilled into the detector.

The balloon film pieces used in these experiments were cut from left over pieces of the original KamLAND balloon. The balloon film was cut into circles with a 25 mm radius. A balloon film geometry calibration was established for the Ge detector to allow for an absolute activity measurement. The general procedure developed for the study of adsorption and desorption from the balloon was:

1. A 125 ml Nalgene Bottle was filled with LS loaded with ^{220}Rn source.
2. The bottle was counted with a Ge detector to determine initial ^{212}Pb activity.
3. A balloon piece was cleaned and then placed into the loaded LS for 1.5 hrs.
4. The balloon piece was removed and all excess LS was pushed to the bottom with compressed N_2. The excess LS on the bottom was dabbed with a KimWipe, and then the balloon piece was dried with a hair dryer and counted on the Ge detector to determine the ^{212}Pb activity.
5. A new 125 ml Nalgene Bottle was filled with clean LS.
6. The balloon piece, with now known activity, was placed into clean LS. A desorption time of 3 hrs was allowed for all measurements.
7. The balloon was removed from the bottle and dried as described in step 4.
8. The LS was counted with the Ge detector to determine its absolute activity and background was subtracted when appropriate.

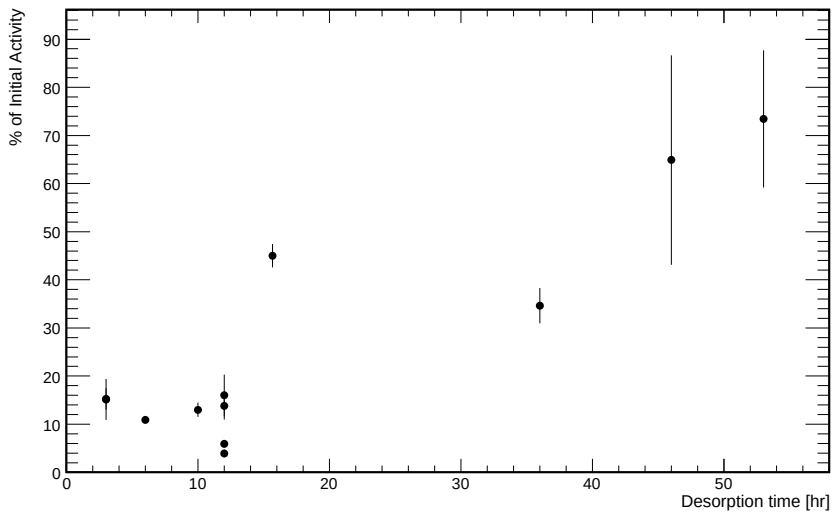

Figure 6.16: Plot of the desorption of ^{212}Pb from the surface of the KamLAND balloon film into clean LS. The plotted values include statistical and systematic errors summed in quadrature.

An in depth study of the systematic error with respect to the procedure is summarized in Table 6.10. This study proved that adsorption of ^{212}Pb onto the balloon does occur. The time constant

for this process is 8 ± 2 hrs, taken from the fit shown in Fig 6.15. The total amount of initial activity that will adsorb to the surface of the balloon was found to be 6.8 ± 0.8 %. A study of the leaching (desorbtion) from the balloon surface back into clean LS clearly shows that leaching does occur as shown in Fig. 6.16. However, the systematic error is 60% due to the low event rate and does not allow a free fit to the data. If only statistical errors are used and the total amount leached is fixed to 100% of the initial activity, a time constant of 111 hrs is obtained.

Chapter 7

KamLAND Liquid Scintillator Purification

During initial filling of KamLAND, the LS was purified using water purification and N_2 stripping procedures [74]. However, while care was taken during the initial purification process, the analysis presented in Ch. 5 showed the resultant background was insufficient to measure ^{7}Be solar ν_e. The largest background contributions were found to be associated with ^{85}Kr and ^{210}Pb decays in the detector. Based on these results Ch. 6 presented the studies undertaken to understand how to remove these trace impurities from the LS. These laboratory studies were instrumental in the design of the large purification system built to purify KamLAND. Furthermore, they provided guidance into the definition of operational procedures for the large scale system. This chapter presents the design and operational conditions of the KamLAND purification system as well as quality control measures which were implemented to monitor the system's performance.

The purification of KamLAND has been divided into two phases. Phase I started on May 5, 2007 and ended on June 16, 2008. The actual LS circulation and purification did not span the entire length of these dates. KamLAND LS was continuously circulated throughout the newly developed purification system and back into KamLAND from May 5 to Aug 1, 2007 [1]. During this period a total of 1500 m^3 of KamLAND LS were circulated and purified.

Phase II was performed after modifications to the purification system were implemented. These were designed to improve its effectiveness and operational capacity. KamLAND LS were circulated

[1] There was down-time incurred during this period associated with pump maintenance, filter exchanges, emergency filling stops and other circumstances related to the safety of the personnel, the detector and the system as a whole.

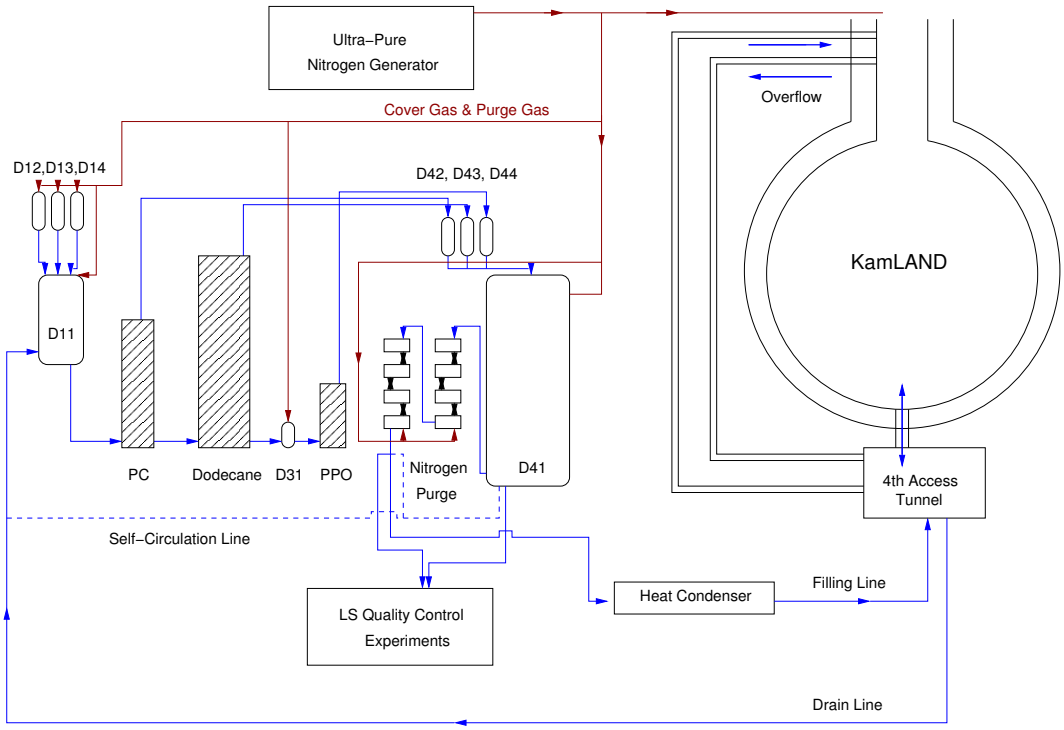

Figure 7.1: Schematic indicating the major components to KamLAND's newly developed purification system. Liquid flow (blue) and ultra-pure N_2 gas (red) flow are indicated with arrows. The dashed blue line denotes the LS flow during a self-circulation mode during which no LS was taken from, or transferred to, KamLAND). The hatched boxes represent the distillation towers while all boxes with rounded edges are holding tanks. Filling was performed top-down and bottom-up as represented by the double arrows at the bottom of the KamLAND detector. This figure is a general representation and is not to scale. The subsystems themselves are highly complex and the simplification is meant only to provide a succinct overview of the purification system.

continuously from June 16, 2008 until Feb 6, 2009 in which approximately 3600 m^3 was purified. This volume constitutes approximately 3 full volume exchanges. In total, the two phases purified more then 5000 m^3 of LS, or the equivalent of 2 Olympic size swimming pools. While the total volume may seem insignificant, the level of radio-purity reached with this liquid is among the purest reported in the scientific literature, and by sheer volume is unmatched by any known facility. Furthermore, the purification system was operated in a remote mining facility, 1 km underground in the Japanese Alps.

7.1 Purification System Design and Operation

This section will describe the major components of KamLAND's purification system, depicted in Fig. 7.1. It consists of three distillation towers, two N_2 purge towers, an ultra-pure N_2 generation plant, a water purification system, and subsidiary LS quality control systems. Building and shake-down of the purification system took approximately one year. The distillation system was built by Mitsui Engineering & Shipbuilding Company, LTD. (MESCO). During construction, the purification system was regularly cleaned and the engineers and workers were monitored my KamLAND experts to ensure adherence to cleanliness standards.

Major purification system components and their positions in conjunction with flow lines are indicated in Fig. 7.1. In general, the LS was drained from KamLAND, sent through the purification system and filled back into KamLAND. Manipulation of the LS density and temperature between purified and unpurified LS established a layering effect to minimize mixing.

When draining LS from KamLAND, it was sent to a 0.5 m^3 holding tank (D11) before entering the first distillation tower. D11 was used to add new Dodecane and PC to the system to make-up for lost components and manipulate the final LS density. PC has a high vapor pressure (0.28 kPa at 25°C) resulting in some loss to the vacuum lines [2] while Dodecane was primarily lost during PPO distillation.

Return lines from KamLAND to D11 were further equipped with sampling ports such that measurements of KamLAND's LS composition, radio-purity, and optical properties could be performed with the subsidiary systems discussed in Sec 7.2. The total amount of PC and Dodecane added to KamLAND during both stages of purification was less then 1% by volume. Fig. 7.2 is a picture of the distillation area and shows the positioning of the components discussed below.

From D11 the LS was sent to the first distillation tower. Table 7.1 provides the operating conditions of distillation towers. The PC was distilled first, as it has the lowest boiling point of all the components. The denser, higher boiling point liquids are then transferred to a second distillation tower to separate the Dodecane from the PPO. As Dodecane makes up 80% of the LS by volume this was the largest of the three distillation towers. PPO has the highest density and can be removed by taking the liquid from the bottom portion of the distillation tower. However, this liquid is still composed of approximately 25% Dodecane and could not be immediately transferred to the PPO distillation tower.

[2] The vacuum line drains typically contained a mixture of oil and water. They were monitored regularly to check for inconsistencies in operational conditions. Furthermore, the mass of PC lost was measured for accountability.

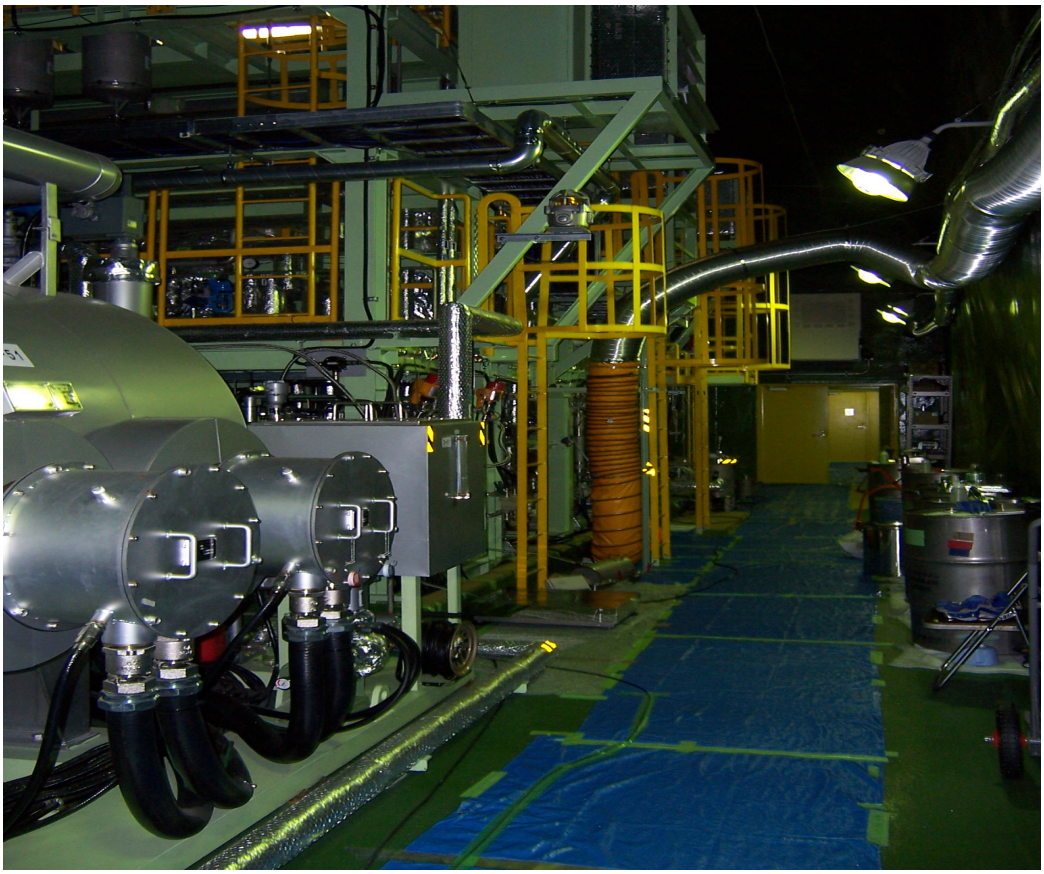

Figure 7.2: KamLAND's distillation and N_2 purge facility. The object in the foreground is the boiler system used for heating all the lines and supplies steam to the PC and Dodecane purge towers. The PPO tower uses heated oil instead of steam for distillation. Immediately behind the boiler tank begins the three stages of distillation with PC, Dodecane and then the PPO tower. At the end, before the fist set of yellow doors, are the N_2 purge towers. Inside the first set of yellow doors are two 20 m^3 tanks (D41-A and D41-B) used for mixing the purified LS. Through the second set of yellow doors is a class 10 clean room. This is were all the quality control measurements took place.

Due to the large amount of dissolved Dodecane, the PPO-Dodecane mixture was directed into a self-circulation loop equipped with a secondary heating and distillation system. This is a closed loop system in which the same liquid makes multiple passes through a small boiler to concentrate the PPO. The density of the liquid in this circulation loop was monitored and the distillate was sent back to the Dodecane tower. Through proper temperature and flow control the final PPO mixture was further condensed to contain approximately $5 - 10\%$ Dodecane by volume.

As indicated in Table 7.1, there are large differences in the operating temperature and pressure of the Dodecane and PPO towers. These conditions made it impossible to supply a continuous feed

Purification System Component	**Pressure [kPa]**	**Temp. [°C]**
PC Distillation Tower	2.000 ± 0.0016	62.4 ± 1.9
Dodecane Distillation Tower	2.000 ± 0.0032	96.9 ± 0.8
PPO Distillation Tower	0.600 ± 0.0029	174.8 ± 1.2
N_2 Purge Tower A and B	40.0	29.0 ± 3.0

Table 7.1: Purification system operating conditions. The distillation tower's temperature and pressure are measured at the top of the tower. These parameters are controlled to within 1%. They are optimized to minimize degredation in optical properties from oxidation. The N_2 purge towers were kept under partial vacuum to keep ^{222}Rn out of the system and to pump on the N_2 purge gas. The N_2 had a flow rate of approximately 30 Nm^3/h. The total circulation speed of the system was 1.2 m^3 of LS per hour.

of the PPO-Dodecane mixture to the PPO distillation tower. Transferring only a minute amount of this liquid caused the dissolved Dodecane to vaporize immediately. As a result, the vacuum pressures fluctuated rapidly and the force from the vaporized Dodecane propelled liquid PPO into the vacuum line. At one point during shakedown, the transfer of the liquid resulted in more then 20 kg of PPO getting stuck in the vacuum system. This shut down the entire operation for a month until the vacuum lines and pumps could be cleaned.

This description provides a brief picture of the difficulties encountered when separating two components with very different characteristics, especially when one of them is a solid at room temperature (PPO liquefies at 75°C at STP). As a solid PPO cannot be carried through the system. After it has been liquefied and then re-solidifies the PPO is no longer in its original powder form and becomes extremely difficult to handle. All lines which carried PPO had to be heated with steam to ensure it never solidified and special care was taken around joints where heat loss was greatest due to the conductive metal scaffolding. In the end, the most ideal case for the purification procedure was to distill PPO in a batch mode. The optimal operating parameters where found to keep the Dodecane from rapidly boiling and this further required at least 25 kg of PPO in a reserve tank to sustain the continuous LS flow rate to/from KamLAND. While the PPO system operated in batch mode the entire process was continuous.

After decomposing the LS through distillation, all three distillates where transferred to holding tanks (D42, D43, and D44). From these tanks the components were mixed in the appropriate proportions in the 20 m^3 tank (D41-A). Dodecane and PC where continuously fed from the holding tanks into D41-A and periodically PC and PPO where mixed and fed into the D41-A to provide the

correct PPO concentration. The PC/PPO mixture was necessary to dissolve the PPO and keep it from clumping or obstructing the transfer lines. The density of the liquid in D41-A was monitored and samples were taken directly from this mixing tank for quality control measurements during shake-down procedures.

A very important parameter identified during shakedown was the residence time of the LS in the D41-A mixing tank as it affected the measured ^{214}BiPo rate. This is due in part to leaks in the system but is also due to ^{222}Rn out-gassing from the SS components. The sheer volume of the system, and the low specific activity requirements for ^{222}Rn, resulted in D41-A to be filled with $1-2$ m^3 of LS. This provided the minimum residence time before the the LS would be sent to the N_2 purge towers to remove the ^{222}Rn. This LS handling procedure minimized the build-up of ^{210}Pb in the LS.

From D41-A several options could occur:

1. The LS was sent to the clean room where quality control measurements were performed.
2. The LS could be returned to D11 for a second purification. This was the "self-circulation" mode.
3. The LS was sent into the N_2 purge towers.

From the N_2 purge towers the first two options where again possible and during testing option 2 was the nominal operational mode. It was also possible to send the LS down to the third access tunnel and back to D11 to test the operational conditions of the heat exchanger.

The ambient temperature in the purification area was $20-25$°C and the LS leaving the purge towers had approximately the same temperature. In order to place the LS back into KamLAND the LS had to be cooled. When filling from the top the LS had to have a minimum temperature of 15°C to match the LS temperature at the top of KamLAND and when performing bottom filling, the LS had to be cooled to < 10°C.

To cool the LS, the temperature was first reduced by a rudimentary heat transfer system which simply ran mine water over approximately 50 m of the SS filling line. This reduced the LS temperature to approximately 15°C (the temperature of the mine water) and then a heat exchanger was used to further reduce the LS temperature below that of the mine water. Once all of the system operating parameters where optimized, and every quality control tests was passed, the final valves after the heat exchanger were opened and the LS was returned to KamLAND.

7.1.1 Pre-Purification of New PPO with Water Extraction

PPO was purchased [3] during purification from both Packard [110] and Dojindo [131]. Dojindo's manufacturing process supplies 25 kg per month and large orders required a 3 month lead time. This caused delays in purification as the immediate need for large amounts of PPO was unforeseen. The first purchase encompassed 75 kg of PPO and was used to provide a small buffer for a batch mode operation and replace degraded PPO. The total amount of new PPO added to the purification system over both phases was on the order of 300 kg.

Before adding new PPO to the purification system it was purified with water extraction to reduce its intrinsic ^{40}K concentration. 10 l of purified water from Super-Kamiokande [132] was mixed with $20 - 25$ kg of PPO in a clean-room at Tohoku University. The mixture was heated to 80°C in a large SS container and stirred by hand. Afterwords, the mixture was left to settle and the water was siphoned off the top. This procedure was repeated 5 times, each time with fresh purified water. The final batch of PPO was left on the heater to remove as much water as possible. Finally the PPO was left to dry and was shipped to the mine.

Before adding the PPO to the purification system it was again liquefied using heating tapes. Due to the large amount of PPO being added to the purification system at a single time (typically more then 50 kg) it was added directly to the bottom of the PPO purge tower. Ideally the PPO would have been mixed at a high concentration with PC and sent through D11 to minimize contamination from contact with the environment. However, this procedure would have increased the PC concentration in the final LS too much and it would have taken a long time build up $50 - 100$ kg in the PPO distillation system with a LS flow rate of 1 m^3/hr. Instead filling was performed directly into the distillation tower. Care was taken to minimize the exposure of the PPO and the distillation system to air. As the distillation system was under partial vacuum, the liquid was easily pulled into the containment vessel. Extreme care had to be taken to ensure no air was sucked into the vacuum system as this would build up the oxygen concentration in the PPO and resulted in brown PPO. While the new PPO still contained a significant amount of water, the heat media [4] was not supplied to the PPO until after the water had been removed.

[3] PPO is also called DPO since the chemical name is 2,5-Diphenyloxazole.

[4] PC and Dodecane could be distilled using heat transfer from steam. PPO required heated oil to reach the appropriate temperatures.

Figure 7.3: KamLAND N_2 generator. Supplied 40 Nm^3/h of ultra-pure boil-off N_2 gas to be used in the purification system.

7.1.2 Ultra-Pure Nitrogen Supply

One of the most important aspects of a successful purification campaign was the ability to supply large amounts of ultra-pure N_2 gas. N_2 gas was used to maintain positive pressure in all the holding tanks to minimize the effects from small air leaks which supply ^{222}Rn. Most importantly the ultra-pure N_2 gas was used as the stripping/carrier gas in the purge towers. The purge towers removed ^{39}Ar, ^{85}Kr, and ^{222}Rn from the LS. The effectiveness of purifying with a carrier gas is directly proportional to its radio-purity.

As a secondary method for purging the LS, a small N_2 gas flow was introduced into the distillation towers to mimic the effect seen in the laboratory. In the purge towers the vapor phase of the liquid is ideal for stripping gasses from the LS components. However, this form of gas purging was only performed on the PC and Dodecane and was not a constant process due to the extreme difficulty in maintaining vacuum conditions.

Ultra-pure N_2 gas was also used to provide a cover gas to the neck region of KamLAND. In the neck region, close to where the purified LS is being filled, there are many pipes and feed-feedthroughs

for cables making it susceptible to air leaks. The ultra-pure N_2 gas was sent to the neck as a cover gas to minimize contamination of the purified LS. During the second phase, a tent was constructed to encase the entire upper portion of the detector. This volume was then filled with N_2 gas to further inhibit contact with airborne radioactivity.

Lab experiments showed N_2 stripping of ^{222}Rn increased exponentially in effectiveness with the volume of N_2 supplied to the system. It was therefore advantageous to sustain as high a ratio of ultra-pure N_2 gas to LS in the purge towers as possible. Furthermore, the system needed to supply all the other areas with N_2. To meet these requirements an industrial system was designed and built by Air Water Inc. [133].

Fig. 7.3 shows a picture of the ultra-pure N_2 production facility in the mine. Air is taken from the radon free air system [5], CO_2 and water are removed, the air compressed and cooled until condensation occurs. The liquid N_2 is then stored in a 0.668 m^3 dewar. The dewar is continuously supplied with liquid N_2 and maintains a volume of approximately 0.45 m^3. This in turn supplies 40 Nm^3/h of boil-off N_2 gas to be used in the purification system. There is a 5 Nm^3/h reserve which would provide stability to the purification system for short interruptions but would only last for two hours.

Tests were performed to determine the optimal N_2 flow rates and LS volume transfers in the purge towers. Operation of the N_2 purge tower was performed in a top down process in which the cleanest N_2 was first exposed to the LS leaving the towers. The supply of N_2 gas to the top of KamLAND was the second largest consumer of ultra-pure N_2 using 2.7 Nm^3/h during purification. This value was reduced by a factor of 8 after purification and N_2 was supplied by boil-off from commercially available liquid N_2 dewars. 30 Nm^3/h of ultra-pure N_2 was supplied to the purge towers and the remaining N_2 was used as a cover gas in all of the LS holding vessels.

7.1.3 Measurement of N_2 Gas Purity

The specific activity of ^{222}Rn in the ultra-pure N_2 supply was measured directly using an electrostatic collection method to measure the alpha particles from the ^{222}Rn daughters [134]. Sampling N_2 from the 0.668 m^3 dewar, a limit was set of < 23.1 $\mu Bq/m^3$ at the 68% C.L. [6] This measurement shows that the reduction in ^{222}Rn by the N_2 system was almost 6 orders of magnitude, as the typical

[5] Radon free air is just air which is pumped into the mine from outside. The ^{222}Rn in the mine is typically two orders of magnitude higher then outside and this is why it is "radon" free air. There was no ^{222}Rn removal at this stage and the air contains typical natural abundances of ^{222}Rn.

[6] The absolute value for this measurement was 12 ± 11 $\mu Bq/m^3$.

Measured Position	**CO**	**CO_2**	**CH_4**	**C_nH_m**	**H_2**	**O_2**
N_2 Supply Line	0.02	< 0.01	< 0.01	< 0.01	1.95	0.57
N_2 Storage Tank	0.02	< 0.01	< 0.01	< 0.01	0.80 ± 0.48	0.52 ± 0.03
	^{Nat}Ar	**He**	**Ne**	**^{Nat}Kr**	**^{222}Rn**	
N_2 Supply Line	0.03	16.78	57.58	< 0.02	12 ± 11	
N_2 Storage Tank	0.03	6.24 ± 4.74	26.24 ± 13.57	NA	NA	

Table 7.2: Measured contaminant concentrations in ultra-pure N_2 gas. All measured values are in ppm except for ^{222}Rn which is in μBq/m^3. The N_2 supply line was only measured one time while the values from the storage tank represents an average of 3 measurements over a period of 4 hours. The Kr concentration was measured only for the supply line at a later time.

^{222}Rn concentration in the air supply is 10 Bq/m^3. A direct measurement of the ^{222}Rn in the N_2 line throughout the purification area provided a way to leak test the N_2 line. The ^{222}Rn concentration in the mine air is typically $1 - 0.1$ kBq/m^3.

Noble gasses and other contaminants were measured in the N_2 supply line and containment vessel by the manufacturer. These values are provided in Table 7.2. The measured values of Ne, He and H_2 are consistent with their natural abundances in air. This is to be expected as they all have boiling points 100 degree lower then N_2 and therefor are never condensed.

Of all the gasses listed in Table 7.2 O_2 and Ar have the closest boiling points to N_2 (-182.95, -185.85, -195.79 °C respectively) and have a sizable natural abundance [7]. The O_2 concentration is monitored on a daily basis to provide a measure of the N_2 gas quality assuming the other measured values are directly proportional to the O_2 concentration. The ratio of N_2 to O_2 in the air is approximately 4 : 1. Therefore, O_2 measurements on the ppm level in the N_2 supply line imply at least 6 orders of magnitude reduction in O_2, consistent with the ^{222}Rn measurement. The O_2 concentration in the N_2 supply varied between $0.4 - 1.2$ ppm during the entire operation of the purification system.

7.1.4 Purification System Operations and Control

The purification system was monitored and operated 24 hours a day with a minimum of 2 people per shift and 3 shifts per day. MESCO provided the engineering and implemented a prototype monitoring software. The software was later modified to fit the specific goals of KamLAND. A screen-shot of the

[7] The important contaminant in the N_2 gas is the Ar and Kr which contain the ^{39}Ar and ^{85}Kr isotopes. However, 10 ppb concentration limits on Ar and Kr result in negligible amounts of the radioactive isotopes due to their extremely small natural abundances.

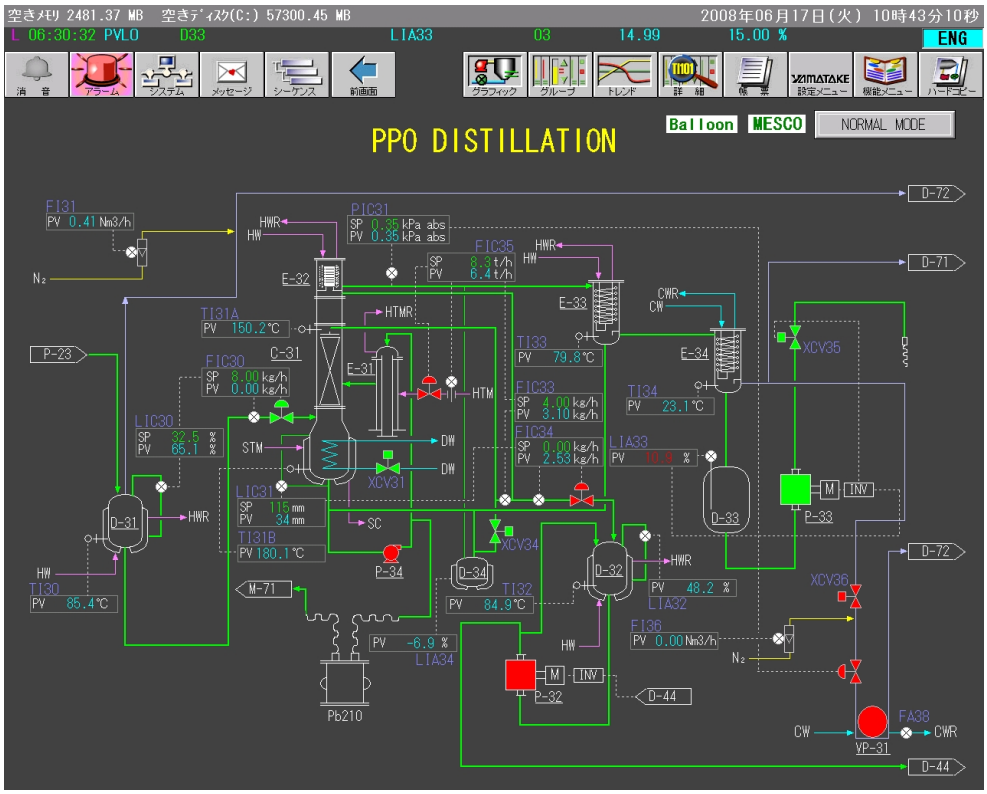

Figure 7.4: Screen shot of the PPO distillation system's monitoring software. Each major purification system component has a designated screen which provided instantaneous updates of the purification system's condition. Other important slow control values were also integrated into this system such as the total balloon weight and BO temperatures.

monitoring software is provided in Fig. 7.4, depicting the PPO distillation page. Each component of the purification system had a designated page from which all the operating parameters could be controlled and monitored. Parameter values were updated every second. To provide the ability to perform off-line analysis of the system's operating conditions and correlate these conditions with KamLAND data, approximately 100 essential parameters were written to a text file every minute.

The nominal operating conditions for the distillation and N_2 purge towers are provided in Table 7.1. All operational conditions and LS flow rates were regulated to within a fraction of a percent. The density of LS transferred to KamLAND was controlled to within 0.1%. The entire process was rigorously monitored and small deviations from any parameter would initiate an alarm on the control PC.

While radio-purity of the KamLAND LS was the ultimate goal, the first priority was the safety of KamLAND collaborators and the detector. Handling and distillation of large amounts of flammable

liquid underground poses a considerable risk, as fires underground are a potentially deadly possibility and spills present an environmental hazard . Specific operational conditions were watched very closely as they represented safety hazards, such as the flow rate to and from KamLAND, distillation tower pressures and temperatures, and flammable gas concentrations in the purification area. If any of these parameters went out of their allowed bounds, the monitoring software would trigger a system shut-down. Furthermore, if the shift members determined the operating conditions were unsafe for any reason, a manual override could be activated to stop flow to/from KamLAND and shut-down the purification system. While a few incidents provoked precautionary shut-down procedures the entire purification went without incident.

Start-up of the purification system and the initiation of flow to/from KamLAND was a very delicate procedure. The situation in the control room during the start-up of the second phase of Purification is shown in Fig. 7.5. The procedure required the opening and closing of manual valves in several locations throughout the mine. Each operation was observed by at least two people to verify the condition of each valve. The flow control during this process was further monitored and controlled by operators at three different control computers. Before any LS flow to KamLAND was initiated emergency shut-down procedures were tested by forcing the system to operate in a manner which would trigger the closing of valves to inhibit all flow from or to KamLAND. After all of these conditions were checked the final valves were opened. The LS flow to KamLAND was increased gradually to provide further safety precautions. The entire process took several hours to complete.

Flow to/from KamLAND was performed in two different operational modes. The first method was to fill LS to the top and remove LS from the bottom. During this process, the LS level was initially filled to the over-flow pipe in the neck of the detector, see Fig. 7.1. After levels reached the over-flow line, the LS was drained from the bottom of KamLAND. There was always a small amount of over-flow LS returning to mix at the bottom of KamLAND and sent back into the purification system. This operating condition provided the best control of the system and minimized the dead space in the neck of the detector where the LS was exposed to the cover gas.

The second operation mode pumped LS in reverse (bottom-up filling), filling from the bottom of KamLAND such that the liquid would rise to the over-flow line. This over-flow line was then used as the return line to the purification system. This allowed the same LS volume during both top-down and bottom-up modes, minimizing variations in operating parameters.

Figure 7.5: Purification control room during the start of Phase II of purification. Opening the valves between the purification system and KamLAND required manual checking their condition by at least two people. Once all the manual valves were opened the procedure was ramped up, supplying only small amounts of purified LS to KamLAND. There were four PCs used for monitoring the flows and conditions of KamLAND, recording operating parameters every second. The author is at the top of the figure in the white t-shirt sitting at a control computer.

7.2 Quality Control of the Purified Liquid Scintillator

Before the onset of the first phase of purification, the KamLAND collaboration took several measures in designing small scale systems to examine the quality of the LS which would be produced by the purification system. The goals for these control measurements were very ambitious, as the precision needed to constrain the radio-purity and optical quality were very stringent. The auxiliary systems were designed to measure specific activities of ^{222}Rn at the level of mBq/m^3, ^{85}Kr to μBq/m^3 and to design detectors which monitor the optical properties, light yield and attenuation length, to within a few percent uncertainty. This section provides a brief description of all the measuring systems and details will be provided for the measurements performed by the author. All other detectors are

the subject of a masters thesis and can be found in the appropriate work[134, 135, 136]. All of the quality control systems were located in a class 10 clean-room at the back of the purification area unless otherwise noted.

7.2.1 ^{222}Rn Measurements

^{222}Rn is not a background in the solar neutrino region, the ^{210}Pb daughter lives 22.3 years and eventually decays by beta emission to ^{210}Po. It is the ^{210}Po decay that, when quenched, has a mean energy of 0.26 MeV and lies inside the solar neutrino energy window. ^{222}Rn is generated by outgassing from construction materials containing ^{238}U and exists in large concentrations in the mine atmosphere, see Sec. 7.1.3. Thus, ^{222}Rn measurements of LS provide a means of determining leak rates for different purification system components.

To establish a baseline, ^{222}Rn levels were measured in the purification area every hour. Radon free air was supplied to the purification area, however, fans were used to disperse organic vapors from the air. This caused a pressure difference which could not be compensated for by increasing the radon free air supply subsequently allowing the mine-air to fill the room. ^{222}Rn specific activities of $0.1 - 1$ kBq/m^3 of air were measured in the purification area. Test were then performed by varying the ^{222}Rn concentration in the purification area and measuring the specific activity of ^{222}Rn in LS.

There were two detectors designed and operated by Tohoku University to measure the specific activity of ^{222}Rn in the purified LS. The first was referred to as miniLAND [136] and was a 0.5 m^3 scintillation detector composed of sixteen independent acrylic tanks. Each tank had was $100 \times 22 \times 17$ cm and was composed of 5 cm acrylic sheets. The boxes were then stacked in a 4×4 grid and surrounded by another acrylic layer and a 3 mm Cu box which was purged with N_2 to remove ^{222}Rn from the air. Finally, the detector was surrounded by a 15 cm outer lead shield to reduce external radiation. The acrylic boxes were coated with 200 μm thick Tyvek, to reflect the scintillation light and increase the light yield.

There were two types of lead used in the shielding around the detector. The specific activity of ^{210}Po for samples of the lead were measured at the University of Alabama [108]. Low background lead from Germany with a specific activity for ^{210}Po of 25 Bq/kg and a cheaper lead from Chile was measured to contain 165 Bq/kg. As a result of these measurements, the lower specific activity lead was placed closest to the LS and then the lower quality lead was stacked on the outer layer.

While the final miniLAND system achieved a sensitivity on the order of 10 mBq/m^3 of ^{222}Rn, this system was not mobile and required designated LS lines to and from the purification system.

Therefore, only LS from D41-A or LS taken after the purge towers could be sampled. This drastically limited the scope of the system. However, after shakedown it provided stable measurements of LS which could be circulated and measured on a routine basis.

The second ^{222}Rn experiment was a portable device which used a PIN photo-diode to measure the alpha particles from the ^{222}Rn decay sequence [134]. This system was very versatile and could be used to measure ^{222}Rn in the N_2 gas line, Sec. 7.1.3, and by modifying the system could further measure the specific activity of ^{222}Rn in LS. Since the system was portable this detector allowed sampling of many different areas along the LS and N_2 flow lines to perform leak tests.

When extracting the ^{222}Rn from LS, the LS was bubbled with a N_2 volume 25 times that of the LS which was 1 l. The carrier gas was sent through an oil trap cooled to -40°C to remove oil vapors immediately after bubbling. Then the N_2 gas was sent into a molecular sieve trap cooled with liquid N_2 to freeze out the ^{222}Rn from the gas stream. Once the ^{222}Rn was trapped, vacuum was pulled on the detector and trap line and the ^{222}Rn trap was heated. A small amount of N_2 was used to push the ^{222}Rn from the trap into the detector. The total detection efficiency was calculated to be 10% for this detector. The final LS system used 1 l of LS and had a sensitivity of 10 mBq/m^3 which provided a cross-check of the miniLAND system. When measuring ^{222}Rn in the N_2 gas stream the sensitivity was increased by three orders of magnitude.

7.2.2 ^{39}Ar and ^{85}Kr Measurements

Development of a ^{85}Kr measuring system was essential for a prosperous purification campaign. As such, a detector was designed by collaborators from Caltech, with the intention of measuring the specific activity of ^{85}Kr with a sensitivity of μBq/m^3 [135]. While ^{85}Kr was the primary gas of interest, it was later found that the same system was highly sensitive to ^{39}Ar. This is due to the multitude of naturally occurring isotopes of each of these noble gasses and their relatively close boiling points.

The final detector design consisted of a trap and release system in which the resultant gas was measured with a residual gas analyzer (RGA). LS was collected in a 5 l bubbling chamber and was continuously sparged with He gas to saturate the He carrier gas with the dissolved gasses from the LS. The saturated He gas was then passed through a molecular sieve cold trap, held at liquid N_2 temperature. Afterwords the trap was heated, releasing the captured gasses into an ultra-high vacuum line (10^{-7} Torr) which was pumped by a turbo-molecular pump. The gas released into the vacuum line was first sent through a titanium sublimation pump to remove N_2 and O_2. Finally, the

gas was directed into a RGA to measure the partial pressures of the gasses as a function of their masses.

The largest background for this detector came from oil vapors which were difficult to remove from the gas line. However, due to the multiple isotopes of argon and krypton, the diversity of mass signals provided a clear signal above the background. The RGA measures the partial pressure and when integrated over the release time, this yields a value that is proportional to the original dissolved gas concentration from the LS. This proportionality constant and the He bubbling efficiency were calibrated using a known volume of air. Under the assumption that the argon and krypton concentrations in the atmosphere are 1.10 ppm and 0.93% respectively, the integrated partial pressures can be used to scale the measurements to a known specific activity of ^{85}Kr and ^{39}Ar.

To enhance the sensitivity of this system, the RGA was operated with an electron multiplier, reaching sensitivities of 10^{-12} Torr. With a five liter sample of LS the detection system achieved sensitivities of 10^{-13}g/g for $^{\mathrm{nat}}$Kr and 4×10^{-8}g/g for $^{\mathrm{nat}}$Ar. This corresponds to a sensitivity of 30 μBq/m^3 of ^{85}Kr and 0.3 μBq/m^3 of ^{39}Ar. This sensitivity was within a factor of 10 of the purity requirements needed for KamLAND and provided an ideal test of the purification system.

7.2.3 Light Yield Measurements

While the radio-purity of the purified LS is an important aspect of quality control and is irrelevant if the LS does not scintillate. The light yield is a measure of the number of p.e./MeV. This quantity is affected by impurities in the LS, oxidation of any of the LS components from heating during distillation, variations in the PPO concentration, or some other unforeseen variable. Therefore, it was important to develop a detector to directly measure the light output of the purified LS before it was put back into KamLAND.

During the first phase of purification a simple detector was developed by the author, which consisted of a single 2-inch PMT, 125 cm^3 glass counting bottles and a commercial ^{60}Co disk source. A CAMAC data taking system was designed using a Fan In/Out, an ADC and a discriminator to collect the ^{60}Co induced charge spectrum. By measuring the position of the ^{60}Co Compton edge in the ADC, changes in LS light yield could be deduced from variations in the mean ADC channel.

In LS measurements the Compton edge is not a true Gaussian with a mean peak energy equal to the expected Compton energy of

$$\mathrm{E_c} = \frac{2\mathrm{E}}{\mathrm{m_e c^2} + 2\mathrm{E}} \tag{7.1}$$

where E is the incident gamma-ray energy and E_c is the electron recoil energy. The Compton edge is defined as the total energy transferred from the incident ^{60}Co gamma-ray to an orbital electron in 180° scattering, producing the maximal energy transfer. This recoil electron produces a prominent spectral feature in the ADC spectrum. LS detectors measure the kinetic energy of the recoil electron not the gamma-ray. Due to the finite size of the LS cell (125 cm^3 bottle) and the rather poor energy resolution of LS detectors, the Compton edge is determined from a Gaussian fit such that

$$\frac{f(\mu + \alpha\sigma)}{f(\mu)} = \frac{2}{3} \tag{7.2}$$

where $f(\mu)$ is a normalized Gaussian function. The factor of α accounts for the shift in the Compton edge due to finite detector resolution. Traditionally 1/2 FWHM is used [78] as a measure for α, however it was shown [137] that the 2/3 point was a more stable measure of the Compton edge for scintillation cells with dimensions on the order of the photon's mean free path.

Using this parametrization the Compton edge can be deduced from a Gaussian fit to the ADC spectrum such that

$$E_c = \mu + \alpha\sigma - \epsilon \tag{7.3}$$

where $\alpha = 0.90052$ is determined from Eq. 7.2 and ϵ is the pedestal measurement. While this is explicitly written in energy, either energy or channel number can be used as they are related by a simple linear transformation. Both quantities are proportional to the deposited charge. The error estimation for the Compton edge must take into account parameter correlations and thus must contain the correlation matrix:

$$\Delta E_c = \sqrt{(\Delta\mu)^2 + (\alpha\ \Delta\sigma)^2 + 2\alpha\ \mathrm{Cov}(\mu, \sigma)}. \tag{7.4}$$

The systematic errors were thoroughly investigated. Each sample was bubbled with N_2 gas before measuring to remove dissolved oxygen from the LS, which affects the light yield. [8] Measurements were performed 10 min after turning on the PMT HV to allow stabilization of the PMT gain. No evidence for time dependent gain shifts were observed for up to 6 hours which was more then 10 times the typical measurement time. The systematic error due to sample preparation and sample placement on the detector was measured to be 2.7%.

For the purification process, only variation in the light yield were relevant. The experimentally

[8] Oxygen is easily dissolved into the LS during the preparation period of the sample.

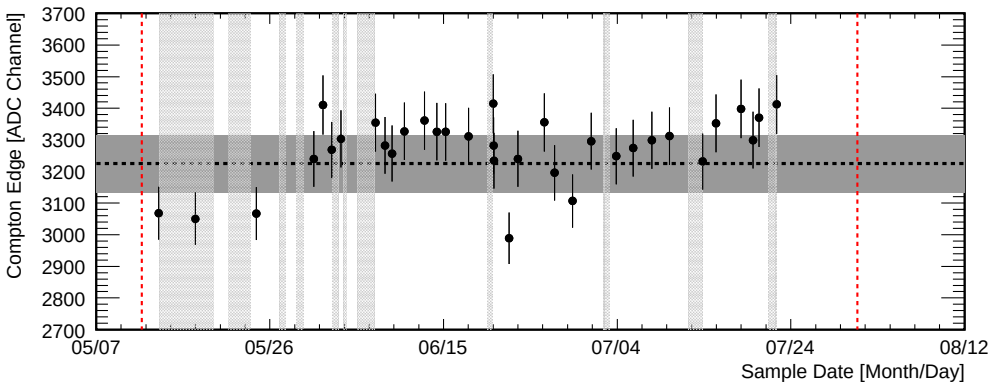

Figure 7.6: Light yield measurements taken with ^{60}Co Compton edge measurements during phase I of purification. The dates represent the day the sample was taken from the purification system. The vertical dashed line is the mean value from LS taken at D11 (from KamLAND) with the grey band representing the 3σ C.L. The vertical dashed red lines are the start and stop of purification and the hatched vertical regions are when the purification had stopped. The errors include at 2.7% systematic plus the statistical errors summed in quadrature.

determined Compton edge for purified LS was compared to a standard of KamLAND LS. This detector was capable of determining light yield changes on the order of 3%.

During the first phase of purification there was no evidence for a loss in light yield, as shown in Fig. 7.6. This figure clearly shows that the light yield is consistent with the mean of 4 samples taken directly from KamLAND during purification. While KamLAND data showed a loss in light yield on the order of 10%, see Sec. 7.3.1, a deviation of this magnitude should have been clearly visible in Fig. 7.6.

Before starting the second phase of purification, a new light yield detector was designed to be more robust and reduce the systematic error to less then 1%. This new detector measured the Compton recoil electron energy from a ^{137}Cs source using two 2-inch PMTs attached to a specially designed acrylic cell. The PMT were at 180° angles to one another and this system was placed at a 90° angle to a NaI detector. The NaI detector was positioned 14 cm from the center of the acrylic cell to measure the scattered photon. The ^{137}Cs source was then centered between the NaI detector and the acrylic scintillation cell.

To reduce background, the DAQ hardware required coincidence with both PMTs and the NaI detector. Requiring a triple coincidence provides a clear Compton peak in the LS instead of the peak plus Compton background seen by the previous detector. Furthermore, both the recoil electron energy

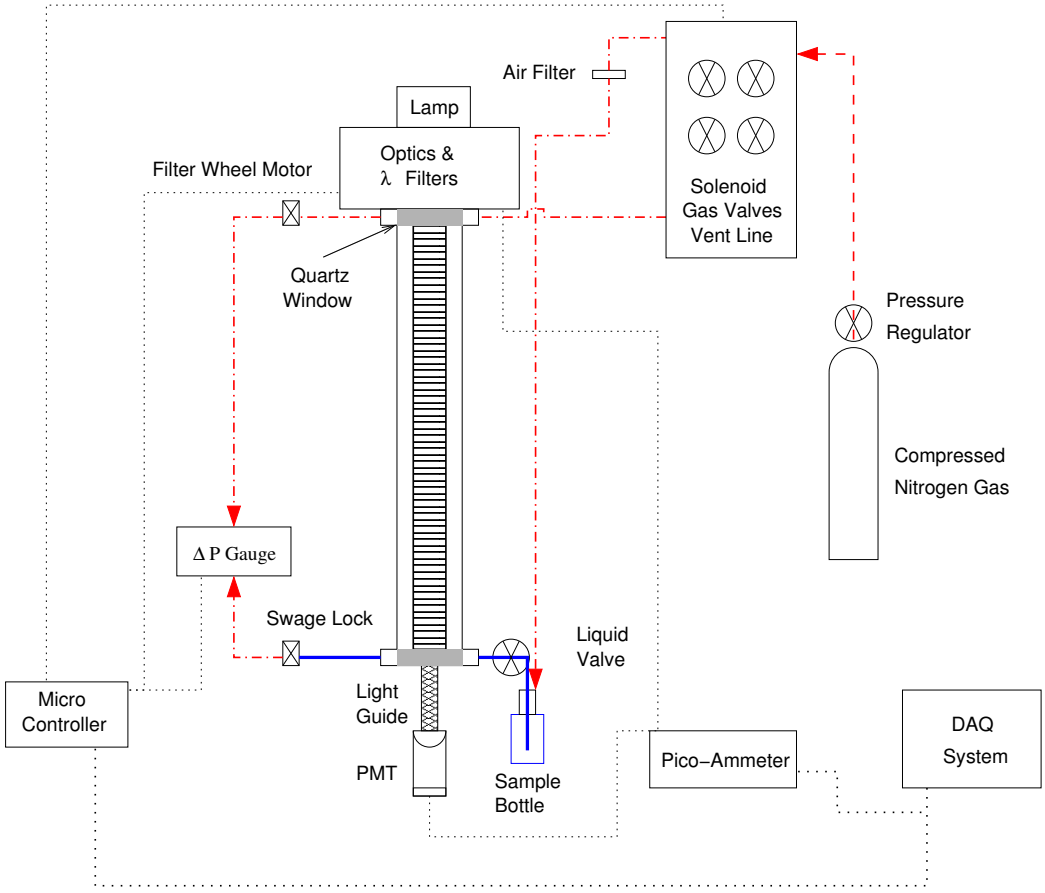

Figure 7.7: Schematic of the detector used to measure liquid light attenuation lengths. The red dash-dot line represents N_2 gas lines, the blue solid line represents the liquid lines and the dashed lines are electrical control lines. The micro controller is programmable and controls the solenoid gas valves, filter wheel and differential pressure gauge. The PMT and photo-diode currents are measured with a pico-ammeter and the entire system is controlled with a DAQ programmed with LabView [138].

and the back-scattered gamma-ray energy were measured. Making cuts on the backscattered gamma-ray energy provides a precise determination of the energy deposited in the LS and its resolution. The resultant systematic error for this system was less then 1%.

7.2.4 Attenuation Length Measurements

When a particle deposits energy in the KamLAND LS, the emitted light must travel through the LS to the PMT arrays on the stainless steel sphere situated 3 - 15 m from an event's vertex. A

1 MeV gamma-ray has a typical interaction length of a 20-30 cm. As the light propagates to the PMTs it interacts with the liquid and undergoes multiple reemission processes which lose energy to non-radiative processes. The totality of these processes are defined as an attenuation length of the gamma-ray when propagating through some liquid. Since the attenuation length is dependent on the composition and the impurities in the LS, it was imperative to measure this optical quantity for the purified LS.

The attenuation length detector [9] used during KamLAND purification is illustrated in Fig. 7.7. This system was maintained and operated by the author and a second UA graduate student, Chris Grant. The optical component consists of a fluorescent lamp whose light is passed through a collimator to create a narrow beam of light 5 mm in diameter. The white light is then focused onto a filter wheel which contains different wavelength filters (313.0, 340.0, 365.0, 379.8, 380.0, 400.0, 405.0, 436.0, 450.0, 500.0, 550.0 nm) to produce a narrow wavelength band ($3 - 10$ nm FWHM). These wavelengths are chosen to lie within the sensitive spectral range of the KamLAND 17-inch PMTs. Inside the filter wheel a blank was used to measure the dark current and a mirror would focus the beam onto a photo-diode to measure the absolute beam intensity through an optical fiber.

After the white light is filtered, the beam is focused onto the column of liquid. At the end of the liquid column was an acrylic light guide which focused the transmitted beam onto the optically couple 3-inch PMT. The inner liquid column is coated with a black liner to adsorb the scattered light such that the light incident on the bottom of the column is fully transmitted light from the original beam.

A micro-controller with programmable logic uses the Max-FORTH [139] language to control the gas and liquid flow. These are programmed as conditional statements based on the read-out of a differential pressure gauge. The differential pressure gauge measures the hydrostatic pressure in the column which in turn translates into a height measurement of the liquid.

LabView [138] was used as the DAQ [10] software which was interfaced with the micro-controller and read-out the PMT's current from a pico-ammeter. Measurement of the PMT current versus liquid height results in an exponential curve with a decay constant equal to the attenuation length of the liquid for a specific wavelength. A single attenuation length measurement took six hours and consisted of the following steps:

1. Move the liquid to some predesignated height and wait 60 second for the liquid to settle.

[9] The detector was donated to the University of Alabama by Byron Dieterle, University of New Mexico.
[10] Written by a UA graduate student, Igor Ostrovskiy.

2. Measure the PMT dark current.

3. Measure the absolute beam intensity with the photo-diode.

4. Cycle through the wavelength filters (313.0, 340.0, 365.0, 379.8, 380.0, 400.0, 405.0, 436.0, 450.0, 500.0, 550.0 nm) and measure the resultant PMT current. The filters to be used in a a run were chosen before starting the measurement.

5. Move liquid to the next height and repeat above procedure. A total of 20 heights were measured.

To reduce the systematic error on each measurement, the heights were broken into an upward and downward liquid motion. Ten points were sampled when raising the liquid in 10 cm steps to its maximum height of 105 cm. The height was then offset by 5 cm and measured in 10 cm steps in a downward motion. This accounts for errors in the differential pressure gauge, height calculation, from pressure changed during a measurement. Furthermore, to reduce the sampling error of the PMT current, each current reading is averaged over a 60 second interval in which the mean and RMS were calculated.

Calibrations are performed on each liquid to establish a relationship between the height and differential pressure. Valves are configured to allow liquid to pass through a transparent line which is situated along a ruler. This configuration is only used during calibrations as the transparent tube would transmit light to the PMT. The DAQ is told to raise the liquid to a specific height and the actual liquid level is measured. This has to be performed for each liquid, and especially when different components are used, as the height conversion is density dependent.

The beam intensity was stable to within 2% and the measured attenuation length for all filter wavelengths was reproduced to better then 1% accuracy for LS, PC, and Dodecane. The photo-diode current and dark current where -1.20×10^{-11} and -2.53×10^{-9} A, respectively. This provided approximately 2 orders of magnitude over which to measure the exponential decrease in beam intensity. A sample of LS taken from KamLAND during the initial filling and a sample of PC where measured regularly over the entire purification phase to monitor long-term effects and diagnose detector problems.

This detector measured an absolute attenuation length for each wavelength filter. However, the attenuation length is wavelength dependent. To better understand the effect a change in light attenuation length has on KamLAND, an effective attenuation length. L_{eff} was calculated by averaging the measured attenuation length $L(\lambda)$ over the PMT quantum efficiency $\epsilon(\lambda)$ and PPO emission

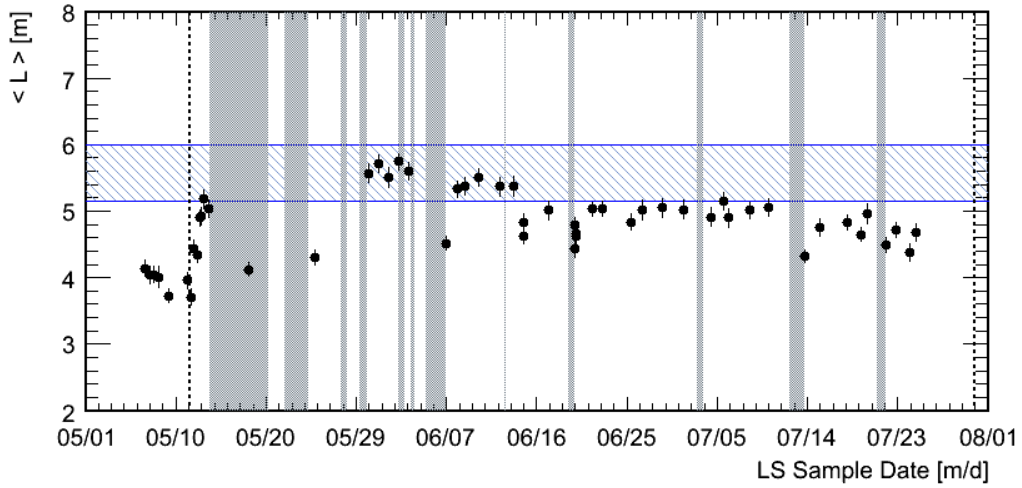

Figure 7.8: Phase I purification measurements of LS average attenuation length. The horizontal hatched area indicates the 3σ C.L. for the measured KamLAND LS. The dashed vertical lines indicate the start and stop of phase one and the horizontal hatched regions indicate down time. This means that no LS was transferred to or from KamLAND and the purification system was in a self-circulation loop.

spectrum $R(\lambda)$, as shown in Fig. 3.2. The effective attenuation length is defined as

$$L_{eff} = \frac{\int L(\lambda)\ \epsilon(\lambda)\ R(\lambda)\ d\lambda}{\int \epsilon(\lambda)\ R(\lambda)\ d\lambda}. \tag{7.5}$$

Fig. 7.8 shows the effective attenuation lengths measured over the first phase of purification [11]. One of the key observations from monitoring the attenuation length can be seen in the first few points in Fig. 7.8 in which there is approximately a 30% decrease in attenuation length. Upon the start of purification, a gradual rise in the attenuation length was observed due to a replenishment of new LS from KamLAND. The maximum point corresponds to the time in which all of the LS from the purification system had been transferred into KamLAND and the new liquid only passed through the purification system a single time.

The conclusion was reached that during self-circulation the Dodecane was losing its transparency. This was thought to be some small oxidation effect which was amplified by the Dodecane making multiple passes through the distillation system. This affect can be seen in Fig. 7.8. The time between stops and restarts of the purification system are correlated with lower L_{eff}. For the LS which was immediately purified and returned to KamLAND, no dramatic loss in attenuation length was

[11] These measurements where the responsibility of UA graduate students: Chris Grant and the author.

observed. The offset observed in the data from June to the end of July is suspected to arise from shifts in the optical alignment of the detector.

7.2.5 PPO Concentration and Density Measurements

During the shakedown of the purification system many measurements were made by the author to calibrate the system's density meters, especially in the mixing tank D41-A. A commercially available density meter [140] was used to measure the specific gravity and density of the purified liquid at 15°C. The error of the density measurements was calculated to be 0.008%. During operation of the purification system, liquid was sampled from different ports to obtain samples for the attenuation and light yield measurements. At this time the density of the liquid was also measured. The density measurements were primarily used to cross-check the purification system read-outs after shakedown.

While the PC and Dodecane concentrations are relatively easy to maintain in a large scale purification system, the PPO concentration was more difficult. A measuring system was developed which used a Gas Chromatograph [12] to determine the PPO concentration in KamLAND with a 1% accuracy. The ratio of integrated mass peaks were used to calculate the PC, Dodecane, and PPO concentrations relative to LS cocktails prepared with known concentrations and measured on the GC. PPO was an expensive addative to the LS and the entire process of PPO purification was rigorously monitored due to the expense and the difficulties associated with distilling this component.

7.3 Quality Control Measurements with KamLAND Data

After the first purification phase many lessons were learned. Two of the most important observations involved a decrease in the light yield which was not seen in the detector, described in Sec. 7.2.3 and an increase in dark rate during filling. This dark rate caused problems with the DAQ and required constant updating of trigger conditions to cope with changing data rates.

Once the first phase of purification was completed a method was developed to calibrate the detector in real time, as described in Sec. 4.5. In-situ calibrations provided the capability to do analysis in real time. On-line monitors were developed to monitor the ^{214}BiPo, ^{212}BiPo, ^{85}Kr, and ^{210}Bi activities as a function of Z-position in KamLAND. As data collection did not stop during purification, these on-line monitors provided invaluable updates on the 2-8 hr time-frames which provided an immediate understanding of the LS purity and optical clarity. The on-line monitors

[12] These samples were shipped to Tohoku University for measurement.

were further equipped with alarms so that non-expert shifters could notify the appropriate personnel immediately.

7.3.1 Light Yield Monitor

The LS attenuation length and the light yield were monitored by small scale systems discussed in Sec. 7.2.3 and 7.3.1. However, due to the size of KamLAND, the detector is extremely sensitive to small changes that may not be observable by the small scale detectors. Furthermore, as previously discussed, an observed deficit was seen in KamLAND after the first purification phase which was not correlated with the auxiliary system measurements. It was therefore important to develop a way to use real-time data to monitor the transparency of the LS in KamLAND.

Analysis of data from the first purification showed that KamLAND's light yield could be monitored using the charge deposit from muons. Muons are a very nice calibration tool in that they do not depend on purification operating conditions and are observed in the detector approximately every 3 seconds. Furthermore, muon tagging is impervious to the small changes seen due to dark rate fluctuations during purification. Their high charge deposit provided a means to monitor the light yield without an energy calibration.

A light yield monitor was developed using the average charge deposited per unit track length in the LS and the BO as described by Eqs. 4.11 and 4.10 . To obtain enough statistics 8 hours of data were integrated. The plots shown in Fig. 4.5 were calculated from on-line reconstructed data. The mean dQ/dx was calculated and added to a time evolution plot as shown in Fig. 7.9. To accommodate possible shifts in the mean dQ/dx from changes in light yield, the total histogram mean and RMS are used instead of Gaussian fit values. This provided a more robust monitor as the two values are directly proportional to one another.

Analysis of phase one purification data, shown in Fig. 7.9, clearly indicates a correlation between dQ/dx and purification activity. The total loss in light yield is $10.4 \pm 0.1\%$ and was consistent with ^{60}Co source calibration estimates. While this figure shows that the dQ/dx parameter could be used to monitor the light-yield, this monitor was not invoked until the second phase of purification.

Fig. 7.10 shows the scintillation charge deposited per unit track length of muons that passed through the active volume ($b \leq 6.5$ m) during the second phase of purification. It can be seen that the light yield of the LS decreased by $9.9 \pm 0.2\%$ over the first month of operation. Much effort went into looking for correlations with purification activities and operating parameters. No purification related activity was found to be associated with this decrease.

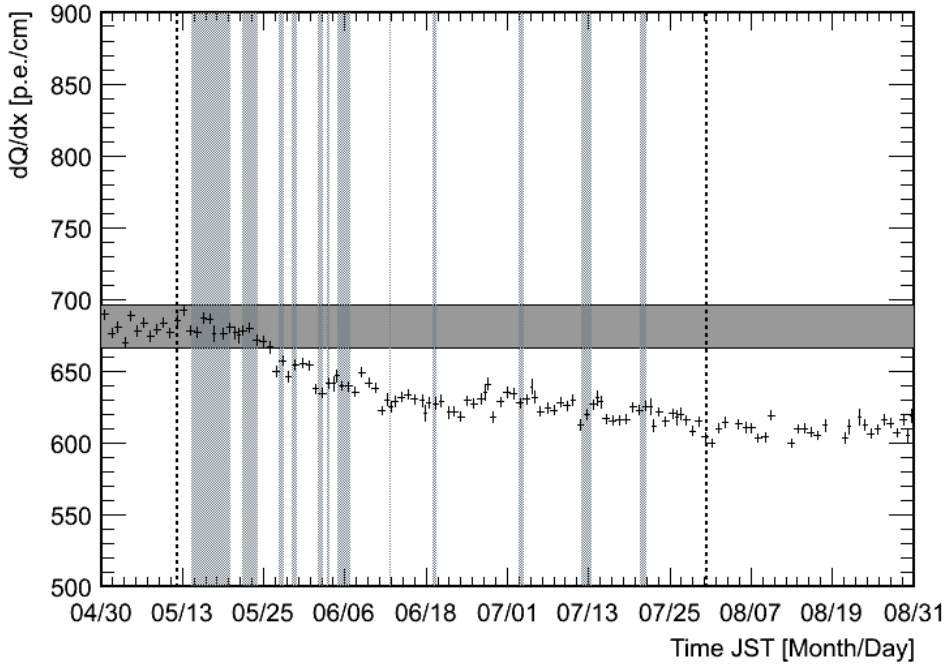

Figure 7.9: On-line light yield monitor showing a decrease in light yield during the first phase of purification. The grey band depicts the 3σ uncertainty of the pre-purification measurement. This figure shows the average charge per unit track length for muons which pass through the LS and clearly indicates a change after the start of purification. The vertical dashed lines indicate the start and stop of the first phase of purification while the hatched regions indicate periods when flow to and from the detector was stopped (self-circulation mode). There is a $10.4 \pm 0.1\%$ overal loss in light yield observed.

While the dQ/dx figures show clear decreases in light yield as a function of time, in order to establish the reason for a decrease in dQ/dx several other diagnostic plots were implemented. These supplementary figures aided in the ability to diagnose if the change in dQ/dx was a DAQ related problem or if it was due to the purification system's operating conditions. The first variable used to associate problems with a particular detector sub-system was the muon rate. Fig. 7.11(a) shows the muon rate as a function of time during the second purification phase. The grey band indicates the 99% C.L. region for pre-purification data and indicates the expected range during normal operating conditions. Changes in the muon rate outside this band were attributed to DAQ problems such as OD-to-ID noise, high voltage problems, VME crate problems, and FBE board problems.

Fig. 7.11(b) shows the average charge deposited by muons which only passed through the BO. Purification did not involve any transfer of oil to or from the buffer region. Therefore this parameter

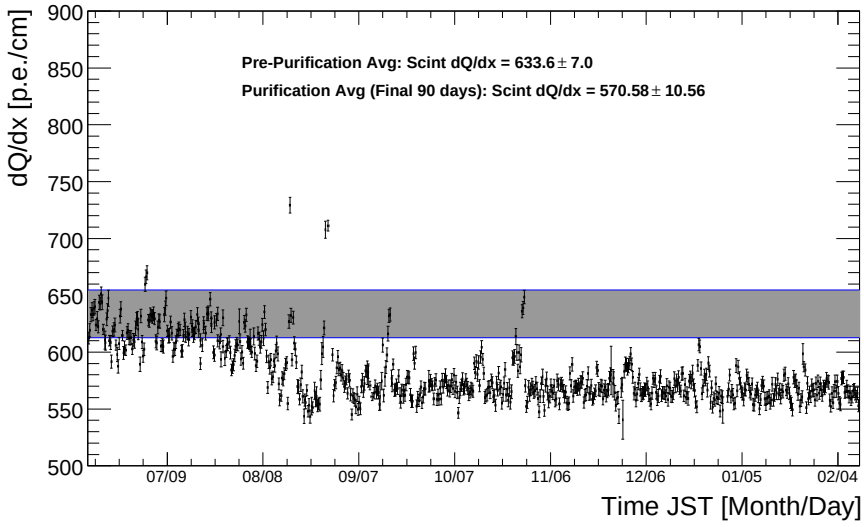

Figure 7.10: On-line light yield monitor showing a decrease in light yield during the second phase of purification. The grey band in all figures depicts the 3σ uncertainty of the measurement before the second phase of purification. This figure shows the average charge per unit track length for muons which pass through the LS and clearly indicates a change in transparency after the start of purification.

should have been a constant. Any large, or long term deviation, would have indicated a leak in the balloon which separates the active volume from the buffer oil or a strong deviation in the volume of liquid in the buffer oil (deformation of the balloon). A balloon deformation would be directly correlated with an increase in the muon rate, as more charge would be deposited on average outside the active volume (b $>$ 6.5 m). A leak would have been a serious problem, and this was the only parameter available in real time to diagnose such a condition.

7.3.2 Trigger Monitor

Purification of KamLAND was aimed at collecting data in an energy interval conducive to observing ^{7}Be solar ν_{e} events. This required lowering the trigger thresholds, as described in Sec. 4.6. During the first phase of purification the dark rate in the detector was observed to increase by more then a factor 5 during purification. This caused problems with the DAQ and required constant monitoring and changing of trigger thresholds.

To better prepare for the second phase of purification an on-line monitor was created to calculate the dark rate every two hours. Notifications were posted to the monitor when conditions were such to require threshold changes. The dark rate was monitored using the 1pps trigger's mean NsumMax as

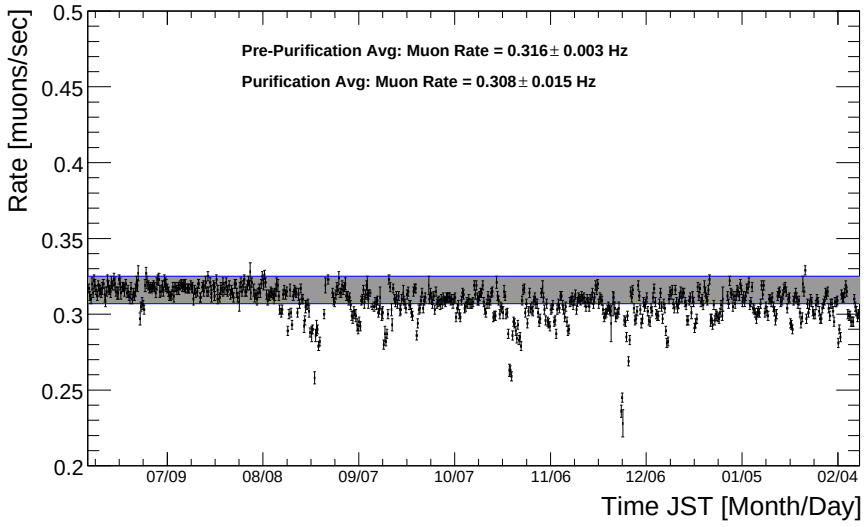

(a)

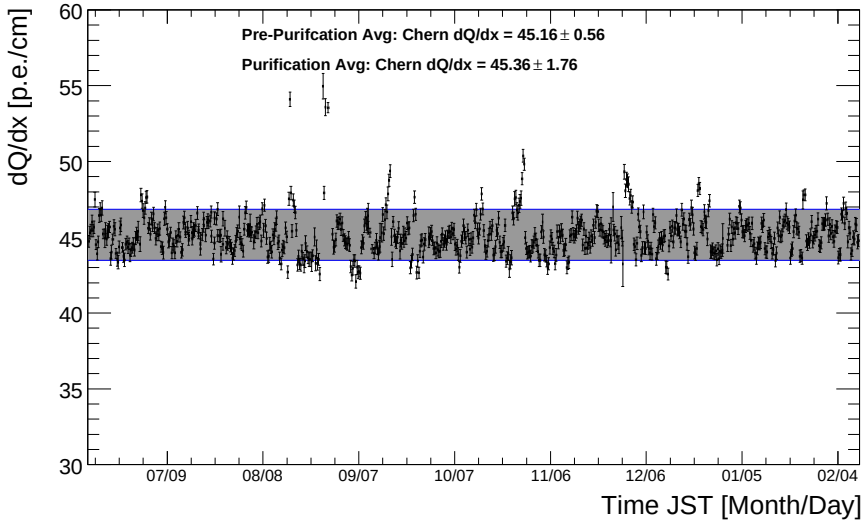

(b)

Figure 7.11: On-line light yield monitor figures during second phase of purification. The grey band in all figures depicts the 3σ uncertainty of the pre-purification measurement. Fig. 7.11(a) shows the muon rate as a function of time. Fig. 7.11(b) gives the average charge per unit track length for muons which only pass through the BOI or BOO region of the detector. This variable should remain constant during purification. Any deviation from the expected gray would indicate a possible change in the balloon shape or a leak in the balloon in which the BOI would begin to scintillate.

a function of time, as shown in Fig. 7.12 for the first phase of purification. This parameter is linearly correlated with the trigger threshold which is based on the variable Nsum, instead of NsumMax. The difference between Nsum and NsumMax is that Nsum is the the number of PMTs over threshold

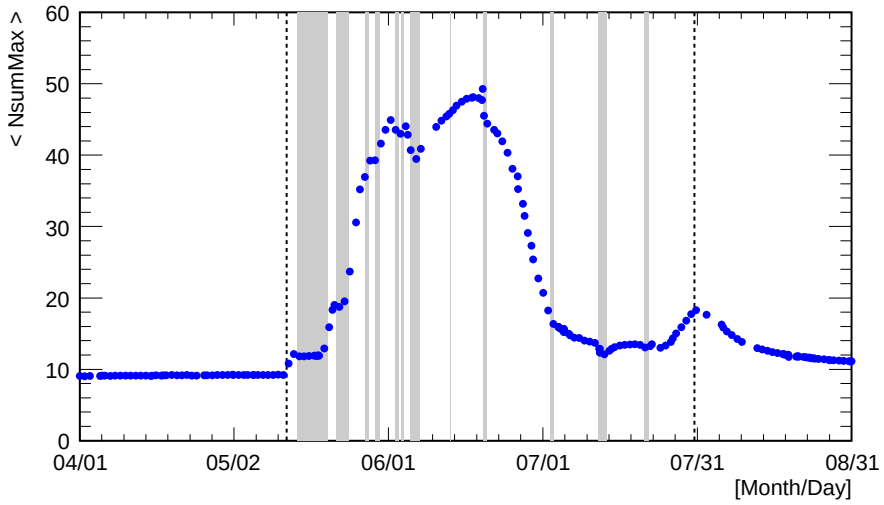

Figure 7.12: Dark rate (1pps mean NsumMax) correlation with LS filling during first the phase of purification. The 1pps trigger mean NsumMax provides a snapshot of the average number of PMTs hit during a 25 ns time-window.

on a single clock tick and is when the trigger issues the acquire command. NsumMax is the largest Nsum in the history trigger record of 200 ns. NsumMax takes into account the situations in which an event's early light will issue an acquire command to the trigger but the late light has more effective charge.

To monitor the trigger, every two hours the difference between the trigger threshold Nsum and the current 1pps mean NsumMax was calculated and compared with a preset value. Such that if

$$|\text{TriggerNsum} - \langle\text{NsumMax}\rangle| > 2, \tag{7.6}$$

the on line monitor would issue an alarm to the shifter. The trigger threshold would the be changed to the appropriate value to account for the dark rate change. This value was typically just that obtained from Eq. 7.6.

While the 1pps mean NsumMax provided a good method for changing the trigger thresholds, this value is not directly related to the increase in raw data rate. The raw data rate depends on the total number of waveforms, which is an integral over all PMT hits in a 250 ns time-frame. For this reason another monitor was developed to analyze the data rates using Nhit which directly related to the data rate. Data rates for the individual trigger types and the total data rates were monitored as a function of time. When the total data rate became too large to handle in terms of data transfer or

storage capacity, the trigger conditions were changed to counteract these extreme conditions. Major changes occurred around the maximum deviation from the pre-purification average, as shown in Fig. 7.12.

Chapter 8

Low Energy Backgrounds in KamLAND After Purification

In the previous sections a full description of the problem in terms of background removal faced by KamLAND has been presented. An in-depth study of the backgrounds associated with making a ^{7}Be solar ν_{e} measurement was provided in Ch. 5. Table 5.1 lists these backgrounds and the required reduction factors needed to observe the elastic scattering spectrum as depicted in Fig. 5.24.

The backgrounds causing trace contaminations were divided into two classes, gasses and metals. While gas purification techniques are understood, the removal of ^{210}Pb from organic scintillator at the concentration of 10^{-18}g/g were unknown. Ch. 6 provides a detailed account of the preparatory studies for removing ^{210}Pb from KamLAND LS. In Ch. 7 the final purification system design was outlined along with its operational modes and the multitude of quality control measures taken to ensure a successful operation.

As the problem and potential solution have been outlined, this chapter is devoted to answering the question: "how effective was KamLAND's purification system in removing the low energy backgrounds." The analysis techniques utilized in this chapter are identical to those presented in Ch. 5 and therefore details will be minimized to focus on the results. Analysis will focus on the determining the effectiveness of the new purification system through consecutive volume transfers. The final section of this chapter will be devoted to quantifying the progress which was achieved by presenting the current sensitivity to ^{7}Be solar ν_{e}s.

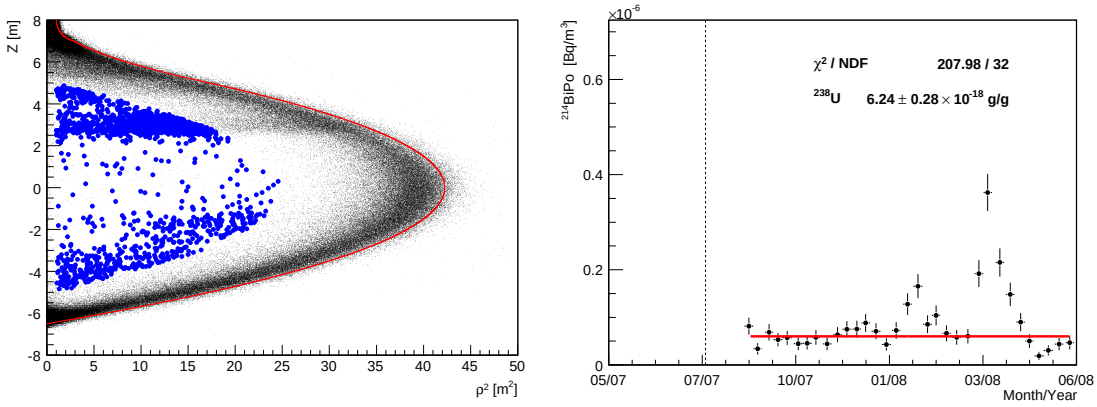

(a) (b)

Figure 8.1: ^{214}BiPo candidate events inside the fiducial cut of R $\leq$ 5.0 m are shown in Fig. 8.1(a) indicating their spatial distribution. The time-dependence of these candidate events is shown in Fig. 8.1(b) with the end of purification denoted by the vertical dashed line. There are two visible spikes in the time distribution which correspond to increases around the extremities of the detector. The central region of the detector is stable.

8.1 After Phase I of KamLAND Purification

During purification the LS contained approximately 10 mBq/m^3 of ^{222}Rn which was unintentional but could be used as a tracer to map out the position of the purified LS. After circulation was stopped, analysis on the effectiveness of purification could not be performed until these short lived backgrounds decayed. Phase I of purification ended on Aug. 1, 2007. The analysis presented in this section covers the period starting Sept. 1, 2007 and is inclusive up to May 16, 2008, yielding a LT of 242 days. Approximately half-way through the analysis period the main physics trigger was changed to optimize the collection of low threshold data, as outlined in Sec. 4.6.

8.1.1 Measurement of ^{232}Th and ^{238}U

The ^{238}U concentration was calculated using the same technique outlined in Sec. 5.1.1. As ^{214}BiPo coincidences are used to quantify ^{238}U, the influence of ^{222}Rn on this calculation makes the analysis difficult. Fig. 8.1(a) shows the spatial distribution of events inside KamLAND. A clear separation of volumes is visible at Z = 3.0 which is consistent with separation between regions seen with the calibration data in Fig. 4.10. The spatial distribution indicates higher concentrations in regions at the top and bottom of the detector.

The specific activity of ^{214}BiPo events inside the FV defined by R $\leq$ 5.0 m was integrated over one week time-frames and is plotted in Fig. 8.1(b). There are small variations from a constant rate seen in the data on one week time-scales, however there are two large increases in the data-set more then 5 months after purification ended. The first increase is observed in January 2008. The excess of events is confined to the upper (Z $>$ 2.0 m) region of the detector. The second, larger variation, begins in March and is confined to the lower hemisphere (Z $\leq$ 2.0 m). These increases can only be attributed to convective zones in the detector which have brought ^{222}Rn from the balloon region into the active volume.

Due to the apparent settling of the LS in the detector, even several months after purification ended, complicates the calculation of the ^{238}U concentration. Three regions were taken to gain some insight into the variation in the detector. A fiducial radius of 5.0 m is used with a 1 m cylinder cut to remove any contributions from the z-axis calibrations. The detector was then split into the one-time and two-time purified volumes, defined by the spatial cuts: Z $>$ 2.0 m and Z $\leq$ 2.0 m respectively. The resultant concentrations in the upper and lower regions are $(7.64 \pm 0.71) \times 10^{-18}$ g/g and $(5.14 \pm 0.30) \times 10^{-18}$ g/g. To find the region with the lowest background, the volume with R $<$ 5.0 m and $-1.0 \leq$ Z $\leq$ 2.0 m is used. The resultant ^{238}U concentration in this region is $(1.92 \pm 0.25) \times 10^{-18}$ g/g and is consistent with the value obtained with pre-purification data.

To estimate the energy uncertainty the ^{214}Bi beta spectrum was fit to Monte Carlo data folded with $8.6\%/\sqrt{\mathrm{E}}$ energy resolution. A linear energy scale factor was allowed to float in the same way as described in Sec. 5.1.1. The resultant systematic error due to the energy scale uncertainty is 1.85%. This is summed in quadrature with the 13% statistical uncertainty to obtain the total uncertainty presented in Table 8.1.

^{232}Th was calculated using the same cuts and methods established in Sec. 5.1.2. There were only 42 ^{212}BiPo events observed in 242 days of LT. Due to the low event rate, fits to the ^{212}Bi beta energy spectrum are not possible. However, all spectra analyzed from Phase I showed similar uncertainties from previous analyses. Thus, the systematic error of 4.92% from energy scale uncertainties obtained from Sec. 5.1.2 is assumed.

Fig. 8.2(a) shows the spatial distribution of events which passed all cuts. There are too few ^{212}BiPo events to discern any non-uniformity and there is clearly no obvious structure at the boundary around Z = 3.0 m which was visible with the ^{214}BiPo data. Further analysis as a function of time required summing data over one month time-frames. The specific activity of ^{212}BiPo is plotted as a function of time in Fig. 8.2(b). A fit to the time-evolution provides a good estimate of the

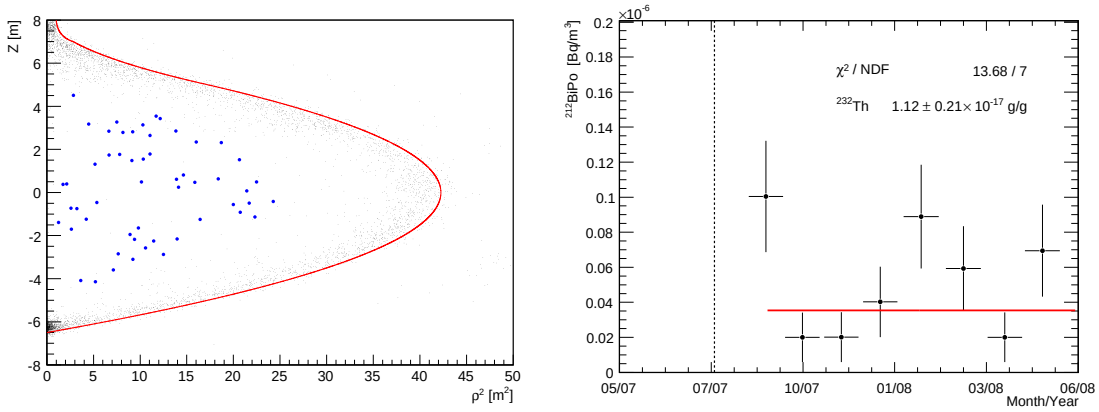

(a) (b)

Figure 8.2: ^{212}BiPo candidate events inside a 5.0 m radial cut are shown in Fig. 8.2(a). The event distribution looks relatively uniform. The time-evolution of these events is given in Fig. 8.2(b). Due to the small event rate, it is difficult to pin down any structure as seen with ^{214}BiPo event candidates.

average ^{232}Th concentration. Adding the energy uncertainty and statistical error in quadrature, a ^{232}Th concentration of $(1.12 \pm 0.21) \times 10^{-18}$ g/g was obtained.

These values are summarized in Table 8.1. The ^{232}Th concentration shows a factor 7 reduction after purification. However, there was evidence provided for a lower concentration of ^{232}Th = $(3.26 \pm 0.72) \times 10^{-17}$ g/g when considering a ^{228}Th background, see Fig. 5.8. The concentration of ^{232}Th measured after Phase I of purification is a factor 3 lower then the ^{232}Th concentration under the assumption of a larger ^{228}Th background. This indicates that the purification may have removed the residual ^{228}Th while further reducing the ^{232}Th concentration. However, to verify this postulate, more LT would need to be accumulated to look for the ^{228}Th decay curve ($T_{1/2}$ = 1.91 y) in the time-evolution of ^{212}BiPo events.

8.1.2 Determination of ^{85}Kr, ^{210}Bi and ^{210}Po

To compare the effectiveness between purifying the LS one time and two times, data analysis was divided into Z-dependent fiducial volumes. The separation between purified volumes is evident in calibration data, as displayed in Fig. 4.10, as well as in the ^{214}BiPo data shown in Fig. 8.1(b). This finding is in excellent agreement with expectations from flow meters.

During Phase I, purification was performed in a top-down filling mode. This implies that the two-time purified volume lies above the Z = 3.0 m boundary. The boundary region is not a perfect

Description	^{14}**C [g/g]**	^{232}**Th [g/g]**	^{238}**U [g/g]**
Required Level	NA	$< 10^{-16}$	$< 10^{-17}$
Reactor Phase	$(3.98 \pm 0.94) \times 10^{-18}$	$(8.24 \pm 0.49) \times 10^{-17}$	$(1.87 \pm 0.10) \times 10^{-18}$
Purification Phase IA	$(2.81 \pm 0.78) \times 10^{-17}$	$(1.12 \pm 0.21) \times 10^{-17}$	$(5.14 \pm 0.30) \times 10^{-18}$
Purification Phase IB	$(2.18 \pm 0.31) \times 10^{-17}$	$(1.12 \pm 0.21) \times 10^{-17}$	$(7.64 \pm 0.71) \times 10^{-18}$
Purification Phase IID	$(2.34 \pm 0.39) \times 10^{-18}$	$(1.94 \pm 0.49) \times 10^{-17}$	$(1.19 \pm 0.29) \times 10^{-18}$

Table 8.1: ^{14}C, ^{232}Th, and ^{238}U concentrations in the KamLAND LS separated by phases of purification. The measured values of ^{238}U for phase IA and IB are higher then the reactor phase due to the increase in events seen in the time-evolution data-set. Tighter spatial cuts result in a value of $(1.92 \pm 0.25) \times 10^{-18}$ g/g which is consistent with the reactor phase. The errors listed from the purification results are dominated by low statistics.

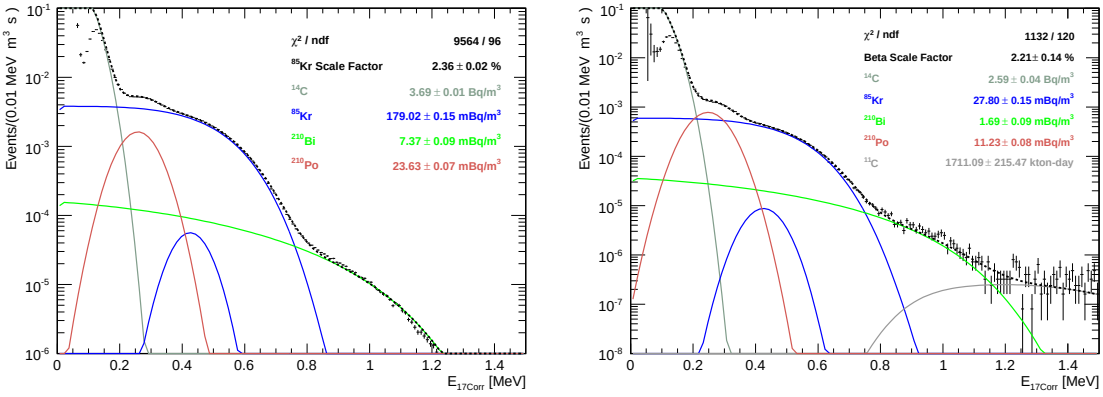

(a) (b)

Figure 8.3: Fits to low energy KamLAND data after Phase I of purification. Fig. 8.3(a) corresponds to R $\leq$ 4.0 m and Z $<$ 2.0m and thus to the LS purified once. Fig. 8.3(b) corresponds to R $\leq$ 5.0 m and Z $>$ 4.0m, covering the doubly purified LS. The χ^2 value, indicating poor fit quality, is dominated by events below 0.3 MeV.

step function as one might expect. Instead a smooth transition between volumes is observed. This is attributed to mixing in the intermediate volume between the two phases. Thus, the purified volumes are defined using the calibration data which provides a better estimate of the transition region with the help of the many calibration points around the boundary.

The one-time purified LS volume (Phase IA) is defined by the spatial cuts R $\leq$ 4.0 m and Z $<$ 2.0 m. The two-time purified volume (Phase IB) is defined by R $\leq$ 5.0 m and Z $>$ 4.0 m. Miss-reconstructed events are removed with the nominal cut: $\chi^2_{\rm TQ} \geq 8.0$, which was introduced in Ch. 5.

The smaller fiducial radius for the one-time purified volume, helps remove effects from instabilities observed in the lower hemisphere with ^{214}BiPo data and effectively reduces any external gamma-ray contribution. To increase the statistics in the two-time purified volume the radial cut was extended.

Data taken after Phase I of purification utilizes a prescale trigger which has approximately a 10% prescale fraction, see Table 3.1. Thus, one month of detector LT will yield 3 days of low energy data from the prescale trigger. A fit to the low energy spectrum for the one-time purified volume is depicted in Fig. 8.3(a). The fit to the two-time purified volume is given in Fig. 8.3(b). Trigger conditions changed during the analysis period requiring that a portion of the data be corrected for the prescale trigger efficiency, as explained in Sec. 4.7. The time-evolution analysis shows a smooth transition of the specific activities during these periods, indicating that no additional systematic error due to the efficiency correction has to be considered.

For the one-time purified volume, the data was split into 30 day intervals. The mean specific activity was determined along with the standard deviation. Mixing occurred in the detector approximately half-way through the first volume transfer. The effect is evident in Table 8.2 which indicates that the internal radiation was reduced by approximately 1/e for all nuclei. There is a disequilibrium between ^{210}Po and ^{210}Bi with no observed growth of ^{210}Bi indicating that ^{210}Pb was purified to a greater extent then ^{210}Po. Disequilibrium between ^{210}Bi and ^{210}Po is consistent with what was observed from Borexino's LS purification campaign [141]. After the first volume transfer a better understanding of the system was achieved. This is evident in the modestly increase in purification efficiency, achieved during the second volume transfer (Phase IB).

8.2 ^{85}Kr, ^{210}Bi and ^{210}Po Activities During Phase II of Purification

Before the beginning of Phase II, many improvements were made to the purification system as was discussed in Ch. 7. Initially LS purification was performed in the same top-down filling mode as during Phase I.

The data analysis performed during purification uses a different vertex fitter [1] from that used in all other analysis. This vertex fitter was found to be more stable under the large increases in dark rate. The energy parameter used is E_{17Corr}, defined in Sec. 4.5.1. Poorly reconstructed events ($\chi^2_{TQ} \geq 8.0$) were removed from the data-set as in previous low energy fits.

[1] Kat [75] vertex fitter was used for the first two KamLAND reactor antineutrino papers [85, 81]

Description	^{85}**Kr [mBq/m^3]**	^{210}**Bi [mBq/m^3]**	^{210}**Po [mBq/m^3]**
Reactor Phase	492.0 ± 11.2	45.2 ± 0.8	50.2 ± 9.9
Purification Phase IA	185 ± 11	7.4 ± 0.5	23.2 ± 1.1
Purification Phase IB	27.9 ± 0.2	1.6 ± 0.1	12.2 ± 0.9
Purification Phase IIB	3.1 ± 0.3	0.43 ± 0.04	3.5 ± 0.4
Purification Phase IIC	0.366 ± 0.078	0.054 ± 0.019	1.14 ± 0.35
Purification Phase IID	0.019 ± 0.004	0.019 ± 0.006	3.27 ± 0.45

Table 8.2: Concentrations of radioactive nuclei in the KamLAND LS which are expected to change after purification. The purification phase is listed and then the letter designates the number of times that volume has seen the purification system. In total there were 4 complete volume exchanges. Phase IB and Phase IIB represent the fact that many changes occurred with improving the purification system and only a few hundred m^3 were analyzed in Phase IB. These therefore constitute the volumes second time through the purification system but are separated by different operating conditions. The specific activity of ^{85}Kr listed for the reactor phase is given for the start of Phase I (05/12/2007).

During purification the trigger threshold was not low enough to allow a precise calculation of ^{14}C. Dark rates made up approximately 50% of the PMT hits in this energy range and a good fit to ^{14}C was impossible to obtain. When fitting the energy region from 0.18 to 2.0 MeV, the fit χ^2 is statistically biased by events below 0.3 MeV. Here the number of events per bin are at least two orders of magnitude larger then in the energy region of interest ($0.40 \leq \mathrm{E} \leq 1.0$ MeV). To remove the bias the beta energy scale factor for ^{14}C was indipendently fixed by minimizing the χ^2. Values of 9.8 and 14.25% were obtained for the two-time and three-time purified volumes respectively.

Fig. 8.4(a) shows the fit of the two-time purified volume (Phase IIB), defined to be during the period $8/16/2008 - 9/9/2008$ and inside the lower hemisphere: $\mathrm{R} \leq 5.0$ m and $\mathrm{Z} < 0.0$ m. Fits to the three-time purified volume (Phase IIC) is shown in Fig. 8.4(b). This period is defined to be between $10/25/2008 - 11/11/2008$ and lie in the upper hemisphere: $\mathrm{R} \leq 5.0$ m and $\mathrm{Z} > 0.0$ m. The change in vertex locations between Phase IIB and IIC is due to the start of bottom-up filling. These fits were performed with fixed beta function energy scale parameters and a fixed mean and sigma for ^{210}Po after much analysis leading to a better understanding of the energy scale parametrization. The beta energy scale χ^2 minimum for the two-time and three-time volume exchanges were found to correspond to -11.25% and -2.5% respectively.

The Gaussian ^{210}Po peak is the second most dominant feature in the low energy region after ^{14}C. The ^{210}Po peak mean and width were estimated from ^{214}BiPo and ^{212}BiPo data, providing estimates

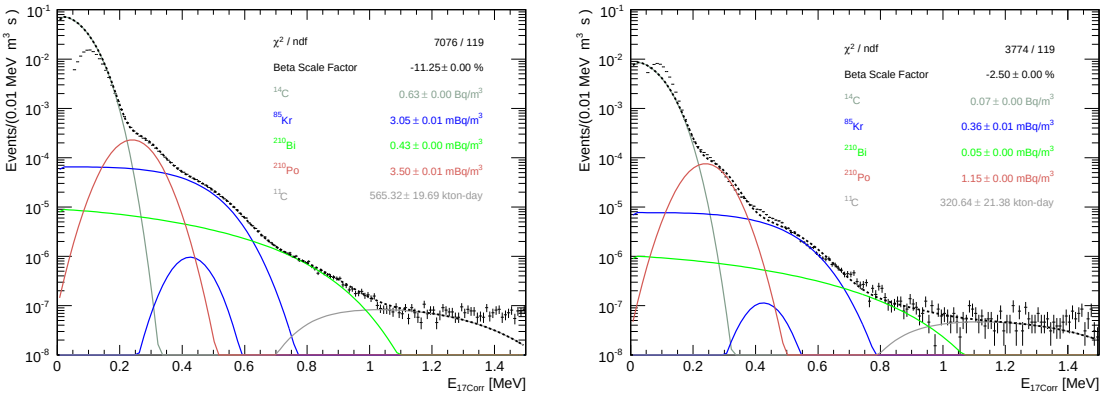

(a) (b)

Figure 8.4: Fits to low energy KamLAND data during Phase II of purification. Fig. 8.4(a) corresponds to R $\leq$ 5.0 m and Z $<$ 0.0 m, 8/16/2008 – 9/9/2008 and thus to the LS purified twice. Fig. 8.4(b) corresponds to R $\leq$ 5.0 m and Z $>$ 0.0 m and 10/25/2008 – 11/11/2008, covering the three time purified LS.

of the expected values. Fits were performed with a fixed mean and width and then alternatively with free parameters and the addition of a χ^2 constraint term.

Due to the large uncertainty in the energy scale an estimate of the impact of this variable on the fit results was studied. The beta energy scale factor was varied from -15 to 5% and a $\Delta\chi^2$ map was created for each parameter entering into the background model. During each incremental change in the beta energy scale (0.01%) all free paramaters were re-minimized using MINUIT. The same procedure was performed by shifting the mean energy of the ^{210}Po peak. The width of the resulting $\Delta\chi^2$ parabola was used to calculate a standard deviation of the fit value. In this way a reasonable estimate was made on the uncertainty of the specific activities, given in Fig. 8.4(a) and 8.4(b), was estimated. The variation of energy scale resulted in approximately a 10% systematic error. The central values including systematics errors are given for each paramter in Table 8.2.

8.3 After Phase II of KamLAND Purification

Phase II of purification was completed on Feb. 6, 2009. At this time more then 4 complete volumes of KamLAND LS had been recirculated and purified. Data analysis during purification showed the background levels in the ^{85}Kr and ^{210}Bi energy regions to be dominated by ^{222}Rn and ^{220}Rn daughters which made estimating the ^{85}Kr and ^{210}Bi difficult.

After purification was stopped the short-lived radioactivities decayed away. The time-evolution of the event rates in the 0.45-1.0 MeV region was studied. While ^{222}Rn decay could be fit to 3.8 days in the low Z region other fitted time-dependencies were less nuclide specific. The most prevalent decay observed was that of ^{210}Bi. The 5.013 day half-life was only observed in the very central region of the detector while time-constants of up to 21 days were found at the extreme Z-regions of the detector.

It took more then 45 days for the short-lived nuclei to decay to their equilibrium levels. As these isotopes decayed, and the detector came into thermal equilibrium, well defined high activity regions were identified. These regions can be see in Fig. 8.5. This finding is reminiscent of Phase I which showed convective zones at the top and bottom of the detector. Approximately 4 months after circulation was stopped, there were again spikes in the time-distribution seen in the low Z-region.

8.3.1 Final Event Selection Cuts

The FV was defined through an iterative procedure in which the time and spatial dependence of event rates were analyzed. For the time analysis, events were categorized into 4 energy intervals: E_{high}: $E \geq 1.0$ MeV, E_{mid}: $0.45 \leq E \leq 1.0$ MeV, E_{low}: $0.16 \leq E \leq 0.3$ MeV, E_{all}: $0.16 \leq E \leq 3.0$ MeV. These energy regions were chosen as they independently classify specific reaction and decay processes. E_{high} analyzes spallation and external gamma-ray contributions, E_{mid} estimates ^{85}Kr and ^{210}Bi and specifically addresses the ^{7}Be solar ν_e analysis region and E_{low} classifies dark rate contributions, ^{14}C, and ^{210}Po events. After applying these energy cuts, all events inside a radius of $R \leq R_{cut}$ were summed into Z-dependent bins and normalized by volume. These Z-slices were then plotted as a function of time.

Fig. 8.5 depicts the time-evolution of the E_{mid} events with a radial cut of $R_{cut} = 4.0$ m, the only energy region showing definite structure. From this analysis a Z-cut of $-1.2 \leq Z \leq 0.6$ m was chosen for the final data-set. A time-analysis of the fitted specific activity for each radioisotope was performed to determine the ideal start time: April 1, 2009 (Run 8474). The stop time of July 15, 2009 (Run 8699) was chosen as it was just prior to a full Z-axis calibration scan. The analysis period is thus fully contained inside two detailed calibration campaigns. The spatial and time cuts are overlaid on Fig. 8.5. The final analysis period further includes a good run selection cut which removes runs with electronics problems, maintenance or other works. This analysis further contains a 2 ms veto after minimum ionizing muons and a 2 s veto was applied after showering muons.

Fig. 8.6(a) shows the external gamma ray contribution to the low energy fit region as a function

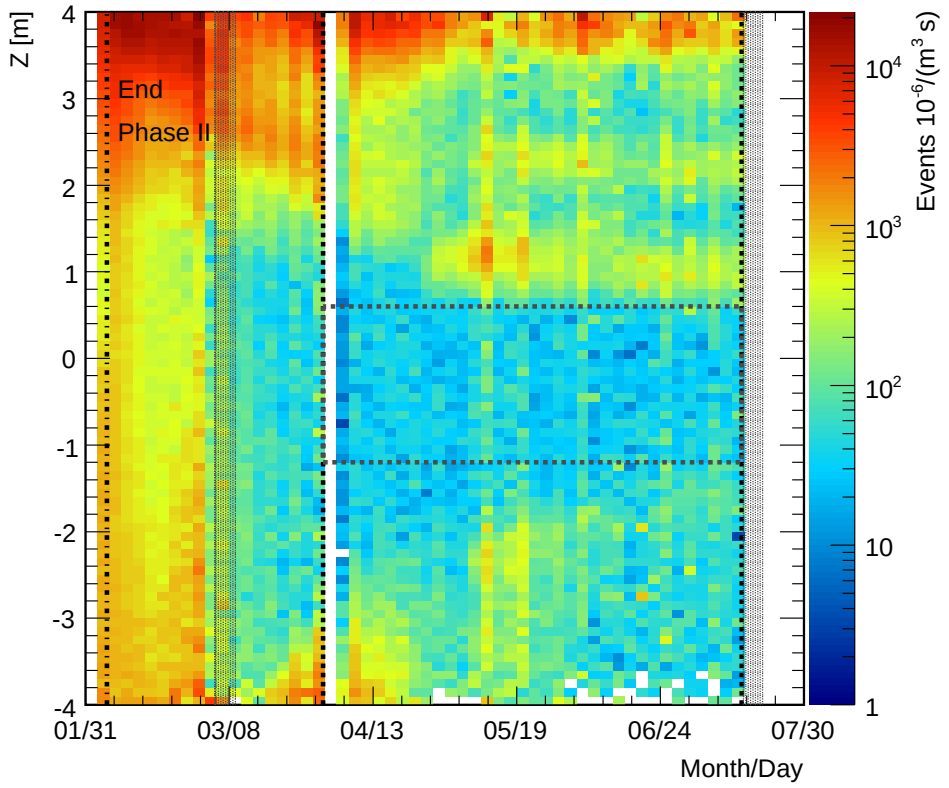

Figure 8.5: Three day integration of Z-distribution for events within R $\leq$ 4.0 m and the energy range of 0.45 $\leq$ E $\leq$ 1.0 MeV. The analysis time periods is indicated with vertical dashed lines showing the total 90.413 days of LT. Calibration periods are denoted by the hatched vertical regions. The spacial Z-cut of $-1.2 \leq$ Z $\leq$ 0.6 m is shown by the horizontal region which completely defines the cut region for this parameter space.

of R_{cut}. While the ^{40}K EC gamma-ray at 1.4 MeV does not visibly appear as a peak in the energy spectrum, there is clearly an effect from Compton scattering of external gamma rays. Thus a fiducial radius of $R_{cut} \leq 3.75$ m was chosen as this cut reduces the external contribution by more then one order of magnitude from $R_{cut} \leq 4.5$ m.

The final analysis volume is defined by the spatial cuts: R $\leq$ 3.75 m and $-1.2 \leq$ Z $\leq$ 0.6 m. Fig. 8.6(b) shows the spatial distribution of all events within 0.16 $\leq$ E $\leq$ 3.0 MeV with the final analysis volume overlaid. This region constitutes 77.486 m^3 of LS with a total detector live time of 90.413 days. The total exposure time is calculated to be 5.448 kton-days.

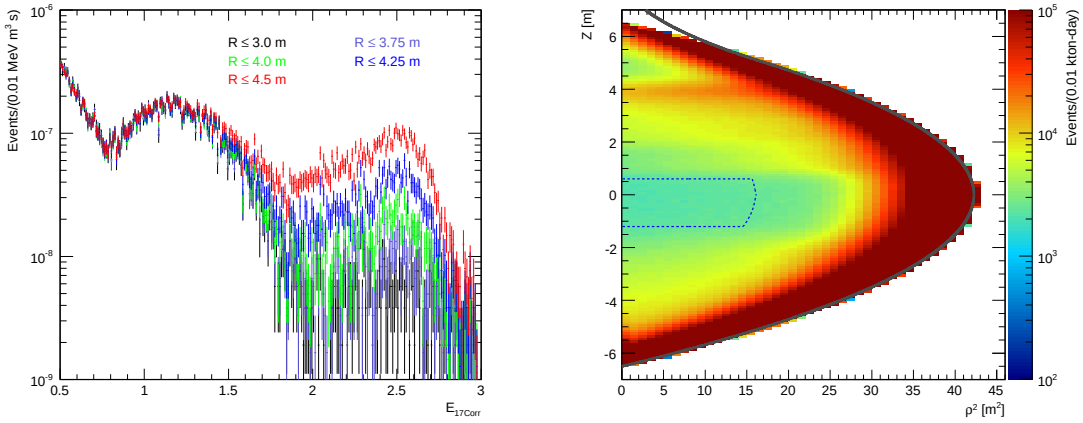

(a) (b)

Figure 8.6: Fig. 8.6(a) shows the external gamma ray contribution to the ^{7}Be solar ν_e analysis region. The change in ^{208}Tl is clearly observed and the external Compton spectrum is seen to primarily influence the spectral shape of ^{10}C. Fig. 8.6(b) shows the spacial distribution of events within the energy range of $0.16 \leq E \leq 3.0$ MeV. The final analysis region ($R \leq 3.75$ m and $-1.2 \leq Z \leq 0.6$ m) is outline with the blue dashed line.

8.3.2 Final Low Energy Analysis of Specific Activities after Phase II of Purification

Using these selection criteria, fits to the energy spectra were performed to estimate the radio-purity of KamLAND after purification. The final analysis considers the energy region from $0.18 - 2.0$ MeV and uses two χ^2 constraint terms. The first constraint was on the beta scale factor, defined through Eq. 5.2. The constraint was derived from ^{137}Cs calibration data, which defines the E_{vis} to E_{real} off-set as 2.45% with a standard deviation of 0.24% (Eq. 5.1).

. The second constraint was much weaker, restricting the fitted spallation product ^{11}C, to the published value of 1106 ± 178 events/(kton-day) [80]. The ^{11}C analysis was performed on data taken during the reactor phase of KamLAND and is a direct measurement free of detector systematics.

^{238}U and ^{232}Th concentrations were calculated using ^{214}BiPo and ^{212}BiPo data respectively. Due to the coincidence requirement, the ^{238}U and ^{232}Th analysis region could be extended to a fiducial radius of 5.0 m and $-2.0 \leq Z \leq 2.0$ m, to fully include the analysis region. 19 ^{214}BiPo events and 17 ^{212}BiPo events were observed, resulting in concentrations of ^{238}U and ^{232}Th consistent with those obtained during the reactor phase. These results are listed in Table 8.1.

Internal ^{40}K was estimated by varying the FV with $R_{cut} \in [3.0, 4.0]$ m in 0.25 m increments.

Further systematics were obtained by searching for time-variations in one month time-intervals. These analyses provide a measurement of -0.583 ± 0.881 μBq/m^3 and gives an upper limit [126] of < 0.41 μBq/m^3 at the 68.27% C.L. This corresponds to a concentration of $< 1.9 \times 10^{-18}$ g/g, resulting in more than a factor 69 reduction in internal ^{40}K in KamLAND LS compared to the reactor phase.

The specific activities of ^{14}C, ^{85}Kr, ^{210}Bi, ^{210}Po are determined from the same energy spectrum analysis, allowing a FV and time related error calculation. The calculated mean values along with their 1σ systematic errors are given in Table 8.2 and Table 8.1. ^{14}C is measured to be 0.30 ± 0.05Bq/m^3. The central value is 60% lower than during the reactor phase, but both values are consistent within the quoted errors. ^{85}Kr was measured to be 19 ± 4 μBq/m^3 which is a factor 2.6×10^4 reduction from the reactor phase. Finally the ^{210}Bi is determined to be $= 19 \pm 6$ μBq/m^3, which corresponds to a factor 2×10^3 reduction compared to the reactor phase. These purification results are within a factor of 10 of the strict requirements set forth in Ch. 5.

^{210}Po was the most difficult radioisotope to remove from LS. The fitted specific activity of 3.27 ± 0.45 mBq/m^3 shows an increase in ^{210}Po compared to the previous measurement from Phase IIC. Fig. 8.7 shows the results of purification graphically by plotting all singles spectra on the same figure. This clearly shows the reduction provided by purification and indicates the increase in ^{210}Po between Phase IIC and II Final as the spectral shape crosses the previous spectrum at 0.3 MeV. This figure along with the tabulated values clearly indicates the success of KamLAND's repeated purification. KamLAND has successfully reduced the event rate above 0.5 MeV to 100 events per day in the 77 m^3 analysis volume!

8.4 First Evidence for ^{7}Be Solar Neutrinos in KamLAND

It was only two years ago that Borexino claimed the first real-time detection [142] of ^{7}Be solar ν_es. Before this measurement radiochemical experiments could only infer the ^{7}Be solar ν_e rate from theoretical predictions of the total flux and the measured integral rate. Physics, as an experimental science, deems it imperative that a second real-time measurement of ^{7}Be solar ν_e be performed independent of Borexino. The previous sections have shown that KamLAND's low energy background rate was reduced by more then four orders of magnitude in the energy region of interest. This is within a factor of 10 of the requirements outlined in Ch. 5. With the improved signal-to-background ratio after purification it is therefore of interest to look for a ^{7}Be solar ν_e signal in the KamLAND

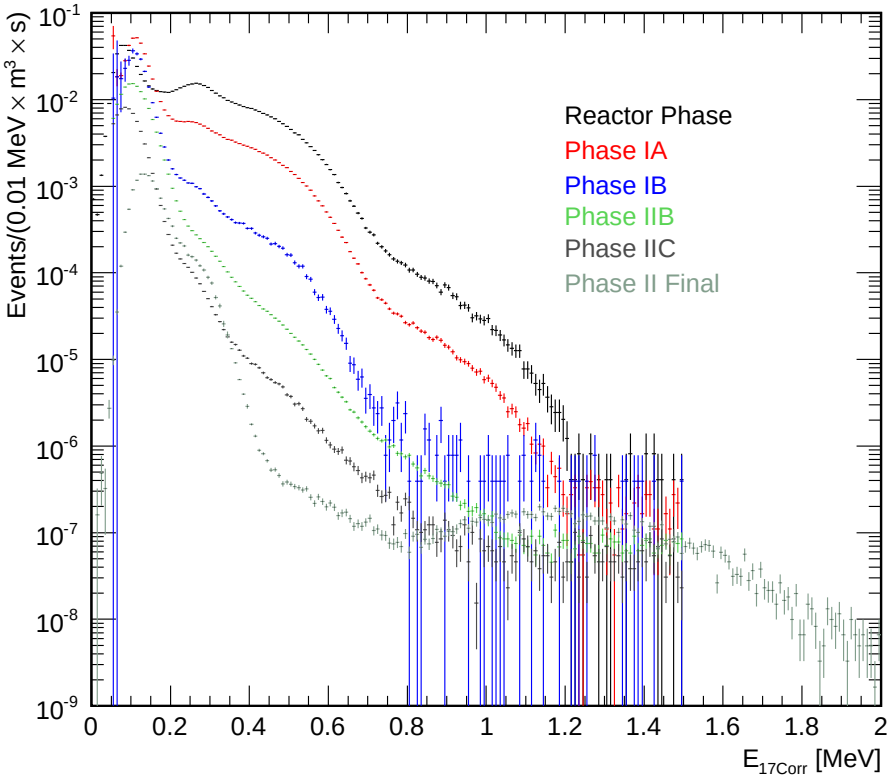

Figure 8.7: Overlay of energy spectrum analyzed for the successive purifications of KamLAND. A clear reduction in event rate is seen after each volume transfer.

data.

Analysis of KamLAND data covers an exposure time of 5.448 kton-days. Even when using the rather conservative analysis volume, this exposure is still only a factor three less then the most recent ^{7}Be solar ν_e result from Borexino [17]. In this paper Borexino reported a ^{7}Be solar ν_e rate of $49 \pm 3_{\rm stat} \pm 4_{\rm syst}$ events/(day 100 tons), consistent with 49.2 events/(day 100 tons) from solar model expectations as described in Sec. 5.5.

The background levels in KamLAND are not such that the data presented here would provide a "smoking gun" signal for solar neutrinos, as discussed in Sec. 5.5. However, the rates are low enough to test the hypothesis of a ^{7}Be solar ν_e signal hidden in the KamLAND data. This is done by testing four different hypotheses:

1. Analyze the $[0.18, 2.0]$ MeV energy region using the same χ^2 constraints for the beta scale factor and ^{11}C flux described in the previous section.

Hypothesis	χ^2**/NDF**	$\chi^2_{^7\mathrm{Be}}$**/NDF**	$\Delta\chi^2$	^{7}**Be [kton-day]**	S : B
$[0.18, 2.0]$ MeV:					
No EC Constraint	359/172	348/173	11	45 ± 175	$174 : 1,889,688$
EC Constraint	367/172	353/173	14	-191 ± 141	$-746 : 1,892,411$
$[0.5, 2.0]$ MeV:					
No EC Constraint	247/140	234/141	13	186 ± 229	$239 : 2963$
No Constraints	235/140	201/141	34	663 ± 268	$795 : 2389$

Table 8.3: Summary of goodness of fit for the different analysis hypotheses. For each fit hypothesis the associated χ^2/NDF is given under the assumption of no ^{7}Be and then after assuming a ^{7}Be signal. The ^{7}Be rate is determined by means of the fits with 68.3% C.L. statistical errors. The signal to background (S : B) is calculated from the integrated fit functions.

2. Analyze the $[0.18, 2.0]$ MeV energy region using the same χ^2 constraints for the beta scale factor and ^{11}C flux described in the previous section. However, in this case the ^{7}Be EC spallation reaction is constrained to the result from Hagner [100] scaled to the KamLAND muon energy and overburden [80] which yields 132.8 ± 8.7 events/(kton-day).

3. Analyze the $[0.5, 2.0]$ MeV energy region to increase the signal-to-background ratio. The nominal χ^2 constraints for the beta scale factor and ^{11}C flux are used.

4. Analyze the $[0.5, 2.0]$ MeV energy region and in this case all constraints on the data are removed.

The data is fit under two assumptions: 1) no ^{7}Be solar ν_e signal in KamLAND 2) allow for ^{7}Be solar ν_e signal. The results from these fits and the $\Delta\chi^2$ are then compared as a test for the statistical significance of a hypothetical ^{7}Be solar neutrino signal.

All fits are performed using MINUIT [91] and statistical errors and reported at the 68.3% C.L. For case 1, the spectral fit under the assumption of no ^{7}Be solar ν_e signal is shown in Fig. 8.9(a). The fit containing ^{7}Be solar ν_es is provided in Fig. 8.9(b) which yields a value of 45 ± 175 ^{7}Be solar ν_e events/kton-day. The $\Delta\chi^2 = 11$, indicates that the fit prefers a ^{7}Be solar ν_e signal. The residual plot is provided in Fig. 8.9(c) to give an indication of the overall strength of the fitted signal. Case 2 is shown in Figures 8.10(a) $-$ 8.10(c). It should be noted that while the central value is -191 ± 141 events/kton-day, the $\Delta\chi^2 = 14$.

The second scenario uses the restricted energy region to remove the low energy backgrounds from ^{14}C and ^{210}Po. By increasing the analysis threshold to 0.5 MeV the signal-to-background ratio

was improved by a factor 1000 compared to the previous fit. Fig. 8.11(a) through 8.11(c) show the results from case 3 which is equivalent to case 1 only with a restricted fit range. The reduction in signal-to-background is evident in the χ^2/NDF decreasing from 2.02 down to 1.76. The inclusion of ^{7}Be solar ν_e is favored with a $\Delta\chi^2 = 13$. Very similar to the results from case 1 with an increased central value for the ^{7}Be solar ν_e rate.

The final test was to remove all constraints on the fit. The results are shown in Fig. 8.12(a) through 8.12(c). This situation provides the best fit to the data and including ^{7}Be solar ν_e produced a $\Delta\chi^2 = 34$ indicating the presence of ^{7}Be solar ν_e with high statistical significance.

In all instances the fit prefers a ^{7}Be solar ν_e signal. The total expected number of ^{7}Be solar ν_e events from the BP05(OP) solar model for 5.448 kton-days under the assumption of no oscillations is 1136 events for the restricted $0.5 - 2.0$ MeV analysis region. While under the assumption of oscillations, the expected number of events is 598. This is in line with the integral values given in Table 8.3. However, at this time it is not possible to determine a robust central value given the current understanding of the underlying background.

It should be noted that there are very strong correlations of the solar neutrino signal with these backgrounds which readily influence the central value. Fig. 8.8(a) shows the strongest anti-correlation of ^{7}Be solar ν_e with ^{85}Kr. Fig. 8.8(b) indicates there is also an anti-correlation with ^{210}Bi. When the ^{7}Be solar ν_e spectrum is included in the fit both of these backgrounds decrease. Thus, any constraint on either of these backgrounds would improve the significance of the fit.

While the fit is very lightly correlated with ^{11}C (see Fig. 8.8(c)) and primarily through ^{210}Bi, there is a strong correlation with the ^{7}Be EC (see Fig. 8.8(d)). While the literature provides some guidance on the expected value for ^{7}Be EC, KamLAND's recent spallation paper [80] shows measured deviations from this result by more then a factor of 10 in some cases for other spallation products. Furthermore, the large amount of PPO which had to be added to KamLAND (see Sec. 7.1.1) provides a further source of uncertainty in the expected rate of ^{7}Be EC events due to cosmogenic build-up at the surface. While calculations have been performed on the suggested limit, the uncertainty in the error from the literature makes this one of the largest uncertainties in the fit. In all instances the fit prefers to have a larger value of ^{7}Be EC events. This is at most a factor 50 more then Hagner and a factor 2 more then calculations based on the Monte Carlo from ref [80].

The KamLAND collaboration is currently considering the benefits of performing a third round of purification in hopes of further reducing the ^{85}Kr and ^{210}Bi backgrounds. Table 8.2 indicates approximately a factor 10 reduction in ^{85}Kr and a factor 3 reduction in ^{210}Bi could be expected

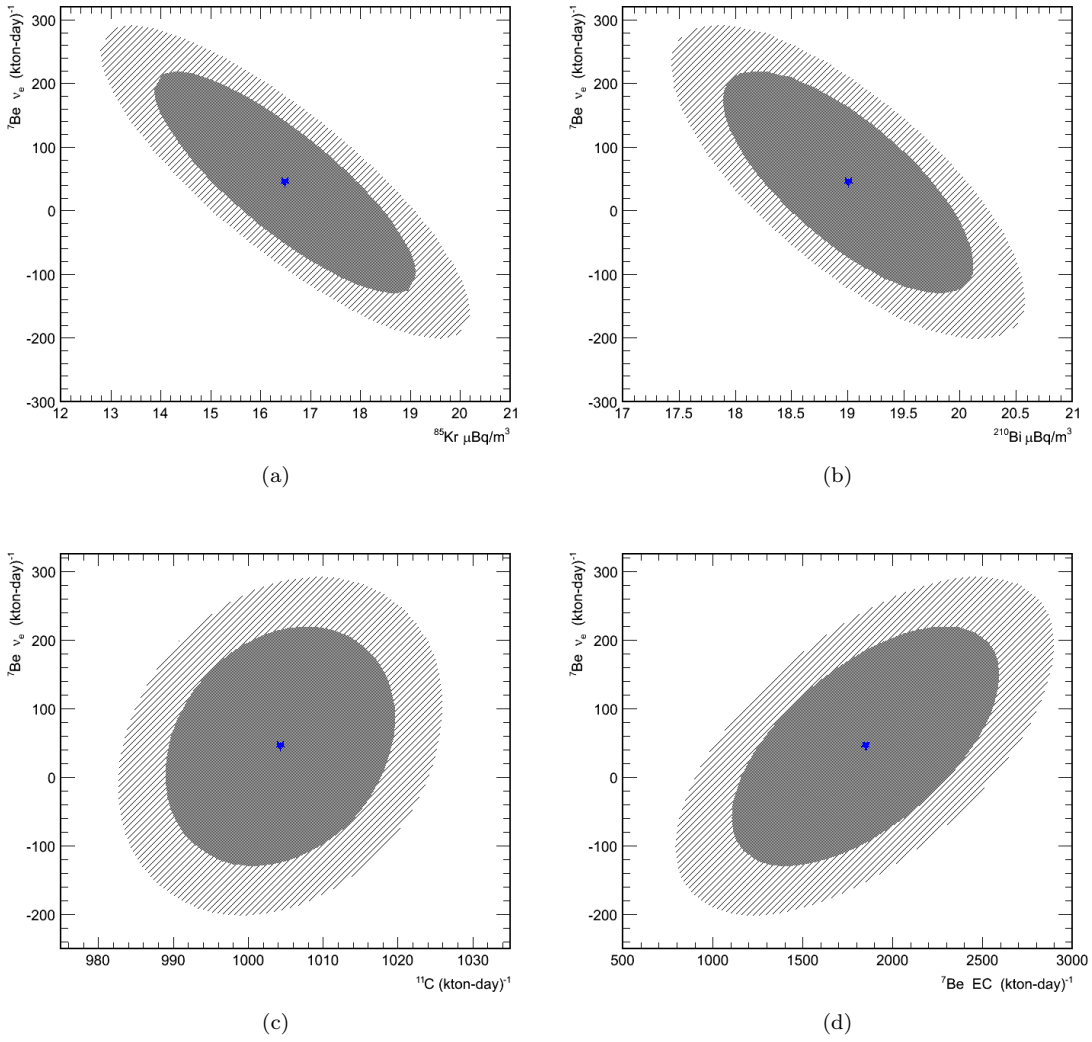

Figure 8.8: Contours of ^{7}Be solar ν_e with ^{85}Kr, ^{210}Bi, ^{7}Be EC, and ^{11}C. The contours are drawn from the fit of a $[0.18, 2.0]$ MeV analysis window and χ^2 constraints for the beta scale factor and ^{11}C flux.

from another volume exchange. The best fit interval is the reduced energy region. Due to the strong correlation of the ^{7}Be solar ν_e with ^{85}Kr and ^{210}Bi, KamLAND would benefit greatly from a modest reduction in these backgrounds. A factor 10 reduction in these backgrounds would potentially reveal a "smoking gun" ^{7}Be solar ν_e signal in KamLAND.

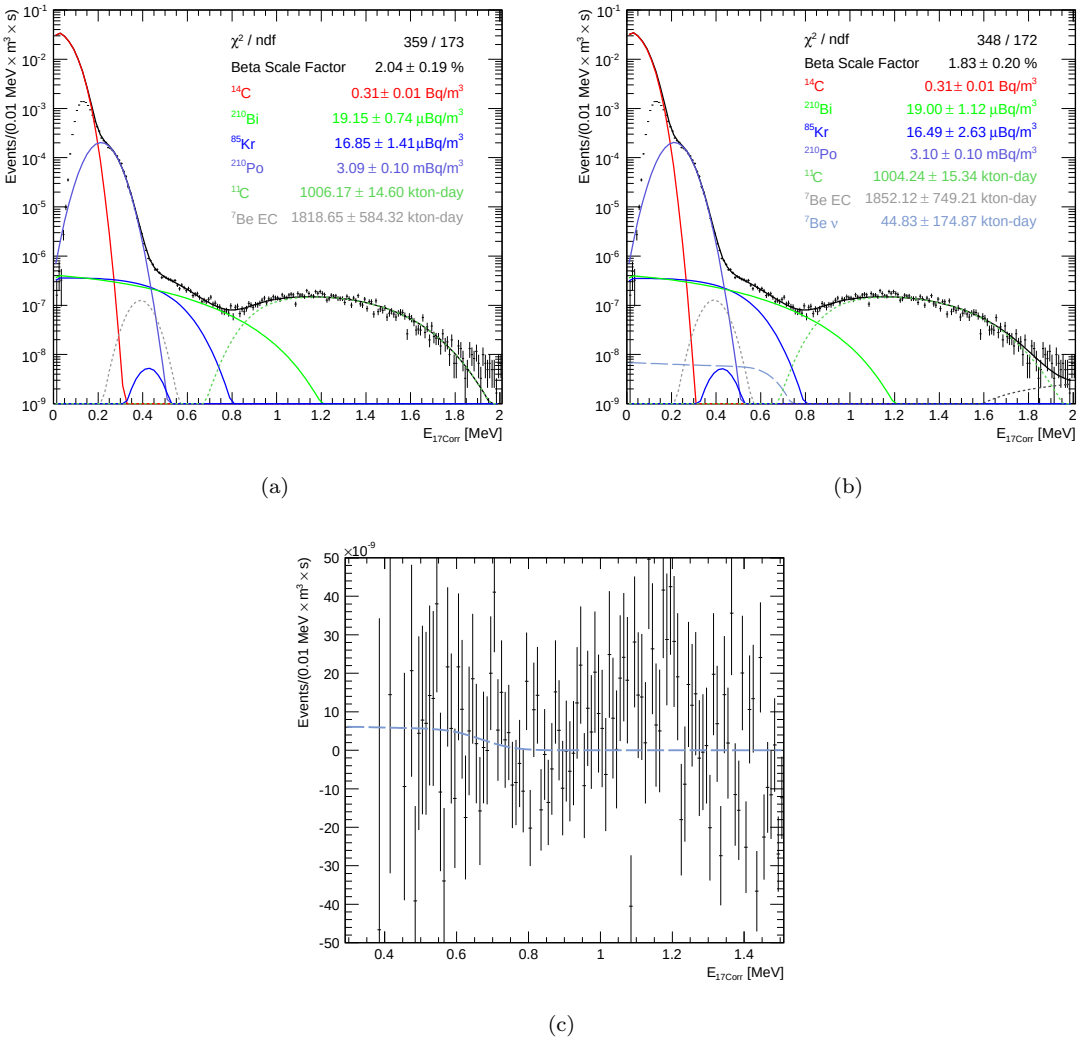

Figure 8.9: Fits to low energy spectrum. Fig 8.9(a) shows the fit to data which use only χ^2 constraints for the beta scale factor and ^{11}C. Fig 8.9(b) adds the assumption of a ^{7}Be solar ν_e contribution. Fig 8.9(c) is the backgrounds subtracted signal overlaid with the ^{7}Be solar ν_e fit to indicate the overall significance of the spectral signal.

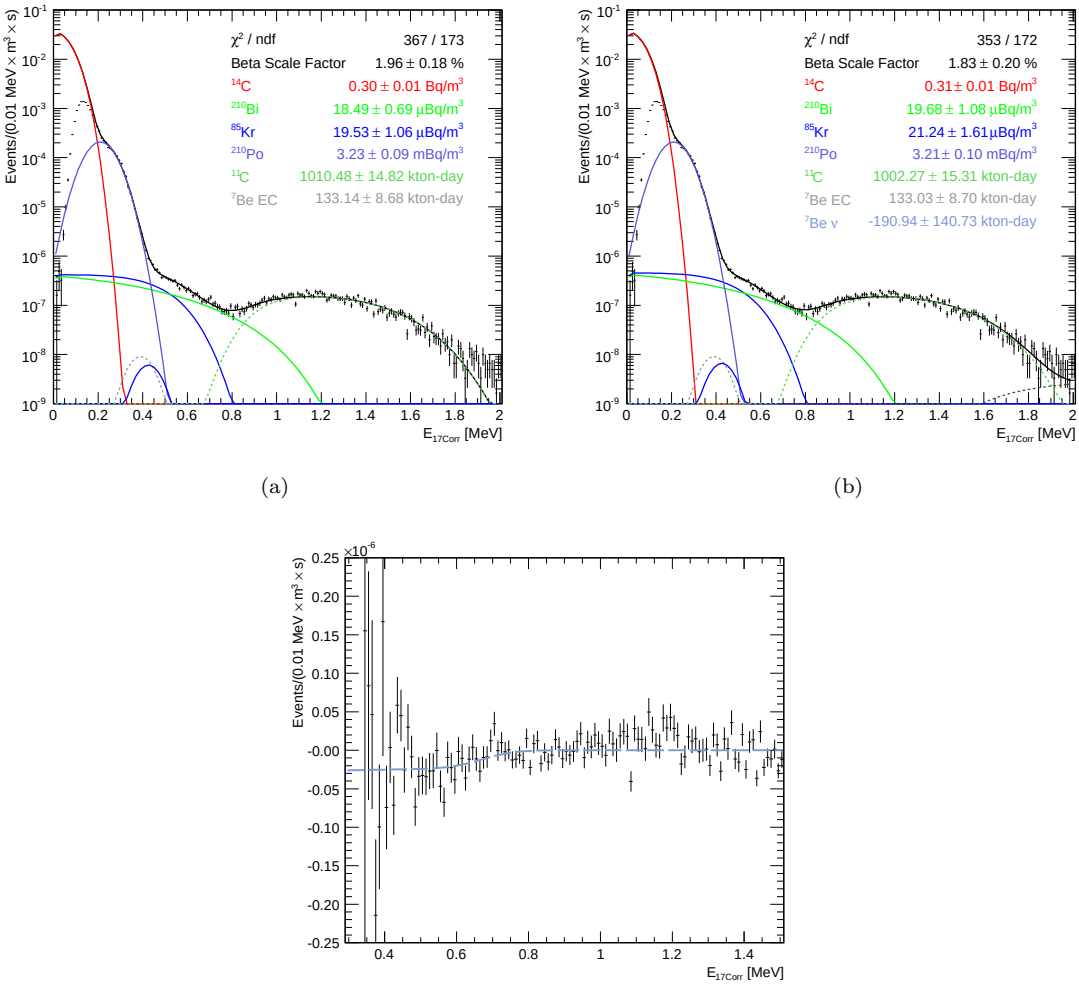

Figure 8.10: Fits to low energy spectrum. Fig 8.10(a) shows the fit to data which uses χ^2 constraints for the beta scale factor, ^{7}Be EC, and ^{11}C. Fig 8.10(b) adds the assumption of a ^{7}Be solar ν_e contribution. Fig 8.10(c) is the backgrounds subtracted signal overlaid with the ^{7}Be solar ν_e fit to indicate the overall significance of the spectral signal.

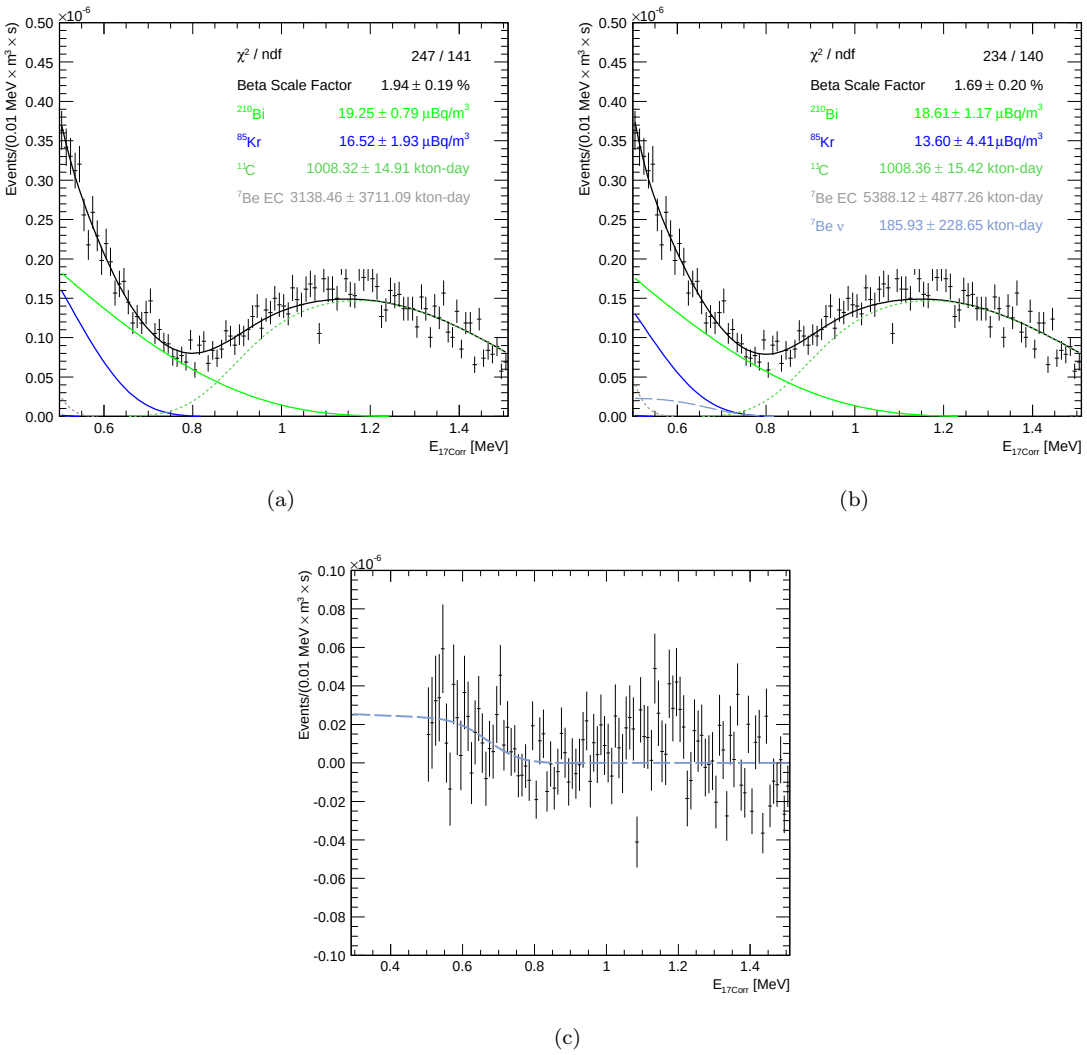

Figure 8.11: Fits to low energy spectrum with a restricted energy region to increase signal to background. Fig 8.11(a) shows the fit to data which uses χ^2 constraints for the beta scale factor and ^{11}C. Fig 8.11(b) adds the assumption of a ^{7}Be solar ν_e contribution. Fig 8.11(c) is the backgrounds subtracted signal overlaid with the ^{7}Be solar ν_e fit to indicate the overall significance of the spectral signal.

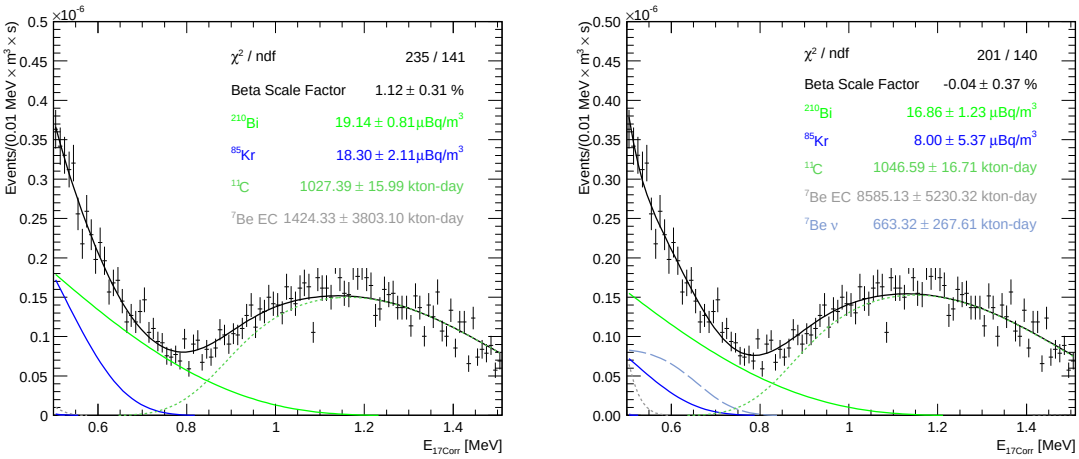

Figure 8.12: Fits to low energy spectrum with a restricted energy region to increase signal to background. Fig 8.12(a) shows a free fit to data which uses no χ^2 constraints. Fig 8.12(b) adds the assumption of a ^{7}Be solar ν_e contribution. Fig 8.12(c) is the backgrounds subtracted signal overlaid with the ^{7}Be solar ν_e fit to indicate the overall significance of the spectral signal.

Chapter 9

Conclusion

In this work it has been shown that KamLAND must reduce the internal radioactivity of ^{85}Kr and ^{210}Bi by more then 4 orders of magnitude in order to provide a sufficient signal-to-background ratio of 2 for a ^{7}Be solar ν_e signal. Laboratory studies were performed to determine how to purify ^{210}Pb from LS at the concentration levels of 10^{-20}g/g. It was shown that distillation was the only method to provide purification factors of 10^4 for ^{212}Pb at these concentration levels in the laboratory. As a result of the laboratory studies carried out in this work, a large scale purification system was designed and implemented in the Kamioka Mine, Gifu, Japan.

The purified LS was measured to have a ^{85}Kr specific activity of 19 ± 4 μBq/m^3, which is a factor 2.6×10^4 less then before purification. Furthermore, the ^{210}Bi specific activity was measured to be 19 ± 6 μBq/m^3, which is a factor of 2×10^3 reduction. Internal ^{40}K was reduced to $< 1.9 \times 10^{-18}$ g/g, resulting in more then a factor 69 reduction in internal ^{40}K from KamLAND LS prior to purification. It has been shown that with multiple purifications of the KamLAND LS, the KamLAND collaboration has successfully reduced the event rate above 0.5 MeV to 100 events per day in the 77 m^3 analysis volume!

For an exposure time of 5.448 kton-days, the KamLAND data is fit under two assumptions: 1) no ^{7}Be solar ν_e signal in KamLAND 2) allow for ^{7}Be solar ν_e signal. The results from these fits and the $\Delta\chi^2$ are then compared as a test for the statistical significance of a hypothetical ^{7}Be solar neutrino signal. It is shown that a ^{7}Be solar ν_e signal is statistically favored over a null hypothesis in all scenarios. As a result, this work reports the first observation of ^{7}Be solar ν_es with KamLAND.

Appendix A

Solar Fusion Cycles and Radioactive Background Decay Schemes

A.1 Solar Fusion Cycles

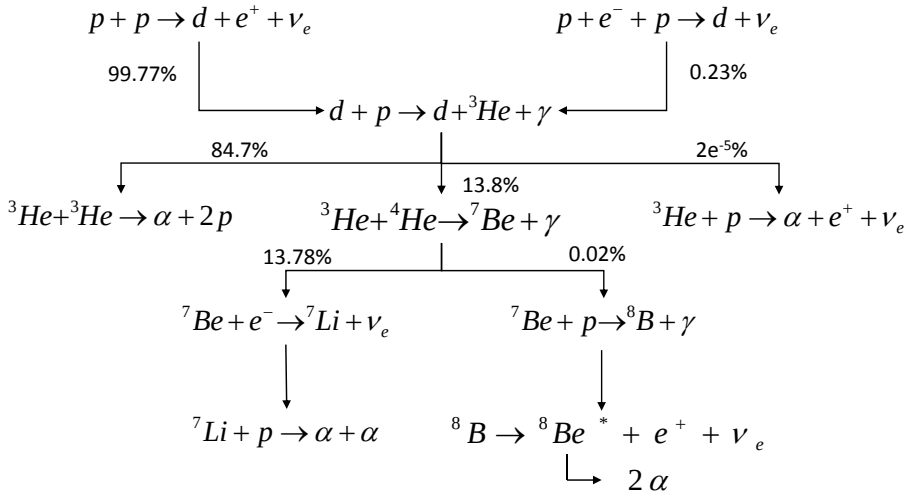

Figure A.1: PP fusion cycle in the Sun and the relative intensities of the different reactions.

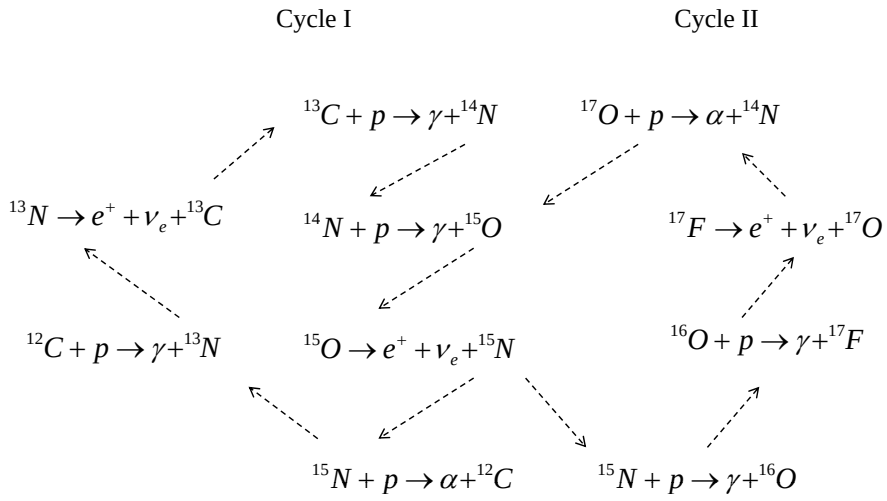

Figure A.2: The predominant CNO fusion cycles in the Sun which produce neutrinos. Cycle I begins with ^{12}C and cycles back on itself with the production of ^{12}C through the reaction ^{15}N(p, α)^{12}C. Cycle I makes up 99% of the CNO energy production. The second cycle branch is approximately 0.1% with the beta decay reaction ^{15}O $\rightarrow$ e$^+$ + ν_e + ^{15} N. There are two more subdominant CNO production cycles not shown which terminate in with the production of ^{20}Ne.

A.2 Decay Chains of Internal Backgrounds in KamLAND

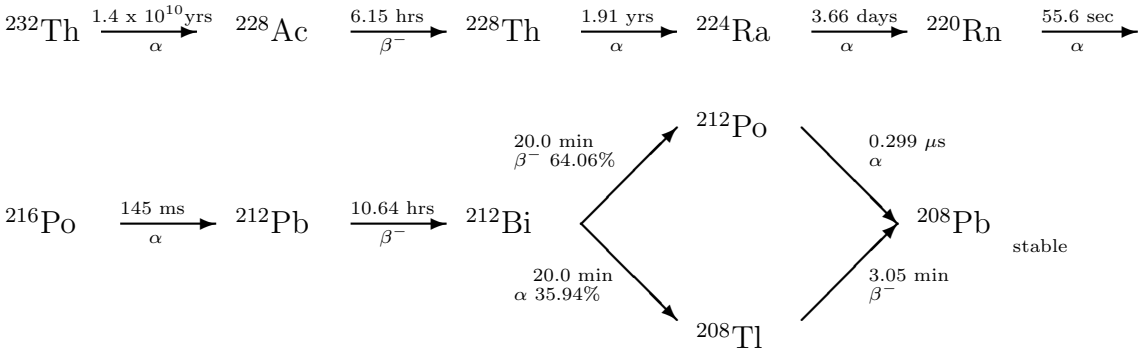

Figure A.3: ^{232}Thorium Decay Chain

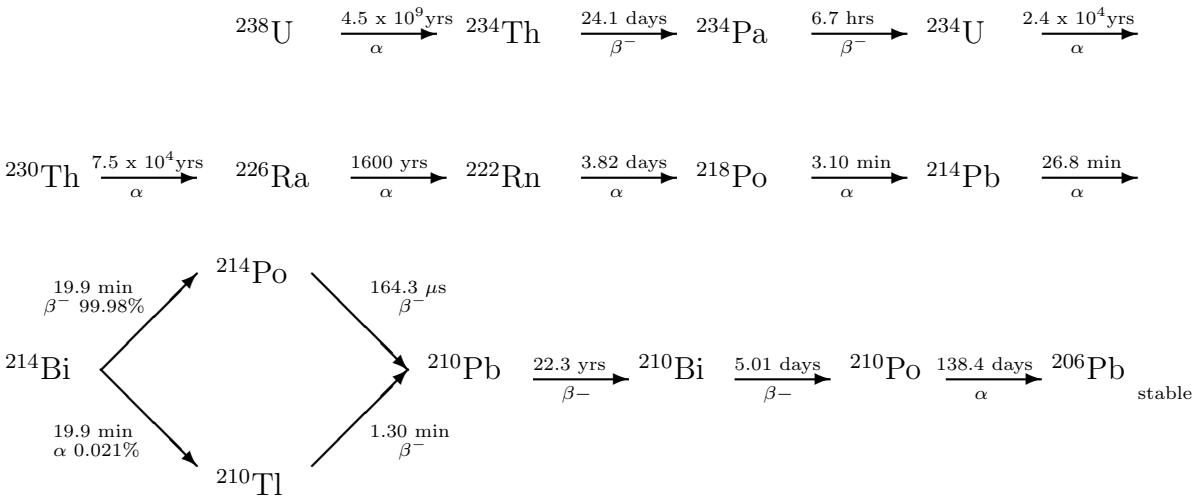

Figure A.4: ^{238}Uranium Decay Chain

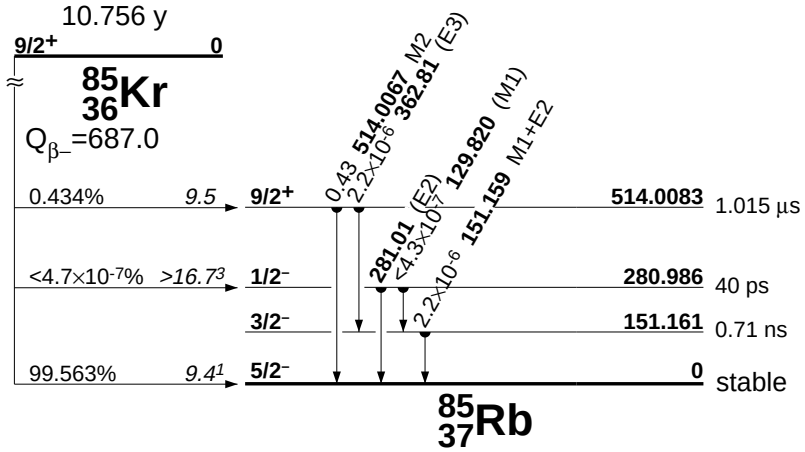

Figure A.5: Beta decay mode of ^{85}Kr which has a meta-stable state transition to the ground state of ^{85}Rb. This mode is used as a means to tag and single out a portion of the beta decay isotopes.

Appendix B

KamLAND Beta Decay Generator

The KamLAND collaboration has developed a detector simulation based on the Monte Carlo (MC) package Geant4 [143] called KLG4sim (KamLAND Geant4 Simulation). The base code to this simulation has been made available to the general antineutrino community as GLG4sim [144]. To simulate decay process in KLG4sim, Geant4 uses the Fermi function for allowed decay modes to internally generate beta spectra when calling the local decay generator. Two isotopes of interest to KamLAND (^{40}K and ^{85}Kr) are highly forbidden decays which produce large deviations from an allowed spectral shape.

Therefore, it was deemed necessary to produce p.d.f. functions using a more accurate model of beta decay. The theory in this section was used to develop a Monte Carlo (MC) code that produces e^- and e^+ spectra independent of the Geant4 platform. The functions were written [1] as part of a C++ class referred to as KBeta (KamLAND Beta decay generator), and is used as the primary beta decay generator for KamLAND analysis. The following sections will provide the theoretical background and compare the calculated beta spectra with other theoretically generated spectra and tabulated data.

[1] The original code was written in FORTRAN by the author and Andreas Piepke and translated later into the C++ platform to be compatible with KamLAND analysis tools.

B.1 Theoretical Considerations in Constructing a Beta Decay Generator

Electron and positron spectra have been calculated according to the theoretical formula in Konopinski's text on the theory of beta decay [145, 146, 147]. To cross-check the output of the code and test the validity of the spectra produced by the theory outlined in this text, the KBeta spectra have been compared with spectra obtained in the low Z limit provided by Konopinski and Wu [145, 148] and with tabulated beta spectra from Landolt-Börnstein [149]. Several papers [146] suggest methods for taking into account atomic electron's screening from Coulomb field interactions. These corrections are accounted for and their effect will be described in detail. The final effect which must be considered when making a beta decay generator are the inclusion of experimentally determined correction factors. For the decays of interest to KamLAND correction factors to the theoretical spectra exist for ^{14}C [150] and ^{210}Bi [151].

The expected energy spectrum for a beta particle can be deduced from considering a two-body decay. Under the assumption that the electron and neutrino share their kinetic energies the spectral shape can be calculated from considerations of particle ensembles and the availability of phase space $p^2\ dp\ q^2\ dq$, where p is the electron and q the neutrino momentum. For this reason the basic form for the expected beta energy spectrum is referred to as the "statistical" shape. Specifically, the fraction of decays, $d\lambda$, emitted as a function of electron energy dW is expressed as

$$d\lambda = W(W_0 - W)^2 p_e dW \tag{B.1}$$

where W is the total energy of the electron in units of $m_e c^2$, $W_0 = [M(Z) - M(Z \pm 1)]c^2$ is the end-point energy of the electron given by the difference in nuclear masses, and p_e is the electron momentum in units of $m_e c$.

B.1.1 Corrections to the Statistical Shape

In the standard model of particle physics described in Sec. 2.1, the mass of the neutrino is assumed to be zero. However, while we know this is not true, the small mass (< 2 eV) [40] relative to the energy and momentum of the neutrino permits this approximation. A zero mass neutrino can be seen as the first order term in a Taylor series approximation of $P_\nu \sqrt{1 + \frac{P_\nu}{m_\mu}}$ which allows the relationship $W_\nu = p_\nu$ and thus the integral over the neutrino momenta can be performed. Energy

Transition Nomenclature	$L = \Delta J$	**Parity Change** $[\pi_i \pi_f]$
Allowed	0, 1	$+1$
First non unique forbidden	0, 1	-1
$\mathrm{n^{th}}$ non unique forbidden	> 1	$(-1)^L$
$(\mathrm{n}-1)^{\mathrm{th}}$ unique forbidden	> 1	$(-1)^{L-1}$

Table B.1: Nomenclature for beta decay transitions. The label applied to the decay mode is determined by the total change in lepton angular momentum ΔJ between the parent and ground state nucleus and the parity change in these nuclear states. As an example, ^{85}Kr ($\mathrm{J_i} = \frac{9}{2}$ $\pi_\mathrm{i} = +1$) decays to the ground state of ^{85}Rb ($\mathrm{J_f} = \frac{5}{2}$ $\pi_\mathrm{f} = -1$) [89] resulting in $\Delta J = 2$ and a parity change of -1. This obeys the rule $(-1)^{L-1}$ of a 1^{st} unique forbidden decay. Odd total angular momentum changes expect a parity change in the nuclei. In the case that this does not occur it is classified as "unique" forbidden.

conservation allows the neutrino momenta to be expressed in terms of the electron energies. After these approximations and treating the nucleus as a point charge, the most general form for beta decay is expressed as

$$\mathrm{d}\lambda = \frac{\mathrm{G_F^2 m_e^5 c^4}}{2\pi^3\hbar^7}\ \mathrm{W\left(W_0 - W\right)^2\, p_e\, F\left(\pm Z, W\right)\ S\left(\pm Z, W\right)\ dW} \tag{B.2}$$

where $\mathrm{G_F}$ is the Fermi constant, Z is the charge of the parent nucleus and $\pm$ refers to an $\mathrm{e^+}$ or $\mathrm{e^-}$ decay respectively.

There are two dimensionless correction factors to the statistical form given in Eq. B.1. $F(\pm Z, W)$ is referred to as the Fermi correction and accounts for the Coulomb force from the positive charge of the nucleus. The explicit form of the Fermi correction is

$$\mathrm{F(\pm Z, W)} = 2(1+\gamma_0)\mathrm{e}^{\pi\nu}\Big(\frac{2\mathrm{p_e R}}{\hbar}\Big)^{2(\gamma_0-1)}\frac{|\Gamma(\gamma_0+\mathrm{i}\nu)|^2}{[\Gamma(2\gamma_0+1)]^2} \tag{B.3}$$

where $\gamma_0 = [1-(\alpha Z)^2]$, $\nu = \pm\frac{\alpha Z W}{p_e}$, and $R = \frac{1}{2}\alpha A^{\frac{1}{3}}$ is an approximation to the nuclear radius in units of $\frac{\hbar}{mc}$. Z is the number of protons in the daughter nucleus, A is the number of nucleons, and α is the fine structure constant. The form for the Fermi correction treats the nucleus as a point charge and is the ratio of the electron density evaluated at a nuclear radius R to the density at infinity. Due to the attractive nature of this force it effectively increases the number of low energy electrons.

The second correction to the statistical shape is $\mathrm{S(\pm Z, W)}$ which is an energy dependent correction which changes according to the nuclear decays degree of "forbiddeness." The terminology

and conditions for forbiddeness is described in Table B.1.1. The specific form for the forbiddeness correction is

$$\mathrm{S}(\pm\mathrm{Z},\mathrm{W}) = \frac{8\pi(\mathrm{J}-1)!\mathrm{R}^{2(\mathrm{J}-1)}}{(1+\gamma_0)(2\mathrm{J}-1)!!}\sum_{\mathrm{j}}\frac{(2\mathrm{j})!!}{(2\mathrm{J}-2\mathrm{j})!!}\frac{\mathrm{L}_{\mathrm{j}-\frac{1}{2}}(\mathrm{W}_0-\mathrm{W})^{2(\mathrm{J}-\mathrm{j})-1}}{(\mathrm{j}-\frac{1}{2})!(\mathrm{J}-\mathrm{j}-\frac{1}{2})!}\mathrm{M}_{\mathrm{j}}^2(\mathrm{j}) \tag{B.4}$$

where ΔJ is defined as the difference in total angular momentum and the sum is performed over the change in lepton angular momenta between the parent and ground state nuclei where $j = \frac{1}{2}, .., \Delta J - \frac{1}{2}$. Inside the shape factor appears the term

$$\mathrm{L}_{\mathrm{j}-\frac{1}{2}} = \frac{1}{2}(2\mathrm{p_e})^{2(\gamma-\gamma_0)}\left[\frac{\Gamma(2\gamma_0+1)}{\Gamma(2\gamma+1)}\right]^2\left|\frac{\Gamma(\gamma+\mathrm{i}\nu)}{\Gamma(\gamma_0+\mathrm{i}\nu)}\right|^2\mathrm{R}^{2(\gamma+\gamma_0)-(2\mathrm{j}-1)}\mathrm{k}(\mathrm{k}+\gamma) \tag{B.5}$$

where $\gamma = [(j+\frac{1}{2})^2 - (\alpha Z)^2]^{\frac{1}{2}}$ and $k = j + \frac{1}{2}$.

The last term which has not been discussed is $M_j^2(j)$ which is a linear combination of the appropriate nuclear matrix elements. This is a measure of the overlap in the wave-functions for the initial and final nuclear states given explicitly by the Hamiltonian

$$H_\beta = \sqrt{2}g\sum_{a=1}^{A}\beta^a\gamma_\alpha^a(C_V - C_A\gamma_5^a)\tau_+^a J_\alpha^a + h.c. \tag{B.6}$$

where the sum is over the total number of nucleons and the fermion current is expressed as

$$J_\alpha = \phi_e^\dagger\beta\gamma_\alpha\phi_\nu = \bar{\Psi}_e\gamma_\alpha\frac{1}{2}(1+\gamma_5)\Psi_\nu \tag{B.7}$$

and is evaluated at the nuclear radius of the A^{th} nucleon. The terms in the Hamiltonian are the same as those described in Ch. 2 for fermion interactions.

For allowed and 1^{st} non unique forbidden decays the shape correction is replaced with just the matrix element $\mathrm{S}(\pm\mathrm{Z},\mathrm{W}) \rightarrow \eta$. The form of the nuclear matrix elements is independent of the energy and Z of the nucleus. The correction takes the form of a simple sum

$$\eta = C_V^2\left\langle 1\right\rangle^2 + C_A^2\left\langle\sigma\right\rangle^2 \tag{B.8}$$

where $\langle\sigma\rangle$ is the Gamow-Teller β-moment and $\langle 1\rangle$ is the Fermi β-moment. Typically one of these terms will vanish depending on the total change in angular momentum.

In the normal approximation it can be seen from Eq. B.4 that the forbidden corrections are

proportional to $R^{2(J-1)}$. Furthermore, unique forbidden transitions are governed by a single beta moment of the form

$$M_j(J) = C_A R^{J-1} \left\langle \bar{\sigma} \cdot \bar{T}_J^{J-1} \right\rangle \tag{B.9}$$

and is also proportional to the power of the nuclear radius. The explicit form of the coupling can be found in ref [147]. Furthermore, Konopinski argues [145] that for unique forbidden decays the matrix elements are nearly constant. It therefore seems plausible to neglect the matrix elements in the sum as they are not energy dependent and only the first order term dominates allowing it to be pulled out of the sum and considered an overall constant.

The beta moments for non unique forbidden decays takes the form of

$$\begin{aligned} M_j(J) \ = C_V & \left[\left\langle \bar{\alpha} \cdot \bar{T}_{J-1}^{J} \right\rangle \mp \left(\frac{\alpha Z}{2j+1} \right) \left(\frac{J}{2J+a} \right)^{\frac{1}{2}} \langle Y_J \rangle \right] \\ & + \left(\frac{\alpha Z}{2j+1} \right) \left(\frac{J}{2J+a} \right)^{\frac{1}{2}} C_A \left\langle \bar{\sigma} \cdot \bar{T}_J^J \right\rangle \end{aligned} \tag{B.10}$$

where $\mp$ represents e^- and e^+ decays respectively. It can be seen that there is no additional radial dependence and in general for higher order moments one could expect cancellations or amplifications from the cross terms in the sum. However, most decays which are non unique forbidden decays tend to be of the 1^{st} order. This term is independent of energy and can treated as an overall constant. Furthermore the expected nuclear decays in KamLAND do not have high order non unique forbidden transitions and thus the contribution of the nuclear matrix elements are neglected in KBeta.

B.1.2 Electron Screening Correction

As a beta particle exits the nucleus it will be influenced by the Coulomb field of the nucleus accounted for by the Fermi correction. However, the assumption of the point charge Coulomb field needs to be corrected for due to the influence of the electron "cloud" orbiting the nucleus. The effect of the electron cloud would be to increase the kinetic energy of the electrons via a repulsive force. This term is most important for high Z elements and can produce up to a 2 - 3% correction in the shape. The electron screening correction is applied as a multiplicitive term, directly to Eq. B.2. It is given by the dimensionless factor [147]

$$\mathrm{F}(\pm \mathrm{Z}, \mathrm{W}) \rightarrow \mathrm{F}(\pm \mathrm{Z}, \mathrm{W} \mp \mathrm{V}_0) \left[\frac{(\mathrm{W} \mp \mathrm{V}_0)^2 - 1}{\mathrm{W}^2 - 1} \right]^{\frac{1}{2}} \left(\frac{\mathrm{W} \mp \mathrm{V}_0}{\mathrm{W}} \right) \tag{B.11}$$

where $V_0 \approx 1.13\alpha^2 Z^{\frac{4}{3}}$. Since S(±Z, W) is a correction due to the ability, or inability, of the atom to decay with the needed angular momenta electron screening does not influence this term.

There is a problem in the Fermi correction for the electron momentum if one considers electron screening at low energies. This is due to the momentum being represented as $p_e = \sqrt{(W - V_0)^2 - 1}$ in which there are now possible values for the electron kinetic energy which lead to imaginary momenta. In KBeta this is fixed by making $V_0 = 0$ when imaginary momenta are obtained. This obviously is not justified theoretically other then the observation that real particles must have real momenta. However, this effect only occurs for small momenta and thus energies below 100 keV which are not observable in KamLAND.

B.1.3 Energy Dependent Correction for Special Decays

Due to the nuclear matrix elements not being accounted for in the sum there are some instances in which the cancellation of terms does not occur and the matrix elements become energy dependent. For these decays there are analytical corrections from fits to data which provide an energy dependent correction to the allowed shape.

The most well known deviation from the expected shape is seen for ^{210}Bi [2]. Fits to data for ^{210}Bi were used to determine the correction factor provided by Daniel [151] are used in KBeta. The form for the energy dependent correction factor is

$$C(W) = 1 + aW + \frac{b}{W} = cW^2 \tag{B.12}$$

where a = 0.578, b = 28.466, and c = −0.658. ^{210}B is a first unique forbidden decay however the correction factor is used in place of S(±Z, W) to reproduce the experimentally measured beta spectrum for ^{210}Bi.

B.2 Verification of Spectral Shapes Generated with KBeta

To establish that the analytical functions were properly coded KBeta was tested with a separate code written by Hirsch [152], which produces allowed spectra, and tabulated values given in Landolt-Börnstein [149, 153]. First unique forbidden transitions were used to determine the correct form for

[2] In older literature ^{210}Bi is referred to as RaE. Radium decays are historically labeled from ^{226}Ra starting with ^{218}Po as RaA, ^{214}Pb as RaB, ^{214}Bi as RaC, ^{214}Po as RaC', ^{210}Tl as RaC*, ^{210}Bi as RaE and the rest of the decays follow sequentially.

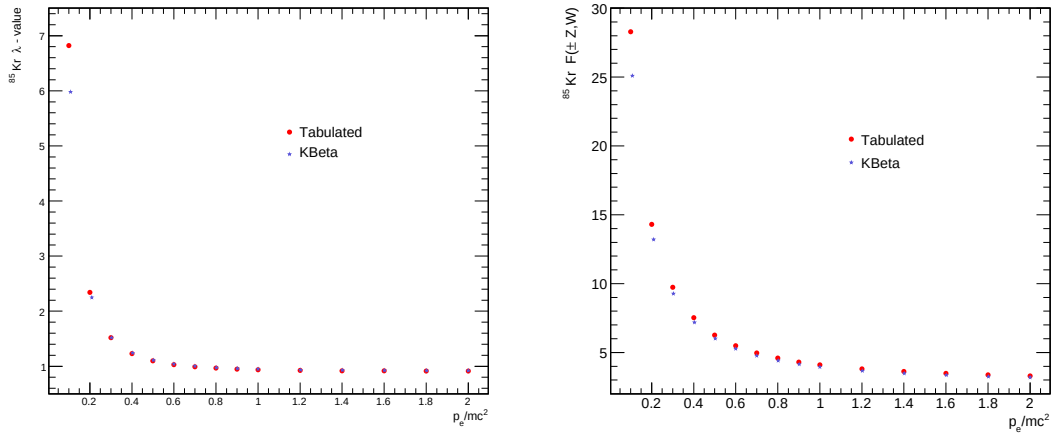

(a) (b)

Figure B.1: Fig. B.1(a) shows the calculated Lambda values from KBeta vs the tabulated values in Landolt-Börnstein [149] while Fig. B.1(b) shows the Fermi correction for ^{85}Kr.

$\frac{d\lambda}{dW}$ as the tabulated values provide the expected spectra for the statistical shape, Fermi corrected shape and forbidden corrections independently. Furthermore, a previous code which was written for allowed transitions was used to check the expected spectral shape.

B.2.1 First Unique Forbidden Decays of ^{39}Ar and ^{85}Kr

In comparing the two spectral forms given by Konopinski [145, 147] and Landolt-Börnstein [149], it was found that they did not match initially. To determine the cause for this inconsistency the terms in the Fermi correction and shape factor were analyzed independently with the tabulated data. KBeta spectra are produced in 1 keV bins and produces a smooth spectrum in comparison to what is obtained in the tables. To obtain a comparable curve from the tabulated values (which are tabulated in p_e) a linear interpolation of the data was performed. The functional form of the λ values is non-linear at low energy which fails to interpolate correctly. However, this is only a problem for energies below 40 keV which are deemed to be irrelevant for our purpose. Fig. B.1(b) show the calculated Fermi correction as a function of p_e. It can be seen that the generated values from KBeta matches the tabulated data very well for momenta greater than 0.3 which is equivalent to an electron kinetic energy (KamLAND's observable) of approximately 40 keV.

To determine the correct form for the shape factor, the sum in Eq. B.4 was initially expanded in

the low Z approximation proposed by Konopinski an Wu [145, 148]. This gives a shape factor

$$S(W, Z) = p_e^2 + (W_0 - W)^2. \tag{B.13}$$

However, this form does did not reproduce the spectra in the tables. The deviation was found to be due to the approximation $\alpha Z << 1$ not being valid. Konopinski suggests [145] a modification to this form such that

$$p_e^2 + (W_0 - W)^2 \longrightarrow p_e^2 + (W_0 - W)^2 + 9\frac{L_1}{L_0}. \tag{B.14}$$

The additional terms are obtained from tabulated values of the electron wave-functions. This correction is explained only as an effect due to large Z. Due to this explanation, the explicit form of the sum found in Konopinski [145] was used as it accounts for all Z. Since the shape factor in Landolt-Börnstein [149] is given as

$$C(W) = \frac{R^2}{9}({}^{A}F_{211}^{(0)})^2(p_\nu^2 + \lambda_2 p_e^2) \tag{B.15}$$

the expression given by Eq. B.4 for $S(\pm Z, W)$ was expanded to find the momentum dependent term λ_2 in the table. This was performed by expanding the sum for $\Delta J = 2$ which gives two terms, $j = \frac{1}{2}, \frac{3}{2}$. Separating terms and performing some algebra one can show that

$$\lambda_2 = 72\frac{\gamma + 2}{\gamma_0 + 1}(2pR)^{2(\gamma - \gamma_0 - 1)}\left[\frac{\Gamma(2\gamma_0 + 1)}{\Gamma(2\gamma + 1)}\right]^2\left|\frac{\Gamma(\gamma + i\nu)}{\Gamma(\gamma_0 + i\nu)}\right|^2. \tag{B.16}$$

Fig. B.1(a) shows the comparison between the calculated and tabulated λ value as a function of p_e. The values for λ_2 are comparable for $p_e > 0.2$, which corresponds to an electron kinetic energy of $\approx$ 10 keV. It can be verified that this expansion is the same as Eq. (3) in ref. [154].

The difference in beta spectra depicted in Fig. B.2 show a large variation in the spectral shapes between the purely statistical shape and the forbidden corrected shapes. While the spectra begin to converge at higher energy the deviation seen below 500 keV indicates the need for applying all known corrections to the purely statistical spectral shape.

The last correction which has not been tested was the correction due to electron screening as described in Eq. B.11. The beta spectra for ^{85}Kr were generated and compared with the electron screening correction. The correction due to the effect of orbital electrons is found to be less than a 1%. While the effect is negligable compared to the Fermi and shape factor corrections, it is still

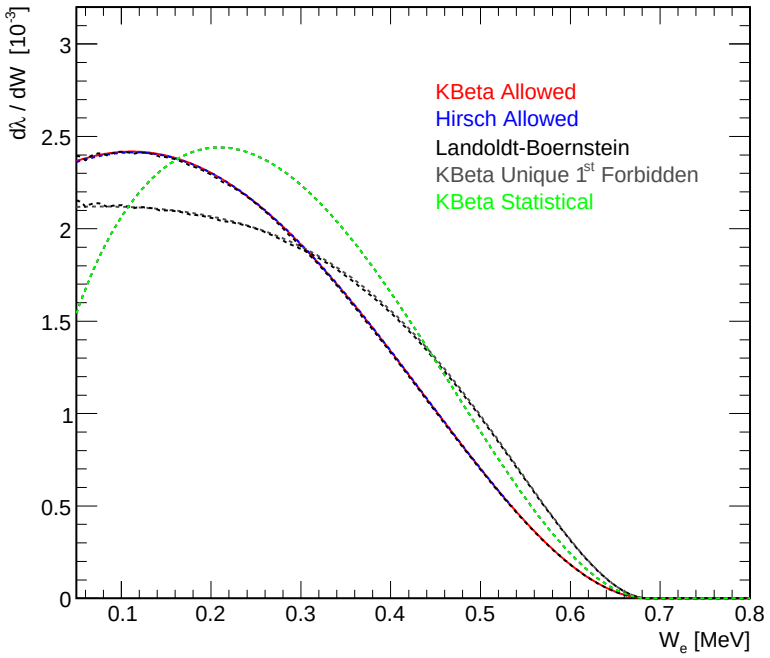

Figure B.2: Comparison of KBeta and tabulated beta spectra for ^{85}Kr for a purely statistical shape, Fermi corrected shape, and the expected shape after adding the forbiddeness correction. The Fermi corrected spectral shape was further cross-checked with a second code from Hirsch [152]. All three KBeta spectra agree to within 1% of the tabulated data above 80 keV. Below 80 keV the tabulated data is not smooth due to the breakdown in linear interpolation.

accounted for in the KBeta code.

The same analysis described for ^{85}Kr was applied to ^{39}Ar. The tabulated λ values and Fermi correction factors agree to within 1% except for momenta below 0.3 which is consistent with what was observed for ^{85}Kr. Fig. B.3 shows the statistical, allowed, and forbidden spectra for ^{39}Ar. There is very good agreement between the KBeta spectra, the tabulated spectra and the allowed spectrum from Hirsch [152].

B.2.2 Summary of Beta Decay Generator

The data shown in Fig. B.2 and B.3 indicate the need for an independent beta decay generator from that provided by Geant4 [143]. The functional form for the allowed decay is simple to implement in a beta decay generator but the spectral shapes are very different between the statistical, Fermi corrected and forbidden corrected spectra. Care was taken to expand the shape corrections to verify the assumptions which were made in the tabulated data.

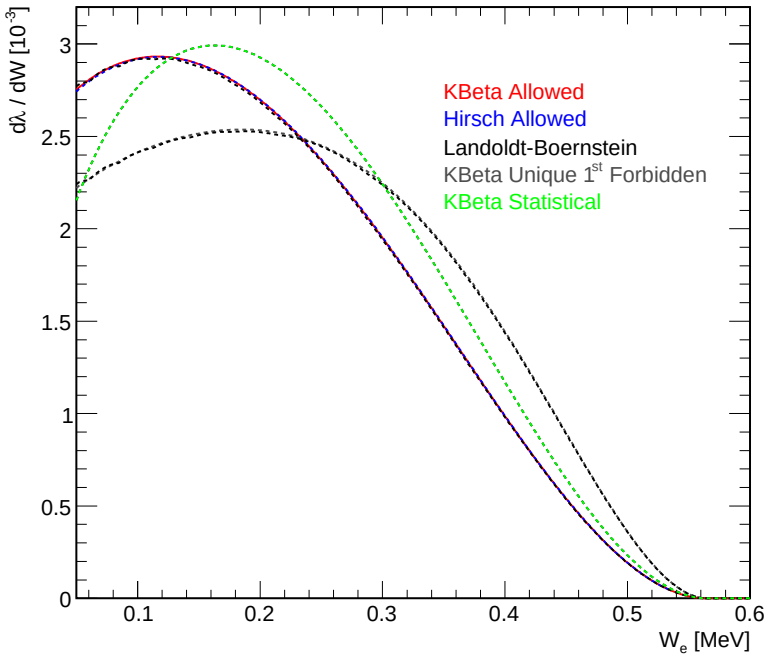

Figure B.3: Comparison of KBeta and tabulated beta spectra for ^{39}Ar for a purely statistical shape, Fermi corrected shape, and the expected shape after adding the forbiddeness correction. The Fermi corrected spectral shape was further cross-checked with a second code from Hirsch [152]. The data agree with the tabulated data to better then 1%.

In the verification of the spectra generated with KBeta the hard cut-off for imaginary momenta due to the electron screening potential in the Fermi function produce an adverse effect on the expected energy distribution. The deviation from the calculated energy spectrum are compared starting at 20 keV. From this point the KBeta generated spectra are consistent with the Landolt-Börnstein tabulated spectra to within < 1.0 % which is more then sufficient for KamLAND. Furthermore, this shows that the effect of the matrix elements on the unique forbidden decays of ^{39}Ar and ^{85}Kr are negligable and verifies the assumption that these matrix elements could be neglected.

While ^{39}Ar and ^{85}Kr are explicitly depicted in this appendix all the beta decays relevant to KamLAND have been tested against several other codes. The ^{40}K beta decay spectrum was tested against a code used to generate the expected geologically produced anti-neutrino spectrum [73] in KamLAND. The neutrino and electron energy spectra are related by energy conservation. This code uses an approximation provided by Konopinski and Rose for ^{40}K which is an expansion of the dominating terms in the sum in Eq. B.11. Furthermore there was no electron screening applied to the spectra and as such KBeta agreed to within a 2% of the alternate code.

Appendix C

Probability Density Functions for KamLAND Analysis

KBeta is the primary generator for KamLAND p.d.f. functions involving electron and positron decays and is described in detail in App. B. Unlike most experiments which look to measure the beta spectrum of specific nuclei, KamLAND is a calorimeter, and as such the beta spectra are not pure beta spectra in the sense that the detector records all energy deposited in the detector within a 250 ns time-window. Thus the beta emission will include the excited state gamma energies which are typically emitted on pico-second time-scales after the decay. The resultant effect on the beta spectra introduces and energy shift which is equal to the gamma ray energy. In the same manner, positrons emitted in the detector are shifted by the annihilation energy of 2×511 keV.

C.1 KamLAND's Energy Scale

Another effect that must be taken into account is the relationship between the expected real energy deposit and the resultant visible energy observed in the detector. Ionizing radiation produces a non-linear effect on the visible light deposit. For highly ionizing charged particles, such as alpha particles, the region around the particle can become completely ionized while the particle is coming to rest in the detector. Once this point is reached, no more particles can be ionized and thus the amount of visible light is reduced. Birk's formula [155] is used to model the effective loss in light due to quenching. The formula describing the light yield as a function of particle energy deposit is given

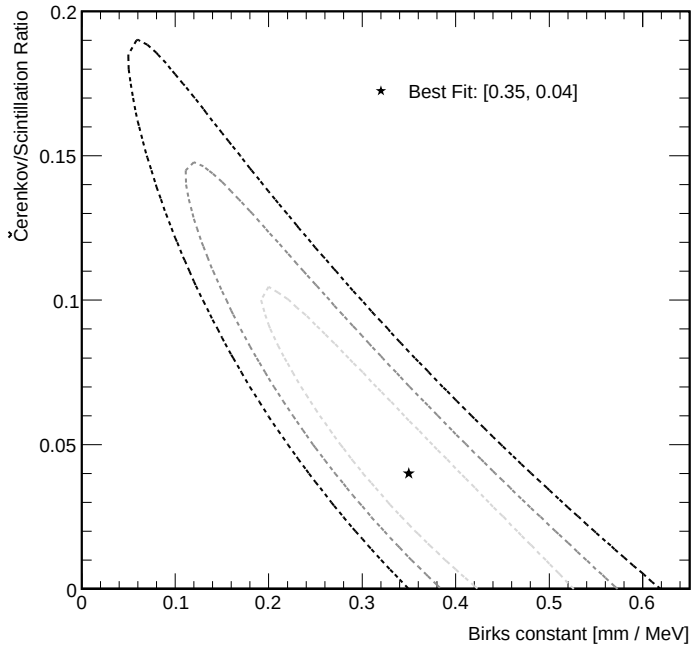

Figure C.1: Best fit value with 1, 2 and 3 sigma contours for fits to data yielding Birk's constant and the Čerenkov-to-Scintillation ratio in KamLAND.

by Birk's formula

$$\frac{dL}{dx} = \frac{S\frac{dE}{dx}}{1 + k_0\frac{dE}{dx}} \tag{C.1}$$

where k_0 is Birk's constant, L is the luminescence, S is the luminescence at low specific ionization density, dL/dx is the luminescence energy emitted per unit track length and dE/dx is the energy loss per unit track length in the LS. The numerator represents the density of damaged particles along the path of particle.

Birk's constant is a tunable parameter [78] and is calculated for KamLAND by fits to data. Fig. C.1 shows the contours and best fit value to Birk's constant yielding $k_0 = 0.35$ mm/MeV. Details on the fitted calibration data and methodology can be found in other work [76].

The resultant E_{Vis} to E_{real} conversion is calculated using a Monte Carlo to generate the dE/dx for different particle types and Birk's formula with the fitted values to produce the curves in Figs. C.2 and C.3. Overlaid on these figures are the mean fitted values with errors for the calibration data described in detail in Ch. 4.3.

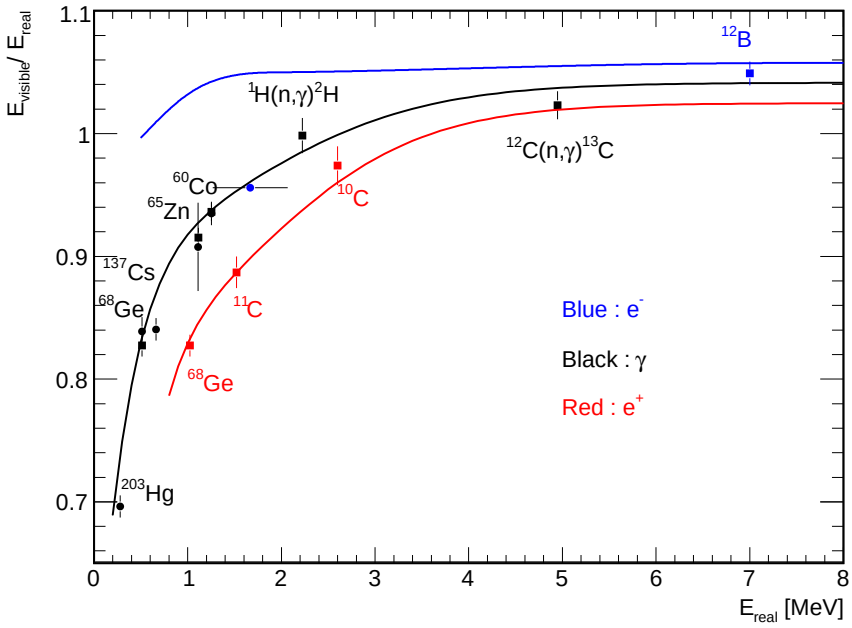

Figure C.2: Electron, Positron and Gamma E_{Vis} to E_{real} conversion factors based on Birk's quenching model. The measured calibration and in-situ measurement of different expected source data are shown to agree to within 3% over the entire energy scale and for all three particle types.

C.2 Generating a Beta Energy Spectrum for KamLAND

Once the real energy spectrum for electrons and positrons is calculated and the energy can be converted into the expected visible energy in KamLAND the p.d.f. function can be calculated. Let $f(E_{Vis})$ be the resultant p.d.f. needed to fit KamLAND data. As an example let us consider the decay scheme of ^{212}Bi depicted in Fig C.4. The level diagram shows that the beta particle leaves the ^{212}Po nucleus in 7 different states to include the ground state. Each of these states, i, is represented by a transition probability I_b^i where the transition to the ground state has $I_b = 55.46\%$. Furthermore, every transition results in a different total angular momentum and a total parity change of -1 and as App. B explained, this results in a different beta spectrum.

If the resultant nucleus is in an excited state it will transition to the grounds state via different modes, j, with different probabilities denoted by I_γ^j. The values listed in Fig. C.4 are a bit confusing as they are the total intensities for the gamma-ray and not the transition probability from that excited state. To get the transition probability one needs to take the sum of all the possible modes to get the absolute value and then divide each total intensity to get I_γ^j.

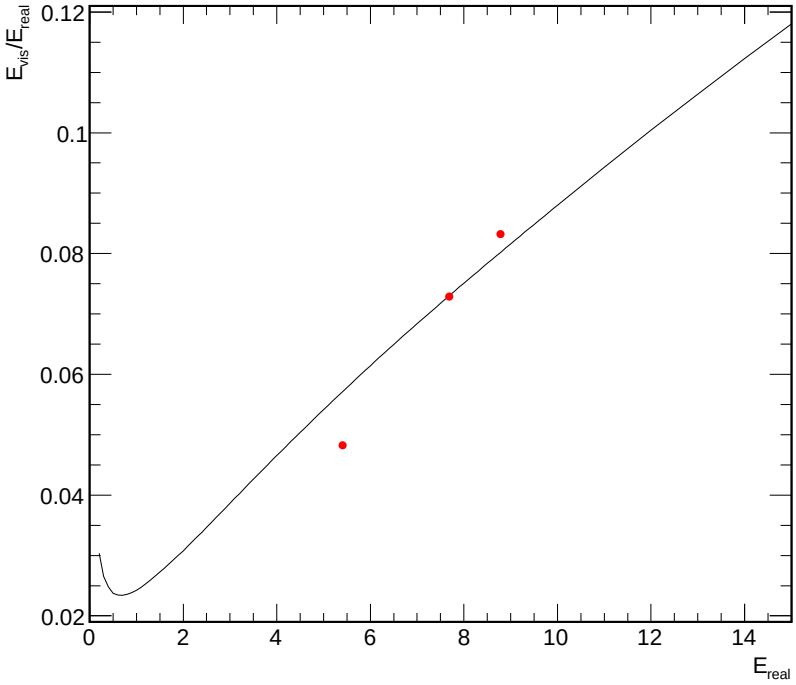

Figure C.3: E_{Vis} to E_{real} conversion for alpha particles in KamLAND. Alpha particles are highly ionizing which reduces the expected 8.784 MeV energy deposit of ^{212}Po to a visible energy of 0.731 MeV.

KBeta does not consider the possibility for internal conversion electrons to be emitted instead of the gamma ray from the nuclear de-excitations. This is a highly sub-dominant process and KamLAND has no particle identification. The internal conversion occurs only for $0^+ \rightarrow 0^+$ nuclear transitions and only effects the inner shell s-state electrons due to their overlapping wave-function with the nucleus. The internal conversion electron has an energy equal to $E_e = E_\gamma - E_B$ where E_B is the binding energy of the orbital electron. The total energy is conserved through E_e plus de-excitation gammas from the electrons which fill the missing inner shell. All of this occurs on pico-second time-scales and therefore the only effect seen in KamLAND would be a broadening of the gamma-ray line due to differences in quenching between the electrons and gamma-rays. These differences are less then the energy resolution of KamLAND and as such these transitions are not considered in the calculation of the beta spectrum.

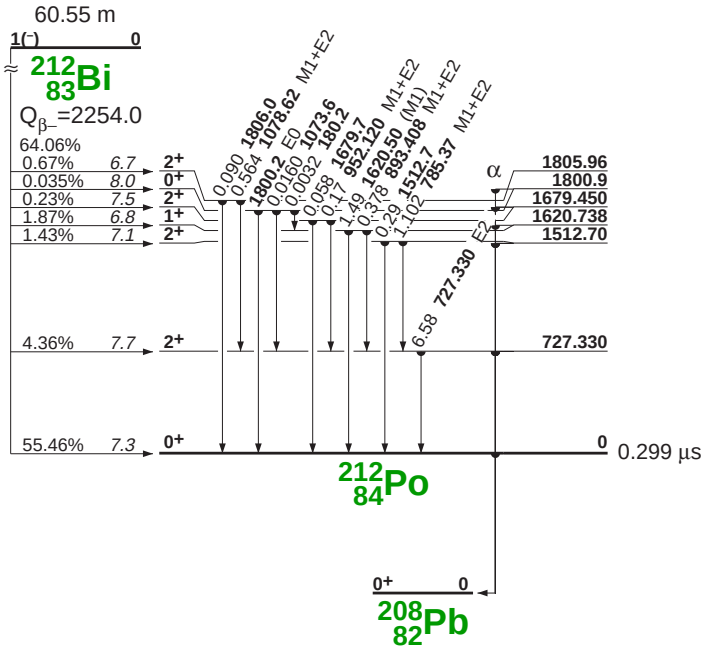

Figure C.4: ^{212}Bi beta decay transitions taken from the Table of Isotopes [156].

At this point the beta spectrum can be calculated as follows:

$$f(E) = \sum_{i}^{N} \sum_{j}^{M} I_b^i \, I_\gamma^j \int_0^\infty f(E_\beta + E_\gamma^j) \, dE_\beta \tag{C.2}$$

where $f(E_\beta)$ is the expected visible energy of the beta particle generated from KBeta with the total lepton angular momentum change ΔJ and parity change $\pi_i \pi_f$. From this point the visible gamma-ray energy, E_γ^j, must be added to the beta energy. The sums run over all possible gamma transitions M and all resultant nuclear states. There are special cases such as ^{85}Kr which has a meta-stable state of the excited state nucleus. If the transition time for a nuclear transition is beyond 150 ns then care must be taken to correctly consider electronics effects. Fig. C.2 shows the expected distribution after such summing for ^{220}Rn of which ^{212}Bi is apart of the plotted distribution. The effect of the addition of the gamma transitions are visible in the spectrum as step function transitions above the continuous beta spectrum. The delta function peaks are the addition of alpha energies which are summed according to their visible energies and expected branching ratios.

The spectrum looks coarse and if KamLAND had infinite energy resolution this would be the final product. However, this is not the case for any scintillation detector and Table 4.2 lists the measured

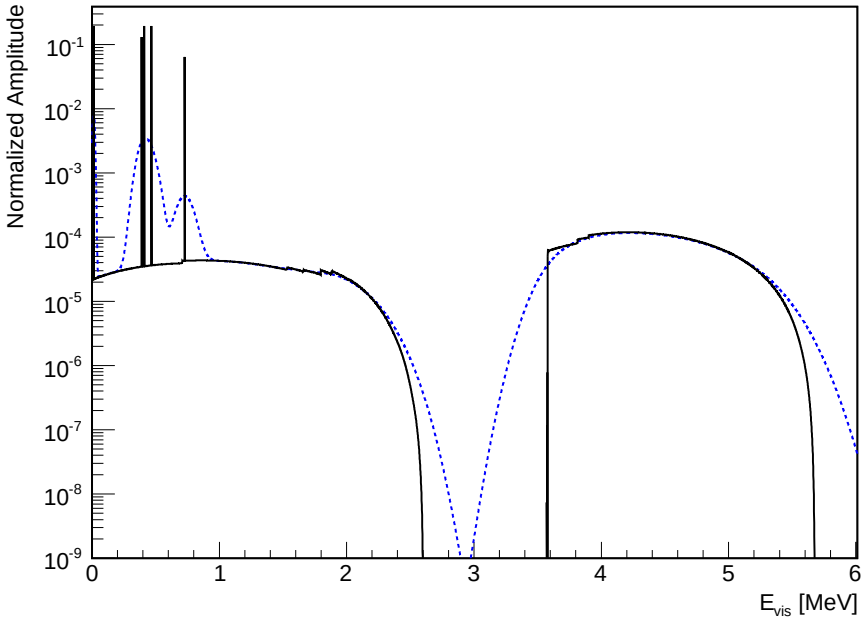

Figure C.5: The expected visible energy spectrum for the entire ^{220}Rn decay chain. The delta function lines are the points in which the alphas appear in the spectrum. The step function signature of the non-continuous beta functions is due to the addition of the transition gammas from the excited state nucleus. The blue dashed line overlaid on the plot is the resultant spectrum after adding detector response in the form of Gaussian smearing.

resolution measured from calibrations. Given the measured energy resolution, σ, the function in Eq. C.2 must be smeared according to

$$\mathrm{f(E_{Vis}; E, \sigma)} = \int_{-\infty}^{\infty} \mathrm{dE} \frac{\mathrm{f(E)}}{\sqrt{2\pi}\sigma} \mathrm{e}^{-(\mathrm{E_{vis}}-\mathrm{E})^2/2\sigma^2} \tag{C.3}$$

where now Ef($_{\mathrm{Vis}}$) represents the expected energy spectrum with the correct detector response as shown in by the spectrum represented by the blue dashed curve overlaid in Fig. C.2. This produces a continuous spectrum which is normalized to unity for fitting the KamLAND data.

Bibliography

[1] C. L. Cowan, Jr. et al. Detection of the Free Neutrino: A Confirmation. *Science*, pages 103–104, 1956.

[2] B. T. Cleveland et al. Measurement of the solar electron neutrino flux with the Homestake chlorine detector. *Astrophys. J.*, 496:505–526, 1998.

[3] J. Bahcall and R. Davis, Jr. Solar Neutrinos: A Scientific Puzzle. *Science*, 1:264–267, Jan 1976.

[4] M. Altmann et al. GNO solar neutrino observations: results for GNO I. *Phys. Lett. B*, 490(1-2):16 – 26, 2000.

[5] J. N. Abdurashitov et al. Measurement of the solar neutrino capture rate by the Russian-American gallium solar neutrino experiment during one half of the 22-year cycle of solar activity. *J. Exp. Theor. Phys.*, 95:181–193, 2002.

[6] K. S. Hirata et al. Results from one thousand days of real-time, directional solar-neutrino data. *Phys. Rev. Lett.*, 65(11):1297–1300, Sep 1990.

[7] Q. R. Ahmad et al. Measurement of the Rate of $\nu_e + d \rightarrow p + p + e^-$ Interactions Produced by ^8B Solar Neutrinos at the Sudbury Neutrino Observatory. *Phys. Rev. Lett.*, 87(7):071301, Jul 2001.

[8] S. Fukuda et al. Solar ^8B and hep Neutrino Measurements from 1258 Days of Super-Kamiokande Data. *Phys. Rev. Lett.*, 86:5651–5655, 2001.

[9] S. Abe et al. Precision Measurement of Neutrino Oscillation Parameters with KamLAND. *Phys. Rev. Lett.*, 100:221803, 2008.

[10] Q. R. Ahmad et al. Direct Evidence for Neutrino Flavor Transformation from Neutral-Current Interactions in the Sudbury Neutrino Observatory. *Phys. Rev. Lett.*, 89(1):011301, Jun 2002.

[11] L. Wolfenstein. Neutrino oscillations in matter. *Phys. Rev. D*, 17(9):2369–2374, May 1978.

[12] S. P. Mikheev and A. I. Smirnov. Resonant amplification of neutrino oscillations in matter and solar-neutrino spectroscopy. *Nuovo Cimento C*, 9:17–26, February 1986.

[13] C. A. Iglesias and F. J. Rogers. Updated Opal Opacities. *Astrophys. J.*, 464, June 1996.

[14] N. R. Badnell et al. Updated opacities from the Opacity Project. *Mon. Not. R. Astron. Soc.*, 360:458–464, June 2005.

[15] Solar Heliospheric Observatory (SOHO) spacecraft Michelson Doppler Imager (MDI) project. `http://soi.stanford.edu/`.

[16] C. Pena-Garay and A. Serenelli. Solar neutrinos and the solar composition problem. 2008.

[17] C. Arpesella et al. Direct Measurement of the ^{7}Be Solar Neutrino Flux with 192 Days of Borexino Data. *Phys. Rev. Lett.*, 101(9):091302, 2008.

[18] T. Araki et al. Experimental Investigation of Geologically Produced Antineutrinos with KamLAND. *Nature*, 436:499, 2005.

[19] J. Bahcall. *Neutrino astrophysics*. Cambridge University Press, 1989.

[20] F. Boem and P. Vogel. *Physics of Massive Neutrinos*. Cambridge University Press, second edition, 2003.

[21] F. Kayser, B. with Gibrat-Debu and F. Perrier. *The Physics of Massive Neutrinos*. World Scientific Lecture Notes in Physics Vol. 25. World Scientific Publishing Co., 1989.

[22] C. Quigg. *Gauge Theories of the Strong, Weak, and Electromagnetic Interactions*. Advanced Book Classics. Westview Press, first edition, 1997.

[23] M. C. Gonzalez-Garcia and M. Maltoni. Phenomenology with Massive Neutrinos. *"Phys. Rep.*, 460:1–129, 2008.

[24] S. L. Glashow. Partial Symmetries of Weak Interactions. *Nucl. Phys.*, 22:579–588, 1961.

[25] S. Weinberg. A Model of Leptons. *Phys. Rev. Lett.*, 19(21):1264–1266, Nov 1967.

[26] E. C. G. Sudarshan. Elementary Particle Theory: Relativistic Groups and Analyticity. *Nobel Symposium 8*, pages 367–377, 1968.

[27] R. Mohapatra and G. Senjanović. Neutrino Mass and Spontaneous Parity Nonconservation. *Phys. Rev. Lett.*, 44(14):912–915, Apr 1980.

[28] S. F. King. Neutrino Physics. *arXiv:0712.1750v1*, 2007.

[29] G. 't Hooft. Prediction for neutrino-electron cross-sections in Weinberg's model of weak interactions. *Phys. Lett. B*, 37(2):195 – 196, 1971.

[30] P. Vogel and J. Engel. Neutrino electromagnetic form factors. *Phys. Rev. D*, 39(11):3378–3383, Jun 1989.

[31] J. Bahcall. Neutrino-electron scattering and solar neutrino experiments. *Rev. Mod. Phys.*, 59(2):505–521, Apr 1987.

[32] J. Bahcall, M. Kamionkowski, and A. Sirlin. Solar neutrinos: Radiative corrections in neutrino-electron scattering experiments. *Phys. Rev. D*, 51(11):6146–6158, Jun 1995.

[33] L. B. Okun. *Sov. J. Nucl. Phys.*, 44:546–549, 1986.

[34] J. F. Beacom and P. Vogel. Neutrino Magnetic Moments, Flavor Mixing, and the Super-Kamiokande Solar Data. *Phys. Rev. Lett.*, 83(25):5222–5225, Dec 1999.

[35] H. T. Wong et al. Search of Neutrino Magnetic Moments with a High-Purity Germanium Detector at the Kuo-Sheng Nuclear Power Station. *Phys. Rev.*, D75:012001, 2007.

[36] A. G. Beda et al. The first result of the neutrino magnetic moment measurement in the GEMMA experiment. 2007.

[37] D. W. Liu et al. Limit On the Neutrino Magnetic Moment Using 1496 Days of Super-Kamiokande-I Solar Neutrino Data. *Phys. Rev. Lett.*, 93:021802, 2004.

[38] Ziro M., Masami N., and Shoichi S. Remarks on the Unified Model of Elementary Particles. *Prog. Theor. Phys.*, 28(5):870–880, 1962.

[39] B. M. Pontecorvo. Neutrino experiments and the conservation of lepton charge. *Zh. Eksp. Teor. Fiz+*, 53:1717–1725, 1967.

[40] C. Amsler et al. Review of Particle Physics. *Phys. Lett. B*, 667(1-5):1 – 6, 2008.

[41] C. Kraus et al. Final Results from phase II of the Mainz Neutrino Mass Search in Tritium β Decay. *Eur. Phys. J.*, C40:447–468, 2005.

[42] R. D. McKeown and P. Vogel. Neutrino masses and oscillations: Triumphs and challenges. *"Phys. Rep.*, 394:315–356, 2004.

[43] V. Barger, D. Marfatia, and K. Whisnant. Progress in the physics of massive neutrinos. *Int. J. Mod. Phys.*, E12:569–647, 2003.

[44] T. Schwetz, M. Tortola, and J. W. F. Valle. Three-flavour neutrino oscillation update. *New J. Phys.*, 10:113011, 2008.

[45] P. Adamson et al. Measurement of Neutrino Oscillations with the MINOS Detectors in the NuMI Beam. *Phys. Rev. Lett.*, 101:131802, 2008.

[46] M. Apollonio et al. Limits on Neutrino Oscillations from the CHOOZ Experiment. *Phys. Lett.*, B466:415–430, 1999.

[47] J. Bahcall, P. I. Krastev, and A. Yu. Smirnov. Where do we stand with solar neutrino oscillations? *Phys. Rev.*, D58:096016, 1998.

[48] S. J. Parke. Nonadiabatic Level Crossing in Resonant Neutrino Oscillations. *Phys. Rev. Lett.*, 57(10):1275–1278, Sep 1986.

[49] J. F. Beacom and A. B. Balantekin. A semiclassical approach to level crossing in supersymmetric quantum mechanics. *hep-th/9709117*, 1997.

[50] T. K. Kuo and J. Pantaleone. Neutrino oscillations in matter. *Rev. Mod. Phys.*, 61(4):937–979, Oct 1989.

[51] A. B. Balantekin. Exact solutions for matter-enhanced neutrino oscillations. *Phys. Rev. D*, 58(1):013001, May 1998.

[52] L. D. Landau. *Phys. Z. (USSR)*, 1:426, 1932.

[53] C. Zemmer. *Proc. Roy. Soc.*, A(137):696, 1932.

[54] M. Bruggen, W. C. Haxton, and Y.-Z. Qian. Landau-Zener treatments of solar neutrino oscillations. *Phys. Rev. D*, 51(8):4028–4034, Apr 1995.

[55] D. Nötzold. Exact analytic solutions for Mikheyev-Smirnov-Wolfenstein level crossings. *Phys. Rev. D*, 36(6):1625–1633, Sep 1987.

[56] J. Bahcall. Solar Neutrinos. I. Theoretical. *Phys. Rev. Lett.*, 12(11):300–302, Mar 1964.

[57] R. Davis, Jr. Solar Neutrinos. II. Experimental. *Phys. Rev. Lett.*, 12(11):303–305, Mar 1964.

[58] J. Bahcall et al. Standard solar models and the uncertainties in predicted capture rates of solar neutrinos. *Rev. Mod. Phys.*, 54(3):767–799, Jul 1982.

[59] J. N. Bahcall, A. M. Serenelli, and S. Basu. New solar opacities, abundances, helioseismology, and neutrino fluxes. *Astrophys. J.*, 621:L85, 2005.

[60] E. G. Adelberger et al. Solar fusion cross sections. *Rev. Mod. Phys.*, 70(4):1265–1291, Oct 1998.

[61] J. Bahcall, A. Serenelli, and S. Basu. New solar opacities, abundances, helioseismology, and neutrino fluxes. *Astrophys. J.*, 621:L85–L88, 2005.

[62] R. Mitalas and K. R. Sills. On the photon diffusion time scale for the sun. *Astrophys. J.*, 401:759, December 1992.

[63] W. T. Winter et al. The ^{8}B neutrino spectrum. *Phys. Rev. C*, 73(2):025503, 2006.

[64] J. Bahcall. Software and Data for Solar Neutrino Research. `http://www.sns.ias.edu/~jnb/SNdata/sndata.html`.

[65] L. C. Stonehill, J. A. Formaggio, and R. G. H. Robertson. Solar neutrinos from CNO electron capture. *Phys. Rev. C*, 69(1):015801, Jan 2004.

[66] L. Winslow. *First Solar Neutrinos from KamLAND: A Measurement of the ^{8}B Solar Neutrino Flux*. PhD thesis, University of California, Berkeley, 2008.

[67] K. S. Hirata et al. Experimental Study of the Atmospheric Neutrino Flux. *Phys. Lett.*, B205:416, 1988.

[68] R. J. Kumar. Characterization of the Hamamatsu R1449 PMT tube. Master's thesis, Queens University, Kingston, Ontario, Canada, 1987.

[69] W. Jiang. Pulse Measurement for 17-inches KamLAND Photomultiplier Tube. Master's thesis, The University of Tennessee, Knoxville, Tennessee, 2002.

[70] W-IE-NE-R, Plein and Baus, Ltd., Burscheid, Germany. 6000 Series VME Crates. `http://www.wiener-d.com/index2.php`.

[71] N. Tolich. *Experimental Study of Terrestrial Electron Anti-Neutrinos with KamLAND*. PhD thesis, Stanford University, California, 2005.

[72] K. Tolich. *Measurement of Neutrino Oscillation Parameters and Investigation of Uranium and Thorium Abundances in the Earth using Anti-Neutrinos*. PhD thesis, Stanford University, California, 2008.

[73] S. Enomoto. *Neutrino Geophysics and Observation of Geo-Neutrinos at KamLAND*. PhD thesis, Tohoku University, Sendai, Japan, 2005.

[74] O. Tajima. *Measurement of Electron Anti-Neutrino Oscillation Parameters with a Large Volume Liquid Scintillator Detector, KamLAND*. PhD thesis, Tohoku University, Sendai, Japan, 2003.

[75] I. Shimizu. *An Evidence for Spectral Distortion of Reactor Anti-Neutrinos and A Study of Three Flavor Neutrino Oscillation*. PhD thesis, Tohoku University, Sendai, Japan, 2004.

[76] K. Ichimura. *Precise measurement of neutrino oscillation parameters with KamLAND*. PhD thesis, Tohoku University, Sendai, Japan, 2008.

[77] M. Batygov. *Combined Study of Reactor and Terrestrieal Antineutrinos with KamLAND*. PhD thesis, The University of Tennessee, Knoxville, Tennessee, 2006.

[78] G. F. Knoll. *Radiation Detection and Measurement*. John Wiley and Sons Inc., 3rd edition, 2000.

[79] G. Cowan. *Statistical Data Analysis*. Oxford University Press, 2002.

[80] Abe, S. and others. Study of the Production of Radioactive Isotopes through Cosmic Muon Spallation in KamLAND. 2009. Submitted to Phys. Rev. C.

[81] T. Araki et al. Measurement of neutrino oscillation with KamLAND: Evidence of spectral distortion. *Phys. Rev. Lett.*, 94:081801, 2005.

[82] B. E. Berger et al. The KamLAND full-volume calibration system. *J. Instrum.*, 4(04):P04017, 2009.

[83] J. Beacom, W. Farr, and P. Vogel. Detection of supernova neutrinos by neutrino-proton elastic scattering. *Phys. Rev. D*, 66(3):033001, Aug 2002.

[84] L. Cadonati, F. P. Calaprice, and M. C. Chen. Supernova neutrino detection in Borexino. *Astropart. Phys.*, 16(4):361 – 372, 2002.

[85] K. Eguchi et al. First results from KamLAND: Evidence for reactor anti-neutrino disappearance. *Phys. Rev. Lett.*, 90:021802, 2003.

[86] L. Hoffman et al. Background Estimates for KamLAND from Natural Radiactivity of the Detector. *Internal KamLAND Note*, 2001.

[87] A. Piepke. Summary of KamLAND material samples measured by low level gamma ray spectroscopy. *Internal KamLAND Note*.

[88] Z. Djurcic et al. Novel technique for ultra-sensitive determination of trace elements in organic scintillators. *Nucl. Instrum. Meth. A*, 507(3):680 – 690, 2003.

[89] National Nuclear Data Center (NNDC) Database. `http://www.nndc.bnl.gov/ensdf/index.jsp`.

[90] ROOT: An Object-Oriented Data Analysis Framework. `http://root.cern.ch/root/`.

[91] MINUIT - Function Minimization and Error Analysis. `http://wwwasdoc.web.cern.ch/wwwasdoc/minuit/minmain.html`.

[92] Baker S. and R. D. Cousins. Clarification of the use of CHI-square and likelihood functions in fits to histograms. *Nucl. Instrum. Meth.*, 221(2):437 – 442, 1984.

[93] G. Alimonti et al. Measurement of the ^{14}C abundance in a low-background liquid scintillator. *Phys. Lett. B*, 422(1-4):349 – 358, 1998.

[94] J. Shirai. KamLAND Collaboration Meeting, 2005.

[95] C. Sutour et al. Determination of the argon concentration in ambient dry air for the calculation of air density. *Metrologia*, 44(6):448–452, 2007.

[96] P. Collon, W. Kutschera, and Z. Lu. Tracing Noble Gas Radionuclides in the Environment. *Annu. Rev. Nucl. Part. S.*, 54:39–67, 2004.

[97] P. Hesse et al. Solubility of Gases in Liquids. 20. Solubility of He, Ne, Ar, Kr, N_2,O_2,CH_4,CH_4, and SF_6 in *n*-Alkanes *n*-C_lH_{2l+2} ($6 \leq l \leq 16$) at 298.15 K. *J. Chem. Eng. Data*, 41:195–201, 1996.

[98] N. Aoki and Y. Makide. The Concentration of Krypton in the Atmosphere -Its Revision after Half a Century-. *Chem. Lett.*, 34(10):1396, 2005.

[99] M. J. Berger et al. Xcom: Photon cross section database (version 1.4). `http://physics.nist.gov/xcom`, 2009.

[100] T. Hagner et al. Muon-induced production of radioactive isotopes in scintillation detectors. *Astropart. Phys.*, 14(1):33 – 47, 2000.

[101] Li Cang. private communication. Provided many useful discussions on adsorbents as well as supplied all Selecto silica gels.

[102] K Shaughnessy. private communication. Provided Gas Chromatograph and useful discussions on adsorbents.

[103] G. Schweitzer. private communication. Assisted in work performed on understanding the organo-metallic component of ^{212}Pb in LS.

[104] L. S. Niedermeier. *High Efficiency Purification of Liquid Scintillators for the Solar Neutrino Experiment Borexino*. PhD thesis, University of Technology, Munich, 2005.

[105] L. Niedermeier et al. Experimental scintillator purification tests with silica gel chromotography. *Nucl. Instrum. Meth. A*, 568:915, 2006.

[106] K. K. Unger. *Porous Silica, its properties and use as support in column liquid chromatography*, volume 16 of *J. Chromatogr. Lib.* Elsevier, New York, NY, 1979.

[107] L. T. Zhuravlev. Concentration of Hydroxyl Groups on the Surface of Amorphous Silicas. *Langmuir*, 3:316–318, 1987.

[108] D. S. Leanard et al. Systematic study of trace radioactive impurities in candidate construction materials for EXO-200. *Nucl. Instrum. Meth. A*, 591:490–509, 2008.

[109] Pylon Electronics Inc. `http://www.pylonelectronics.com/pylonradioactive.php`. Model Numbers: RN-1025 and TH-1025.

[110] PerminElmer, Inc., Waltham, MA, USA. Purchase of Packard PPO, which is sold under the PerkinElmer name. `http://www.perkinelmer.com/default.htm`.

[111] K. Nakajima. *Measurement of Neutrino Oscillation Parameters with Precise Calculation of Reactor Neutrino Spetrum at KamLAND*. PhD thesis, Tohoku University, Sendai, Japan, 2005.

[112] Y Koseki. KamLAND Collaboration Meeting, Sendai, 2003.

[113] T. C. Andersen et al. A radium assay technique using hydrous titanium oxide adsorbent for the Sudbury Neutrino Observatory. *Nucl. Instrum. Meth. A*, 501:386–398, 2003.

[114] Travel Spots Review. `http://travelspots.mayacreative.com/sears-tower/`. The surface area of the Sears Tower quoted was 502,320 square yards = 4.2×10^5 m^3.

[115] S. Tabuse et al. Radiation protection effects by addition of aromatic compounds to n-dodecane. *Radiat. Phys. Chem.*, 62:179–187, 2001.

[116] Y. Kamyshkov. private communication. Assisted in work performed on understanding the organo-metallic component of ^{212}Pb in LS.

[117] E. L. Feinberg. Ionization of the Atom Due to β-Decay. 4(5):423, 1941.

[118] J. S. Levinger. Effects of Radioactive Disintegrations on Inner Electrons of the Atom. *Phys. Rev.*, 90(1):11–25, Apr 1953.

[119] H. M. Schwartz. Theory of Atomic Perturbation in Alpha Decay. *Phys. Rev.*, 100(1):135–137, Oct 1955.

[120] T. Iwamoto. *Measurement of Reactor Anti-Neutrino Disappearance in KamLAND*. PhD thesis, Tohoku University, Sendai, Japan, 2003.

[121] D. Lide, editor. *CRC Handbook of Chemistry and Physics, Sec. 3: Physical Constants of Organic Compounds*. Chemical Rubber Publishing Company, Boca Raton, Florida, 89 edition, 2008-2009.

[122] B. K. Chodhuri et al. *Defence Sci. J.*, 2:34–44, 1961.

[123] M. S. Kharasch. Process of deleading gasoline. *US Patent 2453138*, November 1948.

[124] A. Furuta et al. *JP Patent 97,170411*, 1992.

[125] A. Deratani and B. Sebille. Metal ion extraction with a thiol hydrophilic resin. *Anal. Chem.*, 53(12):1742–1746, 1981.

[126] G. J. Feldman and R. D. Cousins. Unified approach to the classical statistical analysis of small signals. *Phys. Rev. D*, 57(7):3873–3889, Apr 1998.

[127] M. Ogawa. KamLAND Collaboration Meeting, Hilo, 2004.

[128] S. Takeuchi. KamLAND Collaboration Meeting, Hilo, 2004.

[129] M. Ogawa. Liquid Scintillator Purification for Solar Neutrino Observation with KamLAND: Studies on Lead Reduction by Distillation. Master's thesis, Tohoku University, Sendai, Japan, 2005. Written in Japanese.

[130] S. Takeuchi. Research and Development on Distillation-Purification for KamLAND Liquid Scintillator with respect to a ^{7}Be Solar Neutrino Measurment. Master's thesis, Tohoku University, Sendai, Japan, 2005. Written in Japanese.

[131] Dojindo Molecular Technologies, Inc., Rockville, MD, USA. Purchase of new DPO. `http://www.dojindo.com`.

[132] S. Fukuda et al. The Super-Kamiokande detector. *Nucl. Instrum. Meth. A*, 501(2-3):418 – 462, 2003.

[133] Air Water Inc., Osaka, Japan. Supplier of the Nitrogen Supply System. `http://www.awi.co.jp/english/index.html`.

[134] K. Nakajima. High Sensitivity Radon Detector Using a Concentration Method. Master's thesis, Tohoku University, Sendai, Japan, 2007. Written in Japanese.

[135] C. Zhang. This system will be described in greater detail in his doctoral thesis. The description was taken from collaboration meeting talks and personal correspondence.

[136] Y. Konno. Development of Radon Detector for Liquid Scintillator. Master's thesis, Tohoku University, Sendai, Japan, 2007. Written in Japanese.

[137] A. Piepke. Technical Note, 1995.

[138] National Instruments, Inc. , Austin, Tx, USA. LabView is a commercially available programs. `http://www.ni.com/labview/`.

[139] New Micros, Inc. Max-FORTH in a Nutshell, http://forth.newmicros.com/.

[140] Anton Paar, Österreich, Austria. Model DMA 4500. http://www.anton-paar.com/001/en/60/413.

[141] J. Benziger et al. A scintillator purification system for the Borexino solar neutrino detector. *Nucl. Instrum. Meth. A*, 587:277–291, 2008.

[142] C. Arpesella et al. First real time detection of ^{7}Be solar neutrinos by Borexino. *Phys. Lett. B*, 658(4):101 – 108, 2008.

[143] S. Agostinelli et al. G4– A Simulation Toolkit. *Nucl. Instrum. Meth. A*, 506(3):250 – 303, 2003. http://geant4.web.cern.ch/geant4/.

[144] G. Horton-Smith. Generic Liquid-scintillator Anti-Neutrino Detector Geant4 Simulation (GLG4sim). http://neutrino.phys.ksu.edu/~GLG4sim/.

[145] E. J. Konopinski. *The Theory of Beta Radioactivity*. Oxford Univ. Press, New York, 1966.

[146] E. J. Konopinski and G. E. Uhlenbeck. On the Fermi Theory of β-Radioactivity. II. The "Forbidden" Spectra. *Phys. Rev.*, 60(4):308–320, Aug 1941.

[147] E. J. Konopinski and Rose M. E. *Alpha-, Beta- and Gamma-Ray Spectroscopy*. North-Holland, Amsterdam, 1965.

[148] Chien-shiung Wu. Recent Investigation of the Shapes of β-Ray Spectra. *Rev. Mod. Phys.*, 22(4):386–398, Oct 1950.

[149] Behrens and Janecke. *Numerical Data and Functional Relationships in Science and Technology*, volume 4 of *Numerical Tables for beta decay and electron capture*. Springer-Verlag, Berlin-Heidelberg-New York, 1969.

[150] F. E. Wietfeldt et al. Further studies on the evidence for a 17-kev neutrino in a ^{14}doped germanium detector. *Phys. Rev. C*, 52(2):1028–1040, Aug 1995.

[151] H. Daniel. Das β-spektrum des RaE. *Nucl. Phys.*, 31:293 – 307, 1962.

[152] M. Hirsch. private communication.

[153] P. Vogel. private communication.

[154] J. P. Davidson. The First Forbidden Shape Factor and the fnt Products for Beta-Decay. *Phys. Rev.*, 82(1):48–51, Apr 1951.

[155] J. B. Birks. Scintillations from Organic Crystals: Specific Fluorescence and Relative Response to Different Radiations. *P. Phys. Soc. Lond. A*, 64(10):874–877, 1951.

[156] R. Firestone. *Table of Isotopes CD-ROM*.